

# Dissertation

submitted to the

Combined Faculty of Natural Sciences and Mathematics

of Heidelberg University, Germany

for the degree of

Doctor of Natural Sciences

Put forward by

**Meike Kerrin Rotermund**

*Born in: Berlin, Germany*

*Oral examination: June 8, 2021*



**Organic, inorganic and total bromine in the  
extratropical tropopause and lowermost  
stratosphere in fall 2017: Origins, transport  
pathways and consequences for ozone**

**Referees:**

Prof. Dr. Klaus Pfeilsticker

Prof. Dr. Thomas Leisner

*In loving memory of my Grampa.*

## Abstract

Inferred total bromine ( $\text{Br}^{\text{tot}}$ ) was measured in the upper troposphere (UT) and lower stratosphere (LS) from a research aircraft over the North Atlantic and north western Europe in fall 2017 during the WISE (Wave-driven ISentropic Exchange) campaign. The LS weighted-mean  $\text{Br}^{\text{tot}}$  is  $19.2 \pm 1.2$  ppt. A closer look into organic and inorganic bromine, as well as simultaneously measured transport and air mass lag-time tracers, suggests that bromine-rich air masses persistently protruded into the LS in fall creating a high bromine region (HBrR). A subsection, HBrR\*, has a  $\text{Br}^{\text{tot}}$  weighted average of  $20.9 \pm 0.8$  ppt. The most probable source region is former tropical UT air with a  $\text{Br}^{\text{tot}}$  weighted mean of  $21.6 \pm 0.7$  ppt. A secondary smaller source is transport across the extratropical tropopause. Lagrangian transport modelling quantifies these multi-pathway contributions to the LS and HBrR. Further, the influences of the Asian monsoon and its tropical adjacent regions as well as tropical cyclones from Central America on bromine are discussed. And lastly, the consequences of  $\sim 1\text{--}2$  ppt additional bromine in the tropical UT are simulated by a global chemistry transport model resulting in  $3.1 \pm 0.7\%$  ozone decrease within the 20 K potential temperature layer directly above the tropopause.

## Zusammenfassung

Das abgeleitete Gesamtbrom ( $\text{Br}^{\text{tot}}$ ) wurde im Herbst 2017 in der oberen Troposphäre (UT) und unteren Stratosphäre (LS) von einem Forschungsflugzeug über dem Nordatlantik und Nordwesteuropa während der WISE-Kampagne (Wave-driven ISentropic Exchange) gemessen. Der gewichtete Mittelwert  $\text{Br}^{\text{tot}}$  der LS beträgt  $19,2 \pm 1,2$  ppt. Ein genauerer Blick auf organisches und anorganisches Brom sowie gleichzeitig gemessene Transport- und Luftmassenalter-Tracer deutet darauf hin, dass im Herbst bromreiche Luftmassen in die LS transportiert werden, und sie dort eine Region mit hohem Bromgehalt (HBrR) bilden. Eine Untermenge, HBrR\*, hat einen  $\text{Br}^{\text{tot}}$  gewichteten Durchschnitt von  $20,9 \pm 0,8$  ppt. Die wahrscheinlichste Quellregion ist ehemalige Luft aus der tropischen UT mit einem gewichteten  $\text{Br}^{\text{tot}}$  Mittelwert von  $21,6 \pm 0,7$  ppt. Eine sekundäre, relativ kleinere Quelle ist der Transport durch die extratropische Tropopause. Eine Lagrange Modellierung des Transports quantifiziert diese unterschiedlichen Transportweg-Beiträge zu der LS und HBrR. Weiterhin werden die Einflüsse des asiatischen Monsuns und seiner angrenzenden tropischen Regionen sowie von tropischen Stürmen über Mittelamerika auf das UT und LS Brom diskutiert. Abschließend werden die Konsequenzen von  $\sim 1\text{--}2$  ppt zusätzliches Brom in der tropischen UT durch ein globales Chemietransportmodell simuliert welches  $3,1 \pm 0,7\%$  des Ozons in der 20 K Potentielle Temperatur Schicht direkt oberhalb der Tropopause zerstört.



# Contents

<b>Glossary</b>	<b>9</b>
<b>1 Introduction</b>	<b>11</b>
<b>2 Background: Physics and Chemistry of the Atmosphere</b>	<b>15</b>
2.1 The Chapman Cycle . . . . .	17
2.2 Catalytic Ozone Destruction . . . . .	18
2.3 Halogens: Sources and Sinks . . . . .	20
2.3.1 Previous Bromine Measurements . . . . .	22
2.4 Ozone Trends . . . . .	24
2.5 Fundamentals of Radiative Transfer . . . . .	26
2.5.1 Radiative Transfer Equation . . . . .	26
2.5.2 Optical Properties of Aerosols and Clouds (OPAC) . . . . .	27
<b>3 Instrumentation</b>	<b>29</b>
3.1 HALO Aircraft . . . . .	29
3.2 Mini-DOAS Instrument . . . . .	30
3.2.1 Preparations . . . . .	32
3.3 Additional Instrumentation . . . . .	34
3.3.1 BAHAMAS . . . . .	34
3.3.2 FAIRO . . . . .	35
3.3.3 GhOST . . . . .	35
3.3.4 UMAQS . . . . .	36
3.4 Models . . . . .	36
3.4.1 Lagrangian Modelling by CLaMS . . . . .	36
3.4.2 Chemical Transport Modelling by TOMCAT/SLIMCAT . . . . .	39
<b>4 Method and Retrieval</b>	<b>41</b>
4.1 DOAS . . . . .	41
4.1.1 Absorption Cross Sections and DOAS Fit Scenarios . . . . .	43
4.1.2 Total Slant Column Densities . . . . .	49
4.1.3 Sensitivity Test: O <sub>3</sub> -UV Fit Window . . . . .	52
4.2 Scaling method . . . . .	53
4.3 McArtim Radiative Transfer Modelling . . . . .	55
4.3.1 Aerosol Extinction . . . . .	57
4.3.2 Single Scattering Albedo and Asymmetry Parameter . . . . .	58
4.3.3 A Priori Profile: Vertically Adjusted CLaMS Curtains . . . . .	59
4.3.4 Sample Box-AMF and $\alpha$ Factors . . . . .	60
4.3.5 $\alpha$ Factors: Campaign Overview . . . . .	62

<b>5</b>	<b>Measurements</b>	<b>66</b>
5.1	WISE Campaign . . . . .	66
5.2	Key Atmospheric Regions during WISE . . . . .	67
5.3	Sample Flights . . . . .	68
5.3.1	RF04: September 20 <sup>th</sup> , 2017 . . . . .	68
5.3.2	RF08: October 1 <sup>st</sup> , 2017 . . . . .	69
5.4	Campaign Overview of Total Bromine and Lag-Time . . . . .	71
<b>6</b>	<b>Results and Discussion</b>	<b>74</b>
6.1	Bromine as a Function of $\Theta$ -Distance from the Tropopause . . . . .	74
6.2	Total Bromine as a Function of Equivalent Latitude . . . . .	77
6.3	Modelling of the Transport into the LMS . . . . .	84
6.3.1	Major Air Mass Origins and Transport Pathways . . . . .	84
6.3.2	Contributions to UTLS Bromine from Recent Tropical Cyclones . . . . .	89
6.4	Consequences for LMS Ozone . . . . .	92
<b>7</b>	<b>Summary and Outlook</b>	<b>95</b>
<b>A</b>	<b>O<sub>3</sub> Fit Scenario Wavelength Comparisons for All WISE Flights</b>	<b>98</b>
<b>B</b>	<b>Overview Results of Remaining WISE Flights</b>	<b>106</b>
<b>C</b>	<b>All CLaMS Transport Tracers</b>	<b>120</b>
	<b>Publications by the Author</b>	<b>122</b>
	<b>Bibliography</b>	<b>123</b>
	<b>Acknowledgements</b>	<b>140</b>

# Glossary

$\Delta\Theta$  potential temperature distance from the local tropopause [K]

$\Theta$  potential temperature [K]

$\Theta_{\text{high}}/\text{PV}_{\text{low}}$  tropical air mass region with high potential temperature ( $\Theta > 355$  K) and low potential vorticity ( $\text{PVU} < 2$ )

**AMR** Asian monsoon region (surface emission transport tracer)

**Box-AMF** box air mass factor

**Br<sup>org</sup>** organic bromine ( $\text{CH}_3\text{Br} + \text{halons} + \text{VSLS}$ )

**Br<sub>y</sub><sup>inorg</sup>** inorganic bromine ( $\text{BrO} + \text{BrONO}_2 + \text{HBr} + \text{HOBr} + \text{Br} + \text{BrCl}$ )

**CAM** Central America (surface emission transport tracer)

**CFC** chlorofluorocarbon

**dSCD** differential slant column density [ $\text{molecules cm}^{-2}$ ]

**DU** Dobson units

**Ex-TP** extratropical tropopause

**Ex-UTLS** extratropical upper troposphere and lower stratosphere

**Ex-LS** extratropical lower stratosphere

**FOV** field of view

**g** asymmetry parameter

**HBrR** high bromine region (potential temperature:  $\Theta = 350\text{--}385$  K, and equivalent latitude:  $50\text{--}80^\circ\text{N}$ )

**LMS** lowermost stratosphere (tropopause to  $\Theta = 380$  K)

**LS** lower stratosphere (tropopause to  $\Theta \sim 410$  K)

**NH** northern hemisphere

**ODS** ozone depleting substances

**ppb** parts per billion

**ppm** parts per million

**ppt** parts per trillion

**PVU** potential vorticity units [ $10^{-6} \text{ m}^2 \text{ s}^{-1} \text{ K kg}^{-1}$ ]  
**RF#** research flight 01–16  
**RH** relative humidity [%]  
**SCD** slant column density [molecules  $\text{cm}^{-2}$ ]  
**SH** southern hemisphere  
**SSA** single scattering albedo  
**STE** stratosphere–troposphere exchange  
**SZA** solar zenith angle [°]  
**TAR** tropical adjacent region (surface emission transport tracer)  
**TME** tropical marine environment (surface emission transport tracer)  
**TOA** top of the atmosphere  
**TTL** tropical tropopause layer ( $\Theta = 355\text{--}425 \text{ K}$  and equivalent latitudes  $< \sim 27^\circ\text{N}$  and S)  
**UT** upper troposphere  
**UTLS** upper troposphere and lower stratosphere  
**VMR** volume mixing ratio [ppm/ppb/ppt]  
**VSLS** very short-lived substances  
**WISE** Wave-driven ISentropic Exchange campaign

# Chapter 1

## Introduction

Stratospheric ozone plays an important role in the Earth's radiation budget with about 90% of ozone located above an altitude of 10 km (Fahey and Hegglin, 2011). The vertical distribution of ozone is described by the Chapman cycle and results in an 'ozone layer' around 15–25 km altitude (S. Chapman, 1930; Brasseur and Solomon, 2005). It exists in the stratosphere due to the balance between sufficient spectral solar irradiance from the sun above and a high enough density of available oxygen molecules that increases exponentially towards Earth's surface. Through the production of the ozone layer, the majority of the sun's harmful ultraviolet (UV) radiation is absorbed and prevents the UV-B radiation from reaching the surface. This is crucial for the survival and well being of all living organisms.

Other factors also influence stratospheric ozone, namely reactive halogens (bromine, chlorine, fluorine, and iodine molecules) which catalytically react with and destroy stratospheric ozone during photo-dissociation. Stratospheric ozone destruction may occur through cycles involving any of the following families:  $O_x$  (S. Chapman, 1930),  $HO_x$  (Bates and Nicolet, 1950),  $NO_x$  (Crutzen, 1970; Johnston, 1971),  $ClO_x$  (Molina and Rowland, 1974),  $BrO_x$  (Wofsy et al., 1975), and  $IO_x$  (Solomon et al., 1994). The halogens from anthropogenic sources are called Ozone Depleting Substances (ODS). In extreme cases of catalytic ozone depletion an ozone hole forms as was first detected over Antarctica in 1980's (Farman et al., 1985). This can occur when natural halogens or ODS react to release the halogen free radical as well as inorganic halogen reservoirs are activated. It mainly takes place in cold temperatures such as in polar stratospheric clouds (PSC) near the poles and once sunlight becomes available in spring, it then catalytically destroys ozone through photo-dissociation creating a sudden ozone hole. In direct response to this discovery over the south pole, the United Nations Montreal Protocol treaty banned the use of many ODS in 1987 as they are inevitably released into the atmosphere.

Since then, a significant recovery of stratospheric ozone has been observed globally (e.g., Velders et al. (2007); Bekki et al. (2013); Carpenter et al. (2014)). However, recent measurements have shown this is not the case in the lower stratosphere (LS) (Ball et al., 2018). It has been suggested that continuing negative ozone trends observed in the LS may partly be related to increasing levels of organic source gases and their inorganic products (Ball et al., 2018; Barrera et al., 2020). Several studies have reported that very short-lived species (VSLS; global lifetime of  $< \sim 6$  months) play a key role for LS ozone depletion (Hossaini et al., 2015, 2017; Fernandez et al., 2017; Barrera et al., 2020). This is evident particularly along the boundary between the mid-latitudes and the polar regions (polar vortex edges). Additionally, a recent increase of a banned ODS have been measured in eastern Asia, which shows a 40–60% increase of chlorofluorocarbon (CFC)-11 in 2014–2017 compared to previous 2008–2012 measurements (Rigby et al., 2019). On the other hand, others suggested that the changing dynamics and transport due to climate

change is the main driver for the variability and trends in LS ozone (e.g., Chipperfield et al. (2018); Ball et al. (2019)).

The natural halogens and ODS also act as green house gases further altering the radiative forcing and climate. A study by Hossaini et al. (2015) reported that the ozone radiative budget in the lower stratosphere is impacted by brominated VSLs 3.6 times more than by longer lived halo-carbons. Another study by Polvani et al. (2020) also quantified the impact of ODS on radiative forcing in terms of Arctic warming. Their simulations showed that increasing ODS amplify Arctic warming and sea-ice loss by a factor of 2 compared to simulations with constant ODS.

Not only does the ozone depletion have a strong impact on the climate, but it also has direct negative health consequences for all living organisms. There have been many studies discussing the adverse health problems attributed to increases of UV radiation exposure with a thinner ozone layer (e.g., Moan and Dahlback (1992); Slaper et al. (1996); Moan et al. (2015); Lucas et al. (2019)). The study by Henriksen et al. (1990) postulated that for every decreasing 1% of the ozone column there will be a  $\sim 2\%$  increase in future skin cancer incidences. However, there is a time delay of several decades between the UV-B exposure and skin cancer. Martens et al. (1996) found that by the year 2050, the rates of skin cancer in the Netherlands would increase by a factor of 8–16 times compared to 1990 with various ozone depletion scenarios. The United States EPA (environmental protection agency) estimates that with full compliance of the Montreal Protocol restrictions of ODS, 443 million cases of skin cancer, 2.3 million skin cancer deaths, and 63 million cataract cases will be prevented in the USA (U.S. EPA, 2020). Therefore, it is pertinent to continue to monitor the ozone layer.

In order to understand the changes in the stratospheric ozone layer, it is important to determine how much of each of the ODS and natural halogens is present in the upper troposphere and lower stratosphere (UTLS) and track their changes over time (e.g., Riese et al. (2012); Hossaini et al. (2015) and others). Monitoring the trends of ODS and natural halogens is particularly important for surveilling the concentrations of banned ODS and identifying possible origins of any changes in atmospheric concentrations. In the scope of this dissertation, the focus is on bromine in the northern hemisphere (NH) UTLS. Bromine alone is thought to account for approximately 40% of the global stratospheric ozone depletion (Koenig et al., 2020), and it is particularly effective at destroying ozone in the LS (e.g., Salawitch et al. (2005); Hossaini et al. (2015); WMO (2018); Chipperfield et al. (2020)).

Atmospheric bromine is made up of four components. The sum of the first three contributions according to their Br atomicity are the organic bromines ( $\text{Br}^{\text{org}}$ ), namely methyl bromide ( $\text{CH}_3\text{Br}$ ), the halons consisting of H-1211 ( $\text{CClBrF}_2$ ), H-1202 ( $\text{CBr}_2\text{F}_2$ ), H-1301 ( $\text{CBrF}_3$ ), and H-2402 ( $\text{C}_2\text{Br}_2\text{F}_4$ ), and the brominated VSLs ( $\text{Br}^{\text{VSLs}}$ ) which consist of  $\text{CH}_2\text{Br}_2$ ,  $\text{CHBr}_3$ ,  $\text{CH}_2\text{ClBr}$ ,  $\text{CHCl}_2\text{Br}$ , and  $\text{CHClBr}_2$  (Engel and Rigby et al. (2018)). The fourth component is inorganic bromine defined here as  $\text{Br}_y^{\text{inorg}}$  (often referred to as  $\text{Br}_y$ ) and includes the following species: mainly  $\text{BrO}$  or  $\text{BrONO}_2$  as well as small contributions of  $\text{Br}$ ,  $\text{HBr}$ ,  $\text{HOBr}$ , and  $\text{BrCl}$ .

$\text{CH}_3\text{Br}$  and the halons are measured regularly through a network of monitoring stations (e.g., Montzka et al. (2003); Vollmer et al. (2016); Prinn et al. (2018)), and account for 6.8 ppt and 7.8 ppt, respectively, of stratospheric bromine in 2016 (Engel and Rigby et al. (2018)). The brominated VSLs and  $\text{Br}_y^{\text{inorg}}$  are more variable, but have been reported by various dedicated studies. Though the accuracy varies from study to study, they all point to a contribution by brominated VSLs and their inorganic products of 3–7 ppt (with a mean of 5 ppt) to stratospheric bromine. The sum of all four bromine contributions ( $\text{Br}^{\text{tot}}$ ) as reported in 2016 for the middle stratosphere was  $\sim 19.6$  ppt (ranging from 19–20 ppt) (Engel and Rigby et al. (2018)). The majority of  $\text{Br}^{\text{tot}}$  observations have largely only been in the tropics, at the main stratospheric

entry region, as well as in the mid-stratosphere at low, middle, and high latitudes (WMO, 2018).

$\text{Br}^{\text{tot}}$  has been decreasing, reconcilable with decreasing contributions of  $\text{CH}_3\text{Br}$  and the halons which account for the anthropogenic bromines. This trend is discernible in aged stratospheric air until 2013 when the last balloon-borne  $\text{Br}^{\text{tot}}$  measurements in the middle stratosphere were reported (refer to Fig. 1.1). The  $\text{Br}^{\text{tot}}$  rate of change observed is  $-0.15 \pm 0.04 \text{ ppt year}^{-1}$  (Engel and Rigby et al. (2018)), mainly due the banning of anthropogenically produced ODS. As of 2016, it is reported that 46.3% of stratospheric bromine is from human activities (ODS), while the remaining 53.7% come from natural sources (Engel and Rigby et al. (2018)). In their report, the absolute mixing ratios of the natural contributions are assumed to remain constant, which consist of the VSLs and their product gases ( $\text{Br}_y^{\text{inorg}}$ ) as well as some of the  $\text{CH}_3\text{Br}$ . However, other studies have indicated this may not be the case with increasing climate change (Hossaini et al., 2012a; Falk et al., 2017; Ziska et al., 2017).

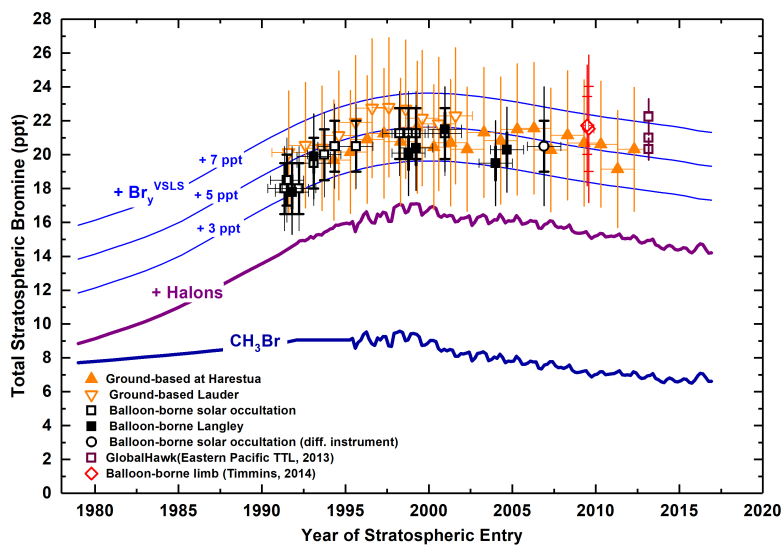


Figure 1.1: The  $\text{Br}^{\text{tot}}$  trend based on various measurements in the troposphere and stratosphere. The orange triangles are ground-based measurements from Harestua ( $60^\circ\text{N}$ ) and Lauder ( $45^\circ\text{S}$ ) (Hendrick et al., 2007, 2008). The black squares are from balloon-borne observations by Dorf et al. (2006b). The purple squares are from airborne measurements with the research aircraft Global Hawk (Werner et al., 2017). And the red diamonds are from balloon-borne observations by previous group members in Timmins, Canada in 2014. The dark blue line indicates  $\text{CH}_3\text{Br}$  mixing ratios and the purple line additionally adds the halons time series as taken from Carpenter et al. (2014). Three scenarios for adding differing  $\text{Br}_y^{\text{VLS}}$  mixing ratios are indicated by +3, +5, or +7 ppt in lighter blue. This figure is adapted from Engel and Rigby et al. (2018) (Fig. 1-16) with recent updates by our group.

$\text{Br}^{\text{tot}}$  and reactive bromines are even less explored in the LS in mid-latitudes for all seasons and the high latitude LS in boreal summer. This region is particularly interesting since it comprises about 40% of the stratospheric background air, though dynamically somewhat separated from the tropical LS and the ‘overworld’ circulation of the global middle stratosphere (e.g., Holton et al. (1995); Bönisch et al. (2009); Birner and Bönisch (2011); Gettelman et al. (2011); Ploeger et al. (2015); Konopka et al. (2015)). It has recently attracted renewed interest since a decrease in ozone is still observed there, particularly in the northern hemisphere (e.g., Ball et al. (2018, 2019, 2020); Chipperfield et al. (2018, 2020)).

The transport of air masses into the extratropical LS (Ex-LS) has two major pathways, either by stratospheric–tropospheric exchange (STE) at mid-latitudes or by isentropic transport of air from the tropical upper troposphere and tropopause layer (UT/TTL) (e.g., Holton et al. (1995); Bönisch et al. (2009); Birner and Bönisch (2011); Ploeger et al. (2015); Konopka et al. (2015);

Inai et al. (2019), and others). Dynamical features such as the Asian monsoon anticyclone and western Pacific convection play a dominant factor in delivering pollutants (and eventually VSLS) to the LS (e.g., Levine et al. (2007); Gettelman et al. (2011); Vogel et al. (2014, 2016); Orbe et al. (2015); Müller et al. (2016); Rolf et al. (2018); Wetzel et al. (2020), and others). However, the continued transport of bromine to the Ex–LS is still insufficiently investigated. Other uncertain factors determining LS bromine include the varying source strengths particularly with respect to future climate change, as well as stratospheric removal processes. Therefore, direct observations on varying bromine mixing ratios, and its consequences for LMS ozone are still lacking.

The present study addresses the spatial variability of  $\text{Br}^{\text{org}}$  and  $\text{Br}_y^{\text{inorg}}$  in the NH extratropical UTLS (Ex–UTLS) in fall 2017 as part of the WISE (Wave-driven and ISentropic Exchange) campaign. The major transport pathways of bromine-rich air masses into the extratropical LS (Ex–LS) are investigated with measurements of transport tracers (CO and  $\text{N}_2\text{O}$ ) and an air mass age tracer ( $\text{SF}_6$ ), and corroborated by Lagrangian chemistry transport model (CTM) simulations. This study of  $\text{Br}^{\text{tot}}$  thus partly complements the recent study of Keber et al. (2020) on the contribution and origins of the different organic source gases to  $\text{Br}^{\text{tot}}$  in the NH Ex–LS during different seasons.

**Outline** This dissertation is organized as follows. Additional background information on the atmosphere, ozone and bromine chemistry, and radiative transfer is described in Chapter 2. The key instruments and models used in the present study are introduced in Chapter 3. The method and retrieval along with some (necessary) reduction in the data are described in Chapter 4. The WISE campaign and a suite of measurements are reported in Chapter 5. The inferred  $\text{Br}^{\text{tot}}$  measurements are presented in Chapter 6 with respect to the distance from the local tropopause (Sect. 6.1) as well as by their geographical distribution in the UTLS indicating source regions of brominated species (Sect. 6.2). Model results of the transport pathways contributing bromine-rich air masses into the LMS are analysed in Sect. 6.3, while the consequences of this additional bromine in the LMS on  $\text{O}_3$  is discussed in Sect. 6.4. And lastly, Chapter 7 summarizes and concludes the dissertation.

## Chapter 2

# Background: Physics and Chemistry of the Atmosphere

The atmosphere is divided into several layers with distinctly different characteristics. These layers can be determined by changes in temperature gradients and becoming increasingly dense towards Earth's surface (Fig. 2.1). The two atmospheric layers relevant to this dissertation consist of the two lowest ones, the troposphere and stratosphere. The physics and chemistry of both of these layers are inherently different and play discrete roles in our climate.

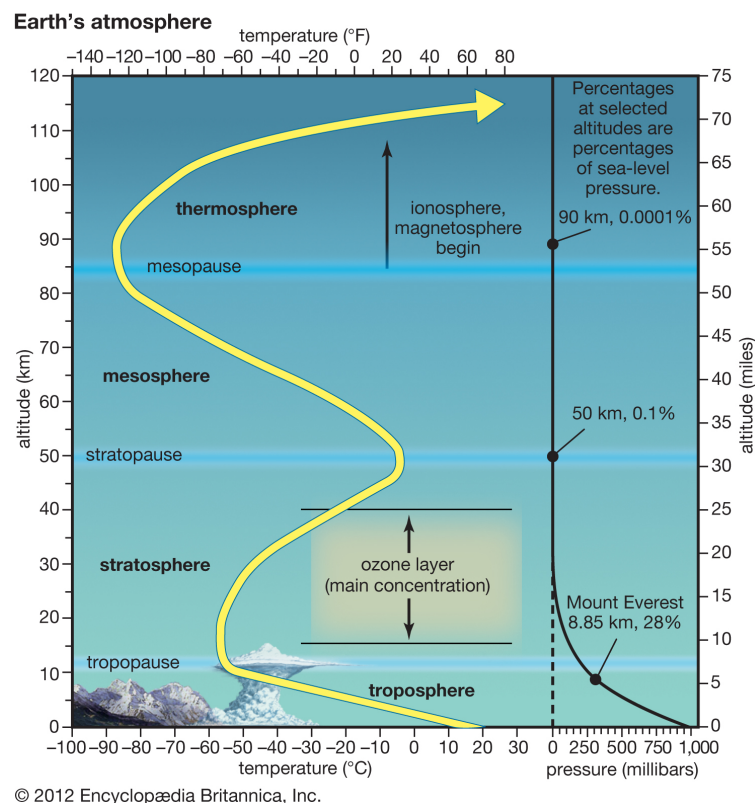


Figure 2.1: The atmospheric layers separated by changes in temperature gradients as well as the corresponding pressure. Figure adapted from Pielke (2021).

The troposphere ranges from Earth's relatively warm and moist surface up to the tropopause (discussed below). In this layer, temperature decreases with altitude classified as a positive lapse rate. It is therefore characterized by both horizontal and vertical turbulence and mixing of

air masses caused by orographic uplifting, frontal wedge lifting, convergence zones or localized convection. Vertical energy transport of air parcels is often described by moist adiabatic processes (the average moist adiabatic lapse rate is  $\sim 6^\circ\text{C km}^{-1}$  (Martin, 2006)) and results in cloud formation in the upper troposphere. Although radiation is important for surface heating during the daytime, it plays a relatively small role in the troposphere compared to in the stratosphere.

The stratosphere ranges from the top of the troposphere to  $\sim 50$  km altitude, and is characterized by the stable temperature stratified layers increasing with elevation due to the influence of solar radiation. The heating of the stratosphere is largely caused by the absorption of solar radiation through ozone production. This leads to the ozone layer forming which acts as a shield by preventing most of the harmful ultraviolet light from reaching the Earth’s surface and harming organic cells. The negative lapse rate with altitude in the stratosphere prevents vertical mixing from occurring, therefore energy is rather transported vertically through radiative transfer. Furthermore, due to the low water content in the stratosphere, there are rarely clouds that form.

The boundary layer between the troposphere and stratosphere is called the tropopause. The height of the tropopause varies by latitude and season but generally is  $\sim 8$  km near the poles and  $\sim 17$  km at the equator. There are multiple definitions that can be used for the tropopause. The World Meteorological Organization (WMO) characterizes it thermally using the temperature lapse rate. This is defined as the lowest point at which the temperature lapse rate decreases to  $2 \text{ K km}^{-1}$  and the average lapse rate in the 2 km above is not larger than  $2 \text{ K km}^{-1}$  (WMO, 1957). Other tropopause definitions include the cold point tropopause, the dynamical tropopause or a chemistry defined tropopause. The cold point tropopause is the altitude of the coldest temperature separating the troposphere and stratosphere (Selkirk, 1993). The dynamical tropopause is often defined by the 2 potential vorticity unit ( $\text{PVU} = 10^{-6} \text{ m}^2 \text{ s}^{-1} \text{ K kg}^{-1}$ ) contour (Holton et al., 1995). And a chemical tropopause is the elevation observing sharp changes of a tropospheric or stratospheric gas such as  $\text{N}_2\text{O}$  or  $\text{O}_3$ , respectively (Shepherd, 2002). The region of interest in this study consists of the UTLS with the tropopause defined by the WMO lapse rate definition, hereafter called the WMO tropopause (WMO, 1957).

The UTLS can further be divided into distinctly unique domains. For example the lowermost stratosphere (LMS) is defined as the atmospheric layer extending from the local tropopause to the potential temperature  $\Theta = 380 \text{ K}$  isentrope (shown in Fig. 2.2; Holton et al. (1995)). The LMS is considered somewhat separate from the stratosphere ‘overworld’ above because  $\Theta$  isentropes do not lie entirely in the layer, but rather cross the bottom boundary that is the tropopause. Furthermore, it is dynamically divided from the tropics as horizontal PV gradients become increasingly stronger towards the equator. In the subtropics the tropopause ( $\sim 2 \text{ PVU}$  contour) crosses the 380 K isentrope, thereby excluding part of the tropics from the LMS. Additionally in this dissertation, the lower stratosphere (LS) is specified from the local tropopause up to the highest measurements of this study around  $\Theta \sim 410 \text{ K}$ . In the definition of the tropical tropopause layer (TTL), this study follows Fueglistaler et al. (2009), i.e., for latitudes  $< \sim 27^\circ\text{N}$  and S and potential temperatures  $\Theta = 355\text{--}425 \text{ K}$ . These atmospheric domains are discussed throughout this study.

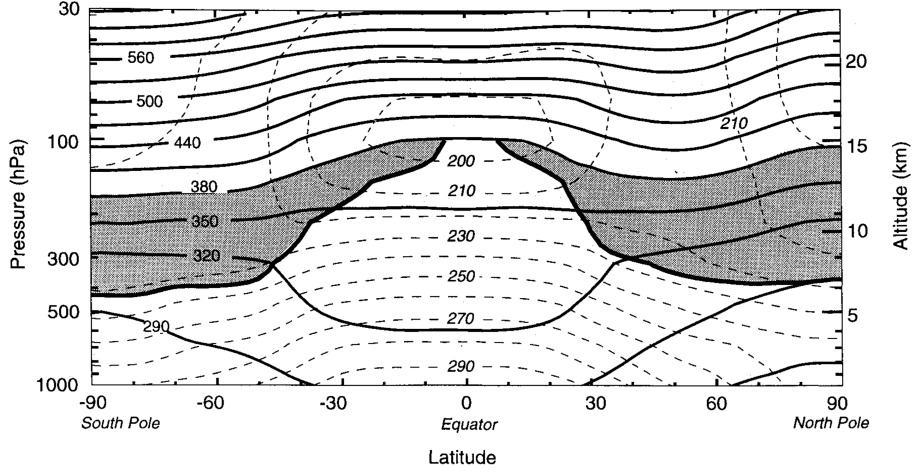


Figure 2.2: A northern and southern hemisphere cross section of the troposphere and stratosphere. The dashed lines indicate the temperature contours while the solid lines indicate the potential temperature isentropes. The solid thick contour marks the 2 PVU (potential vorticity units) tropopause. In the tropics, the tropopause merges with the  $\sim 380$  K potential temperature line. The shaded gray region indicates the LMS, excluding parts of the tropics. The LS extends to slightly higher potential temperatures than the LMS, therefore including the tropics. For more details refer to Holton et al. (1995), from which the figure is adapted from.

## 2.1 The Chapman Cycle

The main chemistry reactions creating the ozone layer in the stratosphere are known as the Chapman cycle (S. Chapman, 1930). First, oxygen molecules are split by photo-dissociation with shortwave UV radiation ( $\lambda < 242$  nm):



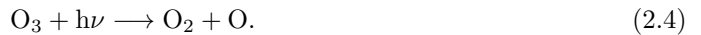
where  $\text{O}({}^3\text{P})$  is an oxygen molecule in its ground state. Then, the atomic oxygen and an oxygen molecule along with a collision partner that is a neutral chemical molecule (M; e.g.,  $\text{N}_2$  or  $\text{O}_2$ ) can form ozone:



while some atomic oxygens also convert back into oxygen molecules. Stratospheric ozone is in equilibrium and is reached by ozone being destroyed by either



or by photolysis via



If Eq. (2.4) occurs at wavelengths  $\lambda < 1180$  nm (Chappius absorption band) the atomic oxygen created is in its ground state. While if the reaction occurs at  $\lambda < 320$  nm (Hartley absorption band) then an atomic oxygen in its excited singlet state ( $\text{O}({}^1\text{D})$ ) is created. The  $\text{O}({}^1\text{D})$  then reacts via a collision partner to convert to  $\text{O}({}^3\text{P})$ . These reactions create an equilibrium of the ozone concentration with a peak in the stratosphere around  $\sim 20$  km balanced by the available UV radiation increasing towards higher altitudes with oxygen molecules increasing towards lower altitudes. The Chapman cycle predicts the vertical shape of ozone and the altitude of the ozone layer reasonably well. However, it significantly overestimates the ozone concentrations compared

to observations (Platt and Stutz, 2008).

## 2.2 Catalytic Ozone Destruction

Additional mechanisms cause catalytic ozone destruction in the stratosphere and account for the difference in ozone calculated between the Chapman cycle and the observed ozone (Platt and Stutz, 2008). Catalytic ozone loss (cycle 1) as a result of free radicals is described by:



where X can be any of the following radicals from the groups  $HO_x$  (H, OH, or  $HO_2$ ) (Bates and Nicolet, 1950),  $NO_x$  (NO or  $NO_2$ ) (Crutzen, 1970; Johnston, 1971),  $ClO_x$  (Cl or ClO) (Molina and Rowland, 1974),  $IO_x$  (I or IO) (Solomon et al., 1994), or  $BrO_x$  (Br or BrO) (Wofsy et al., 1975). These two reactions cause a net ozone loss of



Ozone is destroyed catalytically because the same radical X can be used many times via reaction Eqs. (2.5) and (2.6) to destroy hundreds up to tens of thousands of ozone molecules by a single Cl or Br atom in the stratosphere before they are removed (Fahey and Hegglin, 2011). This cycle is most important in the tropics and mid-latitudes due to the abundance of spectral solar irradiance available to split oxygen.

Additional halogen related catalytic ozone destruction occurs via two additional cycles predominantly in polar regions when sufficient reactive halogens are available and under the right ambient conditions. This occurs mainly in extremely cold temperatures (frequently in polar stratospheric clouds) when some visible light is available during late winter and early spring (Fahey and Hegglin, 2011). Cycle 2 occurs by releasing active chlorine molecules which destroy ozone via



A third cycle for ozone destruction can occur in air masses with chlorine and bromine radicals together via the following reactions:



or



and



Then the atomic chlorine or bromine molecules react with ozone back into ClO and BrO respectively via



Cycles 2 and 3 both create a net ozone loss of



Ozone loss is greatest at the poles due to the large presence of halogens in their reactive forms. Mid-latitudinal depletion of ozone is also observed, but little to no ozone depletion occurs in the tropics via cycles 2 and 3. The tropical LS has fairly young air masses ( $< 18$  months) and therefore most of the halogens are still in their organic forms and have not yet converted to reactive halogen species.

Examples of the polar ozone distributions throughout the troposphere and stratosphere are shown in Fig. 2.3, with the tropopause distinguishable around  $\sim 8\text{--}9$  km. The ozone layer (between  $\sim 10\text{--}30$  km) is in the stratosphere blocking the majority of UV-B radiation (280–315 nm) from reaching the surface (Fahey and Hegglin, 2011). However, when there are large concentrations of ODS (various halogen source gases) and heterogeneous activation of inorganic reservoir gases in cold temperatures such as in PSCs, an ozone hole can occur. An ozone hole is defined as regions with an ozone concentration  $< 220$  DU (Dobson Units) (Fahey and Hegglin, 2011). The most notable occurrences of these catalytic ozone destruction events occurs over Antarctica (Farman et al., 1985), as well as to a lesser degree over the Arctic. A recent study by Fernandez et al. (2017) investigated the importance of brominated VSLs on Antarctic ozone depletion. Their simulations of the ozone hole only agreed with measurements when 5 ppt of brominated VSLs were added, as this reduced their simulated ozone hole by 14%. Further, they found that the VSLs had the largest impact at the edges of the ozone hole expanding the area by  $\sim 5$  million  $\text{km}^2$ . On the other hand, increases of ozone levels at the surface shown in Fig. 2.3, are due to pollution and are harmful to living organisms (Fahey and Hegglin, 2011).

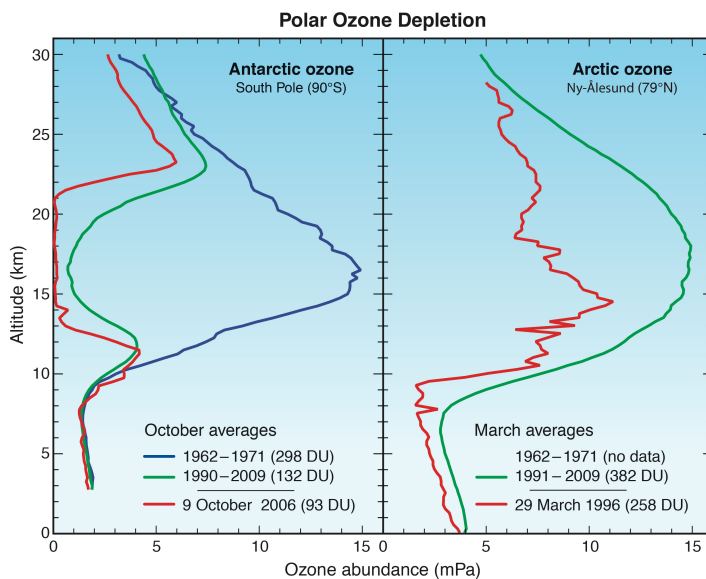


Figure 2.3: Polar ozone vertical profiles throughout the troposphere and stratosphere at different times in the Antarctic (left) and Arctic (right). The total ozone in Dobson Units (DU) is shown in the parentheses. Figure adapted from Fahey and Hegglin (2011) (Q12-3).

## 2.3 Halogens: Sources and Sinks

Halogens (chlorine, bromine, iodine, and fluorine species) have both anthropogenic and natural sources. Anthropogenic halogens are ODS more commonly known as chlorofluorocarbons (CFCs), hydrochlorofluorocarbons (HCFCs), carbon tetrachloride, methyl chloroform, hydrobromofluorocarbons (HBFCs), halons, and methyl bromide ( $\text{CH}_3\text{Br}$ ). They are/were included in refrigerators, air conditioners, aerosol propellants, cleaning of metals and electronic components, fire extinguishers, as well as in agricultural and pre-shipping fumigants (Fahey and Hegglin, 2011). Since most production and usage of chlorines and bromines have been banned by the Montreal Protocol, there has been slow but definitive success in the recovery of the ozone hole. Methyl chloride ( $\text{CH}_3\text{Cl}$ ), VSLS, and in part  $\text{CH}_3\text{Br}$  are naturally produced halogens from coastal and terrestrial ecosystems. Primary  $\text{CH}_3\text{Cl}$  sources are from the organic matter in oceans, salt marshes, and terrestrial plants. Sources of brominated VSLS include seaweed, macroalgae, phytoplankton and ice algae (Yang et al., 2005; Hossaini et al., 2015). Additionally, Bobrowski et al. (2003) reported that volcanic plumes emit  $\text{BrO}$  (a product gas of VSLS) directly or otherwise an organic bromine compound is emitted which breaks down quickly releasing  $\text{BrO}$ . Both anthropogenic and natural halogens can lead to ozone depletion when they are converted to active halogen radicals in the atmosphere.

As of 2016, stratospheric chlorine mixing ratios were  $\sim 3290$  ppt and bromine mixing ratios were  $\sim 19.6$  ppt (WMO, 2018). Although there is significantly less bromine than chlorine in the stratosphere, it is approximately 60–65 times more effective on a per atom basis at destroying ozone. This is partially due to shorter average stratospheric lifetime of bromine source gases compared to chlorine source gases. Additionally, bromine is chemically more effective at destroying ozone than chlorine because the chlorine cycle is also coupled with  $\text{NO}_x$  ozone depletion cycles unlike bromines (Sinnhuber et al., 2009). As chlorine increases it decreases ozone loss via  $\text{NO}_x$  reactions in regions where  $\text{NO}_x$  was the main driver of ozone loss (Sinnhuber et al., 2009).

Natural sources of chlorine ( $\text{CH}_3\text{Cl}$ ) account for  $\sim 17\%$  of stratospheric chlorine while stratospheric bromine has  $\sim 54\%$  natural sources ( $\text{CH}_3\text{Br}$  and VSLS) (WMO, 2018). The natural sources of both chlorine and bromine have largely remained constant over the past decades, but their percentage relative to total chlorine or bromine is slowly increasing as the absolute mixing ratios of both decrease. The anthropogenic sources have decreased by  $-14\%$  (1993–2016) and  $-22\%$  (1998–2016) for chlorine and bromine, respectively (refer to WMO (2018) Fig. ES-3).

The breakdown of the natural and anthropogenic contributions to stratospheric bromine is displayed in Fig. 2.4 for three different years, indicating the  $\text{Br}^{\text{tot}}$  decrease from  $\sim 21.3$  ppt in 1996 to  $\sim 19.6$  ppt in 2016 (Engel and Rigby et al. (2018)).  $\text{CH}_3\text{Br}$  has both natural and anthropogenic sources and while the relative and absolute contribution of  $\text{CH}_3\text{Br}$  from human activities has decreased, the naturally produced absolute quantity of  $\text{CH}_3\text{Br}$  has remained constant but the relative contribution has decreased. Between 1996 and 2012, the change of anthropogenic  $\text{CH}_3\text{Br}$  was the largest portion of total bromine decrease. As of 2015, the anthropogenic  $\text{CH}_3\text{Br}$  has been phased out for all applications except for quarantine and pre-shipping uses due to the Montreal protocol ban (Fahey and Hegglin, 2011). The halons are emitted strictly through human activities, and are the largest cause for the bromine decrease in recent years. They were phased out by the end of 1993 and 2010 in developed and developing nations, respectively (Fahey and Hegglin, 2011). The brominated VSLS which includes the inorganic product gases ( $\text{Br}_y^{\text{inorg}}$ ), only have natural sources which in the WMO Scientific Assessment of Ozone Depletion reports are assumed to be constant (Engel and Rigby et al. (2018)). However, recent studies have indicated that climate change could impact the natural source contributions to atmospheric bromine particularly the relative contribution of VSLS compared to  $\text{Br}_y^{\text{inorg}}$  due to sea surface temperature changes and thereby altering the sea-to-air fluxes (Hossaini et al., 2012a; Falk et al.,

2017; Ziska et al., 2017).

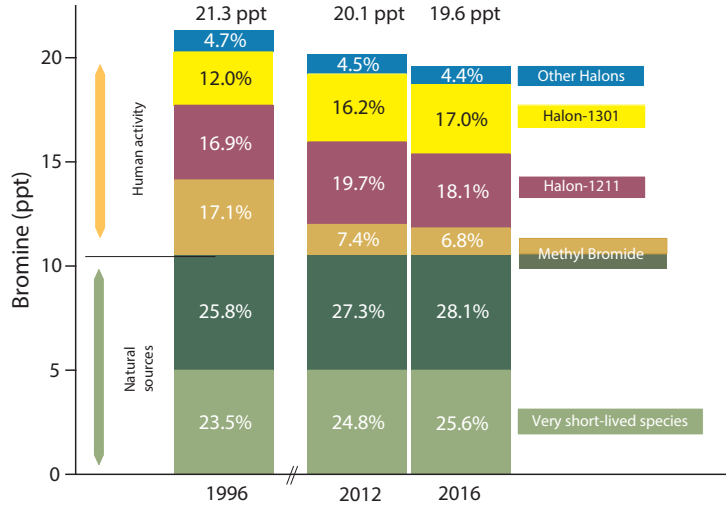


Figure 2.4: The breakdown of bromine contributions transported into the stratosphere is shown for 1996, 2012, and 2016. The longer lived gases are inferred from global surface measurements and the VSLs are assumed to be constant, i.e., 5 ppt. The sum of H–1202 and H–2402 accounts for the ‘other halons’. This figure is adapted from Engel and Rigby et al. (2018) (Fig. 1-17).

In the atmosphere, organic halogens react with hydroxyl radicals (OH) or undergo photolysis to release the halogen molecule (Cl or Br)



In this study the focus will be on the brominated species specifically. The various reaction rates of  $\text{Br}^{\text{org}}$  through photolysis and reaction with OH is used to determine the lifetime of each organic bromine and other halogen species (Yang et al., 2005; Sander et al., 2011; Parrella et al., 2012; Badia et al., 2019). Orkin et al. (2013) found tropospheric lifetimes of  $\text{CHBr}_3$ ,  $\text{CHClBr}_2$ , and  $\text{CHCl}_2\text{Br}$  reacting with OH to be  $\sim 57$  days,  $\sim 72$  days, and  $\sim 96$  days, respectively, assuming a uniform OH concentration in the atmosphere of  $1 \times 10^6$  molecules  $\text{cm}^{-3}$ . The WMO (2018) reports similar lifetimes due to OH loss reactions. The photolysis lifetime of  $\text{CH}_3\text{Br}$ ,  $\text{CHClBr}_2$ , and  $\text{CHCl}_2\text{Br}$  was reported in WMO (2011) to be 36 days, 161 days, and 222 days, respectively. The total lifetime in the troposphere is calculated by summing up the contributions,

$$(\tau^{\text{Trop}})^{-1} = (\tau_{\text{OH}}^{\text{Trop}})^{-1} + (\tau_{h\nu}^{\text{Trop}})^{-1} \quad (2.19)$$

where  $\tau$  is the lifetime of one brominated species (Orkin et al., 2013; WMO, 2018). Similarly the stratospheric lifetime of a brominated species is calculated from the loss reaction with OH as well as reaction with  $\text{O}(^1\text{D})$  and UV photolysis,

$$(\tau^{\text{Strat}})^{-1} = (\tau_{\text{OH}}^{\text{Strat}})^{-1} + (\tau_{\text{O}(^1\text{D})}^{\text{Strat}})^{-1} + (\tau_{h\nu}^{\text{Strat}})^{-1}. \quad (2.20)$$

The total atmospheric lifetime of each species is then calculated by

$$(\tau^{\text{Total Atm.}})^{-1} = (\tau^{\text{Trop}})^{-1} + (\tau^{\text{Strat}})^{-1} + (\tau^{\text{Meso}})^{-1} \quad (2.21)$$

where the mesospheric lifetimes are negligible except for long-lived species (WMO, 2018).

Additional  $\text{Br}^{\text{org}}$  sinks include the ocean and soil (WMO, 2018). Reactive bromine sinks in the atmosphere include reactions with hydrocarbons or  $\text{HO}_2$  to form HBr and HOBr or with

$\text{NO}_2$  to form  $\text{BrONO}_2$  and can then be wet or dry deposited (e.g., Yang et al. (2005); Großmann (2014)). The latest total atmospheric lifetimes can be found in Table 2.1. Due to the shorter lifetimes ( $< 6$  months) of the brominated VSLs, they are converted into  $\text{Br}_y^{\text{inorg}}$  quicker. This releases the active bromine and commences ozone depletion.

Species	Total Atmospheric Lifetime
$\text{CH}_3\text{Br}$	0.8 years
$\text{CH}_2\text{Br}_2$	150 (80–890) days
$\text{CHBr}_3$	16 (8–23) days
$\text{CH}_2\text{ClBr}$	165 (89–1050) days
$\text{CHCl}_2\text{Br}$	66 (38–250) days
$\text{CHClBr}_2$	59 (28–225) days
H–1202	2.5 years
H–1211	16 years
H–1301	72 years
H–2402	28 years

Table 2.1: Total atmospheric lifetimes of brominated organic species (i.e., methyl bromide, the VSLs, and the halons) as reported in WMO (2018). The ranges of the lifetimes are provided in brackets, where available.

### 2.3.1 Previous Bromine Measurements

In order to determine how much bromine is currently in the stratosphere, detailed sampling studies performed at the stratospheric entry level in different regions and seasons are most suitable. This primarily includes the tropics and the Asian monsoon anticyclone region during the convective season where most of the stratospheric air is believed to enter (e.g., Holton et al. (1995); Fueglistaler et al. (2004); Ploeger et al. (2015), and others). However, studies addressing  $\text{Br}^{\text{tot}}$  measurements in aged air of the middle and upper stratosphere at a given location and season are also crucial.

Observational as well as theoretical studies addressing bromine at the stratospheric entry level in the tropics started well over two decades ago. Numerous dedicated research activities have taken place to investigate the fate of atmospheric bromine. These campaigns include ATTREX – Airborne Tropical Tropopause Experiment (Jensen et al., 2013), CAST – Coordinated Airborne Studies in the Tropics (Harris et al., 2017), and CONTRAST – Convective Transport of Active Species in the Tropics (Pan et al., 2017).

The monitoring of  $\text{CH}_3\text{Br}$  (e.g., Montzka et al. (2003)) and the longer lived halons (e.g., Vollmer et al. (2016)), are regularly performed by different observational networks. Notably these include NOAA (National Oceanic and Atmospheric Administration), UEA (University of East Anglia), AGAGE (Advanced Global Atmospheric Gases Experiment; Prinn et al. (2018)), and others at different sampling locations from the surface. These networks report mixing ratios of  $\text{CH}_3\text{Br}$  and the halons to be  $\sim 6.8$  ppt and  $\sim 7.8$  ppt, respectively (Engel and Rigby et al. (2018)). A more recent study by Adcock et al. (2021) observed enhanced  $\text{CH}_3\text{Br}$  mixing ratios of up to 9 ppt at the tropopause associated with the Asian monsoon anticyclone over north eastern India in summer 2017 (with surface samples reaching  $\sim 11.5$  ppt). Their measurements of H–1211 were in agreement with previous reported mixing ratios by Engel and Rigby et al. (2018) and references therein.

The VSLs and  $\text{Br}_y^{\text{inorg}}$  are typically measured during dedicated studies carried out from the ground, ships, manned and unmanned aircrafts, and high-flying balloons at different locations and seasons. Brominated VSLs ( $\text{Br}^{\text{VSLs}}$ ) are produced predominantly from marine emissions of  $\text{CH}_2\text{Br}_2$  and  $\text{CHBr}_3$  with small contributions from other brominated hydrochlorobromocar-

bons ( $\text{CH}_2\text{ClBr}$ ,  $\text{CHCl}_2\text{Br}$ ,  $\text{CHClBr}_2$ ) (Engel and Rigby et al. (2018)). Early measurements at the tropical tropopause of  $\text{CH}_2\text{Br}_2$  and  $\text{CHBr}_3$  indicated that both species may substantially contribute to  $\text{Br}^{\text{tot}}$  (e.g., a few ppt), with a larger influx over the central Pacific during the convective season in boreal winter (Schaufler et al., 1993, 1998, 1999). Since then, there have been many studies from different measurement platforms to determine the VLS contribution. Laube et al. (2008) reported  $[\text{Br}^{\text{VLS}}] = 1.25 \pm 0.08$  ppt at 15.2 km and  $0.98 \pm 0.08$  ppt by 16.4 km entering the stratosphere over north eastern Brazil in June 2005 from balloon-borne soundings. Further balloon-borne measurements by Brinckmann et al. (2012) found that  $[\text{Br}^{\text{VLS}}] = 2.25$  ppt around 14.8 km, and 1.35 ppt by 17.5 km over Brazil in June 2008. Wisher et al. (2014) reported on airborne measurements from Germany to Venezuela/Colombia (2009–2011), Germany to South Africa (2010/2011), and Germany to Thailand/Malaysia (2012/2013) as part of the CARIBIC (Civil Aircraft for the Regular Investigation for the Atmosphere Based on an Instrument Container) campaign with  $[\text{Br}^{\text{VLS}}] = 3.4 \pm 1.5$  ppt in the tropical troposphere between 10–12 km. Further aircraft measurements by Sala et al. (2014) over Borneo in fall 2011 in the tropical upper troposphere (UT) between 10–13 km indicated  $[\text{Br}^{\text{VLS}}] = 4.35 \pm 0.44$  ppt. Airborne measurements over the tropical eastern Pacific (2013) and tropical western Pacific (2014) during the ATTREX mission observed  $[\text{Br}^{\text{VLS}}] = 2.96 \pm 0.42$  ppt and  $3.27 \pm 0.49$  ppt, respectively, at 17 km (Navarro et al., 2015). Wales et al. (2018) reported that there is  $[\text{Br}^{\text{VLS}}] = 2.9 \pm 0.6$  ppt entering the stratosphere over the tropical western Pacific in 2014 during the CONTRAST mission. And a recent study by Keber et al. (2020) reported aircraft measurements of brominated VLS at the tropopause and in the LMS performed during three research missions at northern mid to high latitudes during different seasons. Joint measurements from Aug.–Sept. 2012 and Sept.–Oct. 2017 resulted in  $[\text{Br}^{\text{VLS}}] = 3.99 \pm 1.15$  ppt in the 10 K below the tropopause, while measurements from Dec. 2015–Mar. 2016 showed  $[\text{Br}^{\text{VLS}}] = 5.20 \pm 1.25$  ppt. They ascribed the varying mixing ratios found for the major brominated VLS at the local tropopause to the location and seasonality of their source strengths, transport pathways and atmospheric lifetimes. In summary, the majority of  $\text{Br}^{\text{VLS}}$  measurements are taken in the tropical UT/TTL and range from  $\sim 1$ –4 ppt with a few exceptions.

Experimental studies have also independently established the magnitude of  $\text{Br}_y^{\text{inorg}}$  injected into the stratosphere.  $\text{Br}_y^{\text{inorg}}$  is inferred from measurements of the major inorganic bromine species  $\text{BrO}$  and/or  $\text{BrONO}_2$  and suitable photo-chemical ratios to  $\text{Br}_y^{\text{inorg}}$ . Ground-based studies include e.g., Hendrick et al. (2007, 2008), and others. Measurements from balloon platforms were reported by e.g., Harder et al. (1998, 2000); Pfeilsticker et al. (2000); Dorf et al. (2006b, 2008); Höpfner et al. (2009); Stachnik et al. (2013); Kreycky et al. (2013) and Wetzal et al. (2017). And satellite records are presented by e.g., Sinnhuber et al. (2005); Sioris et al. (2006); Hendrick et al. (2009); Rozanov et al. (2011); Parrella et al. (2013), and others. Dorf et al. (2008) inferred  $\text{Br}_y^{\text{inorg}}$  to be  $2.1 \pm 2.6$  ppt (over Kiruna in 1999) and  $4.0 \pm 2.5$  ppt (over north eastern Brazil in June 2005) from simultaneous stratospheric balloon soundings of  $\text{Br}^{\text{org}}$  and  $\text{Br}_y^{\text{inorg}}$ . Werner et al. (2017) found  $[\text{Br}_y^{\text{inorg}}] = 2.63 \pm 1.04$  ppt with a range from 0.5–5.25 ppt in the TTL over the tropical eastern Pacific during the convective season in 2013. Koenig et al. (2017) inferred  $[\text{Br}_y^{\text{inorg}}] = 2.7$  ppt (2.3–3.1 ppt; 95 % confidence interval) in aged air masses in the lower TTL, and Wales et al. (2018) determined  $\text{Br}_y^{\text{inorg}}$  entering the stratosphere to be  $2.1 \pm 2.1$  ppt for the western Pacific during the convective season in 2014.

Global and seasonal variations in mixing ratios of stratospheric  $\text{Br}^{\text{tot}}$  are influenced by several factors. These include (a) the surface source strengths of the VLS and sea salt (e.g., Quack et al. (2004); Yokouchi et al. (2005); Warwick et al. (2006); Liang et al. (2010); Ordóñez et al. (2012); Ziska et al. (2013); Hossaini et al. (2012b, 2013, 2016); Wang et al. (2019), and many others), and (b) the efficacy of removal of the halogenated product gases from the UTLS (e.g., Sinnhuber

and Folkins (2006); Aschmann et al. (2011); Aschmann and Sinnhuber (2013)). Additionally, it depends on (c) the transport of bromine source and product gases to the stratospheric entry level (e.g., Aschmann et al. (2009, 2011); Aschmann and Sinnhuber (2013); Liang et al. (2014); Navarro et al. (2015); Hossaini et al. (2016); Schmidt et al. (2016); Fiehn et al. (2018); Filus et al. (2020); Adcock et al. (2021), and others), as well as (d) the transport of bromine-enriched air into the LMS via the two major pathways (e.g., Holton et al. (1995); Bönisch et al. (2009); Birner and Bönisch (2011); Ploeger et al. (2015); Konopka et al. (2015); Inai et al. (2019), and others). The major transport pathways to the LMS are considered to be the stratospheric–tropospheric exchange at mid-latitudes and the isentropic transport of air from the tropical UT/TTL. Therefore, it can not be assumed ad-hoc that the sum nor the speciation of the source and product gases for each halogen type (here of bromine) are spatially and temporally constant in the air of each transport pathway and hence the whole LMS.

Studies such as by Vogel et al. (2014) discuss the rapid ( $\sim 5$  week) transport pathway of air masses from the south eastern Asia boundary layer to the LMS over northern Europe during the TACTS (Transport and Composition in the Upper Troposphere and Lowermost Stratosphere) campaign in September 2012, of which the area is spatially and seasonally similar to the current study. While bromine transport to the TTL has been observed in various studies, as mentioned above, the continued transport to the LMS in boreal summer is still insufficiently investigated. In addition, it has been speculated that the varying source strengths, transport pathways, removal processes, and in particular the contributions  $\text{Br}^{\text{VLSL}}$  and  $\text{Br}_y^{\text{inorg}}$  to the LMS  $\text{Br}^{\text{tot}}$ , may be altered as the climate changes (e.g., Hossaini et al. (2012a); Falk et al. (2017); Ziska et al. (2017)).

However, observational studies addressing  $\text{Br}^{\text{tot}}$  around the UTLS may not directly relate to  $\text{Br}^{\text{tot}}$  available in the middle stratosphere. This is due to the variability and heterogeneity in the source strengths, the variable transformation and atmospheric transport of the brominated VLSL, and the amount of bromine inferred by the product gases and sea salt. In addition to this variability, there is the suspected small trend in stratospheric bromine from controlled substances. Additionally, each individual technique has its own accuracy, even though they have largely been improved over time. All these factors make it difficult to infer a trend in  $\text{Br}^{\text{tot}}$  from measurements in the UTLS, even if they may cover mean air mass ages of several years. Therefore, a continuation of high precision  $\text{Br}^{\text{tot}}$  measurements in aged and well mixed air of the middle stratosphere such as from balloon platforms, appears necessary in the coming decades, for monitoring both controlled bromine substances as well as the expected climate-change induced contributions.

## 2.4 Ozone Trends

Since many ODS have been reduced globally over the past two decades, the ozone layer has begun to recover. Considerable recovery has been measured in the upper stratosphere, while the lower stratospheric ozone has continued to decrease (Ball et al., 2018, 2020). The ozone column in the stratosphere as a function of time between 1985–2016 is shown in Fig. 2.5 (Ball et al., 2018). Between 1985 and 1998 the ozone column decreases in all layers of the stratosphere, however after 1998 the upper, middle, and lower stratosphere have differing trends. In the upper stratosphere (32–48 km) the ozone column increases by  $\sim 0.8$  DU between 1998–2016. In the middle stratosphere (24–32 km) the ozone column is still  $\sim 0.4$  DU lower in 2016 than in 1998. While in the lower stratosphere ( $\sim 13$ –24 km) the ozone column continues to decrease almost as consistently as before 1998. From 1998–2016 the lower stratosphere ozone column continued to decrease by  $\sim 2.2$  DU. The lack of an ozone recovery in the lower stratosphere is not well

understood. Therefore further detailed studies of the lower stratospheric halogen loading are crucial.

Barrera et al. (2020) showed that the inclusion of brominated VSLs significantly improves their modelled total ozone column when comparing to observations from 1990–2010. Their model results show that brominated VSLs have the largest impact on the ozone destruction in spring, but the overall ozone loss in the LMS is largest in winter. Further studies have shown that VSLs have a significant impact on the ozone radiation budget (Hossaini et al., 2015), as well as the surface area extent of the ozone hole (Fernandez et al., 2017). However, Chipperfield et al. (2018) indicated that along with the observed increase of LS ozone in 2017, there is an interannual variability of LS ozone rather than a continuing decrease as Ball et al. (2018) suggested. Chipperfield et al. (2018) argue that the atmospheric dynamics play a larger role on the LS ozone variability. Either way, the continued monitoring of ozone as well as the various halogen contributions is required.

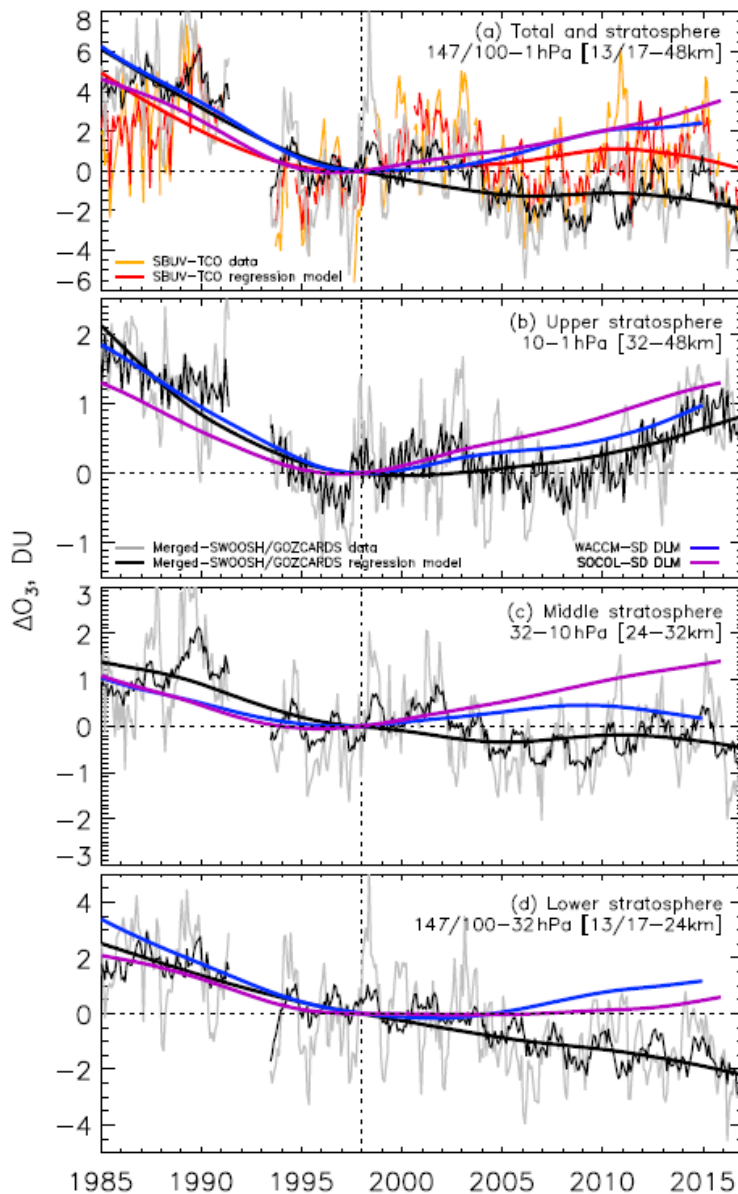


Figure 2.5: The ozone column anomaly trends between 1985 and 2016 is integrated between 60°S to 60°N. The de-seasonalized satellite measured ozone column is shown in gray, while the thin black line shows the regression model time series. The smooth thick black line shows the dynamical linear modelling (DLM) non linear trend of the data. The DLM trend for two models is shown in blue and purple. The different panels show these respective trends in different layers of the stratosphere: (a) for the whole stratosphere ranging from 13/17–48 km, (b) the upper stratosphere (32–48 km), (c) middle stratosphere (24–32 km) and (d) the lower stratosphere (13/17–24 km). Panel (a) additionally has model results of the ozone column time series shown in orange and the regression time series in red. Figure adapted from Ball et al. (2018).

## 2.5 Fundamentals of Radiative Transfer

The atmosphere's energy budget drives the hydrological cycle including evaporation, cloud coverage, and ocean circulations determining the climate (Stephens et al., 2012). The energy fluxes at the top of the atmosphere (TOA), within it, and at Earth's surface are shown in Fig. 2.6. The incoming shortwave radiation from the sun, the outgoing longwave radiation from Earth, and other various processes in the atmosphere redistributing and transferring energy are indicated. When the global climate is stable there is no warming or cooling at the surface or TOA, and the energy budget is balanced.

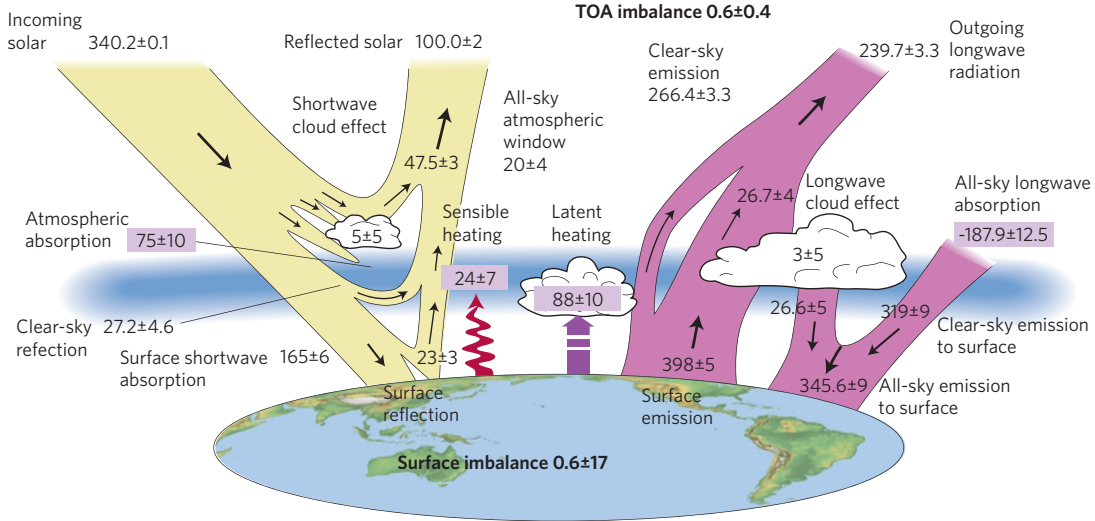


Figure 2.6: The global energy budget of the atmosphere with fluxes given in  $\text{W m}^{-2}$  for the annual mean between 2000–2010. The incoming shortwave solar radiation is shown in yellow. The Earth's outgoing longwave radiation is shown in purple. The four principle fluxes of the atmospheric energy budget (atmospheric absorption, all-sky longwave absorption, sensible heating, and latent heating) are displayed in the purple boxes. Figure adapted from Stephens et al. (2012).

### 2.5.1 Radiative Transfer Equation

The redistribution of radiation in the atmosphere occurs by extinction, emission, and scattering processes. The following description of radiative transfer follows Petty (2006), where the reduction of the initial radiation ( $I$ ) is the sum of each of these processes,

$$dI = dI_{\text{ext}} + dI_{\text{emit}} + dI_{\text{scat}}. \quad (2.22)$$

The extinction of radiance over an infinitesimal distance ( $ds$ ) is due to absorption and scattering and can be defined as the following:

$$dI_{\text{ext}} = -\beta_e I ds = -(\beta_a + \beta_s) I ds, \quad (2.23)$$

where  $\beta_e$ ,  $\beta_a$ , and  $\beta_s$  are the extinction, absorption, and scattering coefficients, respectively. Extinction is determined by the sum of absorption and scattering  $\beta_e = \beta_a + \beta_s$ .

Radiation that is absorbed by a molecule converts the energy into another form such as heat thereby warming that atmospheric layer. The reduction of the initial radiation due to absorption

alone is given by:

$$dI_{\text{abs}} = -\beta_a I \, ds. \quad (2.24)$$

Air molecules and aerosols can then thermally emit energy. When in local thermodynamic equilibrium, Kirchoff's Law states that the absorptivity ( $\beta_a \, ds$ ) is equal to the emissivity. Therefore, the emitted radiation is given by:

$$dI_{\text{emit}} = \beta_a B_\lambda(T) \, ds, \quad (2.25)$$

where  $B_\lambda(T)$  is Planck's Function.

Additionally, when an incoming photon from direction  $\hat{\Omega}'$  is scattered, it changes the propagation direction of the photon to  $\hat{\Omega}$ . An elastic scattering event conserves the photon energy, as in Rayleigh scattering off air molecules or Mie scattering off of aerosol particles or cloud water droplets (Platt and Stutz, 2008). Rayleigh scattering occurs if the particle is smaller than the wavelength of the photon and Mie scattering occurs if the particle is comparable or larger than the photon wavelength. When inelastic scattering occurs energy is exchanged, as in Raman scattering when energy is transferred between the photon and scattering molecule. The transfer of energy from a photon to the molecule is called a Stokes-shift, conversely if the scattering particle transfers energy to the photon it is denoted an anti-Stokes-shift. The change in radiance due to scattering is proportional to the scattering coefficient, and when summed over all directions ( $\hat{\Omega}'$ ) it can be expressed as

$$dI_{\text{scat}} = \frac{\beta_s}{4\pi} \int_{4\pi} I(\hat{\Omega}') p(\hat{\Omega}', \hat{\Omega}) d\hat{\Omega}' ds, \quad (2.26)$$

where  $p(\hat{\Omega}', \hat{\Omega})$  is the scattering phase function. The scattering phase function represents the probability density of an incoming photon with direction  $\hat{\Omega}'$  that it is scattered in the new direction  $\hat{\Omega}$  (within an infinitesimal window  $d\hat{\Omega}$ ). It is normalized when integrating over all  $4\pi$  steradians solid angle,

$$\frac{1}{4\pi} \int_{4\pi} p(\hat{\Omega}', \hat{\Omega}) d\hat{\Omega}' = 1, \quad (2.27)$$

such that energy is conserved in the absence of absorption.

A combination of the extinction, emission, and scattering processes redistribute solar short-wave and Earth's longwave radiation within the atmosphere and is crucial for creating a habitable surface climate. The sum of these processes (Eqs. (2.23),(2.25), and (2.26)) results in the radiative transfer equation (RTE, Petty (2006)):

$$dI(\hat{\Omega}) = -I(\hat{\Omega}) \cdot (\beta_a + \beta_s) ds + \beta_a B_\lambda(T) ds + \frac{\beta_s}{4\pi} \int_{4\pi} I(\hat{\Omega}') p(\hat{\Omega}', \hat{\Omega}) d\hat{\Omega}' ds. \quad (2.28)$$

An analytical solution does not exist, except for strictly limited scenarios. However, a simplified radiative transfer equation in terms of remote sensing is discussed in Sect. 4.1 for absorption and scattering, and a numerical solution using a Monte Carlo method is discussed in Sect. 4.3.

## 2.5.2 Optical Properties of Aerosols and Clouds (OPAC)

The relative fraction of light that is scattered in the atmosphere compared to the total extinction is known as the aerosol single scattering albedo (SSA):

$$\text{SSA} = \frac{\beta_s(\lambda)}{\beta_a(\lambda) + \beta_s(\lambda)}, \quad (2.29)$$

where as mentioned above, the total extinction coefficient is the sum of the absorption and scattering coefficients ( $\beta_a(\lambda) + \beta_s(\lambda)$ ) and are wavelength ( $\lambda$ ) dependent (Petty, 2006; Platt

and Stutz, 2008).

In the atmosphere, the assumption can be made that particles are spherical or randomly oriented, which simplifies the scattering phase function (Eq. (2.27)). In this case, the scattering phase function only depends on the angle ( $\vartheta$ ) between the original ( $\hat{\Omega}'$ ) and scattered ( $\hat{\Omega}$ ) direction, i.e.,  $\cos(\vartheta) \equiv \hat{\Omega}' \cdot \hat{\Omega}$  (Petty, 2006). The normalization condition described above in Eq. (2.27) can then be expressed as

$$\frac{1}{2} \int_{-1}^1 p(\cos \vartheta) d \cos \vartheta = 1. \quad (2.30)$$

However, frequently only the relative portion of forward vs backward scattered photons is relevant, which is described by the asymmetry parameter ( $g$ ),

$$g \equiv \langle \cos \vartheta \rangle = \frac{1}{2} \int_{-1}^1 p(\cos \vartheta) \cdot (\cos \vartheta) d \cos \vartheta. \quad (2.31)$$

and must be  $-1 \leq g \leq 1$ . A model phase function known as the Henyey-Greenstein phase function ( $p_{\text{HG}}$ ) can then be defined in terms of the asymmetry parameter as follows:

$$p_{\text{HG}}(\cos \vartheta) = \frac{1 - g^2}{(1 + g^2 - 2g \cdot \cos \vartheta)^{3/2}}. \quad (2.32)$$

If all scattering events occur in one direction either the forward direction ( $\vartheta = 0$ ) or the backward direction ( $\vartheta = \pi$ ), then the ratio of forward to back scattering is defined by

$$\left[ \frac{1 + g}{1 - g} \right]^3. \quad (2.33)$$

Forward scattering is favored when  $g > 0$ , while backscattering is favored for  $g < 0$ . Typical tropospheric aerosol asymmetry factors are  $g \sim 0.7$  while for only forward scattering  $g = 1$ .

Both the SSA and  $g$  are calculated by the Optical Properties of Aerosols and Clouds (OPAC; Hess et al. (1998)) model. Although the OPAC model is more suitable for characterizing tropospheric properties, it includes a sulfate component (75%  $\text{H}_2\text{SO}_4$ ) in the stratospheric background to account for nucleation processes with  $\text{H}_2\text{O}$ . The stratospheric aerosol concentrations are assumed to be 3 particles  $\text{cm}^{-3}$ , corresponding to an optical depth of 0.005. The OPAC model results of the SSA and  $g$  agree with a previous study by Pollack et al. (1981), which focused on stratospheric aerosol scattering properties.

OPAC calculates the scattering properties for several scenarios, namely for the Arctic, Antarctic, continental clean/ average/ polluted, desert, sulfate, urban, and maritime clean/ tropical/ polluted scenarios. It further specifies the SSA and  $g$  for 10 different wavelengths between 250–700 nm in 50 nm increments, and eight different relative humidity (RH) settings which are 0%, 50% 70%, 80%, 90%, 95%, 98%, and 99% RH. These micro-physical properties are important to parametrise the optical properties when calculating the radiative transfer using the Monte Carlo RT model in Sect. 4.3.

# Chapter 3

## Instrumentation

In this study, several instruments that were assembled on the German HALO aircraft (refer to Sect. 3.1 below) platform are utilized. The mini-DOAS instrument (refer to Sect. 3.2 below) is a remote sensing instrument which is used to infer various trace gases such as  $\text{O}_3$ ,  $\text{NO}_2$ , and  $\text{BrO}$  among other trace gases and will be the focus of the data analysis in this dissertation (Hüneke et al., 2017). Other instruments on board HALO which are used for the analysis of  $\text{Br}^{\text{tot}}$ , consist of BAHAMAS (refer to Sect. 3.3.1 below) for avionic and meteorologic data, FAIRO (refer to Sect. 3.3.2 below) for in situ  $\text{O}_3$  (Zahn et al., 2012), and GhOST (refer to Sect. 3.3.3 below) for the in situ measurements of the organic brominated source gases and  $\text{SF}_6$  mean air mass ages (Sala et al., 2014). Additionally, UMAQS (refer to Sect. 3.3.4 below) measures  $\text{N}_2\text{O}$  and  $\text{CO}$  data which is used for the interpretation of air mass transport (Kunkel et al., 2019). The measurements and the dynamics of the air mass transport in the UTLS are corroborated by simulations from the CLaMS model (refer to Sect. 3.4.1 below) (McKenna et al., 2002b; Vogel et al., 2015) and the bromine impact on  $\text{O}_3$  is simulated by the TOMCAT/SLIMCAT model (refer to Sect. 3.4.2 below) (Chipperfield, 1999, 2006).

### 3.1 HALO Aircraft

The High Altitude and LOng Range Research Aircraft (HALO) is operated by the Flight Experiments (FX) facility from the German Aerospace Center (DLR–Deutsches Zentrum für Luft- und Raumfahrt). Its home base is at the Special Airport of Oberpfaffenhofen, Germany (ICAO code: EDMO). HALO is a refurbished Gulfstream G550 business jet (refer to Fig. 3.1), with the interior stripped allowing for a variety of instrument racks to be set up based on the scientific payload desired for each research campaign. HALO is used by the German scientific community, along with occasional international collaborators, for atmospheric (and earth) observations in particular for the study of transport and photochemistry at a variety of scales. It is well suited for such experiments as it has the capability for research flights up to  $\sim 10$  hours, reaching altitudes of  $\sim 15$  km, and a maximum payload of 3 tons with  $20\text{--}30$  m<sup>2</sup> for ample space for a variety of instruments (Minikin et al., 2020; Wendisch and Schwarz, 2020). HALO is capable of flying low in the boundary layer all the way up through the LS reaching potential temperatures of  $\Theta \sim 420$  K (Riese et al., 2017). The HALO platform is well suited for the WISE campaign (refer to Sect. 5.1 below), as it allows for extensive measurements in the Ex–UTLS region for the study of trace gas distributions, as well as dynamical and chemical processes in the NH (Riese et al., 2017).



Figure 3.1: The HALO research aircraft with the red arrow pointing to the location of the mini-DOAS instrument at the back of the aircraft in the boiler room (picture from November 2019 in Rio Grande, Tierra del Fuego, Argentina).

## 3.2 Mini-DOAS Instrument

The mini-DOAS (Differential Optical Absorption Spectroscopy) is a remote sensing instrument operated by our group at the University of Heidelberg (Hüneke et al., 2017). It weighs 58 kg and is located in the unpressurized boiler room at the back of the HALO aircraft and is physically inaccessible during a flight. The instrument consists of six optical spectrometers with two each in the UV, visible (vis), and near-infrared (NIR) wavelength ranges. The UV spectrometer wavelengths range between  $\sim 310\text{--}440$  nm, the visible spectrometers are from  $\sim 417\text{--}640$  nm, and the NIR spectrometer wavelengths range from  $\sim 1102\text{--}1690$  nm. In this study only the UV and visible channels are used. The spectrometers are connected with fiber bundles to three scanning limb and three fixed nadir telescopes. The optical properties (wavelength range and field of view (FOV)) of these spectrometers are listed in Table 3.1 with which scattered skylight is collected. The recorded spectra are an average measurement over the atmospheric volume based on the distance travelled by the aircraft during a single measurement, over the FOV of the telescope and the light path length. This in turn is dependent on the exposure time, the elevation, cloudiness and other atmospheric conditions. Due to the large range of wavelengths of the channels a variety of trace gases can be analysed, including various halogen species BrO, OClO, IO, IO<sub>2</sub>, and I<sub>2</sub>; O<sub>x</sub> species O<sub>3</sub> and O<sub>4</sub>; H<sub>2</sub>O (vapour, liquid, ice); and many different pollutants NO<sub>2</sub>, HONO, CH<sub>2</sub>O, C<sub>2</sub>H<sub>2</sub>O<sub>2</sub>, C<sub>3</sub>H<sub>4</sub>O<sub>2</sub>, SO<sub>2</sub>, CO<sub>2</sub>, and CH<sub>4</sub>.

Table 3.1: mini-DOAS optical properties of the six spectrometers. The vertical (V.) and horizontal (H.) field of view (FOV) measurements are from Knapp (2016).

Spectrometer	Wavelength [nm]	V. FOV [°]	H. FOV [°]
Nadir UV1	310–440	$0.321 \pm 0.008$	$3.10 \pm 0.02$
Limb UV2	313.6–441.5	$0.465 \pm 0.012$	$3.34 \pm 0.01$
Nadir VIS3	417–640	$0.356 \pm 0.010$	$3.12 \pm 0.01$
Limb VIS4	417–640	$0.469 \pm 0.012$	$3.11 \pm 0.01$

The mini-DOAS instrument is shown in Figure 3.2 excluding the aperture plate which sits below the instrument in the fuselage of the aircraft. The schematic of the mini-DOAS is shown in Figure 3.3 which shows the three main components of the instrument: the control unit (top), the spectrometer unit (middle) and the aperture plate (bottom). The control unit consists of a power supply with a peltier cooling option and an electronic box to control the spectrometers and save data. The spectrometer unit includes the six spectrometers in a vacuum housing encapsulated by an ice-water bath along with insulation to keep the spectrometers at a constant temperature near 0°C. And lastly, the aperture plate is the housing for the six telescopes including three motors to control the limb telescopes as well as a camera in the limb direction. The nadir telescopes have a fixed orientation pointing directly perpendicular below the aircraft and do not compensate for the aircraft's change in roll angle or pitch.



Figure 3.2: The mini-DOAS instrument installed in the boiler room of the HALO aircraft (picture from February 2018). The upper half consists mainly of the two electronic boxes, one on either side. The bottom half is the water and ice bath housing within which the spectrometers are placed for stable temperatures. At the very center, the white lid to the ice bath unit is visible and just below the lid to the left is the connector to the vacuum housing with the spectrometers. The blue and white cables on the left provide power and connect the mini-DOAS instrument via an ethernet cable to the HALO aircraft cabin to access the instrument computer during flights. The aperture plate (not shown) is placed below the mini-DOAS spectrometer unit.

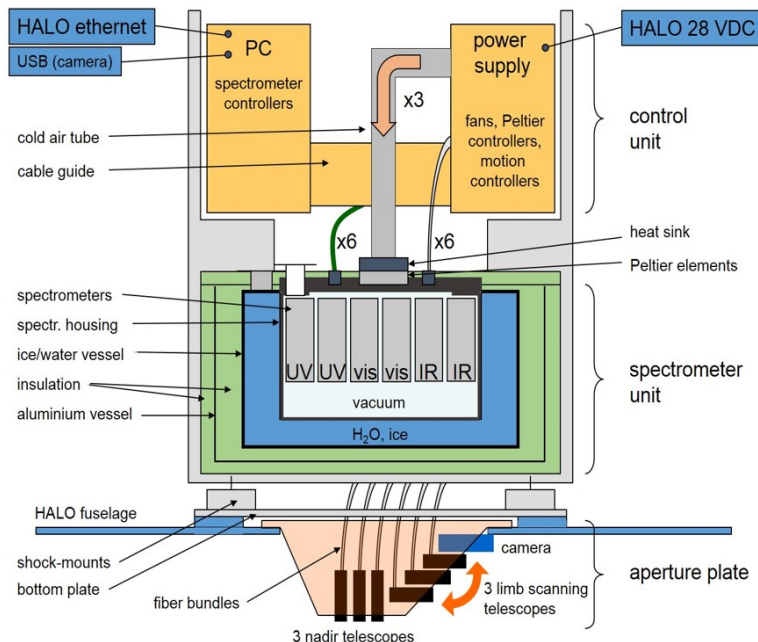


Figure 3.3: The schematic of the mini-DOAS instrument consisting of three main components. The control unit with the two electronic boxes is at the top (shown in yellow), the spectrometer unit with the spectrometers in a vacuum housing and the surrounding ice bath is in the middle (shown in gray and blue respectively), and at the bottom is the aperture plate with the telescopes (shown in orange). Figure adapted from Hüneke et al. (2017).

In this study only the UV and vis channels in the limb orientation are used, i.e., the air masses observed are perpendicular to the aircraft main axis on the right hand side. The limb telescopes are adjusted continuously in flight to compensate for changes in the roll angle of the HALO aircraft for constant alignment with the flight altitude. Motorized telescope gears

(updated at 10 Hz) are used in-flight to adjust for the roll angle of the aircraft, however right hand curves with roll angles larger than  $5^\circ$  cannot be corrected and subsequently this data is removed from analysis. Leftward curves can be corrected for up to  $90^\circ$  and are therefore not a problem. Additionally, during sharp flight turns the time delay of the correction for the roll angle may cause for further elimination of individual data points if the alignment is too slow. As such, all data collected from misaligned telescopes are removed. Additional details of the HALO mini-DOAS instrument and its development can be found in Hüneke (2016) and Hüneke et al. (2017) and references therein.

### 3.2.1 Preparations

Prior to measurements, a few preparations for the mini-DOAS instrument are required. Because the instrument is situated in the boiler room which is open to the ambient temperatures and pressures, to ensure consistent and stable retrievals the spectrometers are kept under vacuum and cooled. To achieve constant vacuum conditions, the spectrometer housing is evacuated using a Pfeiffer HiCube vacuum pump to remove dust and other particles and to ensure a steady pressure during flights. A minimum of a two-week period is required prior to taking measurements to reach values of  $10^{-6}$  mbar if the spectrometer housing was open to room temperature and pressure conditions. During the campaign the spectrometer housing is kept sealed to ensure stable low pressures. Typical leakage rates are  $2 \times 10^{-5}$  mbar L s $^{-1}$  (Hüneke et al., 2017) allowing for stable pressures typically throughout the 4–5 weeks long campaign. The option to further pump the instrument between flights is possible, if the spectrometer lid or the fiber bundle connectors are losing vacuum pressure too quickly. However, additional vacuum pumping during the WISE campaign was not required.

After the instrument has been successfully installed in HALO with the assistance and approval of the DLR-FX team, the limb telescope motors must be calibrated and aligned with the aircraft lateral axis. This is accomplished with a slit lamp light source positioned approximately 10 m away at the same height ( $\pm 0.5$  cm) from the ground as the center of the limb telescopes when pointing horizontally to the left. The limb telescopes are scanned up and down to capture the slit lamp emission source. With the mini-DOAS calibration software the peak of the light source is measured and represents the corresponding calibration angle. This calibration angle along with the roll angle of the aircraft relative to the Hangar ground in its current parked position are added to create an offset for each telescope motor. This offset is then included in the mini-DOAS script throughout the campaign and defines the  $0^\circ$  direction (aligned with the aircraft main axis) of the telescope.

For this study the offsets calibrated for the NIR, vis, and UV telescope motors were  $-1.1^\circ$ ,  $-0.29^\circ$ ,  $-1.3^\circ$ , respectively. These offsets as well as all in-flight roll-angle adjustments have pointing errors of  $\pm 0.11^\circ$ ,  $\pm 0.09^\circ$ , and  $\pm 0.03^\circ$  for the NIR, vis, and UV telescope gears, respectively, due to the lag in the upwards and downwards direction (Fig. 3.4 (a–c)). This leads to a slightly less precise viewing direction of the FOV along the horizon (Table 3.1). After the WISE campaign in fall of 2017, but prior to the next campaign (EMeRGe-Asia (Effect of Megacities on the Transport and Transformation of Pollutants on the Regional to Global Scales)) in spring of 2018, the lag of the motors was improved through cleaning and replacing the ball bearings inside the motor drums. The lag of the pointing errors were improved for the NIR, vis, and UV motors resulting in  $\pm 0.025^\circ$ ,  $\pm 0.00^\circ$ , and  $\pm 0.01^\circ$ , respectively (Fig. 3.4 (d–f)).

Additionally, during the WISE campaign there was a 3 s delay between the actual roll angle of the aircraft (from BAHAMAS, Sect. 3.3.1) and mini-DOAS receiving the information leading to further pointing errors. This time delay was later eliminated for the SouthTRAC (Southern Hemisphere–Transport Composition Dynamics) campaign in 2019 by upgrading the mini-DOAS

instrument to access the aircraft avionics system directly and circumventing the BAHAMAS instrument. The time delay would result in a slightly larger distribution around the horizon ( $0^\circ$  elevation angle), and will be quantified once a comparison with SouthTRAC data has been done where the time delay is eliminated.

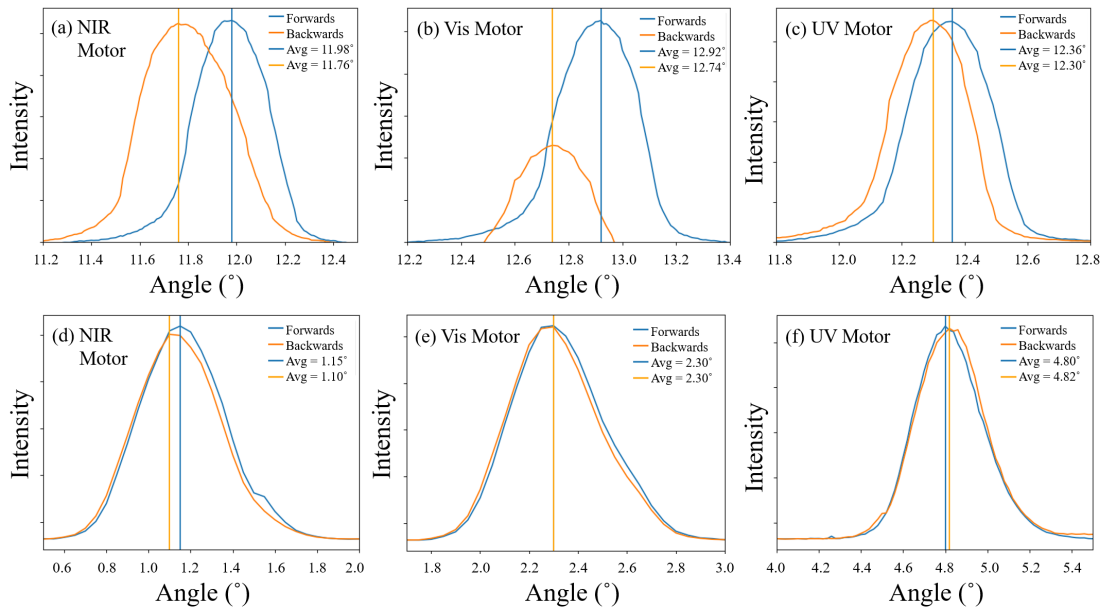


Figure 3.4: Telescope motor lab measurements of the forward and backward directions taken immediately following the WISE campaign at the end of 2017 (a–c) and after the ball bearings inside the motor drums were replaced in January 2018 (d–f). In (a–c) the pointing errors are  $\pm 0.11^\circ$ ,  $\pm 0.09^\circ$ , and  $\pm 0.03^\circ$  for the NIR, vis, and UV motors, respectively. In (d–f) the pointing errors are reduced to  $\pm 0.025^\circ$ ,  $\pm 0.00^\circ$ , and  $\pm 0.01^\circ$  for the NIR, vis, and UV motors, respectively. Figure courtesy of Ben Schreiner (personal communication).

Further preparations for the mini-DOAS instrument prior to any measurement, requires the cooling of the spectrometers by supplying 4 kg of ice and 3 L of cooled water to the bath surrounding the spectrometer housing (shown in blue in Figure 3.3) to stabilize the spectrometer temperatures near  $0^\circ\text{C}$ . Due to the nature of this particular study (flying at high altitudes with low ambient temperatures as well as ground temperatures around  $10^\circ\text{C}$ ), the UV and vis spectrometer temperatures were generally below  $2^\circ\text{C}$  (the NIR is generally  $1^\circ\text{C}$  warmer due to its placement) enabling steady analysis conditions.

Once the spectrometers reach  $< 2^\circ\text{C}$  they need to be optically and electronically characterized and calibrated to minimize the noise in the measured spectrum. A spectrograph analogue-digital converter is used to convert the analogue signal to a digital one, however it can only process positive signals. Therefore, an artificial electronic offset is added to each recorded analogue signal. Once this spectrum has been converted to a digital signal, the offset must be subtracted again. The noise from the CCD (charge-coupled device) detector known as the dark current which if from thermal excitation of electrons must be subtracted as well. Therefore, measurements of the dark current and offset voltages are required to reduce noise in the measured spectra. The telescopes are covered with a thick black cloth eliminating all light sources from entering the spectrometers to allow for the characterization of the unit. The dark current is measured by collecting one spectrum with an exposure of 10000 ms, while the offset voltage records and adds 1000 scans/spectra at the minimum 13 ms exposure. Examples of the dark current and offset are shown in Fig. 3.5.

In certain cases, recorded spectra will need to be added in order to reduce the total noise (N)

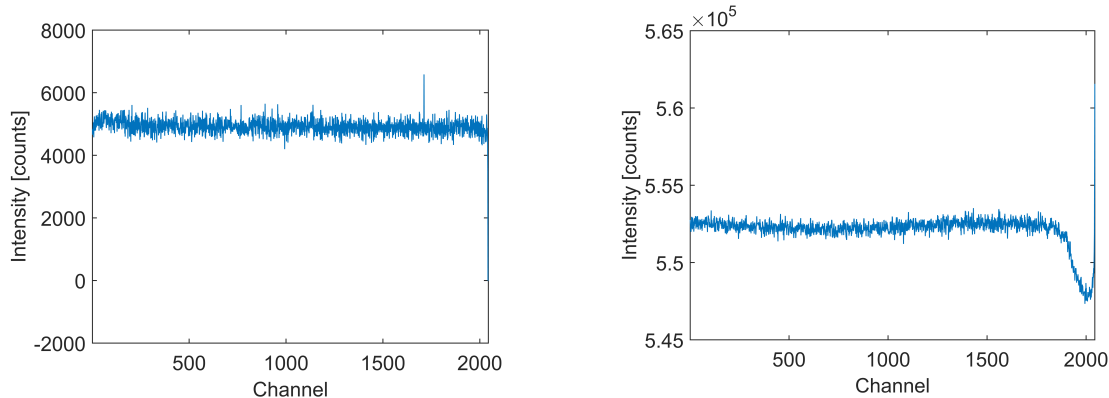


Figure 3.5: An example of the dark current (left) and offset voltage (right) from the limb UV channel recorded on September 11, 2017.

of a spectrum. One component of the total noise is the electronic offset and dark current, which is called the instrument or background noise ( $N_B$ ). And the other type is statistic noise of the spectral irradiance signal due to the fluctuating photons recorded even for identical (lab) conditions. This photon noise ( $N_P$ ) is a Poisson distribution dependent on the number of registered photons. The total noise is then defined as  $N = \sqrt{N_B^2 + N_P^2}$ . For gases with low absorption in the given wavelength range, the total noise will be to large relative to the signal. Spectra can be added as a running mean to reduce the signal to noise ratio and to distinguish the absorption signal better.

Additionally, any recorded spectrum must be calibrated to correspond the channel numbers to the respective wavelengths. This is done using the known emission lines from mercury and krypton Pen-Ray lamps (Mentges, 2021). These calibrations should be done throughout the campaign to potentially avoid pressure drifts of the instrument. A calibration close in time to the actual measurements should be used for each flight. Additional settings and details of the mini-DOAS instrument can be found in previous student theses such as Knapp (2016); Hüneke (2016); Kluge (2018); Schreiner (2018) and in Hüneke et al. (2017).

### 3.3 Additional Instrumentation

Additional instruments operated by external groups also aboard HALO during the WISE campaign are briefly summarized here.

#### 3.3.1 BAHAMAS

The Basic HALO Measurement And Sensor System (BAHAMAS) is permanently installed on HALO and operated by the DLR–FX Sensor and Data group. BAHAMAS records avionic and meteorologic data of HALO’s location including the aircraft position, altitude, roll/yaw/pitch angles, and acceleration as well as the ambient conditions such as pressure, temperature, potential temperature, 3-D wind field, turbulence, and humidity (Krautstrunk and Giez, 2012). The BAHAMAS time server acts as the common reference for all instruments on board. It has a high resolution (10 Hz) providing real time measurements crucial for the mini-DOAS instrument to correct for the roll angle of the aircraft for the limb telescopes. The BAHAMAS roll angle has a root mean square of  $< 0.05^\circ$  allowing for accurate limb telescope pointing directions. Unfortunately, during the WISE campaign there is a time delay of 3 s between BAHAMAS sending the attitude information and the mini-DOAS receiving it (as mentioned above), increasing the

uncertainty of the pointing of the limb telescopes and slightly altering the observed air masses.

### 3.3.2 FAIRO

The Fast AIRborne Ozone monitor (FAIRO) was first deployed in 2012 and is operated by the Karlsruhe Institute of Technology (Zahn et al., 2012). It is a fully custom-built, lightweight, and compact O<sub>3</sub> sensor (14 kg, 19", 13.5 cm high), which uses two methods to accurately measure in situ O<sub>3</sub>: a UV photometer and a chemiluminescence (CL) sensor. The UV photometer measures the O<sub>3</sub> absorption in the Hartley bands around 255 nm using a UV-LED light source and is the more accurate technique of the two ( $\sim 0.08$  ppb), operating at a lower frequency (0.25 Hz, 1 bar). The CL detector measures the light emission between 450–500 nm from the reaction produced by O<sub>3</sub> reacting with an organic dye (Coumarin 47) that is adsorbed on dry silica gel. The CL technique measures at a higher frequency of 10 Hz. The UV photometer results are used to calibrate the CL response, thus combining the accuracy of the UV photometer with the high frequency of the CL sensor. The typical  $1\sigma$  measurement precision is 0.08 ppb for the UV spectrometer and 0.5% for the CL detector. Accuracy for the UV spectrometer measurements is  $\sim 1.5\%$  (mostly determined by the uncertainty of the O<sub>3</sub> cross section). More details can be found in Zahn et al. (2012).

In this dissertation, O<sub>3</sub> is determined from the CL method except during one research flight (on October 9, 2017–RF11, refer to Sect. 5.1 below) for which the UV photometer method O<sub>3</sub> is used as only partial CL O<sub>3</sub> data was available. These O<sub>3</sub> measurements are used for the mini-DOAS post flight analysis when using the scaling method (refer to Sect. 4.2 below) and result in higher accuracy compared to using model results of O<sub>3</sub>.

### 3.3.3 GhOST

The Gas Chromatograph for the Observational Studies using Tracers (GhOST) instrument, operated by the University of Frankfurt, detects stable atmospheric trace gases. It has two gas chromatographic channels, one which is coupled to a mass spectrometer (MS) (Agilent MSD 5975) and the other one to an electron capture detector (ECD) (e.g., Sala et al. (2014), Obersteiner et al. (2016), Keber et al. (2020)). SF<sub>6</sub> and CFC-12 are measured on the ECD channel with a time resolution of 60 s and a high precision of typically about 0.6% for SF<sub>6</sub> and 0.2% for CFC-12, in a similar setup as used in Bönisch et al. (2009). In addition, SF<sub>6</sub> data are smoothed using a local correlation with the CFC-12 data (an atmospheric transport tracer) which has a higher precision. Ten data points surrounding the measurement on both sides are used to determine the local correlation for each data point. This procedure retains the local information without introducing an offset to SF<sub>6</sub> mixing ratios and removes some instrumental scatter.

The mean age of air can be inferred from SF<sub>6</sub> measurements only if a single entry point can be assumed. As air masses observed during the WISE campaign are strongly influenced by transport of air from the NH mid latitudes and from the tropics, a direct derivation of mean age is not possible. Instead the so-called lag-time is used here, i.e., the time lag between the occurrence of a certain mixing ratio of SF<sub>6</sub> in the UTLS with respect to the time when this mixing ratio was observed in the global mean. The lag-time derived in this way has an overall precision better than 0.3 years and an estimated accuracy of 0.6 years. The global mean SF<sub>6</sub> mixing ratio used as a reference is lower than the NH mixing ratios. Particularly close to the tropopause, the observed mixing ratios are often higher than those in the reference time series, resulting in negative lag-times.

The second channel measures bromocarbons and other halogenated species with cryogenic

enrichment (Obersteiner et al., 2016), gas chromatographic separation, and mass spectrometric detection with a time resolution of four minutes (Sala et al., 2014). Atmospheric mixing ratios of  $\text{CH}_3\text{Br}$ , halons H-1301, H-1211, and H-2402 as well as the short-lived bromocarbons ( $\text{CH}_2\text{Br}_2$  and  $\text{CHBr}_3$ ) are reported on the scales used in the AGAGE (Advanced Global Atmospheric Gas Experiment) network (Prinn et al., 2018). Mixed bromochlorocarbons ( $\text{CH}_2\text{BrCl}$ ,  $\text{CHBr}_2\text{Cl}$ , and  $\text{CHBrCl}_2$ ) and H-1202 are calibrated based on inter-calibration experiments with the UEA (University of East Anglia). Due to a decrease of  $\text{CH}_3\text{Br}$  in the calibration gas and poor signal to noise ratios for this compound, a correlation between H-1211 and  $\text{CH}_3\text{Br}$  measured previously during the PGS (three part mission: POLSTRACC (Polar Stratosphere in a Changing Climate), GW-LCYCLE (Investigation of the Life cycle of gravity waves) and SALSA (Seasonality of Air mass transport and origin in the Lowermost Stratosphere)) campaign has been used. This correlation leads to a scaling of 12.5% so as to arrive at typical tropospheric mixing ratios of  $\text{CH}_3\text{Br}$  observed in the NH in 2017 and then applied to the data of the current study. Typical detection limits for the different species during WISE are given in Keber et al. (2020). Typical precisions are 4.22% for  $\text{CH}_3\text{Br}$ , 0.99% for H-1301, 0.49% for H-1211, 7.58% for H-1202, 1.49% for H-2402, 0.67% for  $\text{CH}_2\text{Br}_2$ , 2.21% for  $\text{CHBr}_3$ , 9.16% for  $\text{CH}_2\text{BrCl}$ , 3.43% for  $\text{CHBrCl}_2$ , and 2.22% for  $\text{CHBr}_2\text{Cl}$ . The  $1\sigma$  scatter (the standard deviation) of total  $\text{Br}^{\text{org}}$  measurements in a 10 K potential temperature interval directly below the tropopause is  $\pm 0.81$  ppt (4%), which includes the precision of the measurement as well as the atmospheric variability (Sala et al., 2014).

### 3.3.4 UMAQS

The University of Mainz Airborne QCL (quantum cascade laser) Spectrometer (UMAQS) is operated by the University of Mainz. It simultaneously measures nitrous oxide ( $\text{N}_2\text{O}$ ) and carbon monoxide (CO) from the HALO aircraft. The instrument is in situ calibrated against secondary standards, which are compared to NOAA primary standards before and after the campaign. It uses direct absorption of infrared radiation at  $2200\text{ cm}^{-1}$  using a Hariott cell with a 76 m light path at 50 hPa. Measurements are recorded with a frequency of 1 Hz, and the total uncertainty during the WISE campaign was determined to be  $\pm 0.18$  ppb for  $\text{N}_2\text{O}$  and  $\pm 0.9$  ppb for CO. These tracers are used for the interpretation of air mass transport around the UTLS during the WISE campaign. For more details refer to Müller et al. (2015) and Kunkel et al. (2019).

## 3.4 Models

### 3.4.1 Lagrangian Modelling by CLaMS

#### CLaMS Trace Gas Curtains

The Chemical Lagrangian Model of the Stratosphere (CLaMS) is developed at Forschungszentrum Jülich in Germany. It is a Lagrangian chemistry transport model (CTM) (McKenna et al. (2002b,a); Pommrich et al. (2014) and references therein) which utilizes wind and temperature data of the ECMWF (European Centre for Medium-Range Weather Forecasts) from ERA-Interim re-analysis data (Dee et al., 2011). CLaMS is particularly good at portraying the gradients of trace gases for example at the extratropical tropopause due to its lagrangian nature. AURA-MLS (Microwave Limb Sounder) and ACE-FTS (Atmospheric Chemistry Experiment – Fourier Transform Spectrometer) satellite data as well as tracer-tracer-correlations are used to initialise CLaMS simulations. The simulation used here starts on May 1, 2017 and has a horizontal resolution of 100 km.

The simulations are setup to optimally replicate bromine chemistry reactions in the stratosphere but lacks accuracy for photochemical processes in the troposphere as the heterogeneous reactions of brominated species on ice and liquid water are not yet implemented (Grooß et al., 2014). Also, only the long-lived  $\text{Br}_y^{\text{inorg}}$  is part of the simulation and bromine compounds from VLS are considered to already be converted to  $\text{Br}_y^{\text{inorg}}$ . This may cause offsets in  $\text{Br}_y^{\text{inorg}}$ , but nevertheless ratios like  $\text{BrO}/\text{Br}_y^{\text{inorg}}$  are reasonably determined by this method.

Various trace gas curtains along the flight tracks have been derived for each flight of the WISE campaign. These curtains are defined by the latitude, longitude, and time of the flight track for many altitudes. CLaMS model information for these points was achieved using back-trajectories to the model output time of the previous day at 12:00 UTC. The chemical composition from the 3-D CLaMS simulation is then interpolated to the trajectory endpoints, subsequently the CLaMS chemistry is calculated forward in time along these trajectories to determine the chemical composition along the given curtain. The CLaMS curtain simulations have a one minute time resolution corresponding to  $\sim 13$  km. The vertical coordinates have 41 pressure levels between 10–1000 hPa (up to approximately  $\Theta \sim 900$  K). These are unequal pressure levels for the best vertical resolution around the tropopause.

For the present study, CLaMS curtains are used as input for the radiative transfer simulations for the scaling method of the mini-DOAS data analysis (refer to Sect. 4.3.3 below). These simulated trace gas mixing ratios along the flight track are also used for direct comparisons with the measured data of  $\text{O}_3$ ,  $\text{NO}_2$ , and  $\text{BrO}$  (Sect. 5.3 below). Further, the simulated  $\text{BrO}/\text{Br}_y^{\text{inorg}}$  partitioning is used to infer measured  $\text{Br}_y^{\text{inorg}}$  from mini-DOAS  $\text{BrO}$  data.

### CLaMS Transport Tracers

In previous studies, different kinds of artificial tracers have been implemented in CLaMS to identify the transport pathways and to quantify the transport of air masses from defined atmospheric domains and surface regions to other locations of the atmosphere considering advection and mixing (e.g., Vogel et al. (2011, 2019)). To compare the WISE measurements with the CLaMS artificial tracers, the simulations are interpolated in space and time to the position of the HALO flight track using CLaMS trajectories. The trajectories are started every second along the flight track.

Two different kinds of artificial tracers are used here. The first kind is an artificial air mass origin tracer initialised on May 1, 2017 approximately 5 months prior to the WISE campaign. The air mass origin tracers mark nine distance 3-D domains in the entire model atmosphere which are the low-latitude (tropical) troposphere, upper and lower TTL, tropical pipe, mid-latitude troposphere and LMS, polar troposphere and LMS and lastly the stratospheric background (i.e., the LS above 380 K). The boundary conditions of the air mass origin domains are described in Table 3.2 and shown in Fig. 3.6 (originally from Vogel et al. (2011)). The tropical pipe domain is not shown but is the region above the upper TTL in the tropics. These tracers are used to study vertical and horizontal transport of the air masses to the LMS in the NH within the 5 months leading up to the WISE campaign.

The second kind is an artificial tracer that marks specific regions in the CLaMS model boundary layer referred to as surface emission tracers and are used here to study the transport of young air masses into the LMS in the NH. In contrast to the air mass origin tracers discussed above which are initialised once on May 1, 2017, the different surface emission tracers are continuously released (every 24 h) in the model boundary layer (2–3 km above the surface following orography) from the start of the simulation on May 1, 2017 (for more details see Vogel et al. (2015, 2019)). The surface emission tracers are divided into 24 surface regions shown in Fig. 3.7, defining relatively small regions in south eastern Asia to study in particular the influence of air

Table 3.2: The boundary conditions of the air mass origin tracers for the CLaMS simulations. Adapted from Vogel et al. (2011).

Air Mass Origin Tracer	Latitude	PV	$\Theta$
Low-latitude troposphere	0–30°	<2 PVU	<355 K
Mid-latitude troposphere	30–60°	<2 PVU	<355 K
Polar troposphere	60–90°	<2 PVU	<355 K
Lower TTL	–	<2 PVU	355–380 K
Upper TTL	–	<2 PVU	380–425 K
Mid-latitude LMS	<60°	>2 PVU	<380 K
Polar LMS	30–60°	>2 PVU	<380 K
Lower stratosphere (LS)	–	>2 PVU	>380 K

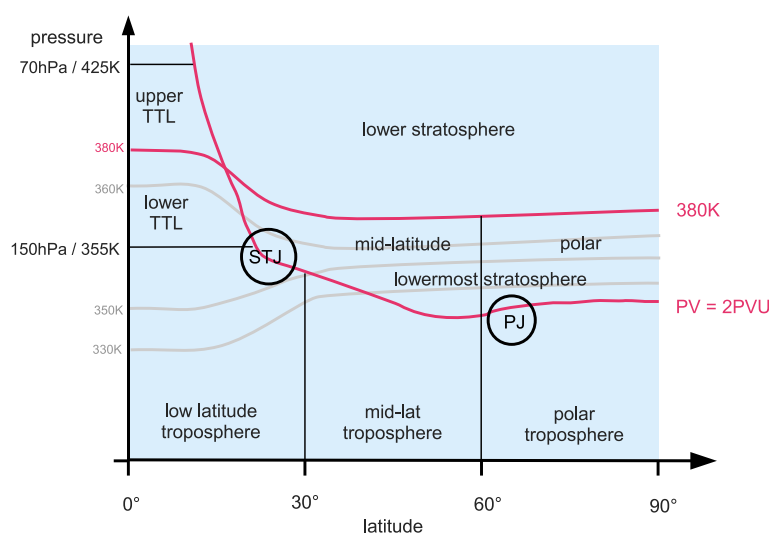


Figure 3.6: The CLaMS air mass origin domains divides the atmosphere for simulations beginning on May 1, 2017. Refer to Table 3.2 for more details. Figure adapted from Vogel et al. (2011).

masses from the Asian monsoon and its tropical adjacent regions on transport into the LMS. Moreover, these surface regions for the WISE campaign cover the entire Earth’s surface with surface emission tracers. For some regions, coastlines or orography (both provided by ECMWF) are used as criteria to define the boundaries between different regions. The same set-up for the surface emission tracers was already used for WISE measurements in Wetzel et al. (2020).

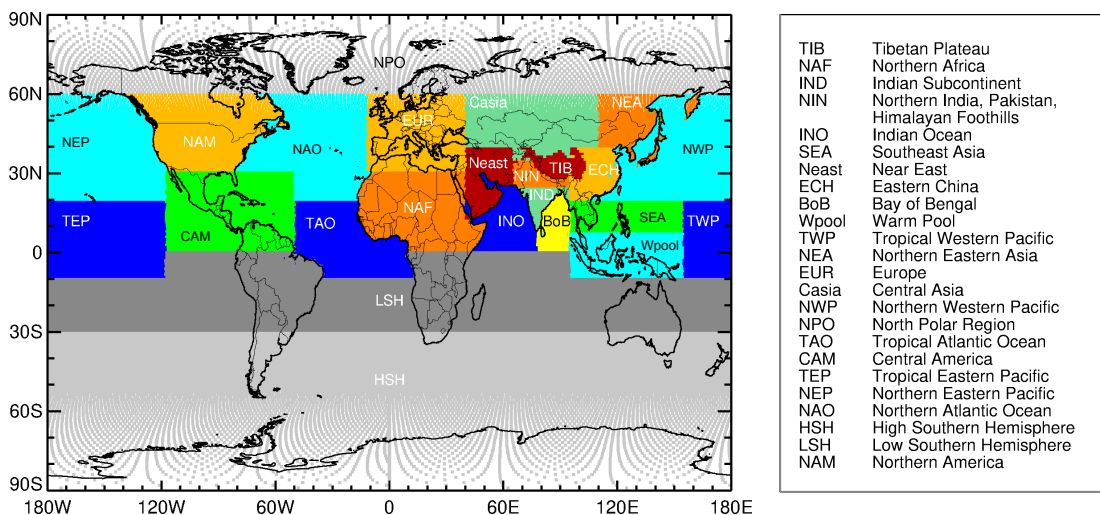


Figure 3.7: CLaMS artificial surface emission tracers by region based on previous simulations described in Vogel et al. (2015, 2019), with higher resolution regions at coastal boundaries mainly in south eastern Asia (INO, IND, NIN, BoB, Neast, and ECH) as well as in other regions (TIB, NEA, NAF, TAO, NAM, NEP, and NAO). Adapted from Wetzal et al. (2020) where these defined regions were also used for the analysis during the WISE campaign.

### 3.4.2 Chemical Transport Modelling by TOMCAT/SLIMCAT

The TOMCAT/SLIMCAT (hereafter TOMCAT) 3-D off-line global chemistry transport model (Chipperfield, 1999, 2006) is used here for the interpretation of the transport of trace gases from the tropical UT/TTL and extratropical tropopause (Ex-TP) regions into the LMS and to assess the corresponding loss in  $O_3$ . Similarly to CLaMS, the off-line model is driven by meteorology (e.g., horizontal winds, temperature, surface pressure, and convective mass fluxes) from ECMWF ERA-Interim reanalyses (Dee et al., 2011), with no feedback of the chemistry on the dynamics. In the setup used here the model employs a hybrid vertical coordinate with terrain-following sigma levels near the surface and pressure levels at higher altitudes. Large-scale vertical motion is calculated from the divergence of the horizontal winds. In these simulations the model uses a detailed stratospheric chemistry scheme TOMCAT (e.g., Chipperfield et al. (2018)) with photochemical information from JPL-2015 (Sander et al., 2011). The  $O_3$  loss reactions are described in Werner et al. (2017) Appendix A.

The simulations used here were initialised from a multi-decadal control simulation which started in 1977 (Dhomse et al., 2019). Output from this run on January 1, 2016 was used to initialise a series of sensitivity runs. These simulations calculated the chemistry and dynamics in 15 min time increments over a high horizontal resolution of  $1.2^\circ \times 1.2^\circ$  with 36 unevenly spaced vertical levels with an altitude range from the surface to around 63 km. The simulations continued until the end of the WISE campaign in late October 2017, i.e., 22 months integration time.

Initial constraints for the brominated species in the UT are given in Table 3.3. Three different TOMCAT sensitivity runs were performed starting from January 2016: a Base run followed by two runs with elevated bromine constraints. The Base run initialises the model with constant bromine contributions along the entire tropopause with the Ex-TP boundary conditions listed with  $[Br^{tot}] = 19.6$  ppt. The additional two runs continue to use the Ex-TP conditions in the extratropics, while elevated bromine in the form of  $Br^{VLSL}$  and  $Br_y^{inorg}$  are initialised in the tropical UT for two differing scenarios. Run 1 uses  $Br^{VLSL}$  constraints from Navarro et al. (2015) and  $Br_y^{inorg}$  from Werner et al. (2017) resulting in  $[Br^{tot}] = 20.8$  ppt for the tropical UT. Run 2

uses  $\text{Br}^{\text{VLS}}$  and  $\text{Br}_y^{\text{inorg}}$  mixing ratios from the current study for the tropical UT/TTL resulting in  $[\text{Br}^{\text{tot}}] = 21.7$  ppt. These runs, with differing bromine mixing ratios in the tropical UT but constant Ex-TP constraints, simulate different air masses being transported into the LMS. The comparison of the model runs allows for the impact of the differing bromine levels on the  $\text{O}_3$  levels in this region to be diagnosed.

Table 3.3: Bromine boundary conditions near the tropopause from various research studies for the extratropical tropopause (Ex-TP) and the tropical UT (Trop-UT) used to initialise the TOMCAT/SLIMCAT model. The Base run uses the Ex-TP bromine boundary conditions along the entire tropopause for all latitudes. There are two further runs with elevated UT bromine initialisations in the tropics ( $30^\circ\text{S}$ – $30^\circ\text{N}$ , run 1 and run 2) while the extratropics are still set to the Ex-TP bromine boundary conditions as in the Base run.

Run	Region	$\text{CH}_3\text{Br}$ [ppt]	Halons [ppt]	$\text{Br}^{\text{VLS}}$ [ppt]	$\text{Br}_y^{\text{inorg}}$ [ppt]	$\text{Br}^{\text{tot}}$ [ppt]
Base	<b>Ex-TP</b>	$7.25 \pm 0.16$ <sup>1a</sup>	$7.80$ <sup>2</sup>	$3.06 \pm 0.56$ <sup>1b</sup>	$1.44 \pm 0.53$ <sup>1b</sup>	$19.6 \pm 0.8$
Run 1	<b>Trop-UT</b>	$7.25 \pm 0.16$ <sup>1a</sup>	$7.80$ <sup>2</sup>	$3.12 \pm 0.47$ <sup>3</sup>	$2.63 \pm 1.04$ <sup>4</sup>	$20.8 \pm 1.2$
Run 2		$7.25 \pm 0.16$ <sup>1a</sup>	$7.80$ <sup>2</sup>	$5.00 \pm 0.54$ <sup>1c</sup>	$1.69 \pm 0.54$ <sup>1c</sup>	$21.7 \pm 0.8$

<sup>1a</sup> Current study all tropopause data:  $\Delta\Theta = -10$  K to the local WMO tropopause

<sup>1b</sup> Current study Ex-TP: equivalent latitude  $40$ – $60^\circ\text{N}$ ,  $\Delta\Theta = -10$  K to the WMO tropopause

<sup>1c</sup> Current study Trop-UT (i.e.,  $\Theta_{\text{high}}/\text{PV}_{\text{low}}$  air, refer to Sect. 5.2):  $\Theta > 355$  K and  $\text{PV} < 2$

<sup>2</sup> WMO (2018) and cited by Keber et al. (2020)

<sup>3</sup> Navarro et al. (2015) average from East and West Pacific

<sup>4</sup> Werner et al. (2017) and Koenig et al. (2017)

## Chapter 4

# Method and Retrieval

The mini-DOAS analysis is a multi-step process and is based on differential optical absorption spectroscopy to obtain differential slant column densities (dSCDs) in units of molecules  $\text{cm}^{-2}$  (Sect. 4.1). This quantity is calculated from the absorption observed due to the trace gas relative to the reference chosen. Next, the absorption in the reference spectrum is determined to compute total slant column densities (SCDs) in Sect. 4.1.2. A radiative transfer model is then used to simulate the optical state of the atmosphere, in particular to compute the light path length distribution and the amount of absorption in the line of sight of the telescope for the specific trace gas (Sect. 4.3). And lastly, the novel scaling method is used to determine the volume mixing ratios (VMRs) of the target trace gases along the flight route (Sect. 4.2).

### 4.1 DOAS

The detection of trace gases by remote sensing spectral analysis is based on the Differential Optical Absorption Spectroscopy (DOAS) method to solve a simplified version of the radiative transfer equation (RTE; refer to Sect. 2.5.1). The primary principle of the DOAS method describes the exponential decrease of light through an absorbing medium as shown in Fig. 4.1 and is defined by Lambert-Beer's law (Eq. (6.108) in Platt and Stutz (2008)):

$$I(\lambda) = I_0(\lambda) \cdot e^{(-\sigma(\lambda) \cdot \rho \cdot L)} \quad (4.1)$$

where  $I_0$  is the spectral radiance emitted by the light source at a given wavelength ( $\lambda$ ).  $I_0$  is often called the Fraunhofer reference spectrum due to the Fraunhofer lines in the sun's spectrum.  $I$  is the irradiance after the light passes through an absorbing medium with an absorption cross section  $\sigma$  measured over a light path length of  $L$  with a corresponding uniform or averaged mixing ratio  $\rho$  along the light path. The absorption cross section of a specific gas ( $\sigma_i$ ) can alternatively be defined by its absorption coefficient ( $\beta_i$ ) in terms of the earlier defined RTE (Sect. 2.5.1):  $\sigma_i = \beta_i / n$ , where  $n$  is the number density.

The irradiance after absorption can alternatively be expressed as:

$$I(\lambda) = I_0(\lambda) \cdot e^{-\tau}, \quad (4.2)$$

where  $\tau$  is the optical density of the medium,

$$\tau = -\ln(I/I_0) = \sigma(\lambda) \cdot \rho \cdot L. \quad (4.3)$$

Atmospheric measurements of trace gases in this study are always of optically thin environments

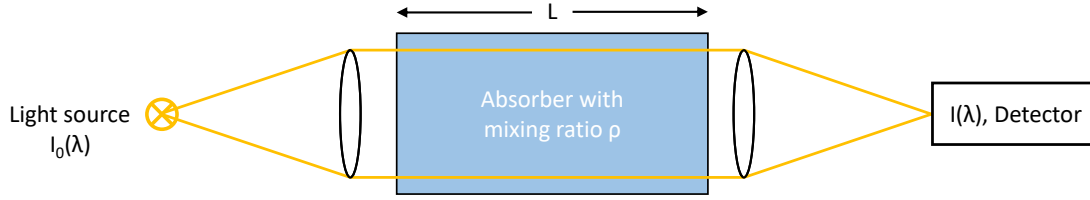


Figure 4.1: The radiance,  $I_0(\lambda)$ , from a light source is absorbed by a medium with mixing ratio  $\rho$  and absorption cross section  $\sigma$ . After a given distance  $L$ , the remaining irradiance received at the detector from all directions is  $I(\lambda)$ .

( $\tau < 10^{-1}$ ).

The mixing ratio of the trace gas along its path length represents the slant column density (SCD) and can be written as an integral, where the SCD is an average of the mixing ratios over the light path:

$$\text{SCD} = S_i(\lambda) = \int_0^{L(\lambda)} \rho_i(s) ds \quad (4.4)$$

where  $i$  represents the different trace gases and  $ds$  is the infinitesimal path length over which the mixing ratio is added. In the atmosphere where there are many trace gases present, the characteristic absorption lines of each trace gas allows for multiple trace gases to be measured simultaneously. The irradiance measured after absorption by multiple trace gases is given by:

$$I(\lambda, L) = I_0(\lambda) \cdot \exp\left(-\sum_{i=1}^m \sigma_i(\lambda) S_i(\lambda)\right) \quad (4.5)$$

for  $m$  absorbers. The DOAS method uses the distinction between narrowband (strong variations with wavelength, i.e., high frequency) and broadband (gradual variations with wavelength, i.e., low frequency) components to improve the evaluation of the mixing ratios of trace gases in the atmosphere. The absorption cross sections of each trace gas are separated into the two components:  $\sigma_i(\lambda) = \sigma'_i(\lambda) + \sigma_i^B(\lambda)$ , where  $\sigma'_i$  is the narrowband feature (determined in the laboratory) and  $\sigma_i^B$  is the broadband component.

In the atmosphere, light extinction not only occurs from trace gas absorption but also by scattering and turbulence. Scattering, such as by inelastic rotational Raman scattering, is impacted by factors including the solar zenith angle, the light path length, cloud cover and aerosol concentration and causes a smoothing of the wavelengths or a 'filling in' particularly in the strong Fraunhofer absorption bands. This convolution due to Raman scattering is known as the Ring effect (e.g., Grainger and Ring (1962); Vountas et al. (1998); Wagner et al. (2001)) and must be taken into account by compensating it with a Ring spectrum,  $R(\lambda)$ , which is calculated from the reference Fraunhofer spectrum. Extinction by Rayleigh scattering with air molecules,  $\beta_R$ , and Mie scattering with aerosols and cloud droplets,  $\beta_M$ , results in broadband extinction that is also included in atmospheric measurements. This leads to a modified Lambert-Beer law when observing the atmosphere:

$$I(\lambda, L) = I_0(\lambda) \cdot \exp\left(-R(\lambda) - \sum_{i=1}^m \sigma'_i(\lambda) \cdot S_i(\lambda)\right) \cdot \exp\left(-L \cdot \left(\sum_{i=1}^m (\sigma_i^B(\lambda) \cdot \rho_i) + \beta_R(\lambda) + \beta_M(\lambda)\right)\right) \quad (4.6)$$

where the terms in the first exponential are all the narrowband components and the terms in the second exponential are the broadband components. To model the irradiance, the individ-

ual absorption cross sections  $\sigma_i$ , given by Keller-Rudek et al. (2013) (refer to Sect. 4.1.1), are convoluted with the mini-DOAS instrument slit function  $H$  before entering Eq. (4.6). However during measurements, due to the given resolution of the spectrograph the observed irradiance,  $I^*(\lambda, L)$ , is given by a convolution of the true irradiance,  $I(\lambda, L)$ , with the instrument slit function,  $H$  (Platt and Stutz, 2008):

$$I^*(\lambda, L) = I(\lambda, L) * H = \int I(\lambda - \lambda', L) \cdot H(\lambda') d\lambda'. \quad (4.7)$$

The difference between the observed irradiance Eq. (4.7) and the model given by Eq. (4.6) (where we make the substitution  $\sigma_i \rightarrow \sigma_i * H$  within the exponential) leads to a discrepancy known as the solar  $I_0$  correction (Platt et al., 1997; Wagner et al., 2001; Lampel et al., 2015).

Furthermore, the irradiance of the light source multiplied by the broadband components can be redefined as a new irradiance,  $I'_0$ , such that the Lambert-Beer law can be reapplied to solely the narrowband components:

$$I(\lambda, L) = I'_0(\lambda) \cdot \exp\left(-R(\lambda) - \sum_{i=1}^m \sigma'_i(\lambda) \cdot S_i(\lambda)\right). \quad (4.8)$$

The differential optical density is now defined as:

$$\tau'(\lambda) = \ln\left(\frac{I'_0}{I}\right) = R(\lambda) + \sum_i \sigma'_i(\lambda) \cdot S_i. \quad (4.9)$$

A software package called DOASIS (DOAS Intelligent System) written by Kraus (2006) at the University of Heidelberg, is used to calculate the Ring effect from the Fraunhofer reference as well as model the  $S_i$ . DOASIS applies the Levenberg-Marquardt algorithm (Levenberg, 1944; Marquardt, 1963) with an iterative approach to minimize the residuals between the measured spectrum and the model. The least squares fit in DOASIS is applied as the following:

$$\chi^2 = \left[ \ln\left(\frac{I'_0}{I}\right) - R - \sum_i \sigma'_i \cdot S_i \right]^2 \quad (4.10)$$

to infer the SCD of each trace gas. In this study, the Fraunhofer reference (or background) spectrum is an in-flight reference which already contains some absorption and therefore the SCD calculated above is actually a differential slant column densities (dSCD). The methods to determine the absorption in this in-flight spectrum are discussed below in Sect. 4.1.2.

#### 4.1.1 Absorption Cross Sections and DOAS Fit Scenarios

Each gas has a unique absorption cross section, frequently with distinctive peaks at different wavelengths at which the gas absorbs more or less light. The three main trace gases analysed in this study are  $O_3$ ,  $NO_2$ , and  $BrO$ . For the DOAS analysis when choosing the absorption cross section the temperature dependency of the cross sections must be considered in addition to the solar  $I_0$  correction and Ring effect discussed earlier.

The absorption cross sections are temperature dependent, for some gases more than others. Therefore, the cross sections measured in the lab should occur at appropriate temperatures which should approximately correspond to the path length distribution weighted temperature in the region of the measurements. Due to the high sensitivity of the  $O_3$  absorption cross section to temperature, two orthogonalized cross sections measured at different temperatures are used in the DOAS analysis.

The absorption cross sections used in this study are retrieved from the “MPI-Mainz UV/VIS Spectral Atlas of Gaseous Molecules of Atmospheric Interest” data base (Keller-Rudek et al., 2013). These lab determined absorption cross sections often have a higher resolution and as such the mini-DOAS instrument slit function of a mercury emission line from the wavelength calibration is used to convolute the absorption cross sections. An example of this slit function is shown in Fig. 4.2 with a full width half maximum (FWHM) of  $0.44 \pm 0.01$  nm. The absorption cross sections for all trace gasses included in the fit scenarios are shown in Fig. 4.3. The fit scenarios used for the DOAS analysis for BrO, NO<sub>2</sub>, and O<sub>3</sub> are outlined in Tables 4.1–4.2 and are discussed below.

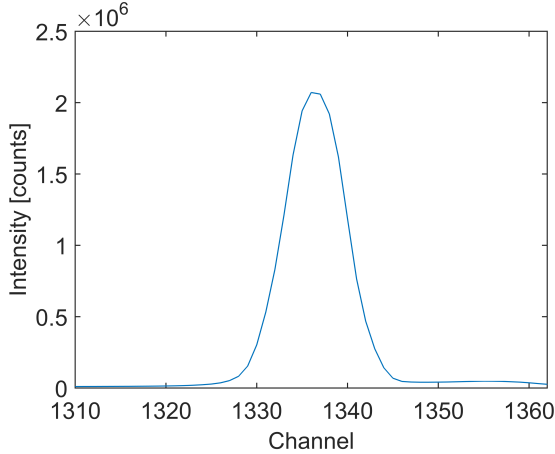


Figure 4.2: An example of the mini-DOAS instrument slit function corresponding to the mercury (Hg) emission peak at 404.66 nm from the limb UV spectrometer recorded on September 11, 2017. The channels displayed correspond to the wavelength range from 403.18–406.19 nm.

When comparing the measured irradiance with the modelled irradiance where the high resolution absorption cross sections are convolved inside the exponential in Eq. (4.6), an additional correction factor known as the solar  $I_0$  effect needs to be considered (Platt et al., 1997; Wagner et al., 2001; Lampel et al., 2015). However, only stronger absorbers need an  $I_0$  correction, which include O<sub>3</sub> and NO<sub>2</sub>. The solar  $I_0$  correction for the O<sub>3</sub> cross section ( $\sim 1.0 \times 10^{20}$  molecules cm<sup>-2</sup>) and the NO<sub>2</sub> cross section ( $\sim 1.0 \times 10^{17}$  molecules cm<sup>-2</sup>) was used as suggested by Aliwell et al. (2002).

Table 4.1: Details of the spectral retrieval absorption cross sections used for the DOAS method analysis (Hüneke et al., 2017; Stutz et al., 2017).

#	Absorber	Temp.	Solar- $I_0$	Reference	Uncert.
1	O <sub>4</sub>	293 K		Thalman and Volkamer (2013)	3-4%
2	O <sub>4</sub>	273 K		Thalman and Volkamer (2013)	3-4%
3	O <sub>3</sub>	203 K	$1.00 \cdot 10^{20}$	Serdyuchenko et al. (2014)	2-3%
4	O <sub>3</sub>	223 K	$1.00 \cdot 10^{20}$	Serdyuchenko et al. (2014)	2-3%
5	O <sub>3</sub>	293 K	$1.00 \cdot 10^{20}$	Serdyuchenko et al. (2014)	2-3%
6	NO <sub>2</sub>	223 K	$1.00 \cdot 10^{17}$	Bogumil et al. (2003)	3.4%
7	BrO	223 K		Fleischmann et al. (2004)	8-10%
8	H <sub>2</sub> O	273 K		Rothman et al. (2009)	8%

### Target Gas BrO: The Spectral Fit Scenario

Bromine monoxide (BrO) absorption bands lie in the UV wavelength range. The absorption cross section used, was recorded by Fleischmann et al. (2004) in the laboratory at 223 K (Fig. 4.3).

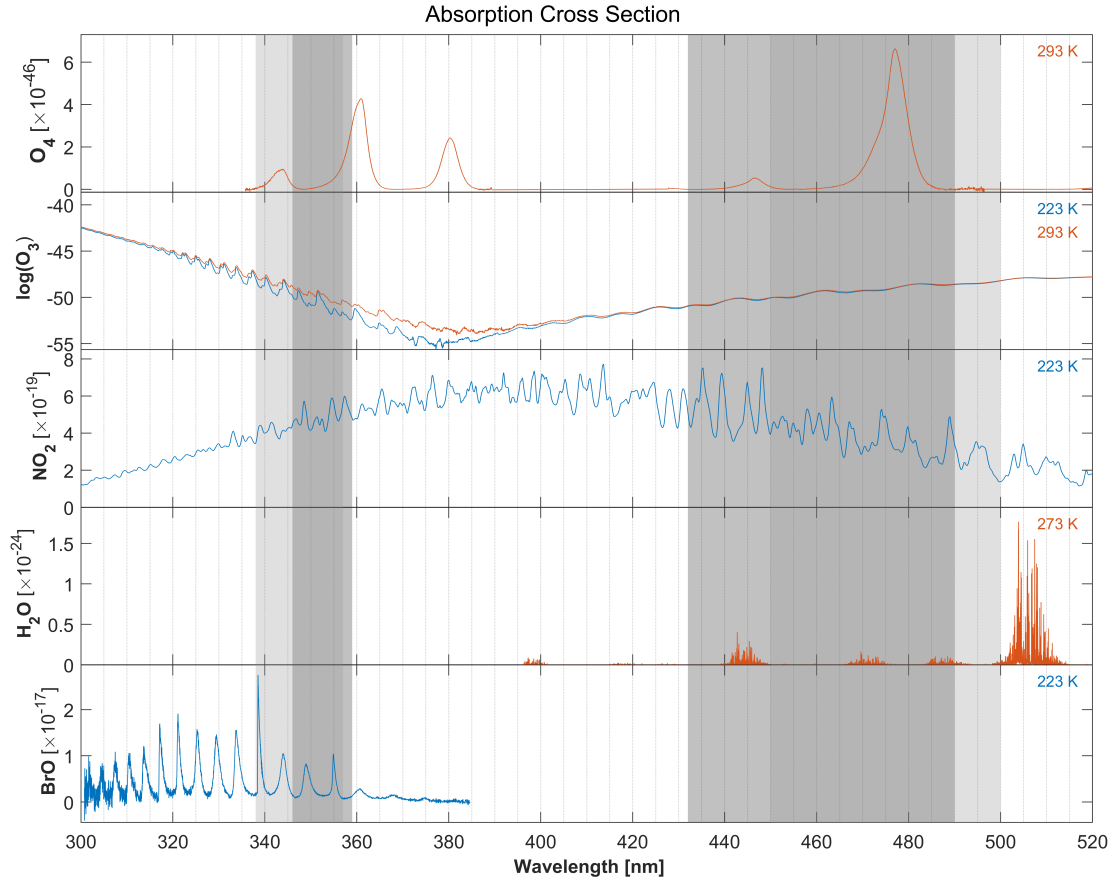


Figure 4.3: The absorption cross sections for  $O_4$  (293 K),  $O_3$  (223 K and 293 K),  $NO_2$  (223 K),  $H_2O$  (273 K), and  $BrO$  (223 K) are shown. The  $O_3$  absorption cross section is shown as a logarithm. The units of the cross sections are  $cm^2$  molecule $^{-1}$ , except for  $O_4$  which have units of  $cm^5$  molecule $^{-2}$ . The medium and dark gray shadings correspond to the target gas fit windows ( $BrO$  in the UV and  $NO_2$  in the visible channel). The light and dark gray shadings correspond to the scaling gas ( $O_3$ ) fit windows in the UV and visible wavelength. The dark gray shadings indicates the overlapping wavelength ranges between the scaling and target gas. For details refer to Tables 4.1–4.2.

Table 4.2: DOAS spectral analysis details for the various trace gases and their spectral fitting intervals. Refer to Table 4.1 for the corresponding fitted absorbers. The  $\sigma$  [dSCD] are typical errors in molecules  $cm^{-2}$ .

Gas	Spectral interval [nm]	Fitted absorbers	Additional Parameters	$\sigma$ [dSCD]
$O_3$ –UV	338–357 <sup>(a)</sup>	1, 4, 5, 6, 7	<sup>(i)</sup> $I_{Ofs}$ , <sup>(ii)</sup> $R$ , <sup>(iii)</sup> $R \cdot \lambda^4$	$2.5 \times 10^{17}$
$BrO$	346–359 <sup>(b)</sup>	1, 4, 5, 6, 7	$I_{Ofs}$ , $R$ , $R \cdot \lambda^4$	$2.4 \times 10^{13}$
$O_3$ –vis	450–500 <sup>(c)</sup>	2, 3, 4, 6, 8	$I_{Ofs}$ , $R$ , $R \cdot \lambda^4$	$3.2 \times 10^{17}$
$NO_2$	432–490 <sup>(c)</sup>	2, 3, 4, 6, 8	$I_{Ofs}$ , $R$ , $R \cdot \lambda^4$	$2.8 \times 10^{14}$

<sup>(a)</sup> Pukite and Wagner (2016)

<sup>(b)</sup> Aliwell et al. (2002)

<sup>(c)</sup> Hüneke et al. (2017)

<sup>(i)</sup> Offset spectrum

<sup>(ii)</sup> Ring spectrum

<sup>(iii)</sup>  $R$  multiplied by the wavelength

An extensive inter-comparison study done by Aliwell et al. (2002) comparing the DOAS analysis of  $BrO$  with six independent instruments, recommend a 2 band fit scenario from 346–359 nm. This is a 2 band fit of the vibrational transitions 4,0 and 5,0 of the  $A^2\Pi_{3/2} \leftarrow X^2\Pi_{3/2}$  electronic

transition (Wilmouth et al., 1999). Aliwell et al. (2002) showed that the lower side of the interval range has a much higher sensitivity to changes than the upper side of the interval range resulting in less consistent BrO differential slant column densities (dSCD). Due to this previous extensive study, the wavelength range of 346–359 nm is chosen for the retrieval of BrO dSCDs and is highlighted in Fig. 4.3 by the medium and dark gray shading on the left.

Other trace gas species included in the DOAS analysis of BrO include O<sub>4</sub> (294 K), a cold (223 K) and warm (293 K) O<sub>3</sub> orthogonalized to the colder O<sub>3</sub>, and NO<sub>2</sub> (223 K) provided in Tables 4.1 and 4.2. The WISE campaign measurements were primarily in the UTLS of the NH in mid-latitudes where ambient temperatures ranged from 206–293 K, with the majority of the flight levels around 210–235 K. As such the absorption cross sections used, largely correspond to the colder temperatures. The Huggins band of O<sub>3</sub> has a stronger temperature dependency, therefore a second warmer absorption cross section is included.

These cross sections are used in DOASIS to calculate the dSCD for BrO. Due to the low mixing ratios of BrO, a running mean of five spectra is used for the dSCD analysis to improve the signal to noise. An example of the fit details for BrO with relatively large signal to noise (S/N > 12) is shown in Fig. 4.4. The blue curves are the components of the measured spectrum and the red lines are the DOASIS simulated results. The root mean square (RMS) is the residual and should only be made up of random noise if all trace gas species have been identified appropriately by the model. DOASIS calculated a spectrum of  $\text{dSCD}_{\text{BrO}} = (2.1 \pm 0.2) \times 10^{14}$  molecules cm<sup>-2</sup> relative to the specific in-flight reference spectrum chosen.

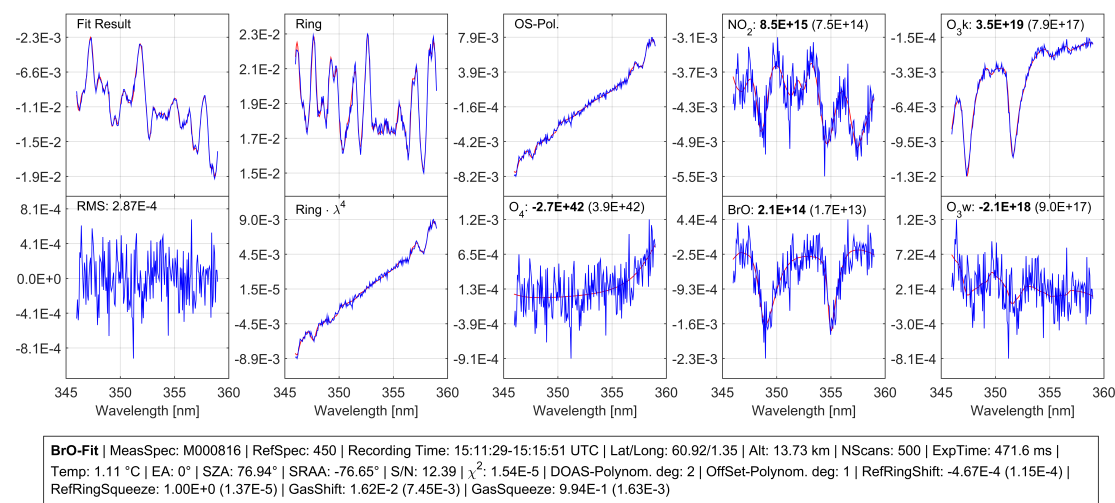


Figure 4.4: An example of a BrO spectral fit scenario from research flight RF09 on Oct. 4, 2017 in the UV wavelength range 346–359 nm. This dSCD has a relatively high signal to noise (S/N>12) for BrO. The optical density (OD) of the observed measurement is shown in blue signal and the modelled least squares fit OD from DOASIS is shown as the red line. The fit result shows the entire measured and modelled spectrum. The RMS is the root mean square indicating the residual after subtracting all components. The Ring spectrum, Ring·λ<sup>4</sup>, and the offset polynomial (OS-Pol.) are displayed, followed by the OD of the absorption of the various trace gases. The gases include O<sub>4</sub>, NO<sub>2</sub>, BrO, O<sub>3</sub>k (cold ozone), and O<sub>3</sub>w (warm ozone). The OD are relative to an in-flight reference spectrum, which during this flight was spectrum 450.

### Target Gas NO<sub>2</sub>: The Spectral Fit Scenario

The nitrogen dioxide (NO<sub>2</sub>) absorption bands have distinct features in the visible wavelength range as shown in Fig. 4.3 for the cross section measured at 223 K by Bogumil et al. (2003). The fit window of 432–490 nm was chosen similar to Hüneke et al. (2017) but with an adjusted lower

limit due to the change and update in wavelength range of the spectrometer to avoid instabilities in the fitting procedure. The fit range used is highlighted in Fig. 4.3 by the medium and dark gray shading on the right hand side. The following other trace gas species are included in the NO<sub>2</sub> fit scenario: O<sub>4</sub>, two O<sub>3</sub>, and H<sub>2</sub>O (for details refer to Tables 4.1 and 4.2). Each spectrum is evaluated individually for NO<sub>2</sub> as the mixing ratios as well as the signal to noise are larger than for the BrO retrieval and therefore no running mean spectra are necessary. An example of the fit details for NO<sub>2</sub> is shown in Fig. 4.5. The dSCD<sub>NO<sub>2</sub></sub> of this spectrum calculated by DOASIS is  $(3.2 \pm 0.03) \times 10^{16}$  molecules cm<sup>-2</sup> relative to the chosen in-flight reference spectrum.

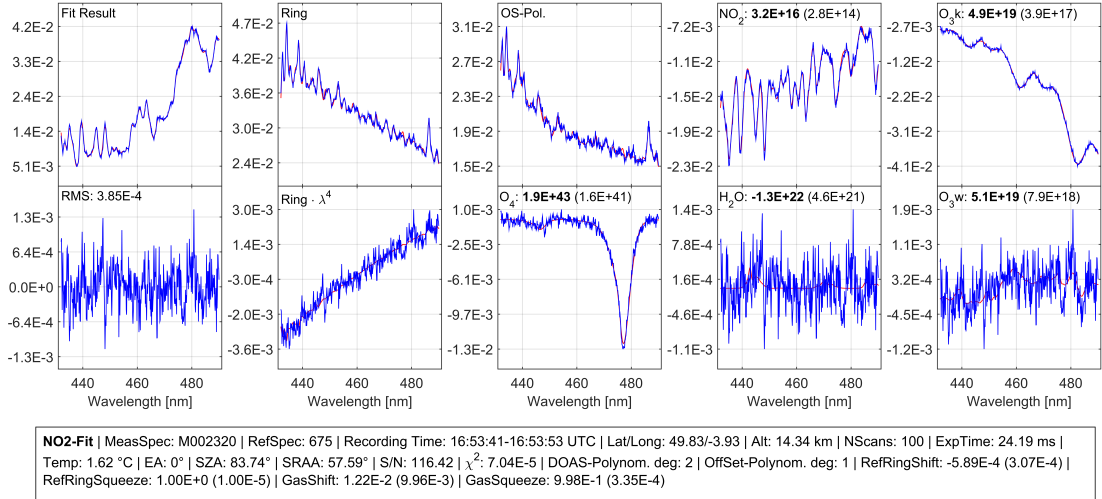


Figure 4.5: Research flight RF09: Oct. 4, 2017 example of the NO<sub>2</sub> spectral fit scenario in the visible wavelength range 432–490 nm for a high signal to noise ( $S/N > 100$ ). The panels are as given in Fig. 4.4 with the exception of the panel for optical density of BrO, which is replaced by H<sub>2</sub>O.

### Scaling Gas O<sub>3</sub>: The Spectral Fit Scenario

Ozone (O<sub>3</sub>) absorption occurs in both the UV (Huggins band) and visible (Chappius band) wavelength ranges as shown in Fig. 4.3. It has a strong temperature dependence, therefore absorption cross sections at two different temperatures measured by Serdyuchenko et al. (2014) are used, 223 K and 293 K. The two temperatures of the absorption cross sections represent the varying ambient temperatures during the WISE campaign.

For O<sub>3</sub>–UV dSCDs, used as the corresponding scaling gas for BrO analysis, a fit window of 338–357 nm is applied (Puķīte and Wagner (2016)). In Sect. 4.1.3 below, a test comparison for several wavelength ranges is discussed. O<sub>3</sub>–vis dSCDs, the scaling gas for the NO<sub>2</sub> analysis, are evaluated between 450–500 nm (Hüneke et al. (2017)). These fit windows are indicated in Fig. 4.3 by the light and dark gray shading. Due to the light path length dependency on the wavelength, it is important for the scaling and target gas to have similar and ideally overlapping fit scenario wavelength ranges for the equivalence theorem to apply which is discussed below (Irvine, 1964; Partain et al., 2000; Knecht, 2015). The O<sub>3</sub> fit windows are therefore chosen to have overlapping wavelength ranges with each of the target gases. For details refer to Tables 4.1 and 4.2. An example of the fit details for the dSCD simulation for O<sub>3</sub>–UV/vis is shown in Figs. 4.6 and 4.7, respectively. The dSCD<sub>O<sub>3</sub></sub> of each of these spectra are calculated by DOASIS resulting in  $(3.5 \pm 0.02) \times 10^{19}$  molecules cm<sup>-2</sup> and  $(5.0 \pm 0.03) \times 10^{19}$  for the UV and vis wavelength ranges, respectively, relative to each of their in-flight reference spectrum.

Alternatively, the oxygen collisional complex O<sub>4</sub> can be used as a scaling gas. This is appro-

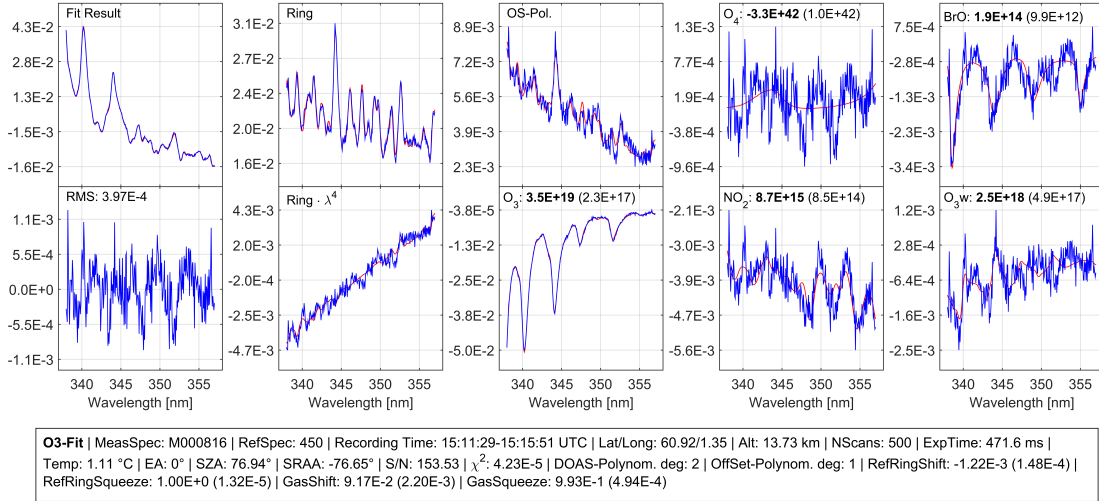


Figure 4.6: Research flight RF09: Oct. 4, 2017 example  $O_3$ -UV spectral fit scenario in the visible wavelength range 338–357 nm for a high signal to noise ( $S/N > 100$ ). The panels are as given in Fig. 4.4.

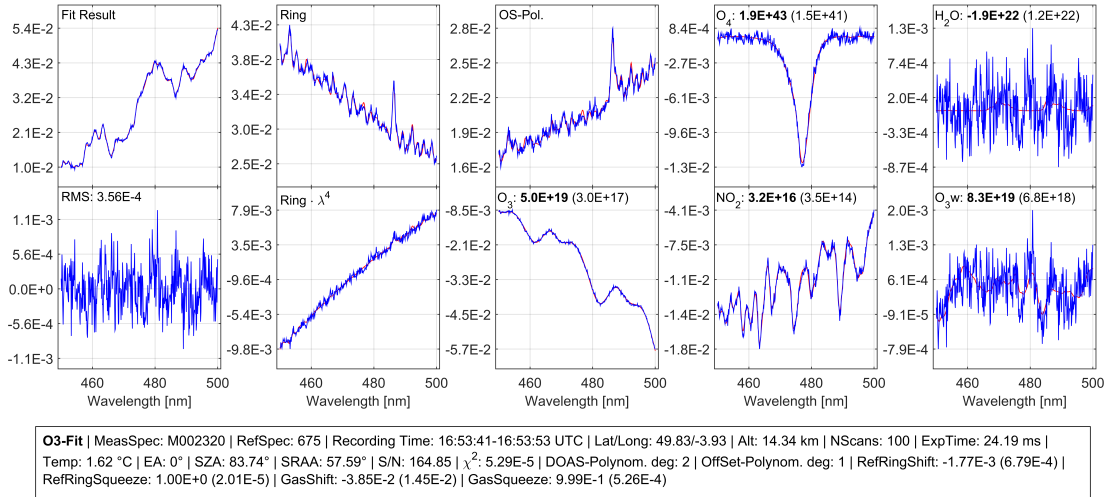


Figure 4.7: Research flight RF09: Oct. 4, 2017 example  $O_3$ -vis detailed fit scenario in the visible wavelength range 450–500 nm for a high signal to noise ( $S/N > 100$ ). The panels are as given in Fig. 4.4 with the exception of optical density of BrO panel which is replaced by  $H_2O$ .

appropriate for tropospheric gases, particularly those with exponential increases towards the surface. The  $O_4$  scaling gas is also useful for low altitude flight legs, i.e., when observing gases in the troposphere. Examples as well as comparisons between the  $O_3$  and  $O_4$  scaling gases can be found in Schreiner (2018) and Kluge (2018).

### In-Flight Reference Spectrum

The dSCDs in this study for the target gases of BrO and  $NO_2$  and the scaling gas  $O_3$  are evaluated with respect to an in-flight Fraunhofer reference spectrum. This Fraunhofer reference spectrum is typically chosen at high altitude, low solar zenith angles (SZA), and clear sky conditions indicated by a low colour index (ratio of the radiances at 420/340 nm). It is assumed that this type of Fraunhofer reference spectrum has the simplest ambient conditions to simulate the light path lengths and weighting factor for the scaling method (described below) compared to the rest of the flight.

Outliers of select individual dSCD data points that deviate by more than  $5 \times 10^{13}$ ,  $10^{15}$  or  $2 \times 10^{18}$  molecules  $\text{cm}^{-2}$  ( $\sim 10\text{--}25\%$  jump) from the 9 point running mean for BrO,  $\text{NO}_2$ , or  $\text{O}_3$ , respectively, are averaged to remove unreliable spectra. Typical errors of the dSCDs for each gas absorption can be found in the last column of Table 4.2.

#### 4.1.2 Total Slant Column Densities

If the Fraunhofer reference spectrum chosen already has absorbed light due to the sun's photosphere and the atmosphere, then the residual absorption present in the reference spectrum must be quantified. In this scenario the  $S_i$  in Eq. (4.10) found by the DOASIS analysis represents the  $\text{dSCD}_i$ . As previously mentioned this is the case for the mini-DOAS spectra because an in-flight Fraunhofer reference spectrum is chosen. Therefore, the absorption of this spectrum ( $\text{SCD}_{\text{ref}}$ ) needs to be determined to calculate the total SCD (refer to equation (1) in Hüneke et al. (2017)),

$$\text{SCD}_i = \text{dSCD}_i + \text{SCD}_{\text{ref}}. \quad (4.11)$$

There are several methods to determine the  $\text{SCD}_{\text{ref}}$ , which may differ for the various gases.

##### Kurucz Method

One option is to evaluate the spectra using an external high resolution absorption-free solar spectrum from Chance and Kurucz (2010) as the Fraunhofer reference to compute total SCDs (further on called  $\text{SCD}^{\text{Kurucz}}$ ). The  $\text{SCD}^{\text{Kurucz}}$  absorption calculated for the spectrum used as the in-flight reference for the dSCD computation represents the  $\text{SCD}_{\text{ref}}^{\text{Kurucz}}$  for the corresponding gas. In Fig. 4.8, an example comparison of  $\text{O}_3$  dSCDs (black points) using an in-flight spectrum is compared with the  $\text{SCD}^{\text{Kurucz}}$  (red points) evaluation using the external absorption-free spectrum. Adding the  $\text{SCD}_{\text{ref}}^{\text{Kurucz}}$  to the  $\text{dSCD}^{\text{in-flight ref}}$  to produce  $\text{O}_3$   $\text{SCD}^{\text{in-flight ref}}$  (black line) generally agrees very well with the  $\text{SCD}^{\text{Kurucz}}$ , indicating the robustness of the evaluation and supporting the use of this method. This combines the smaller uncertainty of the dSCD results with the Kurucz method reference, therefore  $\text{SCD}^{\text{in-flight ref}}$  rather than  $\text{SCD}^{\text{Kurucz}}$  are used for further analysis.

In this study, this method was only used for the evaluation of  $\text{O}_3\text{--UV}$   $\text{SCD}_{\text{ref}}$  as it produced consistently stable  $\text{SCD}^{\text{Kurucz}}$ . The  $\text{SCD}_{\text{ref}}^{\text{Kurucz}}$  for  $\text{O}_3\text{--UV}$  ranged between  $(1.6 - 3.2) \times 10^{19}$  molecules  $\text{cm}^{-2}$  varying between flights due to the different atmospheric conditions of each chosen reference spectrum. These  $\text{SCD}_{\text{ref}}^{\text{Kurucz}}$ s typically only differed by  $0.1 \times 10^{19}$  molecules  $\text{cm}^{-2}$  from the simulated  $\text{SCD}_{\text{ref}}^{\text{simulated}}$  (mentioned below) indicating the consistency of these methods for  $\text{O}_3\text{--UV}$ . Unfortunately, this method does not always produce stable results in the desired wavelength range or gas. Additionally, if there are large errors or negative SCDs this method is not used.

$\text{O}_3$  and BrO have similar daytime vertical profiles in the atmosphere with peaks in the stratosphere, therefore the assumption is made that their total SCDs are proportional to one another by some factor along the flight paths for  $\text{SZA} < \sim 89^\circ$  (which is generally observed)

$$\text{SCD}_{\text{BrO}} = a \cdot \text{SCD}_{\text{O}_3}^{\text{Kurucz}} \quad (4.12)$$

where  $a$  is some constant over the course of the flight. Using the quasi linear relationship observed between the absorption-free spectra SCDs of  $\text{O}_3$  (i.e.,  $\text{SCD}^{\text{Kurucz}}$  (Chance and Kurucz, 2010)) and the BrO dSCDs, the BrO- $\text{SCD}_{\text{ref}}$  can be determined. The quasi linear relationship can be described as

$$\text{dSCD}_{\text{BrO}} = m \cdot \text{SCD}_{\text{O}_3}^{\text{Kurucz}} + b \quad (4.13)$$



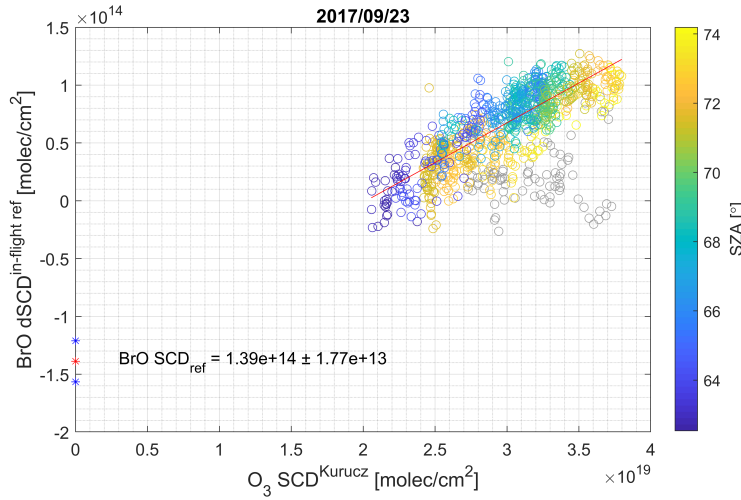


Figure 4.9: Research flight RF05 (Sept. 23, 2017) quasi linear relationship between BrO dSCD<sup>in-flight ref</sup> and O<sub>3</sub> SCD<sup>Kurucz</sup> allows for the inference of BrO SCD<sub>ref</sub> when extrapolating the O<sub>3</sub> SCD to zero. Data points are colour coded by the SZA, and any data points where SZA > 89° as well as from the initial ascent and final descent of the flight are shaded in gray and excluded from the linear relationship calculation.

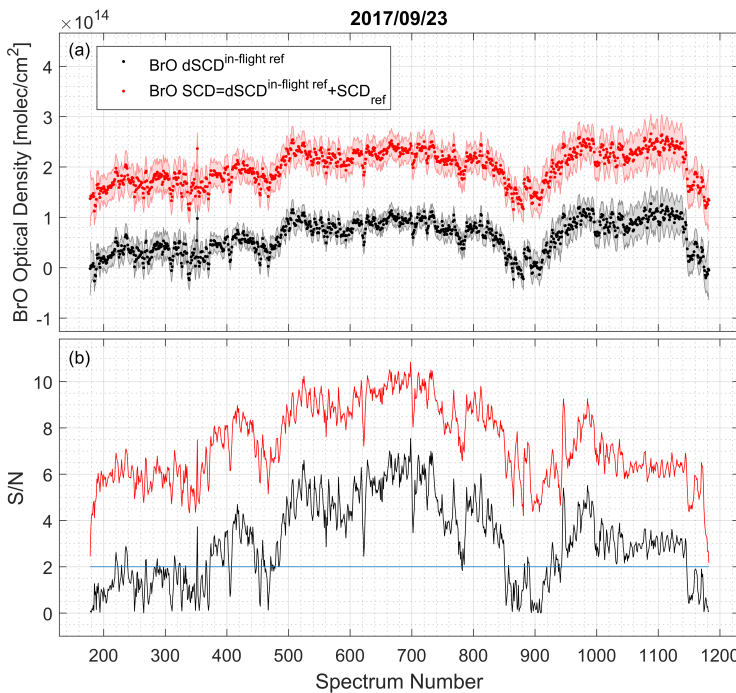


Figure 4.10: BrO column densities from research flight RF05 (Sept. 23, 2017) are shown as an example. (a) BrO dSCD using the spectrum number 871 as the in-flight reference spectrum (black) to which the SCD<sub>ref</sub> (calculated in Fig. 4.9) is added to infer the BrO SCD (red). Panel (b) shows the signal to noise (S/N) of both the dSCDs and SCDs (black and red, respectively). The total SCDs typically have a larger S/N as they are usually strictly positive column densities. The dSCDs fluctuate about 0 as the column densities are relative to the in-flight reference.

### Simulated SCD<sub>ref</sub>

In the visible wavelength analysis of NO<sub>2</sub> and O<sub>3</sub>, the SCD<sub>ref</sub>'s are both simulated using the Monte Carlo atmospheric radiative transfer inversion model (McArtim) described in Sect. 4.3 below (Deutschmann et al., 2011). McArtim simulates the SCDs along the flight track (described below in Sect. 4.2 and 4.3), from which the SCD<sub>ref</sub> is extracted at the flight altitude and corresponding to the time stamp of the in-flight reference used for the dSCD analysis. This method is chosen because the inferred O<sub>3</sub>-vis SCDs from the external absorption free spectrum from Chance and Kurucz (2010) were frequently unreliable. As such, for consistency, all NO<sub>2</sub> and O<sub>3</sub>-vis SCD<sub>ref</sub>s are simulated using the RT McArtim model.

### Alternative Options

Another alternative method if available, is a roof top zenith sky measurement on a clear day where the changing SCDs are solely due to the light path length for trace gases with relatively constant and stable mixing ratios during the course of a day, e.g., O<sub>3</sub>. Due to the stable mixing

ratios the SCD relative to a second geometric viewing direction known as the vertical column density (VCD) can be used, which is defined as the air mass factor (AMF; see Perliski and Solomon (1993); Marquard et al. (2000); Wagner et al. (2007)):

$$\text{AMF} = \frac{\text{SCD}}{\text{VCD}}. \quad (4.16)$$

The AMF can be directly calculated by the McArtim model. Alternatively, at low solar zenith angles ( $\text{SZA} < \sim 75^\circ$ ) the SCD to VCD ratio can be approximated resulting in  $\text{AMF} \approx 1/\cos(\text{SZA})$  (Wagner et al., 2007). A comparison of the dSCDs and the AMFs can be used to create a Langley plot resulting in a linear trend given by  $\text{dSCD} = \text{VCD} \cdot \text{AMF} - \text{SCD}_{\text{ref}}$  where the  $\text{SCD}_{\text{ref}}$  is the negative y-intercept (similar to the Kurucz related plots).

Depending on the target trace gas, different methods are appropriate. For a gas such as OClO with a short photolytic lifetime, a dSCD with respect to an in flight spectrum at low SZA can be used and assumed that the  $\text{SCD}_{\text{ref}} = 0$ . Or tropospheric gases such as formaldehyde with very small mixing ratios present in the stratosphere, can also be assumed to have near zero absorption ( $\text{SCD}_{\text{ref}} = 0$ ) if the dSCD is computed relative to a spectrum taken in the stratosphere.

### 4.1.3 Sensitivity Test: O<sub>3</sub>-UV Fit Window

An O<sub>3</sub>-UV fit scenario of 338–357 nm as suggested by Puķīte and Wagner (2016) is ultimately used for this study. However, various fitting windows shown in Table 4.3 were compared for consistency and accuracy of the SCD results. Seven different wavelength ranges, overlapping with the BrO fit window wavelength range, were tested when evaluating the dSCDs. The comparison of the total SCD results for each flight for the different fit windows also included the comparison of either a Kurucz slant column density reference ( $\text{SCD}_{\text{ref}}^{\text{Kurucz}}$ ) or a simulated reference ( $\text{SCD}_{\text{ref}}^{\text{sim}}$ ). Figure 4.11 shows example results for research flight RF05 on Sept. 23, 2017. Panel (a) shows the dSCD results of each fit window, while in panel (b) the total SCDs using either the  $\text{SCD}_{\text{ref}}^{\text{Kurucz}}$  (solid lines) or the  $\text{SCD}_{\text{ref}}^{\text{sim}}$  (dashed lines) are shown. The total SCD of each fit scenario computed with the  $\text{SCD}_{\text{ref}}^{\text{sim}}$  generally converged within  $0.2 \times 10^{19}$  molecules  $\text{cm}^{-2}$ , which also largely overlapped best with the SCD computed using the Puķīte and Wagner (2016) fit window (shown in red) and the  $\text{SCD}_{\text{ref}}^{\text{Kurucz}}$ .

Table 4.3: Different O<sub>3</sub> wavelength fit windows were tested and the total SCDs were compared. The results of the respective fit scenario names are shown in Fig. 4.11 for an example flight as well as in Appendix A for the rest of the flights.

Fit Scenario Name	Wavelength [nm]	Source
O3.346.3547_Stutz	346–354.7	Stutz et al. (2017)
O3.338.357_Pukite	338–357	Puķīte and Wagner (2016)
O3.338.360	338–360	Vogel Sihler test
O3_VogelSihler	330–360	Vogel Sihler test
O3.335.362_Hüneke_wHCHO	335–362	Hüneke (2016)
O3.335.362_Hüneke	335–362	Hüneke (2016)
O3.3381.3599	338.1–359.9	Vogel Sihler test

The O<sub>3</sub>-UV fit window suggested by Puķīte and Wagner (2016) shown in red (and frequently the similar fit window from 338.1–359.9 nm (black curve)) was the only fit window that had consistent agreement between the SCD results calculated with the  $\text{SCD}_{\text{ref}}^{\text{Kurucz}}$  and the  $\text{SCD}_{\text{ref}}^{\text{sim}}$ . They generally agreed closely with the majority of fit windows using a simulated reference. The

Comparing O<sub>3</sub> Fit Scenarios of Flight 2017/09/23

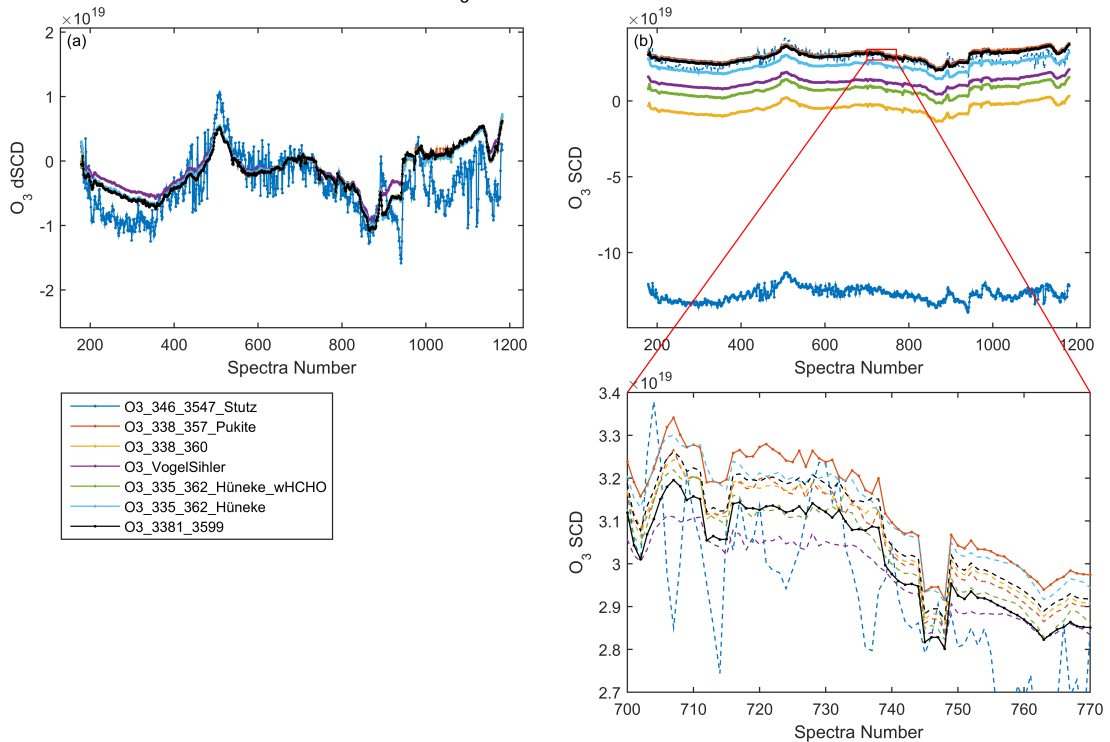


Figure 4.11: A comparison of SCD results for different O<sub>3</sub> wavelength fit scenario windows described in Table 4.3 for research flight RF05 on Sept. 23, 2017. The O<sub>3</sub> dSCD results for the various fit scenarios are shown in (a). In panel (b), the SCDs computed using either SCD<sub>ref</sub><sup>Kurucz</sup> (solid lines) or SCD<sub>ref</sub><sup>sim</sup> (dashed lines) are shown. At the bottom right panel there is a zoomed in section of (b).

dSCDs using the fit scenario suggested by Stutz et al. (2017) (shown in dark blue in Fig. 4.11 (a)), mainly result in unstable dSCDs as well as significantly different SCD<sub>ref</sub><sup>Kurucz</sup> compared to the other fit windows. As such the total SCDs differ most significantly than all other fit windows tested and can thus be disregarded. Fit windows as suggested by Hüneke (2016) (light blue and light green data) always have an offset, frequently by a factor of 2 smaller and on occasion have unstable Kurucz SCDs as compared to results from Puķite and Wagner (2016). The fitting windows 338–360 nm (yellow curve) as well as the largest fit window used for Vogel Sihler plots of 330–360 nm (purple curve) often had a consistent offset between the SCDs using a SCD<sub>ref</sub><sup>Kurucz</sup> compared to the SCD<sub>ref</sub><sup>sim</sup>. Therefore, all further analysis is completed using the fit window of 338–357 nm (Puķite and Wagner (2016)). These wavelength comparison results for all flights can be found in Appendix A.

## 4.2 Scaling method

The second part of the mini-DOAS analysis relies on the novel scaling method (Hüneke et al., 2017; Stutz et al., 2017). This technique is used to retrieve mixing ratios of a target gas from SCDs. The main advantage of the scaling method is that spectra can be evaluated for all sky conditions where as previous inversion methods largely had to exclude cloudy measurements due to the inherently complex scattering scenarios of aerosols and clouds. The scaling method largely cancels out any RT differences of the atmospheric conditions by considering the ratio of light path length probability density distributions between the target gas and scaling gas, as given by the

equivalence theorem (Irvine, 1964; Partain et al., 2000). Rayleigh and Mie scattering processes are wavelength dependent, therefore to successfully allow for these atmospheric process to be accounted for, the wavelength ranges of the target and scaling gas should be similar. Additionally, the atmospheric distributions of both gases should also be similar.

The SCD computed from the DOAS method can alternatively be defined as

$$\text{SCD}_X = \sum_i [X]_i \cdot B_{X_i} \cdot z_i \quad (4.17)$$

where  $\text{SCD}_X$  is the total slant column density retrieved for a given target gas,  $[X]_i$  is the a priori mixing ratio of the target gas in a height layer  $i$ ,  $B_{X_i}$  is the Box–AMF in layer  $i$  and  $z_i$  is the height of layer  $i$ . The Box–AMF is “a measure of the sensitivity of a particular viewing direction towards an absorber being present in a specific vertical ‘box’ (or layer)” (Platt and Stutz, 2008). The Box–AMF is used as a weighting factor representing how sensitive the instrument is to a measurement for a given elevation. The above equation can be rewritten to express the mixing ratio of the target gas in the layer  $j$ , which is at flight altitude for the limb telescope observations of the mini-DOAS instrument:

$$[X]_j = \frac{\text{SCD}_X - \sum_{i \neq j} [X]_i \cdot B_{X_i} \cdot z_i}{B_{X_j} \cdot z_j}. \quad (4.18)$$

This can similarly be expressed for the scaling gas  $P$ :

$$[P]_j = \frac{\text{SCD}_P - \sum_{i \neq j} [P]_i \cdot B_{P_i} \cdot z_i}{B_{P_j} \cdot z_j}. \quad (4.19)$$

By considering the ratio of the target gas to the scaling gas mixing ratios, i.e., dividing Eq. (4.18) by Eq. (4.19) their relative mixing ratios are

$$\frac{[X]_j}{[P]_j} = \frac{\text{SCD}_X - \sum_{i \neq j} [X]_i \cdot B_{X_i} \cdot z_i}{\text{SCD}_P - \sum_{i \neq j} [P]_i \cdot B_{P_i} \cdot z_i} \cdot \frac{B_{P_j}}{B_{X_j}}. \quad (4.20)$$

The Box–AMFs of the scaling and target gas within the same (or similar) wavelength range can be considered equal (within the uncertainty) when the optical density of both the scaling and target gas is  $\ll 1$  (for weak absorbers as is the case in this study), therefore  $B_{X_j} \approx B_{P_j}$  and the final term is approximately unity.

Additionally a weighting factor, the so-called  $\alpha$  factors can be defined as the ratio of the absorption observed in the line of sight (layer  $j$ ) relative to the total absorption of all layers for the target gas

$$\alpha_{X_j} = \frac{[X]_j \cdot B_{X_j} \cdot z_j}{\sum_i [X]_i \cdot B_{X_i} \cdot z_i} = \frac{\text{SCD}_X - \sum_{i \neq j} [X]_i \cdot B_{X_i} \cdot z_i}{\text{SCD}_X} \quad (4.21)$$

and for the scaling gas

$$\alpha_{P_j} = \frac{[P]_j \cdot B_{P_j} \cdot z_j}{\sum_i [P]_i \cdot B_{P_i} \cdot z_i} = \frac{\text{SCD}_P - \sum_{i \neq j} [P]_i \cdot B_{P_i} \cdot z_i}{\text{SCD}_P}. \quad (4.22)$$

The ratio of the  $\alpha$  factor equations is given by

$$\frac{\alpha_{X_j}}{\alpha_{P_j}} \cdot \frac{\text{SCD}_X}{\text{SCD}_P} = \frac{\text{SCD}_X - \sum_{i \neq j} [X]_i \cdot B_{X_i} \cdot z_i}{\text{SCD}_P - \sum_{i \neq j} [P]_i \cdot B_{P_i} \cdot z_i} \quad (4.23)$$

which can be substituted into Eq. (4.20) on the right hand side.

Following this, the main equation of the scaling method (Hüneke et al., 2017; Stutz et al.,

2017) is used to retrieve trace gas mixing ratios  $[X]_j$  in an atmospheric layer  $j$ ,

$$[X]_j = \frac{\alpha_{Xj}}{\alpha_{Pj}} \cdot \frac{SCD_X}{SCD_P} \cdot [P]_j. \quad (4.24)$$

In this study the target gas  $X$  is either  $\text{BrO}$  or  $\text{NO}_2$  while the scaling gas  $P$  is  $\text{O}_3$  due to their similar profiles in the UTLS. The  $SCD_X$  and  $SCD_P$  are the total slant column densities of the target gas and scaling gas, respectively, evaluated from the mini-DOAS data (as described in Sect. 4.1). The scaling gas mixing ratio  $[P]_j$  is given by the in situ  $\text{O}_3$  VMR as measured by the FAIRO instrument aboard HALO (refer to Sect. 3.3.2). Alternatively, the oxygen collisional complex  $\text{O}_4$  can be used as the scaling gas for analysis of tropospheric trace gases. The  $\alpha$  factors are calculated from Box-AMF which are simulated by the RT model McArtim (refer to Sect. 4.3 below).

Due to the wavelength dependent atmospheric processes of radiative transfer included in the Box-AMFs, the target and scaling gas should have similar or largely overlapping wavelength fit windows (refer to Table 4.2). Hüneke (2016) showed that  $\text{NO}_2$  Box-AMFs simulated at 457 nm compared to 477 nm vary by 20% in the lower troposphere for the nadir telescope viewing direction, but only 5% deviation in the limb viewing direction.

The scaling method compensates for most effects of the light path length modifications (e.g., scattering by aerosol and clouds) observed in the SCDs and includes instrumental, celestial and climatological data in the  $\alpha$  factor. However, for a given wavelength the  $\alpha$  factor ratio is insensitive to scattering by aerosols and clouds due to the equivalence theorem (Irvine, 1964; Partain et al., 2000) as shown in simulations performed by Knecht (2015) or in the supplement of Hüneke et al. (2017). The study by Knecht (2015) showed that the  $\alpha$  ratio between the target gas ( $\text{CH}_2\text{O}$ ) and scaling gas ( $\text{O}_4$ ) is mainly dependent on the ratio of the absorption or concentration profile with altitude (performed in the altitude interval 0–15 km) rather than the atmospheric conditions. In fact, the  $\alpha$  ratio of the target and scaling gas agreed well for cloudy and clear-sky simulations at all altitudes. There was a weak dependency on the SZA at low altitudes, but negligible at higher altitudes. Therefore, if the target and scaling gas are analyzed in a similar wavelength window, the light path length distributions will be similar and the inferred target gas mixing ratio is largely independent of the atmospheric optical state.

The mixing ratio of the target gas,  $[X]_j$ , for these limb UV/vis measurements is an average mixing ratio over a given atmospheric volume. This volume is based horizontally on the distance the aircraft has travelled during a single measurement, vertically on the FOV of the telescope to the right of the aircraft, and the light path length distribution in the given conditions (for examples see Kluge et al. (2020) Figs. 2 and 6). Typical precision errors for the VMRs calculated by the  $\text{O}_3$ -scaling method for the WISE campaign data are  $\pm 0.6$  ppt for  $\text{BrO}$  and  $\pm 8$  ppt for  $\text{NO}_2$ . A detailed description and a breakdown of the error budget can be found in Hüneke et al. (2017).

### 4.3 McArtim Radiative Transfer Modelling

For the retrieval of absolute mixing ratios at flight altitude the recently developed  $\text{O}_3$ -scaling method is used (refer to Sect. 4.2 and Stutz et al. (2017); Hüneke et al. (2017)). For this method, the radiative transfer (RT) conditions during the measurement should approximately be known to account for the atmospheric, instrumental, and celestial (e.g., Sun position) parameters and geolocation. As the RT equation does not have an exact analytical solution, techniques along with simplifications and assumptions are made to solve it numerically.

In this study the Monte Carlo atmospheric radiative transfer inversion model (McArtim) was

used to simulate the RT conditions in a refractive spherical atmosphere (Deutschmann et al., 2011). It was developed here at the University of Heidelberg and has been a useful tool for spectroscopy analysis. It is designed to simulate the RT of the atmospheric conditions, including the absorption, scattering and reflection by molecules, aerosols and Earth’s surface. In particular, McArtim is used to simulate the Box–AMFs from which the  $\alpha$  factors are calculated to infer mixing ratios via the scaling method for Eq. (4.24).

The McArtim model calculates the intensity weighted photon path length ( $L_i$ ) in a given box (i) of a specific height ( $h_i$ ) based on the radiative transfer equations (refer to Sect. 2.5.1) with respect to the reduction of incoming radiance by absorption of a gas. The Box–AMF for an individual box in the atmosphere is then defined as:

$$B_i = \frac{L_i}{h_i} = -\frac{1}{h_i} \frac{d \ln(I_*)}{d\beta_i}, \quad (4.25)$$

where  $I_*$  is the normalized solar radiance and  $\beta_i$  is the absorption coefficient of a certain gas in height layer i (Deutschmann et al., 2011). The absorption coefficient of a specific gas is determined by its absorption cross section ( $\sigma$ ) and the number density ( $n$ ), i.e,  $\beta = \sigma \cdot n$ .

The Box–AMFs along the flight track indicate the sensitivity of the absorption of a specific trace gas in the line of sight compared to the total absorption in all height layers. For the limb telescope set up, the Box–AMFs have the highest sensitivity at the flight altitude layer as well as in the few layers directly above flight altitude and then decrease with altitude, while below the flight altitude they are quite small (Knecht, 2015; Lörks, 2019). These simulations are done for different gases, namely the target (BrO or NO<sub>2</sub>) and scaling gas (O<sub>3</sub>–UV or O<sub>3</sub>–vis, respectively). For the scaling method, the  $\alpha$  ratio of the target to scaling gas is used which as mentioned above cancels out the light path length distribution dependency due to scattering by aerosols and clouds as stated by the equivalence theorem (Irvine, 1964; Partain et al., 2000; Knecht, 2015). Therefore the  $\alpha$  ratios are mainly dependent on the relative absorption between the target and scaling gas and hence their mixing ratios.

McArtim is initialised with a variety of prior known parameters and settings to best reproduce the atmospheric conditions during the WISE campaign. It takes into account the spatial subdivisions (co-latitude and longitude) to map out the actual flight tracks. It also includes the corresponding thermodynamic and microphysical properties such as temperature, pressure, and relative humidity along each flight. The profile of the potential temperature and pressure (recorded by the BAHAMAS instrument during flights) with altitude is shown in Fig. 4.12 for all WISE flights.

McArtim is calculated for a specific wavelength often in the center of the DOAS analysis fit windows of the respective gases (i.e., 350 nm for the UV analysis and 477 nm for the vis) and individual gas absorption coefficients (same as in the DOAS analysis detailed in Table 4.1). The simulation is done for a given surface albedo, which in this study is chosen as the ocean surface albedo of 0.06 due to the majority of flight hours spent over the Atlantic Ocean and Norwegian Sea. The simulation is done for 10000 photons, where generally only the output smoothness is dependent on the number of chosen photons. Other constraints used to initialise McArtim include:

- the vertical aerosol extinction profile
- the single scattering albedo and asymmetry parameter
- the a priori profiles of the target and scaling gases.

These are all discussed in the following sections.

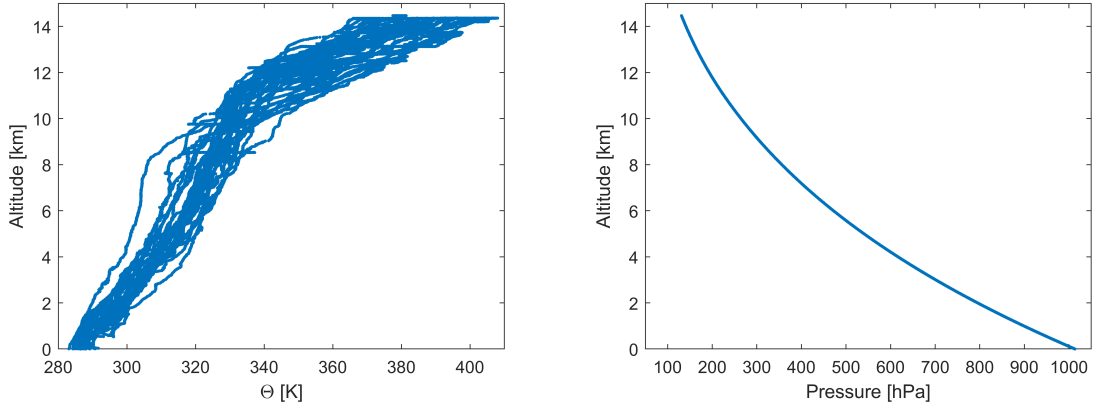


Figure 4.12: The left panel shows the potential temperature ( $\Theta$ ) in Kelvin with altitude in km measured by the BAHAMAS system during all WISE flights. The right panel indicates the pressure in hPa with altitude.

### 4.3.1 Aerosol Extinction

Light is attenuated by absorption and scattering events as it is propagated through the atmosphere, known as Rayleigh (gases) and Mie (aerosols) extinction. This is included in the McArtim simulation of the Box-AMF and inferred  $\alpha$  factors. The aerosol extinction is measured by various lidars and satellites. The data used in this study include the European Aerosol Research Lidar Network (EARLINET; Pappalardo et al. (2014)) stationed around north western Europe, as well as Stratospheric Aerosol and Gas Experiment III on the International Space Station (SAGE III ISS; NASA/LARC/SD/ASDC (2017)) satellite. The aerosol extinction profile of the combined EARLINET and SAGE III ISS data from late summer and fall season is shown in Fig. 4.13.

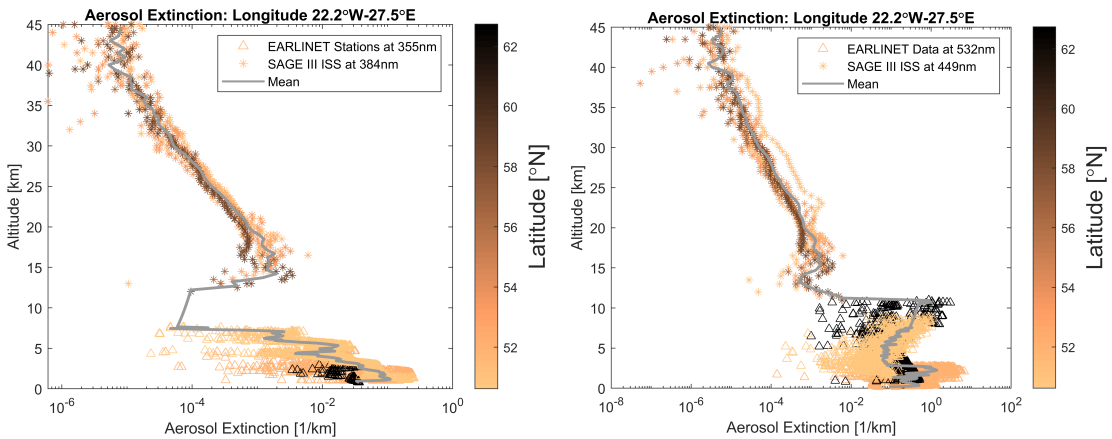


Figure 4.13: Aerosol extinction profile with altitude in the UV (left panel) and visible (right panel) wavelengths from EARLINET lidar stations (in north western Europe) and SAGE III ISS satellite data (mainly over the Atlantic Ocean) from late summer and fall.

The EARLINET lidar stations with available UV extinction data were recorded at 355 nm with the following systems: Caeli (in Cabauw, Netherlands), PolyXT-FM Lidar (in Vehmassmäki, Finland), and LILAS (in Lille, France). The visible lidar measurements taken at 532 nm were from lidar systems Polly1v2 (in Leipzig, Germany), UCLID (in Cork, Ireland), PolyXT-FM Lidar, and LILAS. These measurements were taken in Aug.–Oct. (2014–2017) and only reached  $\sim 10$  km altitude, therefore additionally SAGE III ISS satellite data are also used. The satellite

data is taken over Ireland and the surrounding region between longitudes of 22.2°W and 27.5°E and latitudes ranging from 51.0° – 58.3°N overlapping with the region of the WISE flights (refer to Sect. 5.1). The SAGE III ISS UV data is taken at 384 nm, while the visible measurements were recorded at 449 nm between Sept.–Oct. 2017.

The UV aerosol extinction profiles for EARLINET data has a high vertical resolution of 7.5 m for measurements ranging from 0.75–7.6 km in altitude, while the SAGE III ISS satellite data has a vertical resolution of 500 m with measurements ranging from 12–45 km altitude. The UV aerosol extinction profile is linearly interpolated in the altitude gap between 7.6 km and 12 km. The visible lidar data ranges from 0.15–11 km altitude, and the satellite data ranges from 11–45 km. The average aerosol extinction profile per altitude for the UV and visible wavelengths are indicated by the gray thick lines in Fig. 4.13 and are used as input for McArtim.

### 4.3.2 Single Scattering Albedo and Asymmetry Parameter

The OPAC model (Hess et al., 1998) is used to calculate the aerosol single scattering albedo (SSA) and asymmetry parameter ( $g$ ) described in Sect. 2.5.2. The maritime clean conditions scenario is used in this study as it best represents the WISE flights over the North Atlantic. The parameters are calculated at 350 nm and 450 nm for the UV and visible analysis, respectively. The majority of the flights were at high altitudes (8.5–15 km) where the relative humidity (RH) varied between 3% and 45% (refer to Fig. 4.14), therefore either of the smallest settings would have been appropriate but ultimately the 0% RH setting was chosen.

The resulting optical parameters calculated with OPAC are  $SSA=0.9888$  and  $g=0.6818$  for the UV, with similar results in the visible ( $SSA=0.9912$  and  $g=0.6788$ ). At higher RH (e.g., 50%) both SSA and  $g$  become slightly larger ( $SSA\sim 1$  and  $g\sim 0.75$  for both UV and vis wavelengths) with little impact on the final analysis. The single scattering albedo and asymmetry factor are both used to initialise the McArtim model.

A study by Pollack et al. (1981) calculated single scattering properties of aerosols for three elevations in the stratosphere (12.2 km, 15.2 km and 18.3 km altitude) in July 1979 for varying wavelengths and concluded similar SSA and  $g$  as used in this study. A sensitivity run of SSA (ranging from 0.6–0.99) as well as  $g$  (ranging from 0.6–0.78) was done by Großmann (2014), which showed that above 5 km there was less than a 2% and 1% change, respectively, in the final target gas VMR in the case of HCHO.

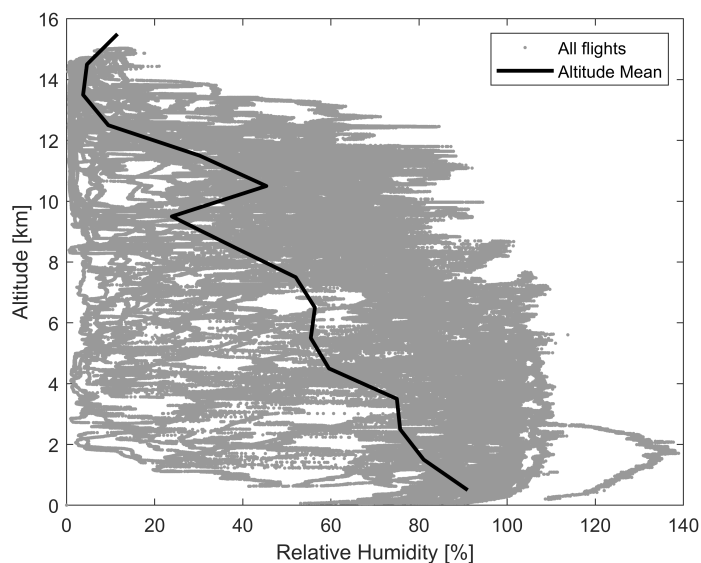


Figure 4.14: The relative humidity (RH) is measured by the BAHAMAS system and shown as a function of altitude in km. Data from all WISE flights are shown in gray. The average RH per km is indicated by the black line.

### 4.3.3 A Priori Profile: Vertically Adjusted CLaMS Curtains

Additionally, McArtim uses a priori profiles of the respective trace gas mixing ratios to simulate the  $\alpha$  factor. The output is particularly sensitive to the a priori vertical profiles of the respective scaling and target trace gases (Knecht, 2015). Therefore, it is essential to use the best prior knowledge which in this case consists of modelled trace gas curtains simulated by CLaMS (refer to Sect. 3.4.1). For each time increment of the spectra a new CLaMS vertical profile is used from the curtain along the flight trajectory. To further converge the vertical CLaMS profile to the exact WISE conditions, vertical discrepancies between the CLaMS model trace gases at flight altitude and the real conditions are compared for the stratospheric tracer  $O_3$ . A similar vertical adjustment of the model data comparing to measured  $O_3$  was done previously in Werner et al. (2017). Generally the CLaMS curtains agree well with the in situ measured  $O_3$ , and adjustments (by vertical shifting) are mainly necessary when crossing a strong  $O_3$  gradient. The CLaMS curtains for all gases are adjusted by a vertical shift at each time increment to match CLaMS  $O_3$  at flight altitude with the in-situ  $O_3$  measured by FAIRO from the HALO aircraft.

The original CLaMS curtains have 41 pressure levels between 10–1000 hPa (i.e., from the surface to  $\sim 32$  km). To allow for smaller adjustments, the curtain is interpolated onto a smaller vertical grid with 500 levels. The adjustment of CLaMS is on average a vertical shift of  $\sim 1$  km (up or down), which corresponds to just over one pressure/altitude grid box of the original CLaMS resolution. The maximum vertical adjustment that can occur is set to 2.5 km.

An example of the CLaMS trace gas mixing ratio at flight altitude for  $O_3$ ,  $NO_2$ , and BrO is shown in Fig. 4.15 for the original CLaMS results (in blue) and the vertically adjusted results (in red). Generally, CLaMS predicts  $O_3$  reasonably well when comparing to the in situ ob-

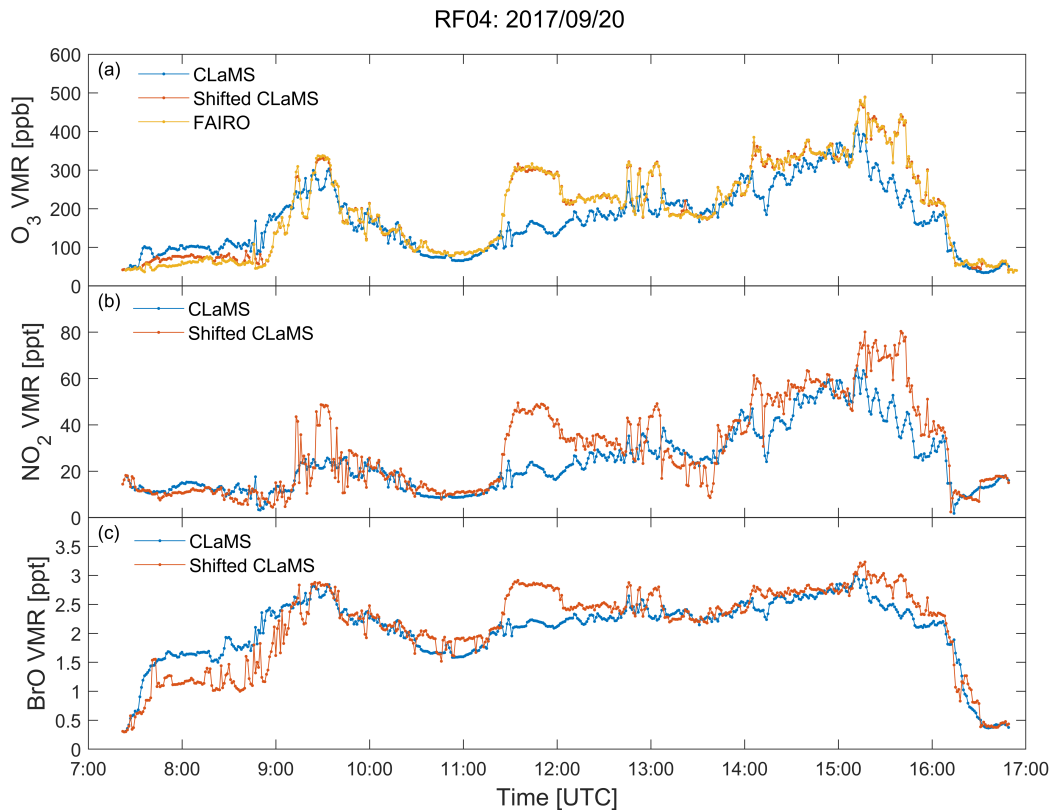


Figure 4.15: CLaMS  $O_3$  (a),  $NO_2$  (b), and BrO (c) VMRs for the original (red) and vertically adjusted (blue) curtain simulations at flight altitude for RF04 on Sept. 20, 2017. Panel (a) additionally shows the in situ measured  $O_3$  by FAIRO (in yellow) used to adjust and match the CLaMS  $O_3$  curtain.

served  $O_3$  from FAIRO. However, occasionally there is a larger discrepancy. For example around 11:30–12:00 UTC during RF04 there is a difference of around  $\sim 150$  ppb. Therefore, the CLaMS curtain is adjusted downwards at this time interval to match simulated  $O_3$  from higher altitudes with the elevated observed  $O_3$ . The corresponding CLaMS curtains of  $O_3$ ,  $NO_2$ , and BrO VMRs is shown in Fig. 4.16 for the original (left panels) and vertically adjusted (right panels) curtains. These adjusted curtains are then interpolated onto the mini-DOAS data timescale to use as input for the RT simulation by McArtim.

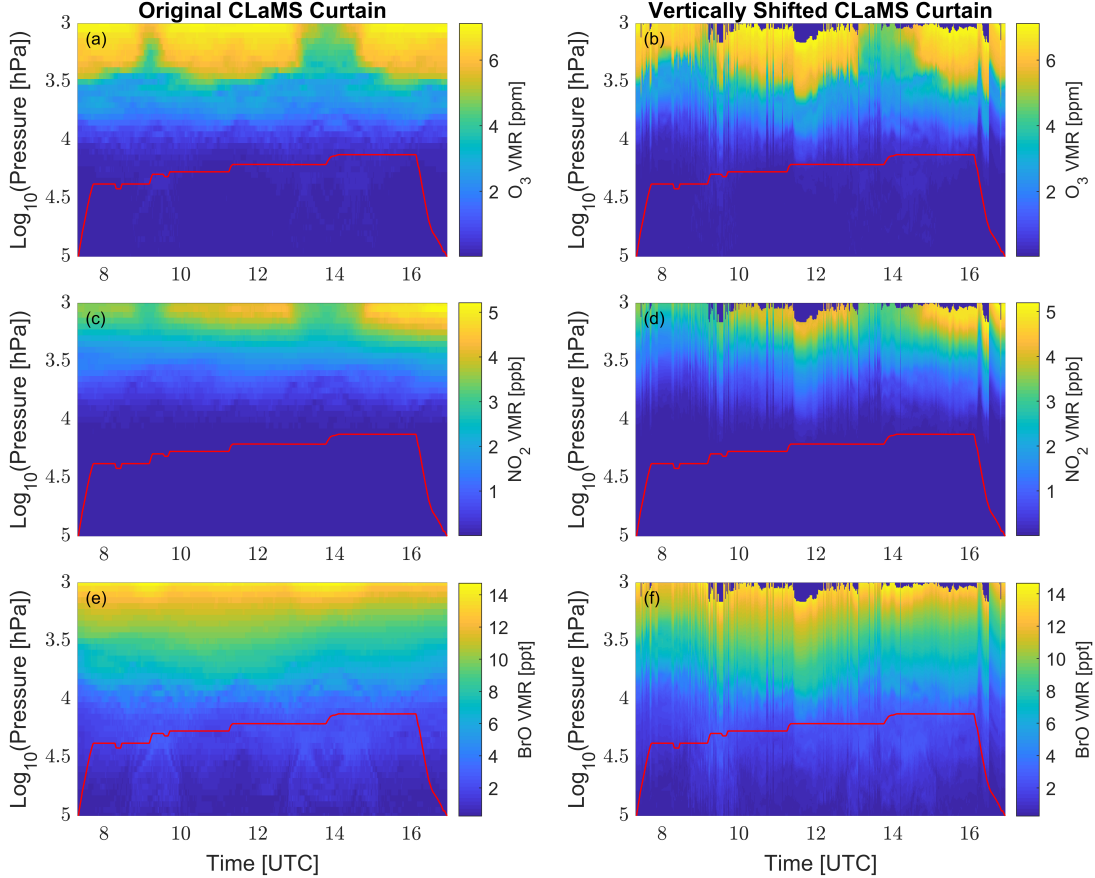


Figure 4.16: CLaMS curtains of  $O_3$  (a–b),  $NO_2$  (c–d), and BrO (e–f) VMRs for the original (a, c, and e) and vertically adjusted (b, d, and f) curtain plotted in  $\log(\text{Pressure})$  against the time for the research flight RF04 on Sept. 20, 2017. The red line indicates the HALO flight trajectory.

#### 4.3.4 Sample Box–AMF and $\alpha$ Factors

The input of these various parameters greatly improves the Box–AMF and  $\alpha$  factor calculation by McArtim. A summary of the various parameter settings can be found in Table 4.4. An example of the adjusted (by vertical shifting) CLaMS curtains for the scaling and target gas ( $O_3$  and BrO, respectively), the Box–AMF from McArtim, the calculated  $\alpha$  factors at flight altitude, total SCDs, and lastly the target gas VMR is shown in Fig. 4.17. The Box–AMF shows the highest sensitivity at flight altitude for the limb telescopes, resulting in the weighting factor ( $\alpha$ ) being largest in the small elevation window near flight altitude and in the limb telescope FOV. This results in  $\alpha_{O_3} \sim 0.1–0.2$  and  $\alpha_{BrO} \sim 0.3–0.4$ , while the ratio of the two results in the  $\alpha_R \sim 2–4$ . The multiplication of the  $SCD_R$  and  $\alpha_R$  with the FAIRO in situ  $O_3$  VMR as in Eq. (4.24) results in the inferred target gas BrO VMR. The resulting BrO VMR is an average

mixing ratio over the volume defined by the FOV of the limb telescope at flight altitude, the light path length in the line of sight, and over the distance travelled during each (running mean) measured spectrum.

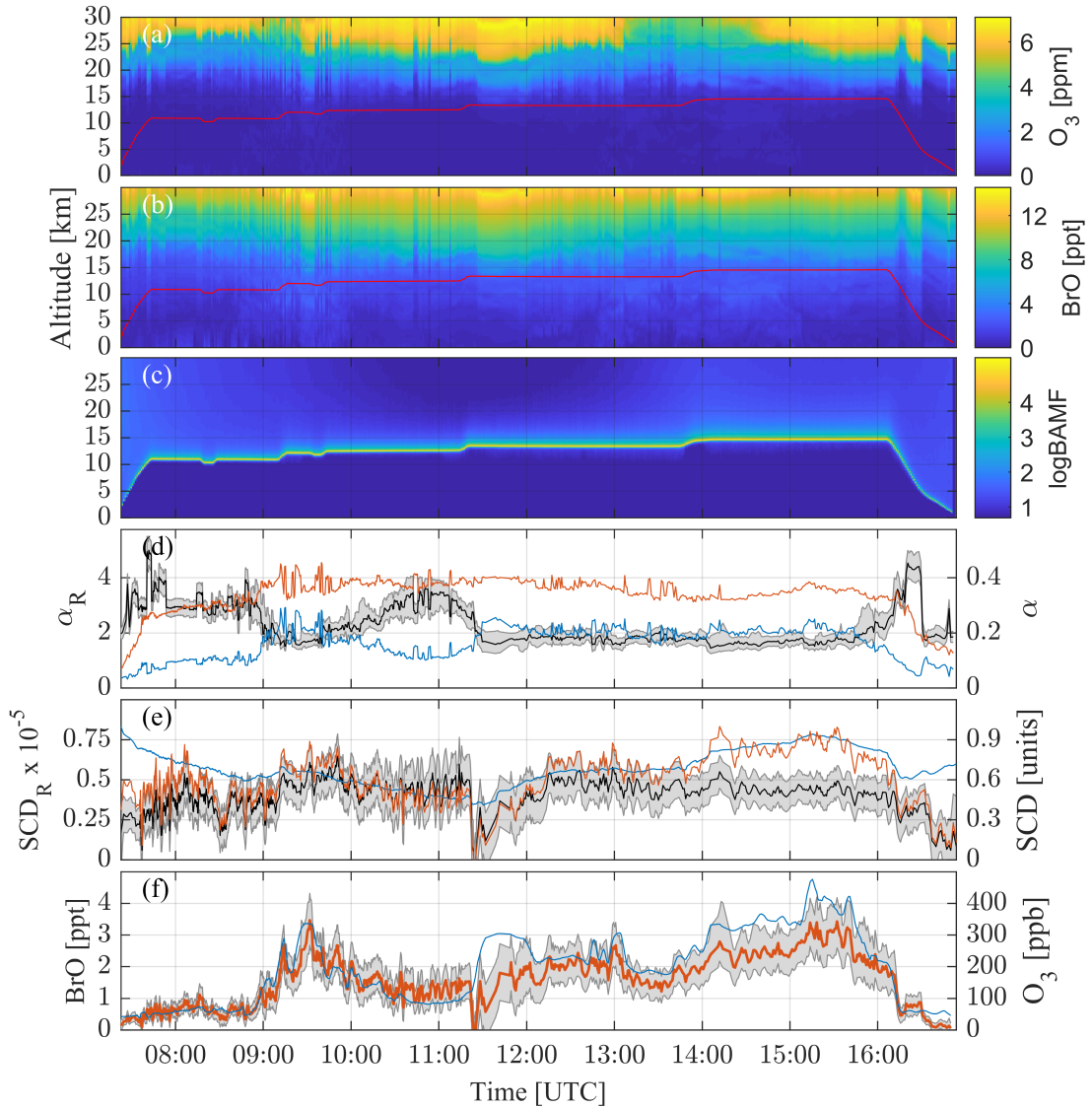


Figure 4.17: Scaling method details from research flight RF04. (a–b) The adjusted CLaMS curtains of the scaling gas  $\text{O}_3$  VMR and target gas BrO VMR, respectively, with altitude. The red line is the flight altitude from the BAHAMAS instrument. (c) The logarithm of the Box–AMF (McArtim output). (d) The  $\alpha$  factor ratio (black; left axis) of the individual  $\alpha$  factors of  $\text{O}_3$  (blue; right axis) and BrO (orange; right axis) calculated from the Box–AMF. (e) The SCD ratio (black; left axis) of the scaling gas and target gas ( $\text{O}_3$ –blue and BrO–orange, respectively; right axis) from the mini-DOAS measurement. The right axis SCDs units are scaled by the maximum SCD of each gas. (f) The BrO VMR (orange; left axis) calculated via the scaling method using the in situ measured FAIRO  $\text{O}_3$  VMR (blue; right axis) as the scaling gas.

Table 4.4: Overview of the settings used in the McArtim simulations when calculating the Box-AMF.

Parameter	Description	Setting
$\lambda$	Wavelength [nm]	350 nm (UV), 477 nm (vis)
T, p	BAHAMAS vertical profiles of temperature [K], pressure [hPa]	WISE campaign average
Albedo	Surface albedo (ocean)	0.06
Photons	Number of photons for Monte Carlo sampling	10,000
Extinction	Vertical profile of extinction [ $\text{km}^{-1}$ ] by aerosols	EARLINET+SAGE III-ISS
OPAC	Optical Properties of Aerosols and Clouds	maritime clean scenario
OPAC $\lambda$	OPAC wavelength settings [nm]	350 nm (UV), 450 nm (vis)
RH	Relative humidity setting in OPAC [%]	0%
SSA	Single scattering albedo	0.9888 (UV), 0.9912 (vis)
g	Asymmetry parameter	0.6818 (UV), 0.6788 (vis)
a priori profile	Vertical profile of the scaling/target gas VMRs	adjusted CLaMS curtains

#### 4.3.5 $\alpha$ Factors: Campaign Overview

The impact of adjusting the CLaMS curtains (by a vertical shift) on the simulated  $\alpha_R$  factors is shown in Fig. 4.18 for all WISE flights. The  $\alpha_R$  of BrO relative to  $\text{O}_3$ -UV is shown in panel (a), and the  $\alpha_R$  of  $\text{NO}_2$  relative to  $\text{O}_3$ -vis is shown in panel (b). The vertically adjusted CLaMS curtains impact the RT output of McArtim in that it only alters the  $\alpha_R$  for individual measurements, resulting in the observed scatter along the 1:1 line. The most important point here, is that there is no systematic shift or drift of the  $\alpha_R$  when comparing the original CLaMS curtains to the vertically adjusted CLaMS curtains. This applies to both the UV and visible analysis. These results further support the robustness of the analysis, and confirms the reliability of the  $\alpha$  factors used as weighting factors in the scaling equation.

The  $\alpha$  factors from all WISE flights at flight altitude (i.e., in the limb telescope line of sight) of BrO relative to  $\text{O}_3$ -UV and  $\text{NO}_2$  relative to  $\text{O}_3$ -vis from the adjusted CLaMS curtain input to McArtim is shown in Fig. 4.19. These are used for the final analysis. The BrO  $\alpha$  factor is generally always (at least  $1.5\times$ ) larger than for  $\text{O}_3$  shown in panel (a). At  $\text{SZA} > \sim 75^\circ$ , the  $\alpha_{\text{BrO}}$  factor decreases with increasingly larger SZA. This SZA dependency is because BrO is no longer produced through photolysis and the remaining BrO is converted to  $\text{BrONO}_2$  at increasingly large SZA (Wetzel et al., 2017). This is less apparent for  $\text{O}_3$  because it has no significant diurnal variation, only a few tenths ppm diurnal variation (e.g., Sakazaki et al. (2013); Schanz et al. (2014)). At very large SZA  $> \sim 89^\circ$ , the  $\alpha$  factor of  $\text{O}_3$  becomes larger than for BrO because at night BrO mixing ratios approach 0 ppt. These large SZA data are excluded from further analysis of the mini-DOAS results.

The  $\alpha_R$  as a function of distance from the local WMO tropopause ( $\Delta\Theta = \Theta - \Theta_{\text{Tropopause}}$ ) is shown in Fig. 4.19 (b). The  $\alpha$  factor ratio between BrO and  $\text{O}_3$ -UV is generally near  $\sim 2$ , with a drift towards smaller ratios further into the stratosphere as the increase in absorption of  $\text{O}_3$  relative to BrO becomes slightly more dominant at higher altitudes (i.e., further in the ozone layer). On the other hand, just below the tropopause around  $\Delta\Theta \sim -10$  K, the  $\alpha_R$  increases up to  $\sim 6$ . The troposphere has larger ratios compared to the stratosphere because  $\text{O}_3$  has a stronger decrease relative to BrO with decreasing altitude in the troposphere. BrO has an approximately linear decrease with decreasing altitude in the UTLS, while  $\text{O}_3$  has a sharp decrease across

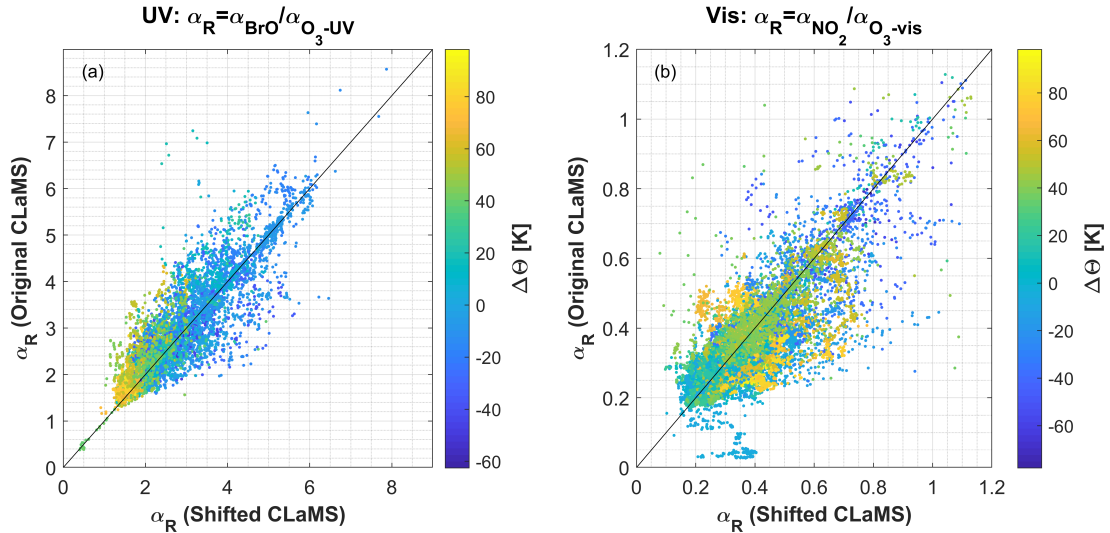


Figure 4.18: Comparing the  $\alpha_R$  for the original and vertically adjusted CLaMS curtains for all WISE flights. Panel (a) shows the  $\alpha_R$  of BrO relative to  $O_3$ -UV calculated at 350 nm in the telescope’s line of sight. Panel (b) shows the  $\alpha_R$  of  $NO_2$  relative to  $O_3$ -vis simulated at 477 nm. The black line is the 1:1. The colour coding of the measurements is the potential temperature distance from the local tropopause ( $\Delta\Theta$  in Kelvin).

the tropopause with generally low mixing ratios in the troposphere. This change in relative absorption is beyond the CLaMS model capabilities and results in an over estimation of BrO in the troposphere which further increases the  $\alpha_R$ . Therefore the change in BrO absorption is less than the change in absorption by  $O_3$  in the troposphere. This likely is the cause of the distinct triangle peak shape and bend between the  $\alpha$  factors in panel (a). The height dependency can also be seen in Fig. 4.18 (a).

The  $\alpha$  factors for  $O_3$ -UV are for the most part larger than for  $O_3$ -vis (Fig. 4.19 (a) and (c) x-axes comparison), and stems from the difference in light path length distributions. The light path length distributions in the visible wavelength range are typically longer compared to those in the UV due to Rayleigh scattering. Longer light path distributions result in more sensitivity towards the line of sight absorption. Because the weighting  $\alpha$  factor acts to cancel out the path length dependency in the target gas VMR, it must be smaller for visible wavelengths than in the UV. Additionally,  $O_3$  absorption in the stratosphere occurs mainly in the UV, where as absorption in the visible wavelength is comparatively weak. This is reflected in the Box-AMF simulated by McArtim shown in Fig. 4.20. Above  $\sim 7.5$  km the  $O_3$ -UV Box-AMF at flight altitude, i.e., in the line of sight of the limb telescopes, are larger than those of  $O_3$ -vis. However, with decreasing altitude the relative  $O_3$  absorption in the visible wavelength range increases compared to in the UV wavelength range. Because the majority of the WISE flight hours are above  $\sim 7.5$  km where the  $O_3$ -UV absorption dominates, the weighting  $\alpha$  factor in the UV will be correspondingly larger compared to in the visible wavelength range. Therefore the  $\alpha_{O_3-vis}$  should be smaller than the  $\alpha_{O_3-UV}$  for most of the WISE flight segments.

The  $\alpha$  factors of  $NO_2$  are generally always smaller than the  $\alpha$  factors of  $O_3$ -vis (Fig. 4.19 (c)). This is largely due to small  $NO_2$  mixing ratios and little absorption near the tropopause compared to the upper stratosphere or lower troposphere. Neither the  $NO_2$  nor the  $O_3$ -vis  $\alpha$  factors have a clear SZA dependency, because the available visible light varies less throughout the day compared to the UV light. Of course once the  $SZA > 90^\circ$ , the  $\alpha$  factors approach zero due to complete lack of visible light. The  $\alpha_R$  of the two gases in the stratosphere is relatively constant around  $\sim 0.2$ – $0.5$  with the exception of a few outliers due to  $SZA > 89^\circ$ . However, in

### WISE Campaign $\alpha$ Factors

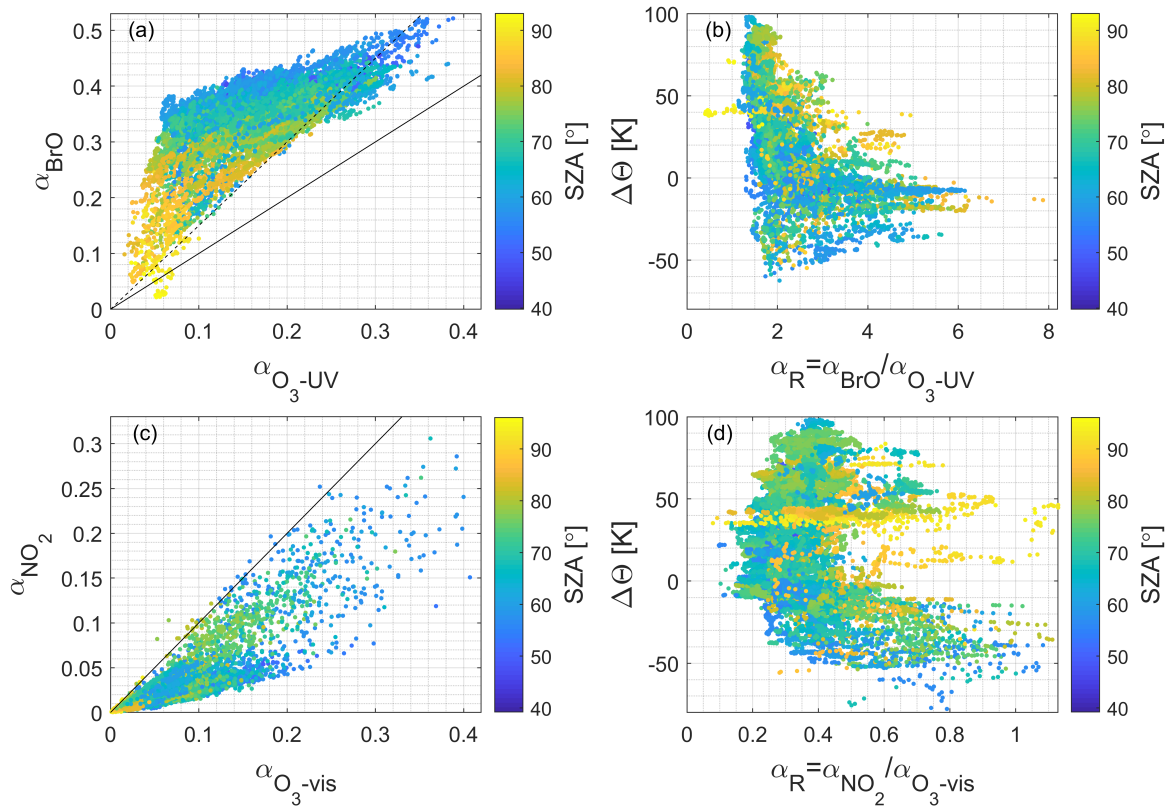


Figure 4.19: Comparison between the target and scaling gas  $\alpha$  factors for the BrO and  $\text{O}_3\text{-UV}$  (a) and  $\text{NO}_2$  and  $\text{O}_3\text{-vis}$  (c). The  $\alpha_{\text{R}}$  with potential temperature distance from the tropopause ( $\Delta\Theta$ ) are shown in (b) and (d) for the UV and visible gases, respectively. All panels are colour coded by the SZA. The solid black line in (a) and (c) is the 1:1 line and the black dashed line in (a) is the 1.5:1 ratio.

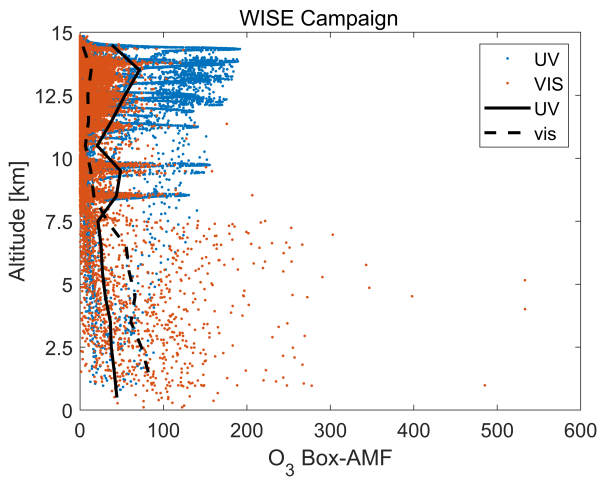


Figure 4.20: The  $\text{O}_3$  Box-AMF at flight altitude of the HALO aircraft during all WISE flights for the UV (350 nm) and visible (477 nm) wavelength chosen for McArtim simulations.

the troposphere the  $\alpha_{\text{R}}$  varies significantly more up to  $\sim 1$ . The larger tropospheric  $\alpha_{\text{R}}$  are due to increases of  $\text{NO}_2$  absorption likely from pollution over Europe, while  $\text{O}_3$  decrease.

The resulting VMRs of the target gases for the entirety of the WISE campaign are compared for the original and vertically adjusted CLaMS curtains shown in Fig. 4.21. The comparison between the  $\text{O}_3$  VMRs of the original CLaMS model results at flight altitude with the FAIRO measurements shows a general agreement (Fig. 4.21 (a) blue points). However, there is a large

scatter observed and more important there is a slight drift and under estimation of the modelled  $\text{O}_3$ . This becomes stronger towards larger VMRs, i.e., in the stratosphere. By vertically adjusting the model for the best agreement with the measurements within a 2.5 km shift, the scatter is forced to reduce (red points).

The impact of adjusting CLaMS curtains on the mini-DOAS BrO and  $\text{NO}_2$  VMRs are shown in Fig. 4.21 (b–c), respectively. The original CLaMS VMRs have a larger discrepancy and scatter between the model and measurement (blue points). When forcing the CLaMS vertical adjustment, it consolidates the cloud of data points around the 1:1 line between the CLaMS model and inferred mini-DOAS measurements for both BrO and  $\text{NO}_2$ .

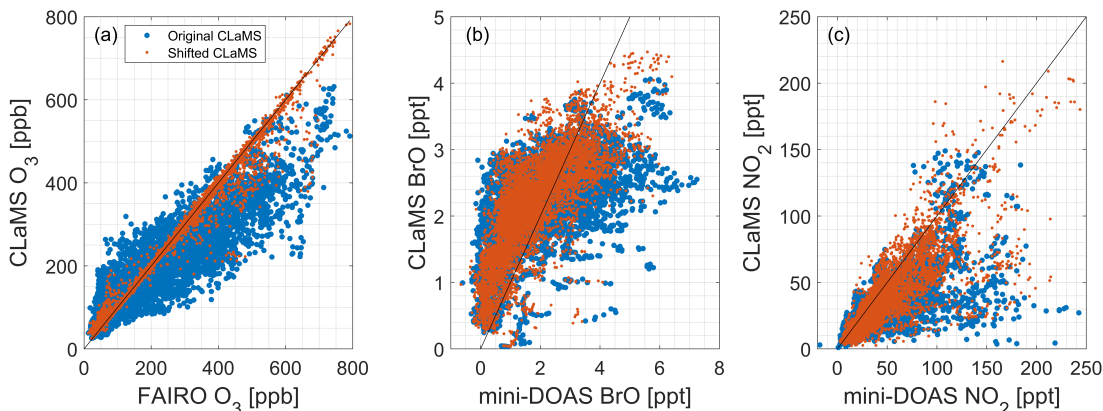


Figure 4.21: Comparison of the CLaMS trace gas along the flight altitude compared to the measured FAIRO  $\text{O}_3$  (a), mini-DOAS BrO (b), and mini-DOAS  $\text{NO}_2$  (c) for all WISE flights. The CLaMS mixing ratios at flight altitude from the original curtains are shown in blue and from the vertically adjusted CLaMS curtains in red. The black line is the 1:1 line.

Although there appears to be reasonable agreement between the model and measured BrO, there is an interesting feature seen in the comparison in Fig. 4.21 (b). The linear relationship between model and measurement changes at low and high VMRs. Between 0–2 ppt of measured BrO and corresponding to 0–2.5 ppt modelled BrO, the CLaMS model estimates are larger than measured BrO. The linear relationship changes to an underestimation at larger VMRs. This highlights the deficit of the CLaMS model regarding bromine chemistry around the troposphere. As mentioned in Sect. 3.4.1, CLaMS assumes all bromine is in the form of long-lived bromine (i.e., all VSLs have converted to  $\text{Br}_y^{\text{inorg}}$ ) which in the troposphere is less the case than in the stratosphere and additionally the troposphere is missing appropriate bromine sinks in the model. Thus, BrO is likely over estimated in the troposphere. This is currently being implemented in the newest CLaMS model based on the inferred  $\text{Br}_y^{\text{inorg}}$  as well as  $\text{Br}^{\text{org}}$  measurements from this study (personal communication with Jens-Uwe Grooß, Jan. 27, 2021). Of course, it needs to be noted that the mini-DOAS VMRs are dependent on the CLaMS model input for the  $\alpha$  factors and are therefore not completely independent, but as shown above the adjustment (by vertically shifting) CLaMS does not systematically affect the  $\alpha$  factors and hence inferred BrO.

$\text{NO}_2$  measurements and model results generally agree well within the scatter around the 1:1. The mini-DOAS measured  $\text{NO}_2$  will generally be able to observe individual larger mixing ratios due to individual sources (e.g., small scale regional pollution, aircraft exhausts or ship exhausts) which the CLaMS model cannot account for. The particularly large mini-DOAS  $\text{NO}_2$  VMRs generally coincides with the few flight sections over mainland Europe and Great Britain where city pollution is likely observed. This is reflected in the larger scatter on the mini-DOAS x-axis. The mini-DOAS  $\text{NO}_2$  VMRs agree even better with the vertically adjusted CLaMS simulations as expected based on these  $\text{NO}_2$  sources that are not implemented in CLaMS.

# Chapter 5

## Measurements

### 5.1 WISE Campaign

The Wave-driven and ISentropic Exchange (WISE) campaign consisted of 15 research flights in the UTLS in late summer and fall 2017 with the German HALO research aircraft based from Shannon, Ireland. Scientific topics of interest during WISE included the transport pathways, time-scales, and mixing processes affecting the late summer and fall in the mid- to high-latitudes over the North Atlantic, Norwegian Sea, and north western Europe. A particular focus was on the role of the transport of air from the TTL and Asian monsoon region on  $\text{H}_2\text{O}$ , trace gas budgets including VLS and their product gases in the LMS, as well as small scale processes leading to irreversible exchange across the extratropical tropopause by Rossby wave-breaking events (Homeyer and Bowman, 2013). In the scope of this dissertation, the main scientific topic of WISE this work contributes to is quantifying the halogen budget in the UTLS region and its impact on ozone. Additional WISE scientific goals targeted in this dissertation include the transport of air masses from the Asian monsoon region into the Ex-UTLS as well as individual stratosphere-troposphere exchange (STE) events both directly related to  $\text{Br}^{\text{tot}}$  mixing ratios.

The first test-research flight (RF01) took place on August 31<sup>st</sup>, 2017 where each instrument that is part of the payload is briefly tested individually for electromagnetic interference with the aircraft. Due to the lack of simultaneous measurements, short duration, and no scientific region-oriented goal for measurements, this flight is excluded from the current study. The following research flights (RF02–RF16) were conducted from September 13<sup>th</sup>, 2017 until October 21<sup>st</sup>, 2017. The campaign consisted of over 140+ flight hours, with the majority spent probing the extratropical upper troposphere and lower stratosphere (Ex-UTLS). The 15 different flight tracks are shown in Fig. 5.1 with four research flights (RF04, RF08, RF14 and RF15) identified by dashed lines as they are discussed in the text. The research flights were mainly based from Shannon, Ireland, with the exception of RF02. RF02 started and landed at the home base of HALO at the DLR facility in Oberpfaffenhofen (near Munich), Germany. Additionally there were two transfer flights (RF03 and RF16) between Oberpfaffenhofen and Shannon, which are also scientific research flights.

The measurement region ranged from longitudes  $48.4^\circ\text{W}$ – $15.7^\circ\text{E}$  and latitudes  $37.9$ – $74.4^\circ\text{N}$ , to observe trace gases within the Ex-UTLS. In equivalent latitudes (e.g., Butchart and Remsberg (1986); Pan et al. (2012)), the investigated air masses ranged from those being recently transported from the tropics ( $\sim 6^\circ\text{S}$ ) up to polar air masses at  $86^\circ\text{N}$ . Flight times varied between 6hr 14min and 9hr 54min with an average of 8hr 45min ranging between 04:25 UTC and 21:58 UTC. The flight hours largely take place during daytime, but there were three take offs at or before sunrise and six landings near or after sunset. The majority of the flight time was spent

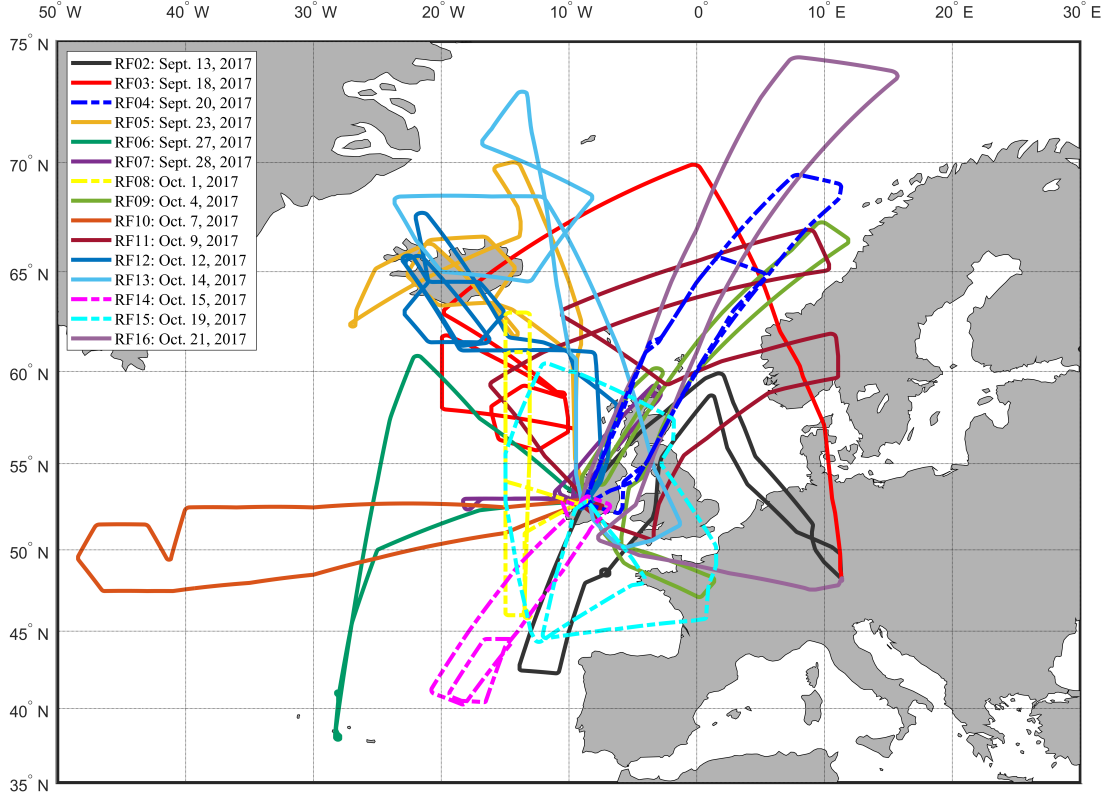


Figure 5.1: Trajectories of the 15 HALO flights during the WISE campaign in the mid- to high-latitudes over the North Atlantic Ocean, Norwegian Sea and north western Europe from September 13, 2017 until October 21, 2017. A prior test flight (RF01) is not included in this study. The first research flight, RF02, was conducted locally from the home base in Oberpfaffenhofen, Germany, and all consequent flights were based from Shannon, Ireland aside from the transfer flights. The dashed flight tracks of RF04: Sept. 20<sup>th</sup> (dashed blue line), RF08: Oct. 1<sup>st</sup> (dashed yellow line), RF14: Oct. 15<sup>th</sup> (dashed magenta line), and RF15: Oct. 19<sup>th</sup> (dashed cyan line) are discussed in the text.

at altitudes between 8.5–14.5 km allowing for measurements along the Ex–UTLS and crossing the tropopause frequently. The measured air masses reach up to a potential temperature of  $\Theta \sim 410$  K, i.e., allowing for observations throughout the northern hemisphere LS (and thereby also the LMS).

The  $\text{O}_3$ ,  $\text{N}_2\text{O}$ ,  $\text{CO}$ , and  $\text{SF}_6$  VMR measurements are available for all 15 research flights. The  $\text{NO}_2$ ,  $\text{BrO}$ , and  $\text{Br}_y^{\text{inorg}}$  VMRs are also available for all flights, however only during the daytime portions of the flights, i.e., any measurements where the  $\text{SZA} > 89^\circ$  are excluded.  $\text{Br}^{\text{org}}$  VMRs are not available during four flights (RF07: Sept. 28<sup>th</sup>, RF09: Oct. 4<sup>th</sup>, RF14: Oct. 15<sup>th</sup>, and RF15: Oct. 19<sup>th</sup>), and during three other research flights (RF02: Sept. 13<sup>th</sup>, RF06: Sept. 27<sup>th</sup> and RF11: Oct. 9<sup>th</sup>)  $\text{Br}^{\text{org}}$  VMRs are only available for a portion of the flight time. As such,  $\text{Br}^{\text{tot}}$  measurements calculated by summing the organic and inorganic bromine contributions (refer to Sect. 2.3), are available during 11 of the 15 WISE research flights.

## 5.2 Key Atmospheric Regions during WISE

The unique atmospheric regions discussed in the text such as the lowermost stratosphere (LMS), the lower stratosphere (LS), and the tropical tropopause layer (TTL) are defined in previous literature (Holton et al., 1995; Fueglistaler et al., 2009) and summarised in the beginning of

Chapt. 2.

Further prominent regions of the atmosphere observed during the WISE campaign are discussed throughout this dissertation and are defined as follows:

- The high bromine region (HBrR) is a region in the LMS between equivalent latitudes 55–80°N and potential temperatures  $\Theta = 350\text{--}385$  K (discussed in Sect. 6.2 and onwards).
- The LS below and above the HBrR are the air masses between equivalent latitudes 55–80°N from the local tropopause up to potential temperatures  $\Theta < 350$  K (base of the HBrR) and above  $\Theta > 385$  K (discussed in Sect. 6.2 and onwards).
- The tropical  $\Theta_{\text{high}}/\text{PV}_{\text{low}}$  region is defined by high potential temperatures ( $\Theta > 355$  K) and low potential vorticity units ( $\text{PVU} < 2$ ). It describes (former) tropical UT air masses from low equivalent latitudes and is briefly discussed in Sect. 5.3.2 and later in Sect. 6.2 and onwards.
- The extratropical tropopause (Ex–TP) is defined as the region between equivalent latitudes of 35–55°N and within  $\pm 5$  K of the local WMO tropopause in potential temperature (discussed in Sect. 6.2 and onwards).

These regions are noteworthy because of either the elevated  $\text{Br}^{\text{tot}}$  observed in the HBrR, tropical  $\Theta_{\text{high}}/\text{PV}_{\text{low}}$  region and to a lesser extent in the Ex–TP region or because of the relative lower bromine mixing ratios observed in the surrounding LS air masses above and below the HBrR. They are core regions relevant to the interpretation and discussion of bromine transport in the following chapter.

## 5.3 Sample Flights

Two flights are chosen as examples, the research flights on September 20<sup>th</sup> and October 1<sup>st</sup>, 2017 (RF04 and RF08, respectively), highlighted in Figure 5.1. RF04 has typical  $\text{Br}^{\text{tot}}$  mixing ratios near the campaign LS average along with a few segments observing elevated  $\text{Br}^{\text{tot}}$  in the HBrR (Fig. 5.1 blue dashed line). RF08 observes elevated  $\text{Br}^{\text{tot}}$  in former tropical  $\Theta_{\text{high}}/\text{PV}_{\text{low}}$  air masses (Fig. 5.1 yellow dashed line).

Figures 5.2 and 5.3 (RF04 and RF08, respectively) provide overviews of the  $\text{O}_3$  measured by FAIRO, CO measured by UMAQS,  $\text{SF}_6$  inferred lag-time measured by GhOST-ECD,  $\text{Br}^{\text{org}}$  measured by GhOST-MS, and  $\text{NO}_2$  and BrO measured by mini-DOAS. The modelled  $\text{O}_3$ ,  $\text{NO}_2$ , and BrO from the adjusted (by vertical shifting) CLaMS curtains (refer to Sect. 4.3.3) shows excellent agreement to measurements particularly for the former two gases. Additionally, the adjusted CLaMS partitioning of  $\text{BrO}/\text{Br}_y^{\text{inorg}}$  and  $\text{BrONO}_2/\text{Br}_y^{\text{inorg}}$  are displayed, which the former is used to infer the  $\text{Br}_y^{\text{inorg}}$  from the mini-DOAS BrO measurements. The tropical marine environment (TME) emission tracer from south eastern Asia and the Central American (CAM) emission tracer from the CLaMS artificial tracer simulations are also shown, which are relevant for the transport interpretation as discussed in Sect. 6.3 below. And lastly, the summed contributions of inferred  $\text{Br}^{\text{tot}}$  is displayed in the bottom panel of the figures. The variety of air masses observed during the WISE campaign are represented in the variability of each of these parameters.

### 5.3.1 RF04: September 20<sup>th</sup>, 2017

The first example flight, RF04, took place on September 20<sup>th</sup>, 2017 with the take-off at 07:20 UTC and landing at 16:56 UTC at Shannon, Ireland (refer to Figs. 5.1 and 5.2). This flight consisted

of two different length, but overlapping-rectangular shuttles northeast of Ireland, up the Scandinavian coast, over the Norwegian Sea, and only briefly crossing landmasses over the United Kingdom and Ireland. The first clockwise rectangular flight track reached  $65.6^\circ\text{N}$  at 09:12 UTC. The second clockwise flight pattern reached a maximum latitude of  $69.4^\circ\text{N}$  at approximately 13:50 UTC and reached its furthest longitude from Ireland of  $11.2^\circ\text{E}$  around 14 UTC.

The final stretch back to Shannon was flown at the highest altitude during this flight of 14.35 km from 14:05–16:07 UTC. At 14:28 UTC the maximum potential temperature of  $\Theta = 399\text{ K}$  was reached over the Norwegian Sea, corresponding to a potential temperature distance above the WMO tropopause of  $\Delta\Theta = 71\text{ K}$ . The BAHAMAS flight level (black solid line) and the WMO tropopause (black dashed line) are shown in potential temperature in Kelvin along with the equivalent latitude (blue; right axis) in Fig. 5.2 (a). The tropopause was crossed a few times, but the majority of the flight time was spent in the LMS. The mean lag-time of the air masses ranged from  $-1.08$  to  $1.85$  years (Fig. 5.2 (f)). The negative mean air mass lag-times are due to higher  $\text{SF}_6$  mixing ratios (compared to the global mean, which is used as the reference) near the major source regions in the NH and in particular the upper levels of the tropical tropopause region (refer to Sect. 3.3.3). This flight is chosen as an example of  $\text{Br}^{\text{tot}}$  mixing ratios near the LS campaign average (indicated by the gray dotted line in Fig. 5.2 (g)) as well as flight segments within the LMS region with elevated bromine that is the HBrR (indicated by the dark gray shading) and discussed in Sect. 6.2 and onwards.

### 5.3.2 RF08: October 1<sup>st</sup>, 2017

The second example flight outlined here is RF08 on October 1<sup>st</sup>, 2017 with a flight time from 11:59 UTC to 21:51 UTC and probing the remnant air masses of Hurricane Maria (refer to Figs. 5.1 and 5.3) (Pasch et al., 2019). This flight consisted of two different length, but overlapping-rectangular shuttles southwest of Ireland, over the Celtic Sea, and the North Atlantic Ocean. The first clockwise rectangular flight track reached the maximum latitude of  $63.0^\circ\text{N}$  at 14:09 UTC. Towards the end of the flight the minimum latitude of  $45.8^\circ\text{N}$  was reached at approximately 20:38 UTC. The longitude of the rectangular patterns ranged between  $5.0^\circ\text{W}$  and  $8.6^\circ\text{W}$  (Shannon Airport).

The final stretch back to Shannon was flown at the highest altitude during this flight of 14.36 km from 20:40–21:20 UTC. At 18:58 UTC the maximum potential temperature of 398 K was reached which also corresponds to the furthest distance above the WMO tropopause with  $\Delta\Theta = 84\text{ K}$ . During WISE, all flights crossed the tropopause several times as was the case in RF08 shown in Fig. 5.3 (a), with mean lag-times of the air masses ranging from  $-1.1$  to  $1.96$  years (Fig. 5.3 (f)).

Large sections of this flight observed subtropical as well as former tropical UT/TTL air masses. These air masses transported from the tropics with high potential temperature ( $\Theta > 355\text{ K}$ ) and low potential vorticity units ( $< 2\text{ PVU}$ ) are further on called tropical  $\Theta_{\text{high}}/\text{PV}_{\text{low}}$  air (as defined in Sect. 5.2) and are indicated by the light gray shading. This flight is chosen representing the variety of air masses observed during WISE, resulting in elevated  $\text{Br}^{\text{tot}}$  mixing ratios largely due to the abundance of VSLs in the tropical  $\Theta_{\text{high}}/\text{PV}_{\text{low}}$  air. Schäfler et al. (2021) discussed in detail the latter half of the flight between 18:40–20:00 UTC including part of the tropical  $\Theta_{\text{high}}/\text{PV}_{\text{low}}$  region. They considered the different mixing regimes which are distinguished in terms of collocated  $\text{H}_2\text{O}$  and  $\text{O}_3$  lidar data, and show the impacts of a tropopause fold around 19:15 UTC. This flight will be further discussed throughout the text in the next chapter.

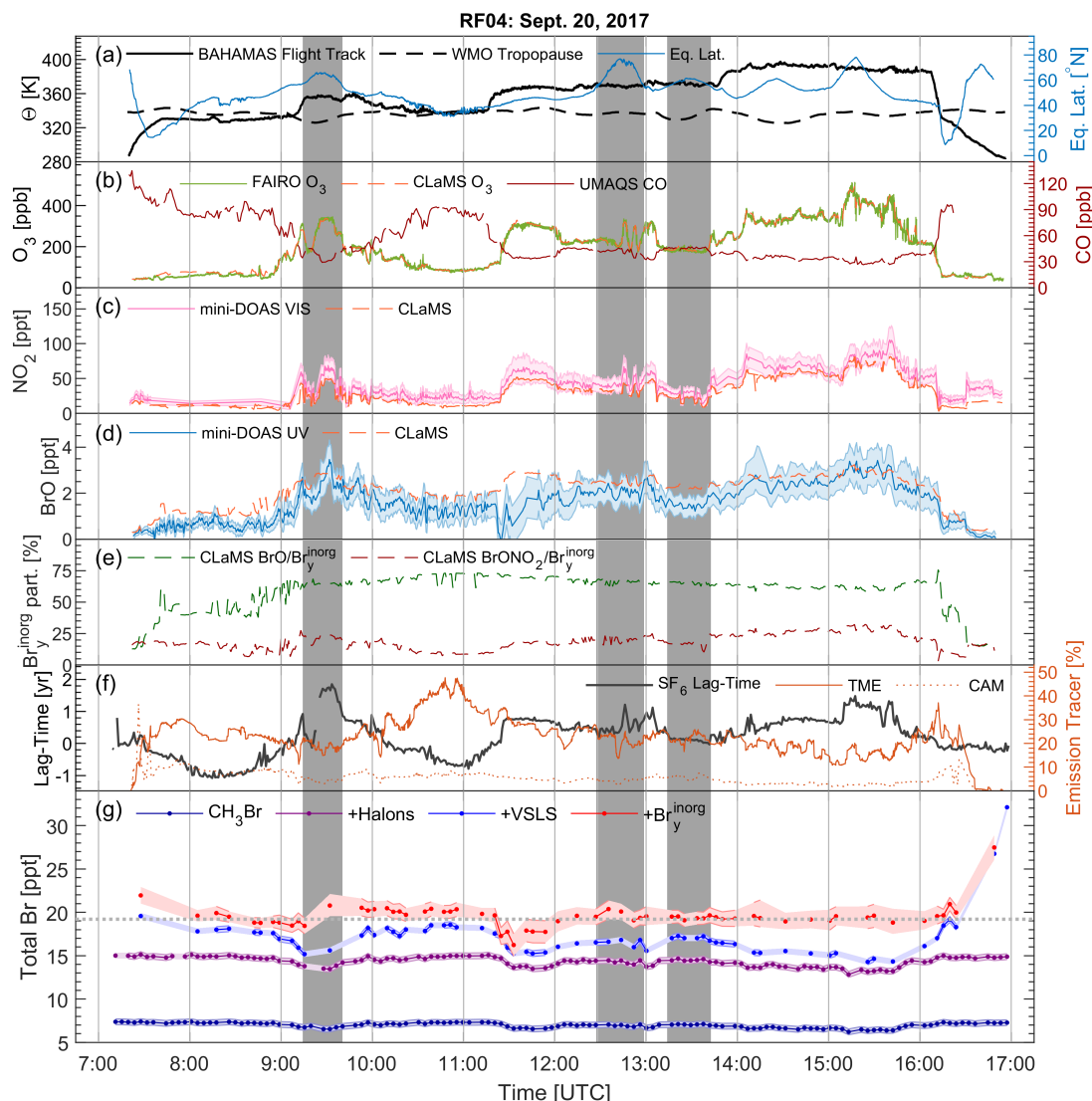


Figure 5.2: Overview of HALO RF04 on Sept. 20, 2017 (blue dashed flight track in Fig. 5.1). The following parameters are displayed in the panels: (a) the flight trajectory (solid black line), WMO tropopause (dashed black line) in potential temperature as well as the equivalent latitude (solid blue line; right axis); (b) FAIRO measured (solid green) and CLaMS modelled (dashed orange)  $O_3$  VMR as well as the UMAQS measured CO (dark red line; right axis); (c) mini-DOAS measured (solid pink) and CLaMS modelled (dashed orange)  $NO_2$  VMR; (d) mini-DOAS measured (solid blue) and CLaMS modelled (dashed orange) BrO VMR; and (e) CLaMS simulated ratios for  $BrO/Br_y^{inorg}$  (dashed green) and  $BrONO_2/Br_y^{inorg}$  (dashed dark red). All trace gas curatins from CLaMS are vertically adjusted as described in Sect. 4.3.3. Further panels include (f) the mean lag-time of air inferred from GhOST-ECD  $SF_6$  measurements (black solid line), as well as the CLaMS emission tracers TME (tropical marine environment) from south eastern Asia (orange solid line; right axis) and CAM (Central America) tracer (dotted orange line; right axis); and (g) GhOST-MS measured  $CH_3Br$  (blue), subsequently added to the halons (purple), brominated VLS (light blue) and inferred  $Br_y^{inorg}$  (red). The gray dotted line in (g) represents the campaign LS weighted average of  $[Br^{tot}] = 19.2 \pm 1.2$  ppt, similar to this flight's average of  $[Br^{tot}] = 19.5 \pm 1.4$  ppt. Dark gray shading indicates flight sections in the HBrR, which is defined in Sect. 5.2 and discussed in Sect. 6.2 and onwards.

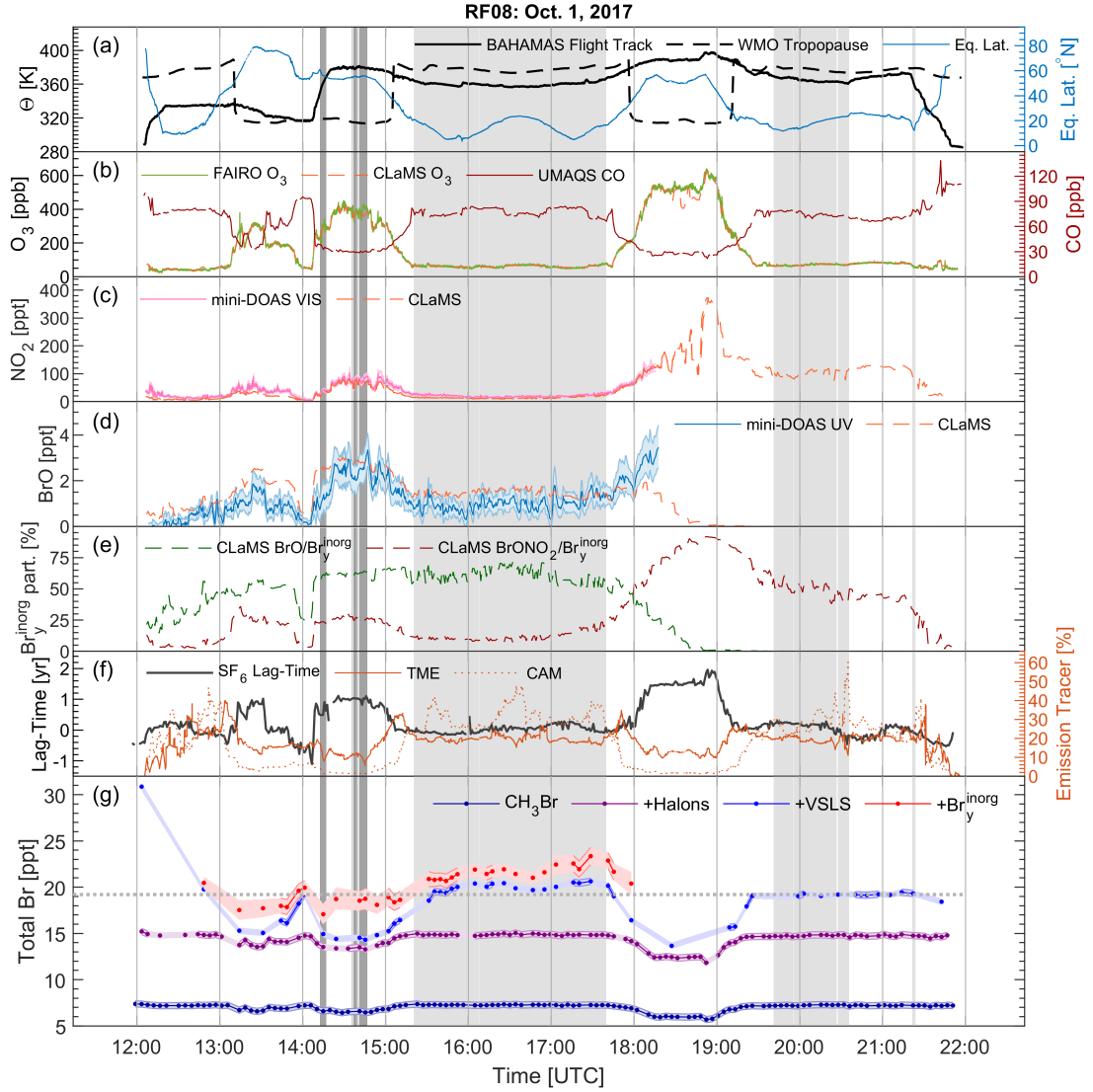


Figure 5.3: Overview of HALO RF08 on Oct. 1, 2017 (yellow dashed flight track in Fig. 5.1). Panels (a–g) are as given in Fig. 5.2. Light gray shading indicates flight segments within the tropical  $\Theta_{\text{high}}/\text{PV}_{\text{low}}$  region and dark gray shading indicates flight segments in the HBrR (defined in Sect. 5.2 and discussed in Sect. 6.2 and onwards). The flight average  $[\text{Br}^{\text{tot}}] = 20.6 \pm 1.7$  ppt, with  $\text{Br}^{\text{tot}}$  VMRs below the LS average (gray dotted line) at the start of the flight and significantly elevated  $\text{Br}^{\text{tot}}$  VMRs in the  $\Theta_{\text{high}}/\text{PV}_{\text{low}}$  flight sections (refer to panel (g)). At  $\text{SZA} > 89^\circ$  mini-DOAS measurements ( $\text{NO}_2$ , BrO, and  $\text{Br}_y^{\text{inorg}}$ ) are unavailable due to the lack in skylight.

## 5.4 Campaign Overview of Total Bromine and Lag-Time

A summary of the weighted mean  $\text{Br}^{\text{tot}}$  of each flight during the WISE campaign can be found in Table 5.1 for all available data. Additionally, the table indicates if any measurements were taken within the two regions discussed throughout this dissertation, i.e., the HBrR and tropical  $\Theta_{\text{high}}/\text{PV}_{\text{low}}$  region (defined in Sect. 5.2). The  $\text{Br}^{\text{tot}}$  average per flight ranges from  $18.3 \pm 1.3$  ppt during RF02 to  $21.0 \pm 0.9$  ppt during RF05. This already indicates some variations of bromine-rich air masses observed throughout the campaign. The detailed results as shown above for the remaining 13 WISE flights can be found in Appendix B.

Table 5.1: Overview of available bromine measurements and weighted mean of  $\text{Br}^{\text{tot}}$  for each flight during the WISE campaign. The uncertainty is the  $1\sigma$  variability of the measurements per flight. Columns 3 and 4 indicate whether the HALO aircraft flew through either the HBrR or  $\Theta_{\text{high}}/\text{PV}_{\text{low}}$  air masses for reference in later discussions. If  $\text{Br}^{\text{tot}}$  is measured within these regions, the flight is marked with a ‘yes’. If  $\text{Br}^{\text{tot}}$  is not measured while flying through the specified air mass, it is indicated by a ‘no’. If no part of the flight was within either region, it is marked with ‘–’.

Research Flight	Weighted Mean $\text{Br}^{\text{tot}}$	HBrR	$\Theta_{\text{high}}/\text{PV}_{\text{low}}$ air
RF02: 13/09/2017	$18.29 \pm 1.26$ ppt	no	–
RF03: 18/09/2017	$19.24 \pm 0.81$ ppt	yes	–
RF04: 20/09/2017	$19.52 \pm 1.36$ ppt	yes	–
RF05: 23/09/2017	$21.02 \pm 0.86$ ppt	yes	–
RF06: 27/09/2017	$19.27 \pm 0.67$ ppt	no	–
RF07: 28/09/2017	missing $\text{Br}^{\text{org}}$ data	no	–
RF08: 01/10/2017	$20.55 \pm 1.74$ ppt	yes	yes
RF09: 04/10/2017	missing $\text{Br}^{\text{org}}$ data	no	–
RF10: 07/10/2017	$18.38 \pm 0.73$ ppt	–	–
RF11: 09/10/2017	$19.98 \pm 0.72$ ppt	yes	–
RF12: 12/10/2017	$18.37 \pm 0.74$ ppt	yes	–
RF13: 14/10/2017	$20.05 \pm 0.60$ ppt	yes	–
RF14: 15/10/2017	missing $\text{Br}^{\text{org}}$ data	–	no
RF15: 19/10/2017	missing $\text{Br}^{\text{org}}$ data	–	–
RF16: 21/10/2017	$19.63 \pm 0.68$ ppt	yes	–

The range of air mass lag-times throughout the WISE campaign, which vary between  $-1.1$  to  $2.6$  years, further reflects the different air masses observed. Figure 5.4, shows the distribution of the mean lag-times throughout the WISE campaign, with an average of  $-0.16 \pm 0.37$  years at the tropopause. The measurements within the HBrR, tropical  $\Theta_{\text{high}}/\text{PV}_{\text{low}}$  region, as well as any UT air with  $\text{Br}_y^{\text{inorg}} > 4$  ppt is indicated by the different colours for reference in later discussions. The latter being an indication of stratospheric air masses intruding into the UT. Typically high  $\text{Br}_y^{\text{inorg}}$  (approximately larger than  $\sim 4$  ppt) is characteristic of the stratospheric mixing ratios but not tropospheric mixing ratios (shown in later chapters for the WISE campaign). Instances where stratospheric  $\text{Br}_y^{\text{inorg}}$  is transported into the UT are discussed in Sect. 6.3.2.

The trend of  $\text{Br}^{\text{tot}}$  VMRs with lag-time is shown in Fig. 5.5 resulting in  $\text{Br}^{\text{tot}} = (-0.11 \pm 0.17 \text{ ppt}) \cdot \text{Lag-Time} [\text{yrs}] + (19.54 \pm 0.12 \text{ ppt})$  where the uncertainties are the 95% confidence interval. This shows that the younger tropospheric air masses observed during WISE may only have a few tenths of a ppt more  $\text{Br}^{\text{tot}}$  than the older stratospheric air masses. However, due to the uncertainty this small trend may in fact not be significant. A larger range of air mass mean lag-times is required for a more definitive trend.

Complementary measurements and insight for a suite of source gases, such as VSLs and halons as well as other gases (e.g., CO,  $\text{N}_2\text{O}$ , and water vapor) and studies of the dynamics, potential vorticity and isentropic mixing of the region have been reported elsewhere for flights during the WISE campaign (e.g., Fix et al. (2019); Kaluza et al. (2019); Kunkel et al. (2019); Hauck et al. (2020); Keber et al. (2020); Schäfler et al. (2021) and Wetzel et al. (2020)). The studies from the WISE campaign defined by the wave-driven isentropic exchange in the extratropical upper stratosphere and lower stratosphere are published in the Atmospheric Chemistry and Physics

(ACP)/ Atmospheric Measurement Techniques (AMT)/ Weather and Climate Dynamics (WCD) inter-journal special issue (refer to [https://www.atmos-chem-phys.net/special\\_issue1061.html](https://www.atmos-chem-phys.net/special_issue1061.html)). The results of this dissertation have likewise been submitted to the ACP special issue WISE.

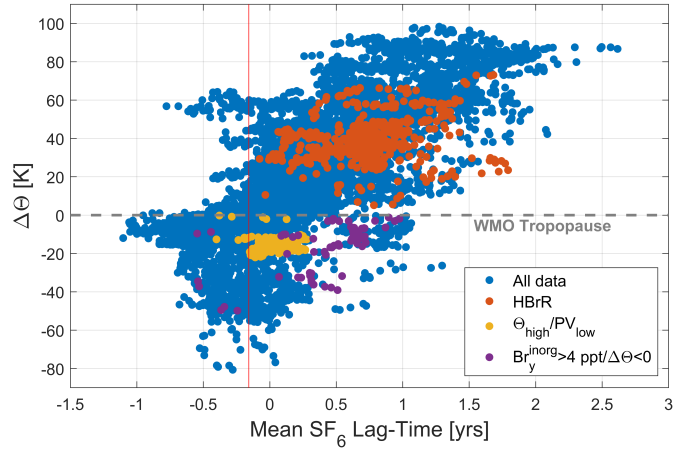


Figure 5.4: Mean lag-time as inferred from GhOST  $\text{SF}_6$  measurements as a function of potential temperature distance from the tropopause ( $\Delta\Theta$ ) in Kelvins. The gray dashed line is the WMO tropopause, and the red line is the campaign average of the mean lag-time within  $\pm 5$  K of the tropopause. All data is shown in blue, while the other coloured dots represent regions discussed throughout this study.

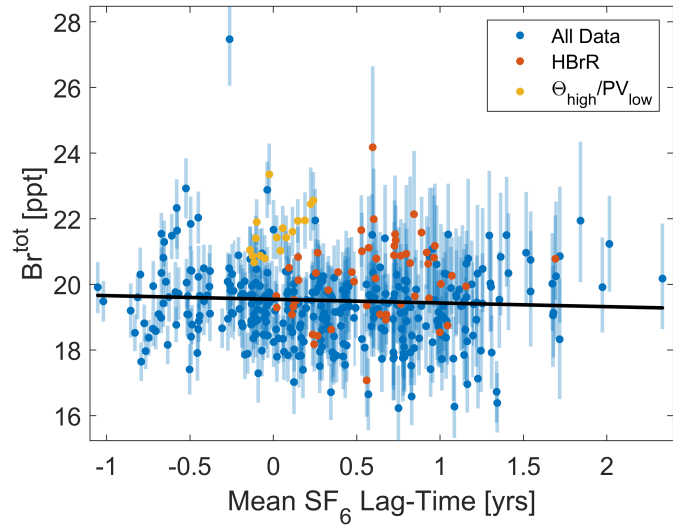


Figure 5.5: Inferred  $\text{Br}^{\text{tot}}$  trend as a function of mean lag-time. All data are shown in blue, while the other coloured dots represent regions discussed throughout this study. The black line is the best fit of all data, indicating the trend of  $\text{Br}^{\text{tot}}$  over the 3+ year time span of air masses probed during WISE. The trend is given by  $\text{Br}^{\text{tot}} = (-0.11 \pm 0.17 \text{ ppt}) \cdot \text{Lag-Time [yrs]} + (19.54 \pm 0.12 \text{ ppt})$  where the uncertainties are the 95% confidence interval.

# Chapter 6

## Results and Discussion

In this chapter measurements of  $\text{Br}^{\text{org}}$ ,  $\text{Br}_y^{\text{inorg}}$ , and  $\text{Br}^{\text{tot}}$  are discussed in relation to distance from the tropopause ( $\Delta\Theta$ ) in Sect. 6.1 and in relation to its geographical distribution within the UTLS in Sect. 6.2. Then in Sect. 6.3 the transport of the air masses into the UTLS in correlation to bromine, as well as the direct influence of two tropical cyclones on bromine are investigated. And lastly in Sect. 6.4 the consequences of bromine on the LS ozone destruction are discussed.

### 6.1 Bromine as a Function of $\Theta$ -Distance from the Tropopause

The UTLS inferred  $\text{Br}^{\text{tot}}$  observed during the WISE campaign in fall of 2017 is first discussed with respect to the potential temperature distance from the local WMO tropopause in Kelvin, defined as  $\Delta\Theta = \Theta - \Theta_{\text{Tropopause}}$ . Figure 6.1 shows the additive break down of the organic ( $\text{CH}_3\text{Br}$  – dark blue, halons – purple, and brominated VLSL – light blue) and inorganic ( $\text{BrO}$  measurements multiplied by the modelled partitioning of  $\text{Br}_y^{\text{inorg}}/\text{BrO}$  – red points) bromine components with  $\Delta\Theta$ . Data points where the SZA is greater than  $89^\circ$  may introduce additional photochemistry-related uncertainties in the  $\text{Br}_y^{\text{inorg}}$  measurements (Kreycky et al., 2013) and are therefore omitted from the following discussion. The majority of  $\text{Br}^{\text{tot}}$  measurements ranged from  $\Delta\Theta = -27$  K below the tropopause (with individual observations down to  $\Delta\Theta = -50$  K) to about  $\Delta\Theta = 88$  K above the WMO tropopause. As the potential temperature range suggests,  $\text{Br}^{\text{tot}}$  measurements were mostly of LMS air during the WISE campaign flights.

The weighted mean  $\text{Br}^{\text{tot}}$  of all tropospheric and stratospheric measurements is  $19.4 \pm 1.3$  ppt (the uncertainty is the  $1\sigma$  variability of the measurements). Excluding the tropospheric measurements, the LS has a slightly smaller weighted average of  $[\text{Br}^{\text{tot}}] = 19.2 \pm 1.2$  ppt, designated by the black solid line in Fig. 6.1. A more rigorous criteria with which to exclude data such as  $\text{SZA} > 85^\circ$ , as well as excluding data based on the CLaMS modelled partitioning of  $\text{BrO}/\text{Br}_y^{\text{inorg}} < 55\%$ , only impacts the  $\text{Br}^{\text{tot}}$  weighted mean by  $\sim 0.1$  ppt decrease.

$\text{Br}^{\text{tot}}$  ranges from 16.2–23.4 ppt with the exception of two larger outliers. One outlier is from large VLSL mixing ratios near the surface and the other at approximately 35 K above the tropopause because of an instability of the  $\text{Br}_y^{\text{inorg}}$  retrieval. The analysis instability of the latter outlier is accounted for with the large uncertainty. The variability of  $\text{Br}^{\text{tot}}$  is partly due to the different origins of the air masses and various inferred mean air mass lag-times which have a spread of more than three years in age.

The LS mean of  $[\text{Br}^{\text{tot}}] = 19.2 \pm 1.2$  ppt within the given uncertainties, is in good agreement with previous data (Engel and Rigby et al. (2018)). The expected  $[\text{Br}^{\text{tot}}] \sim 19.6$  ppt for 2016 (with a range of 19–20 ppt) is primarily based on balloon soundings in the middle stratosphere

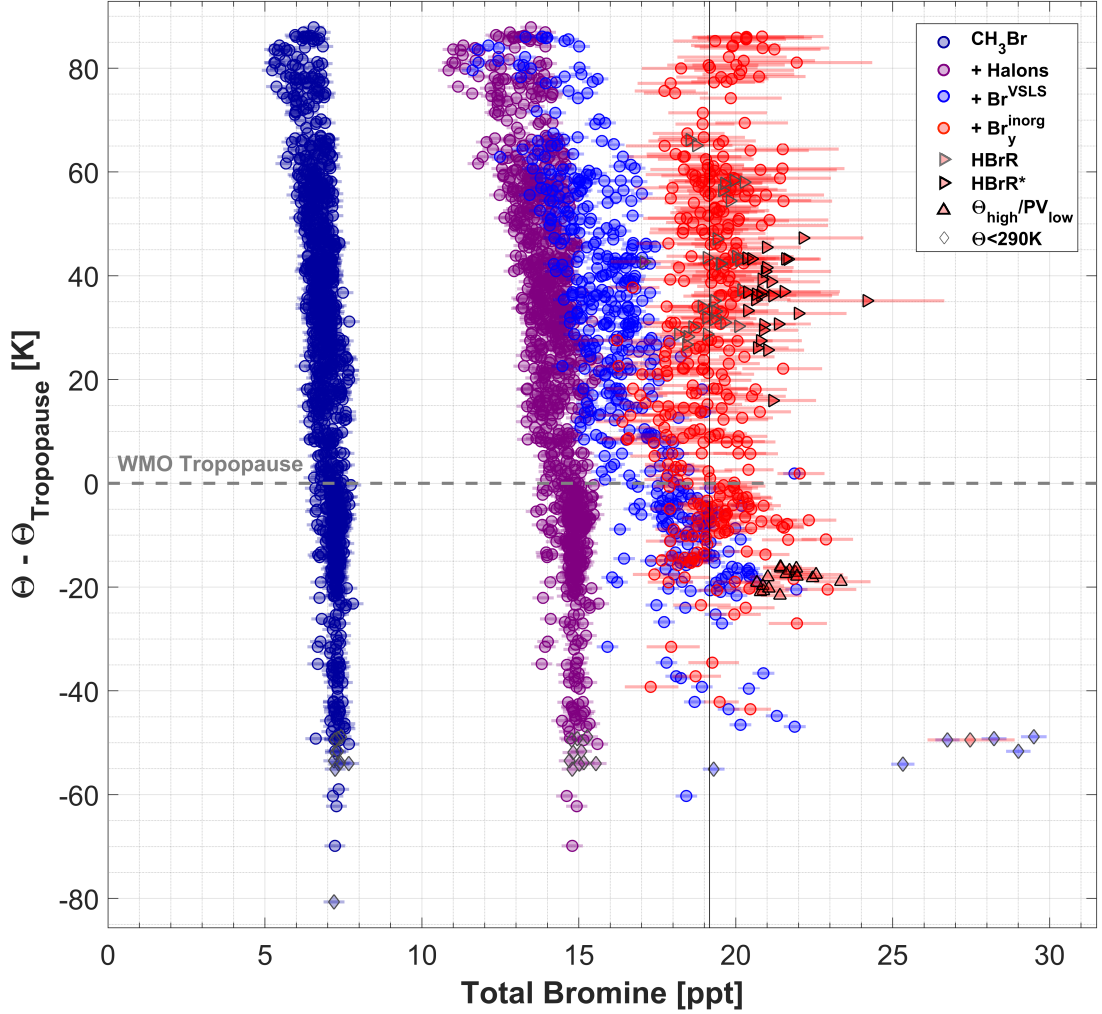


Figure 6.1: Inferred  $\text{Br}^{\text{tot}}$  as a function of potential temperature distance from the WMO tropopause  $\Delta\Theta = \Theta - \Theta_{\text{Tropopause}}$  [K] during the WISE campaign in fall 2017. The  $\text{Br}^{\text{org}}$  species are summed up according to their Br atomicity:  $\text{CH}_3\text{Br}$  (dark blue), four halons (purple) and brominated VSLs (light blue). The inferred  $\text{Br}_y^{\text{inorg}}$  (from BrO measurements multiplied by the  $\text{Br}_y^{\text{inorg}}/\text{BrO}$  partitioning from photochemical modelling) is subsequently added (red) resulting in the UTLS  $\text{Br}^{\text{tot}}$ . The solid black line represents the LS weighted mean  $[\text{Br}^{\text{tot}}] = 19.2 \pm 1.2$  ppt ( $1\sigma$  variability). The  $\text{Br}^{\text{tot}}$  measurements from the high bromine region (HBrR; defined in Sect. 5.2) are indicated by right-pointing (gray and black-edged) triangles with a weighted mean of  $[\text{Br}^{\text{tot}}] = 19.9 \pm 1.2$  ppt. The measurements within the HBrR that are larger than the LS mean by at least  $1\sigma$  are labelled HBrR\* and indicated by the black-edged right-pointing triangles alone with a mean of  $[\text{Br}^{\text{tot}}] = 20.9 \pm 0.8$  ppt. Measurements in the tropical  $\Theta_{\text{high}}/\text{PV}_{\text{low}}$  region (defined in Sect. 5.2) are depicted by the upward-pointing black-edged triangles with a mean of  $[\text{Br}^{\text{tot}}] = 21.6 \pm 0.7$  ppt. Measurements from near the surface during takeoff or landing, i.e.,  $\Theta < 290$  K, are depicted by the gray-edged diamond symbols which include the VSLs mixing ratios  $> 25$  ppt in the lower right corner.

and the reported trend in the stratospheric bromine since the last balloon soundings in 2011. The latter is suspected to now be decreasing by  $-0.15 \pm 0.04$  ppt  $\text{Br yr}^{-1}$  between 2012 and 2016 (refer to Figs. 1.1 and 2.4) (Engel and Rigby et al. (2018)). Furthermore, these results fit well into the expectation based on the total amount of stratospheric  $\text{Br}^{\text{tot}}$  published earlier by previous group members from different measurements (e.g., Dorf et al. (2006a) and Werner et al. (2017)) and others (e.g., Hendrick et al. (2008)).

Within  $\Delta\Theta = \pm 5$  K of the tropopause, the  $\text{Br}^{\text{org}}$ -weighted average VMR (light blue points

in Fig. 6.1) is  $17.8 \pm 1.2$  ppt, with several ppt larger  $\text{Br}^{\text{tot}}$  below the tropopause. Further into the LS at  $\Delta\Theta = 78\text{--}88$  K above the tropopause, the  $\text{Br}^{\text{org}}$  quickly decreases to  $13.5 \pm 1.2$  ppt as the  $\text{Br}^{\text{org}}$  species are being converted to  $\text{Br}_y^{\text{inorg}}$  species. Methyl bromide,  $\text{CH}_3\text{Br}$ , is destroyed with increasing distance into the stratosphere at a slow rate from  $7.1 \pm 0.2$  ppt (with a range of 6.8–7.6 ppt) within  $\Delta\Theta = \pm 5$  K to  $6.1 \pm 0.5$  ppt (5.2–6.8 ppt) measured within  $\Delta\Theta = 78\text{--}88$  K. The tropospheric  $\text{CH}_3\text{Br}$  ( $7.3 \pm 0.2$  ppt) is slightly larger than the 2016 global annually averaged 6.8 ppt as reported in Engel and Rigby et al. (2018), but agrees well with the NH measurements of  $\sim 6.75\text{--}7.75$  ppt from NOAA measurements which show that NH  $\text{CH}_3\text{Br}$  is always larger than the southern hemispheric measurements (Fig. 1-7 of Engel and Rigby et al. (2018)). The four different halons ( $\text{CBrF}_3$  or H-1301,  $\text{CF}_2\text{ClBr}$  or H-1211,  $\text{C}_2\text{Br}_2\text{F}_4$  or H-2402, and  $\text{CBr}_2\text{F}_2$  or H-1202), have a weighted mean mixing ratio of  $7.5 \pm 0.2$  ppt (7.1–7.8 ppt) within  $\Delta\Theta = \pm 5$  K of the tropopause and also decrease slowly to  $6.5 \pm 0.5$  ppt (5.6–7.2 ppt) within  $\Delta\Theta = 78\text{--}88$  K in the LS. The tropospheric halon measurements are in good agreement with the annually averaged tropospheric 7.8 ppt as from 2016 reported by WMO (2018). The larger part of the  $\text{Br}^{\text{org}}$  decrease in the LS is by the VSLS ( $\text{CH}_2\text{Br}_2$ ,  $\text{CHBr}_3$ ,  $\text{CH}_2\text{BrCl}$ ,  $\text{CHBrCl}_2$ , and  $\text{CHBr}_2\text{Cl}$ ) due to their short global lifetime of less than 6 months. Within  $\Delta\Theta = \pm 5$  K, the bromine mixing ratio from the VSLS is  $3.1 \pm 0.9$  ppt (1.7–7.2 ppt), while from  $\Delta\Theta = 78\text{--}88$  K above the tropopause the  $\text{Br}^{\text{VSLS}}$  decreases to  $1.0 \pm 0.3$  ppt (0.7–1.9 ppt). As such, the accumulated decrease of  $\text{Br}^{\text{org}}$  ( $\text{CH}_3\text{Br} + \text{halons} + \text{Br}^{\text{VSLS}}$ ) throughout the LS between the tropopause and  $\Delta\Theta = 88$  K above the tropopause is  $\sim 4.3$  ppt.

Although further into the stratosphere the  $\text{Br}^{\text{org}}$  is destroyed, bromine is converted into  $\text{Br}_y^{\text{inorg}}$  and is compensated for in the  $\text{Br}^{\text{tot}}$  budget. The  $\text{Br}_y^{\text{inorg}}$  near the tropopause ( $\Delta\Theta = \pm 5$  K) is around  $1.5 \pm 0.6$  ppt (with a range of 0.2–3.3 ppt) and increases to  $5.8 \pm 1.8$  ppt (2.9–10.1 ppt) within  $\Delta\Theta = 78\text{--}88$  K above the tropopause. The conversion of  $\sim 4.3$  ppt  $\text{Br}^{\text{org}}$  to  $\text{Br}_y^{\text{inorg}}$  is evident from the  $\text{Br}^{\text{tot}}$  budget, which is approximately constant for the entirety of the air masses probed during the WISE campaign.

The  $\text{Br}^{\text{org}}$  and  $\text{Br}_y^{\text{inorg}}$  measurement distributions of each 10 K layer between  $\Delta\Theta = -60$  K up to  $\Delta\Theta = 90$  K is shown in Fig. 6.2. The decreasing organic bromine trend is mirrored by the increasing inorganic bromine trend higher into the stratosphere. In the LS the weighted mean  $\text{Br}^{\text{tot}}$  ranges from  $18.7 \pm 1.2$  ppt (in the layer  $\Delta\Theta = 5\text{--}15$  K) to  $19.9 \pm 1.2$  ppt (in the layer  $\Delta\Theta = 35\text{--}45$  K). These small changes from the LS  $\text{Br}^{\text{tot}}$  weighted mean of  $19.2 \pm 1.2$  ppt do not result in an obvious trend between the WMO tropopause and  $\Delta\Theta = 88$  K above it but rather hint at air masses of different  $\text{Br}^{\text{tot}}$  mixing ratios, which is discussed in the next sections.

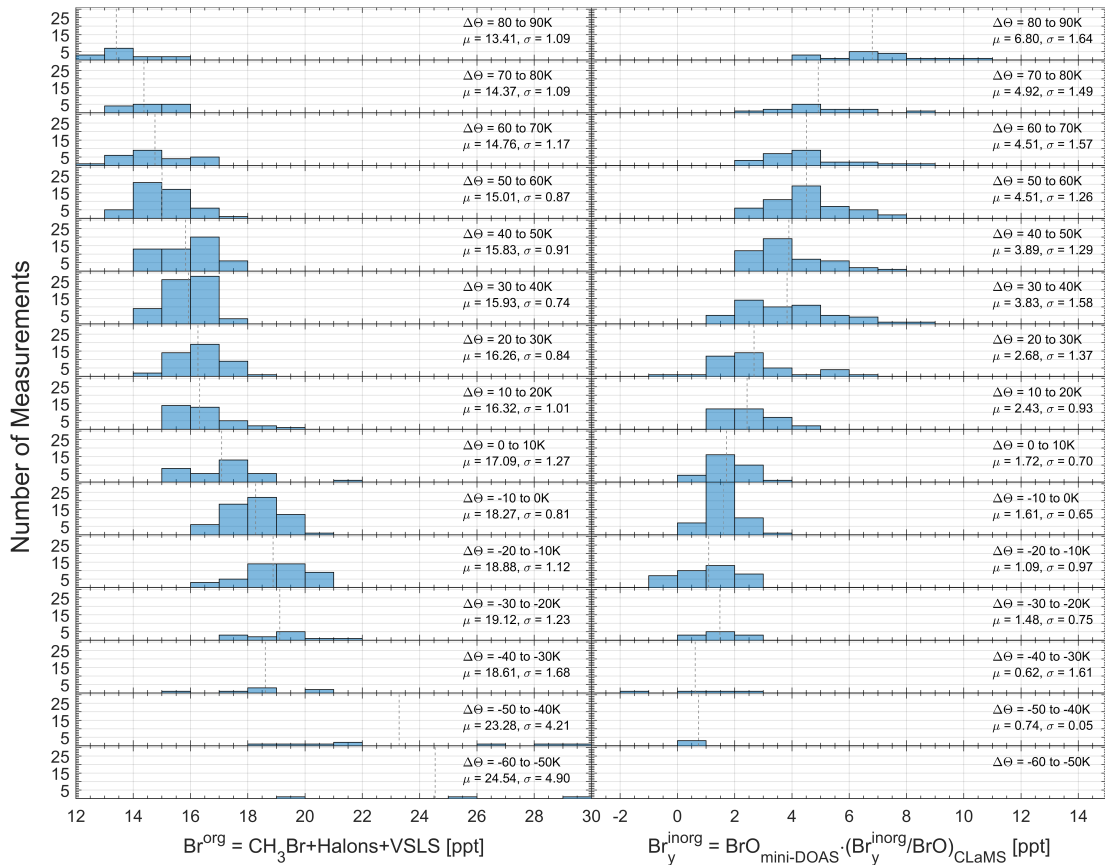


Figure 6.2:  $\text{Br}^{\text{org}}$  and  $\text{Br}_y^{\text{inorg}}$  is displayed separately for each 10 K atmospheric layer with respect to the potential temperature distance from the tropopause ( $\Delta\Theta = 0$ ) and the number of measurements in each layer within the UTLS during WISE. The mean and standard deviation is noted for each layer. Additionally the mean is indicated by the vertical gray dashed line for each layer.

## 6.2 Total Bromine as a Function of Equivalent Latitude

To identify potential source regions and transport pathways of bromine into the LS, various gases measured during the 15 WISE flights are displayed with respect to potential temperature and equivalent latitudes (Butchart and Remsberg, 1986; Pan et al., 2012). The equivalent latitude describes an area of a specific potential vorticity value on a given potential temperature contour (Pan et al., 2012). The VMRs of each trace gas are averaged horizontally in  $5^\circ$  equivalent latitude bins and vertically in 5 K grids to remove the short term atmospheric variability. The campaign mean WMO tropopause varies from  $\Theta \sim 374$  K at low equivalent latitudes to  $\Theta \sim 316$  K at higher equivalent latitudes.

The NH distributions of BrO and  $\text{NO}_2$  VMRs with equivalent latitude and potential temperature are shown in Fig. 6.3. Below the tropopause (black solid line) there are low BrO VMRs present ranging from 0–1.3 ppt. Further into the LMS between  $50\text{--}80^\circ\text{N}$  equivalent latitudes and  $\Theta = 375\text{--}405$  K, BrO increases up to a mean grid VMR of 4.9 ppt, with individual BrO measurements reaching  $\sim 6$  ppt in the LMS. Measurements by Werner et al. (2017) agree well within the uncertainty, reporting BrO mixing ratios down to  $0.5 \pm 0.5$  ppt below the tropical tropopause (at  $\Theta = 355$  K) over the Pacific and mixing ratios between 3–9 ppt in the subtropical LMS.

Similarly to BrO, higher  $\text{NO}_2$  mixing ratios ( $>110$  ppt) are measured in the LMS between

$\Theta = 375\text{--}400$  K in the mid- to high-equivalent latitudes. Lower  $\text{NO}_2$  VMRs down to 10 ppt are measured in the UT particularly directly below the tropopause. In the lower troposphere, there is a slight increase of  $\text{NO}_2$  reaching up to  $\sim 45$  ppt. The majority of the observations from the WISE campaign are over the (clean) marine environment from over the North Atlantic Ocean and Norwegian Sea. These regions do not have substantial anthropogenic  $\text{NO}_x$  sources in the troposphere aside from emissions of ships and aircrafts on selected routes. However, a few shorter flight segments included the occasional overpass of European cities resulting in elevated tropospheric  $\text{NO}_2$ . The UTLS distribution of  $\text{NO}_2$  measurements agree well with the modelled CLaMS  $\text{NO}_2$  (refer to Figs. 5.2 (c) and 5.3 (c) and Appendix B for the remaining flights) as well as with previous measurements (e.g., Hüneke et al. (2017)).

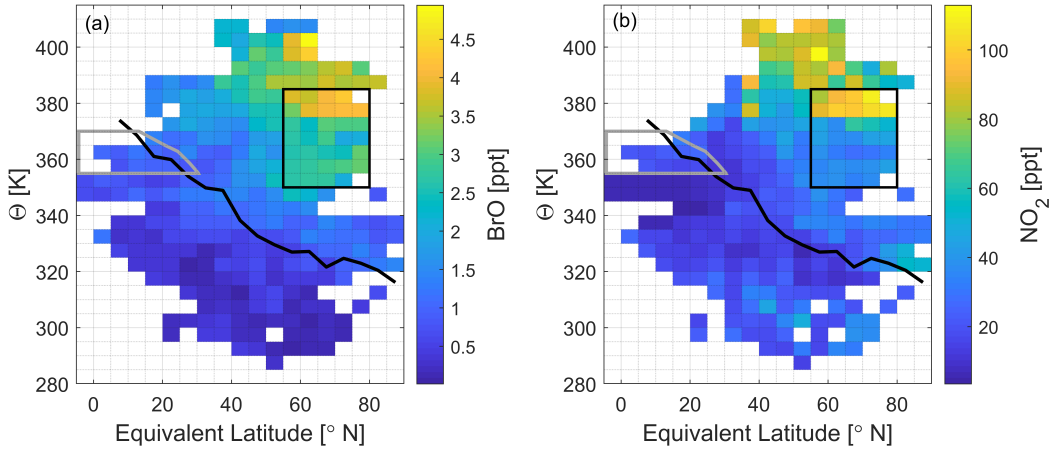


Figure 6.3: BrO VMR (a) and  $\text{NO}_2$  VMR (b) from all 15 flights during the WISE campaign in fall 2017 as a function of the equivalent latitude and potential temperature. The data is binned in  $5^\circ$  grids of equivalent latitude and 5 K grids potential temperatures. The black line is the mean WMO tropopause over the campaign duration. The black box in the LMS from  $55\text{--}80^\circ\text{N}$  and  $350\text{--}385$  K is the high bromine region (HBrR), and the gray outline at  $\Theta > 355$  K and  $\text{PV} < 2$  marks the tropical  $\Theta_{\text{high}}/\text{PV}_{\text{low}}$  region (defined in Sect. 5.2 and discussed throughout the text).

The NH distributions of  $\text{Br}^{\text{org}}$ ,  $\text{Br}_y^{\text{inorg}}$ , and  $\text{Br}^{\text{tot}}$  mixing ratios are shown in Fig. 6.4 (a–c), respectively. Only 11 flights have  $\text{Br}^{\text{org}}$  measurements available, resulting in a sparser distribution. Near the extratropical tropopause (Ex–TP),  $\text{Br}^{\text{org}}$  VMRs are  $\sim 18$  ppt, while the tropical  $\Theta_{\text{high}}/\text{PV}_{\text{low}}$  air mass has higher mean  $\text{Br}^{\text{org}}$  VMRs of up to 20.5 ppt, in agreement with previous studies (e.g., Navarro et al. (2015); Werner et al. (2017); Wales et al. (2018)).

The maximum mean  $\text{Br}_y^{\text{inorg}}$  VMR is 8.3 ppt in the LS at  $\Theta \sim 400$  K and  $\sim 60^\circ\text{N}$  equivalent latitude in contrast to the  $\text{Br}^{\text{org}}$  behaviour. In the troposphere,  $\text{Br}_y^{\text{inorg}}$  ranges from  $\sim 0\text{--}3$  ppt. These results agree well with previous studies, such as Werner et al. (2017) who reported  $7.66 \pm 2.95$  ppt of  $\text{Br}_y^{\text{inorg}}$  measured between  $390\text{--}400$  K in the subtropical LS and reaching down to 0.5 ppt in the tropical troposphere, as well as others (e.g., Wang et al. (2015); Koenig et al. (2017)). A modelling study by Schmidt et al. (2016) reports  $\text{Br}_y^{\text{inorg}}$  mixing ratios at the lower boundary of the TTL and Ex–TP of 3–4 ppt, and daytime BrO mixing ratios of 1–2 ppt, respectively.

Older air (refer to Fig. 6.4 (d)) has generally more  $\text{Br}_y^{\text{inorg}}$  and less  $\text{Br}^{\text{org}}$  present in large part due to the short lifetime of the VSLs. Averaged mean air mass lag-times reach above 2 years around  $\Theta \sim 400$  K and between  $40\text{--}80^\circ\text{N}$  equivalent latitudes. They largely coincide with high  $\text{Br}_y^{\text{inorg}}$  VMRs, with the exception of directly above the tropopause at  $\sim 85^\circ\text{N}$  equivalent latitude. There, a small pocket of older air with lag-times larger than 1 year, has low  $\text{Br}^{\text{org}}$  and  $\text{Br}_y^{\text{inorg}}$ .

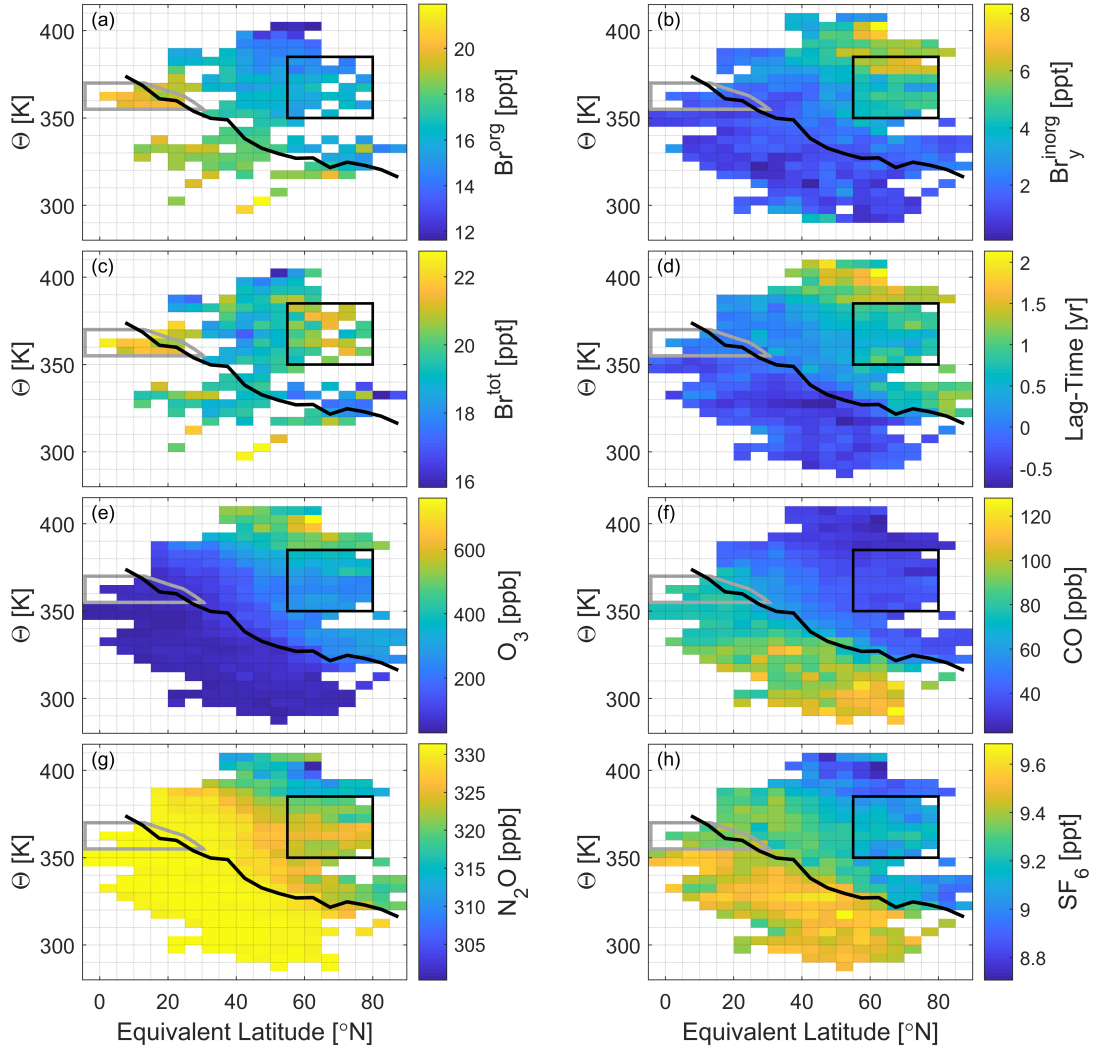


Figure 6.4: The WISE campaign in fall 2017 as a function of equivalent latitude and potential temperature for (a)  $\text{Br}^{\text{org}}$  mixing ratios ( $\text{CH}_3\text{Br} + \text{halons} + \text{VSLS}$ ) from GhOST-MS, (b)  $\text{Br}_y^{\text{inorg}}$  VMR from mini-DOAS BrO scaled by the CLaMS  $\text{BrO}/\text{Br}_y^{\text{inorg}}$  ratio, (c)  $\text{Br}^{\text{tot}}$  VMR, (d) mean air mass lag-time (based on  $\text{SF}_6$  data from GhOST-ECD), (e)  $\text{O}_3$  VMR from FAIRO, (f) CO VMR from UMAQS, (g)  $\text{N}_2\text{O}$  VMR from UMAQS, and (h)  $\text{SF}_6$  VMR from GhOST-ECD. The data is binned in  $5^\circ$  grids of equivalent latitude and 5 K grids potential temperatures. The black line is the mean WMO tropopause over the campaign duration. The HBrR is indicated by the black box in the LMS, and the tropical  $\Theta_{\text{high}}/\text{PV}_{\text{low}}$  region is marked by the gray outline (defined in Sect. 5.2 and discussed throughout the text).

Within  $\pm 5$  K of the tropopause, the mean lag-time is  $-0.16 \pm 0.37$  yrs, with negative averaged lag-times down to  $-0.5$  years in the troposphere (also refer to Fig. 5.4). These negative  $\text{SF}_6$  inferred lag-times are from measurements near the  $\text{SF}_6$  sources (i.e., the NH), where the mixing ratios are larger than the global average which is used as a reference. The relative change of the mean air mass lag-times observed during the WISE campaign, which is greater than 3 years, is more relevant in the context of this study.

The average  $\text{Br}^{\text{tot}}$  mainly varies between 18–20.5 ppt both in the troposphere and stratosphere (refer to Fig. 6.4 (c)), however there are noticeable regions with higher bromine. Of particular interest is the region in the LMS at mid- to high-equivalent latitudes where  $\text{Br}^{\text{tot}}$  local grid means of up to 21.5 ppt are observed. Based on the elevated  $\text{Br}^{\text{tot}}$  mixing ratios observed in the air masses between potential temperatures of  $\Theta = 350\text{--}385$  K and equivalent latitudes of

55–80°N (designated by the black boxes in Fig. 6.4), this atmospheric region is named the high bromine region (HBrR; also outlined in Sect. 5.2). Twelve out of the 15 research flights include flight segments within the HBrR, varying from minutes to several hours, with  $\text{Br}^{\text{tot}}$  measurements available during eight flights namely RF03–05, RF08, RF11–13 and RF16, over eight hours (refer to Table 5.1).

A frequency distribution of inferred  $\text{Br}^{\text{tot}}$  is displayed in Fig. 6.5 (a) showing  $\text{Br}^{\text{tot}}$  in the UTLS (blue) or only in the LS (brown). The distribution of the  $\text{Br}^{\text{tot}}$  in the HBrR (brown) as compared to the rest of the LS excluding the HBrR (blue) shows the characteristically significant increase of bromine in this region (Fig. 6.5 (b)). The HBrR has a weighted mean  $[\text{Br}^{\text{tot}}] = 19.9 \pm 1.2$  ppt and individual measurements ranging from 17.1–24.1 ppt. The HBrR measurements result in the bromine bulge noticeable in Fig. 6.1 around  $\Delta\Theta = \sim 35$  K and are depicted by the right-pointing (gray and black-edged) triangles.

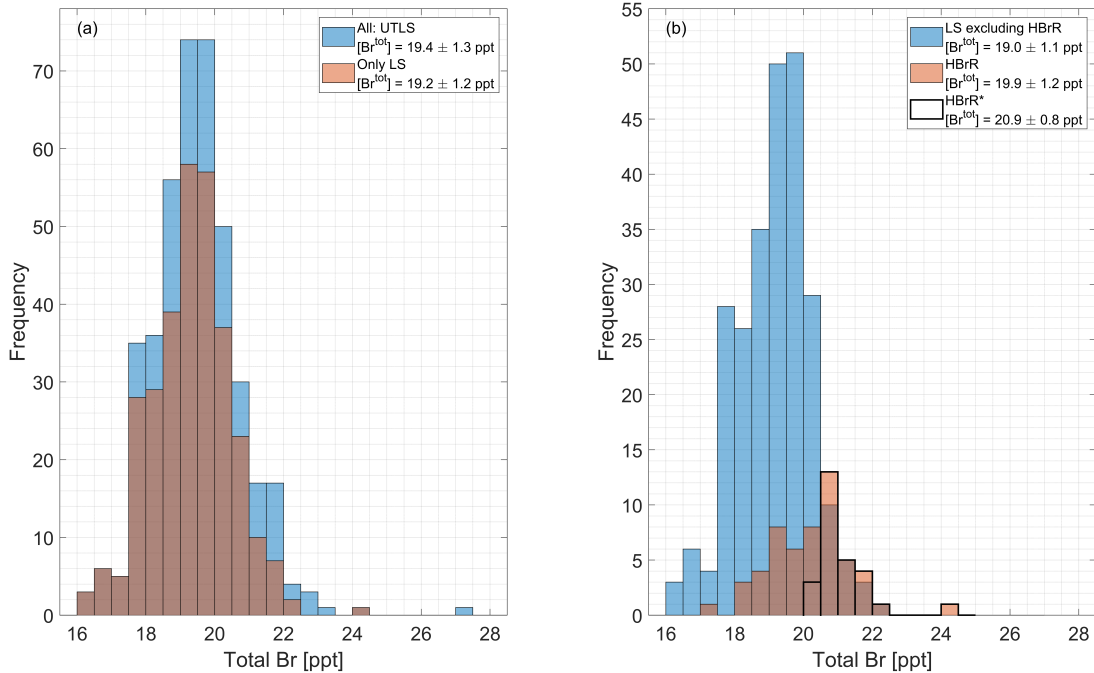


Figure 6.5: Frequency distribution of inferred total  $\text{Br}^{\text{tot}}$ . (a) All data (UTLS) have a weighted mean  $[\text{Br}^{\text{tot}}] = 19.4 \pm 1.3$  ppt (blue) and  $\text{Br}^{\text{tot}}$  measurements from the LS have a weighted mean  $[\text{Br}^{\text{tot}}] = 19.2 \pm 1.2$  ppt (brown). (b) Measurements from the LS excluding the HBrR (defined in Sect. 5.2) have a weighted mean  $[\text{Br}^{\text{tot}}] = 19.0 \pm 1.1$  ppt (blue) while the HBrR (shown in Fig. 6.4 (c) by the black box) has  $[\text{Br}^{\text{tot}}] = 19.9 \pm 1.2$  ppt (brown). HBrR\* (thick black outlined bars) is the distribution of the measurements in the HBrR that are larger than the LS weighted mean by at least  $1\sigma$ . HBrR\* has a weighted mean of  $[\text{Br}^{\text{tot}}] = 20.9 \pm 0.8$  ppt.

Inferred  $\text{Br}^{\text{tot}}$  measurements within the HBrR that are larger than the LS weighted mean by at least  $1\sigma$  are designated by HBrR\*, i.e., only the black-edged right-pointing triangles in Fig. 6.1 and thicker black outlined bars in Fig. 6.5 (b). The HBrR\* has a  $\text{Br}^{\text{tot}}$ -weighted mean of  $20.9 \pm 0.8$  ppt. Here it is important to note that for individual measurements the estimated  $\text{Br}^{\text{tot}}$  in the HBrR air is compatible with the LS average when considering the  $1\sigma$  variability of the measurements. However, the clustering of the independently measured data, in particular of the HBrR\* sample, suggests that the co-added error from the organic and inorganic bromine measurements is actually lower than the stated  $1\sigma$  variability of  $\pm 1.2$  ppt. Therefore, the HBrR is a real and persistent feature over the course of the WISE campaign. HBrR\* then represents the bromine-rich air transported to the LMS which is mixed with air of lower bromine content from rest of the LMS and stratospheric background. The question is therefore what are the

causes of this HBrR\*?

Potential sources include other regions of elevated bromine larger than the LS average, such as from the tropical and extratropical troposphere. These regions have younger (tropospheric) air masses which correspond well with the relatively younger air masses observed within the HBrR (local grid mean lag-times ranging from 0.4–1.2 years) compared to the surrounding air (refer to Fig. 6.4 (d)). The most notable tropospheric region of elevated bromine is observed at high potential temperatures and low potential vorticity ( $\Theta > 355$  K and  $PVU < 2$ ) in the tropics further on named the tropical  $\Theta_{\text{high}}/PV_{\text{low}}$  air (as defined earlier in Sect. 5.2). The observed weighted mean  $Br^{\text{tot}}$  in the tropical  $\Theta_{\text{high}}/PV_{\text{low}}$  region is  $21.6 \pm 0.7$  ppt with individual measurements ranging from 18.2–23.4 ppt. These measurements are from one flight, RF08 (Fig. 5.3), over the course of almost 4 hours. One other flight (RF14) briefly observed tropical  $\Theta_{\text{high}}/PV_{\text{low}}$  air, although  $Br^{\text{tot}}$  data is missing. These tropical UT  $Br^{\text{tot}}$  measurements are largely in agreement with previous experimental and modelling studies (e.g., Wang et al. (2015); Schmidt et al. (2016); Koenig et al. (2017); Werner et al. (2017)). Along with the elevated bromine in the tropical  $\Theta_{\text{high}}/PV_{\text{low}}$  air mass, measurements of the transport tracers (Fig. 6.4 panels (e–h)) suggest that these air masses were eventually entrained by isentropic transport from the tropical  $\Theta_{\text{high}}/PV_{\text{low}}$  air via the shallow branch of the Brewer-Dobson circulation (discussed below) (Levine et al., 2007; Birner and Bönisch, 2011).

Near the Ex–TP, which is defined between equivalent latitudes of 35–55°N and within  $\pm 5$  K of the tropopause in potential temperature (refer to Sect. 5.2), further (slightly) elevated bromine is observed. The  $Br^{\text{tot}}$  here has a weighted mean of  $19.3 \pm 0.9$  ppt and ranging from 17.8–20.5 ppt, indicating a possible second pathway of the air masses entraining bromine into the LMS by STE across the Ex–TP (e.g., Holton et al. (1995); Homeyer and Bowman (2013) and Kunkel et al. (2019)).

A schematic summarizing these regions of elevated  $Br^{\text{tot}}$  and the transport pathways from the UT into the LS is shown in Fig. 6.6. Both possible transport pathways are investigated in the following with observational data from other measured gases (Fig. 6.4) and in Sect. 6.3 by transport modelling. The observational findings are as follows:

- Elevated  $Br^{\text{tot}}$  in the tropical  $\Theta_{\text{high}}/PV_{\text{low}}$  air masses has also been previously observed over the Pacific from 2013 and 2014 (ATTREX, CAST, and CONTRAST campaigns), where inferred  $Br^{\text{tot}}$  mixing ratios were measured to be up to 2 ppt larger in the TTL than expected for the middle stratosphere (Navarro et al., 2015; Werner et al., 2017; Wales et al., 2018). Studies such as by Gettelman et al. (2011); Fueglistaler et al. (2004); Levine et al. (2007) and Ploeger et al. (2013) discuss the transport of air masses into the LMS that primarily stem from the tropics. In this study, this air mass transport is initiated by the Asian monsoon (refer to Sect. 6.3). By the time tropical  $\Theta_{\text{high}}/PV_{\text{low}}$  air reaches the LMS in the mid- to high-latitudes with transport times of  $\sim 0.5$ –1.5 years, significant portions of  $Br^{\text{org}}$  have converted to  $Br_y^{\text{inorg}}$ .
- Mean  $O_3$  mixing ratios from FAIRO range from  $\sim 100$ –760 ppb in the UTLS (Fig. 6.4 (e)). In the LMS, the mixing ratios of  $O_3$  and  $Br_y^{\text{inorg}}$  often have a positive correlation, however it does not include the HBrR. In this region, higher  $Br_y^{\text{inorg}}$  (and  $Br^{\text{org}}$ ) contributes to elevated  $Br^{\text{tot}}$ , while  $O_3$  has a local grid mean minimum of  $\sim 229$  ppb, characteristic for the tropical UT/TTL air. Moreover, below this region around  $\Theta = 330$ –350 K and towards higher equivalent latitudes up to 90°N, there is an increase again of  $[O_3] = 250$ –340 ppb while the  $Br^{\text{tot}}$  decreases. The same trend of higher  $O_3$  is clearly seen above the HBrR due to the prominent ozone layer.

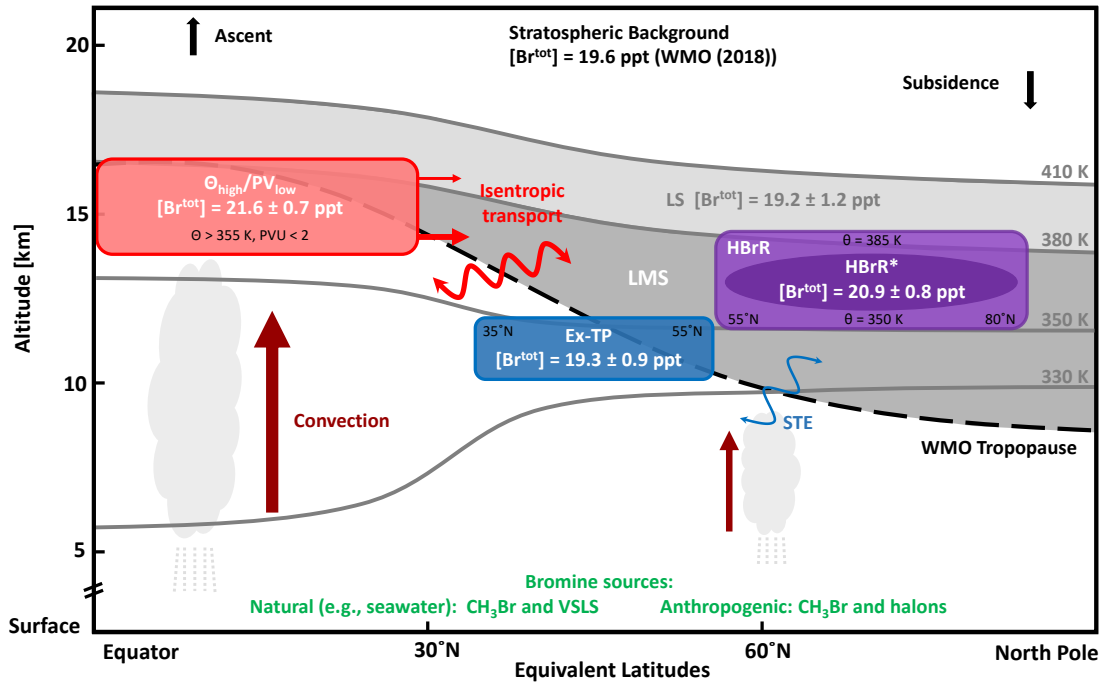


Figure 6.6: Schematic of the bromine transport pathways in the UTLS during the WISE campaign in fall 2017. The black dashed line is the WMO tropopause. The gray lines are constant potential temperature isentropes. The 380 K isentropic marks the upper boundary of the LMS (shaded dark gray region), the 410 K (the WISE campaign upper limit) isentropic marks the upper boundary of the LS (shaded dark + light gray regions). Bromine-rich former tropical UT/TTL air masses are labelled  $\Theta_{\text{high}}/\text{PV}_{\text{low}}$  indicated by the shaded red box. The Ex-TP region is indicated by the shaded blue box. The transport of bromine from these two regions contributes to the elevated bromine in the HBrR marked by the shaded light purple box in the LMS. These three regions are defined in Sect. 5.2. The  $\text{Br}^{\text{tot}}$  inferred measurements larger than the LS mean by more than  $1\sigma$  within the HBrR are indicated by HBrR\* (shaded dark purple oval). The dark red arrows show regions of strong convection transporting surface air masses (from bromine source regions) to the UT. The two main transport pathways of bromine are from the tropical UT/TTL by isentropic transport (light red arrows) and less by STE across the tropopause in the extratropics (blue arrow).  $\text{Br}^{\text{tot}}$  VMRs are from the WISE campaign as discussed in the text.

- $\text{N}_2\text{O}$  is a good transport tracer due to its long lifetime of 114 years (e.g., Ko et al. (2013)). The well-mixed tropospheric air with high  $\text{N}_2\text{O}$  VMRs (measured by UMAQS) from the tropical  $\Theta_{\text{high}}/\text{PV}_{\text{low}}$  region penetrates into the LMS above the tropopause extending to 350–380 K and 50–80°N (Fig. 6.4 (g)), which coincides with the HBrR. Lower  $\text{N}_2\text{O}$  VMRs are seen above and below this region. In the extratropics just above the tropopause,  $\text{N}_2\text{O}$  shows an increasing tropospheric contribution from high to low equivalent latitudes. At equivalent latitudes  $< 40^\circ\text{N}$ ,  $\text{N}_2\text{O}$  shows almost tropospheric mixing ratios of  $[\text{N}_2\text{O}] > 328$  ppb up to  $\Theta = 390$  K.

Von Hobe et al. (2021) also observed elevated  $\text{N}_2\text{O}$  mixing ratios in the tropics associated with the Asian summer monsoon in 2016/2017, extending up to  $\sim 400$  K without sharp discontinuities at the lapse rate tropopause ( $\sim 380$  K) or cold point tropopause ( $\sim 390$  K). This indicates that the tropospheric air masses transported here are not yet mixed with stratospheric air masses. Von Hobe et al. (2021) further concluded that the main outflow of the ‘fast convective chimney’ from the Asian monsoon anticyclonic region in the tropics was below 370 K with slower ascent rates above this as well as a smaller outflow from the chimney up to 380 K, i.e., in direct agreement with the results of this study shown in

Fig. 6.4 (g).

- The SF<sub>6</sub> measurements can also be used for analysis of the transport as it constantly increases and its atmospheric lifetime is in excess of 850 years (e.g., Kovács et al. (2017) and Ray et al. (2017)). As seen in Fig. 6.4 (h), there are higher SF<sub>6</sub> VMRs up to  $\sim 9.6$  ppt below the tropopause and lower VMRs down to  $\sim 8.8$  ppt in the LMS. Similarly to N<sub>2</sub>O, higher SF<sub>6</sub> VMRs (local grid means up to 9.3 ppt) protrude into the LMS at the tropical tropopause and extending to 355–385 K and 50–80°N which overlaps with the HBrR. The dominant transport from the tropical UT/TTL into the LMS has also been previously investigated with SF<sub>6</sub> and CO<sub>2</sub> measurements (Bönisch et al., 2009).
- At the same time, CO (from UMAQS shown in Fig. 6.4 (f)) with a shorter lifetime of 2–3 months (Novelli et al., 1998) has VMRs with an average of [CO] =  $37 \pm 5$  ppb (ranging between 27–44 ppb) in the HBrR. The surrounding LS below and above the HBrR (defined in Sect. 5.2) has an average of  $36 \pm 12$  ppb (influenced by higher CO near the tropopause) and VMRs reaching down to 22 ppb. The CO mixing ratios seen in the HBrR are considerably lower than in the tropical  $\Theta_{\text{high}}/\text{PV}_{\text{low}}$  air (average of [CO] =  $76 \pm 5$  ppb) and Ex-TP (average of [CO] =  $66 \pm 19$  ppb). This indicates that some of the air might not have recently entered the stratosphere (within the past few weeks) but some months (2–3) prior to the measurements.

However, the dominant transport from the tropical  $\Theta_{\text{high}}/\text{PV}_{\text{low}}$  air to the LMS using CO as a tracer was demonstrated in a study by Hoor et al. (2005), the first of its kind. They concluded that transport of air masses to the LMS over Europe in summer and fall is dominated by transport from the tropical UT/TTL up to 55% above  $\Delta\Theta > 25$  K and a slightly smaller contribution from the stratospheric background aged air of up to 45%. The influence from the extratropical troposphere is dominant at the tropopause up to  $\Delta\Theta < 25$  K. The study by Bönisch et al. (2009) came to similar conclusions.

The persistence of the HBrR observed in many flights during the WISE campaign and the already monthly-long presence and respective mixing, generally rules out an origin of this air by some event-like (short-duration) recent transport. That includes events such as by high reaching mesoscale convective systems or any other form of STE process in the extratropics. The wide range of lifetimes of these tracers, the distinct change in VMRs across the Ex-TP, the high VMRs of mainly the two longer lived transport tracers extending from the tropical  $\Theta_{\text{high}}/\text{PV}_{\text{low}}$  region to the HBrR, as well as the low O<sub>3</sub> observed within the HBrR, suggests that the dominant contribution of bromine to the LMS is via the isentropic transport from the tropical UT/TTL rather than by extratropical STE (e.g., Holton et al. (1995); Levine et al. (2007); Fueglistaler et al. (2009); Bönisch et al. (2009); Ploeger et al. (2015)).

Studies such as by Pan et al. (2016) and Garny and Randel (2016) discuss the transport of air from the Asian monsoon that is isentropically entrained into the LMS by shedding of small scale eddies. Another study by Vogel et al. (2016), provides more evidence that portions of the Asian monsoon anticyclone air mass are transported horizontally to the southwest (via eddy shedding) entering the TTL and further into the LMS in late boreal summer.

Other studies discussed a second horizontal transport pathway occurring through filamentation by Rossby wave breaking, east of the anticyclonic event in the extratropics (Vogel et al., 2016). Specific Rossby wave-breaking events producing filaments, irreversibly mix younger tropospheric air into older air of the LMS (e.g., Homeyer and Bowman (2013); Müller et al. (2016) and Kunkel et al. (2019)). The relative contributions of these transport pathways are investigated in the next section.

## 6.3 Modelling of the Transport into the LMS

### 6.3.1 Major Air Mass Origins and Transport Pathways

The transport of air masses from nine atmospheric domains (refer to Fig. 3.6 and Table 3.2) into the northern hemisphere LMS during summer and fall 2017 is simulated by CLaMS using artificial air mass origin tracers. These tracers are released on May 1, 2017 approximately 5 months prior to the WISE campaign (for details refer to Sect. 3.4.1). The advection and mixing processes of the air parcels over the integration time results in the diverse compositions within the UTLS from the various domains of the atmosphere. The fractions of air originating in four of the atmospheric domains most relevant to the discussion here, namely the stratospheric background, tropical troposphere, mid-latitudinal troposphere, and the lower TTL, are shown in Fig. 6.7. All nine domains are shown in Fig. C.1.

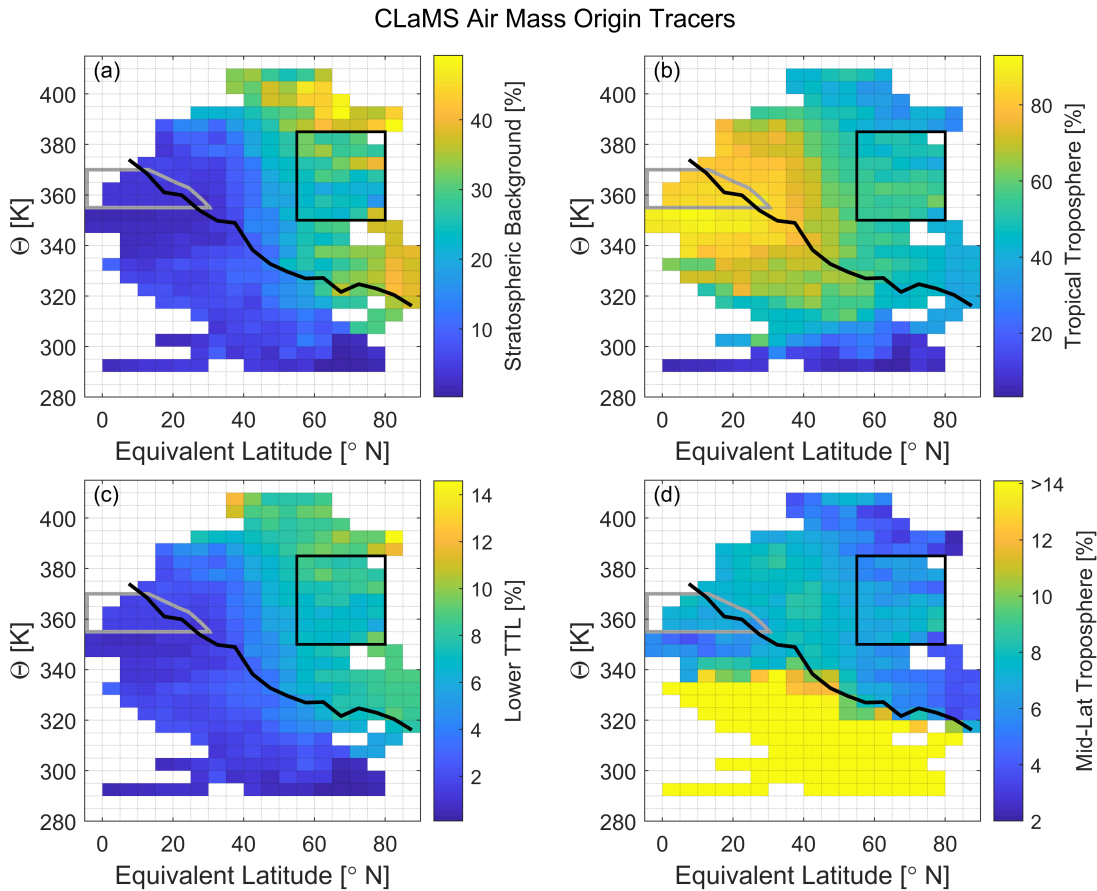


Figure 6.7: CLaMS air mass origin tracers from WISE flights are initialised 5 months prior to the campaign. The atmospheric model is divided into nine domains (refer to Fig. 3.6 and Table 3.2), of which (a) the stratospheric background, (b) the tropical troposphere, (c) the lower TTL ( $\Theta = 355\text{--}380$  K), and (d) the mid-latitudinal troposphere are shown. The remaining domains include the upper TTL ( $\Theta = 380\text{--}425$  K), the tropical pipe, the mid-latitudinal LMS, the polar troposphere, and the polar LMS (shown in Fig. C.1). The black line is the campaign average WMO tropopause, the black box indicates the area of the HBrR and the gray outline marks the tropical  $\Theta_{\text{high}}/PV_{\text{low}}$  region (defined in Sect. 5.2 and discussed in the text).

The HBrR (marked by the black box) is mainly formed by air intruding from the tropics into the LMS. In the HBrR, the fraction of air from the tropical troposphere is 51.2%, while only 27.1% is from the stratospheric background and smaller contributions are from the lower TTL (7.5%), mid-latitudinal LMS (7.0%), the mid-latitudinal troposphere (6.4%) and  $< 1\%$  from the

other domains (refer to Fig. 6.8 (a) and Fig. C.1). The surrounding air masses in the LS below and above the HBrR range from equivalent latitudes  $55-80^{\circ}\text{N}$  between the tropopause and  $\Theta = 350\text{ K}$  and  $\Theta > 385\text{ K}$  (Sect. 5.2). In contrast, these surrounding LS air masses consist of 42.6% from the tropical troposphere, 36.1% from the stratospheric background, 8.3% from the lower TTL, 7.0% from the lower TTL, 7.0% from the mid-latitudinal LMS, 5.2% from the mid-latitudinal troposphere and  $< 1\%$  from the other domains (refer to Fig. 6.8 (b)).

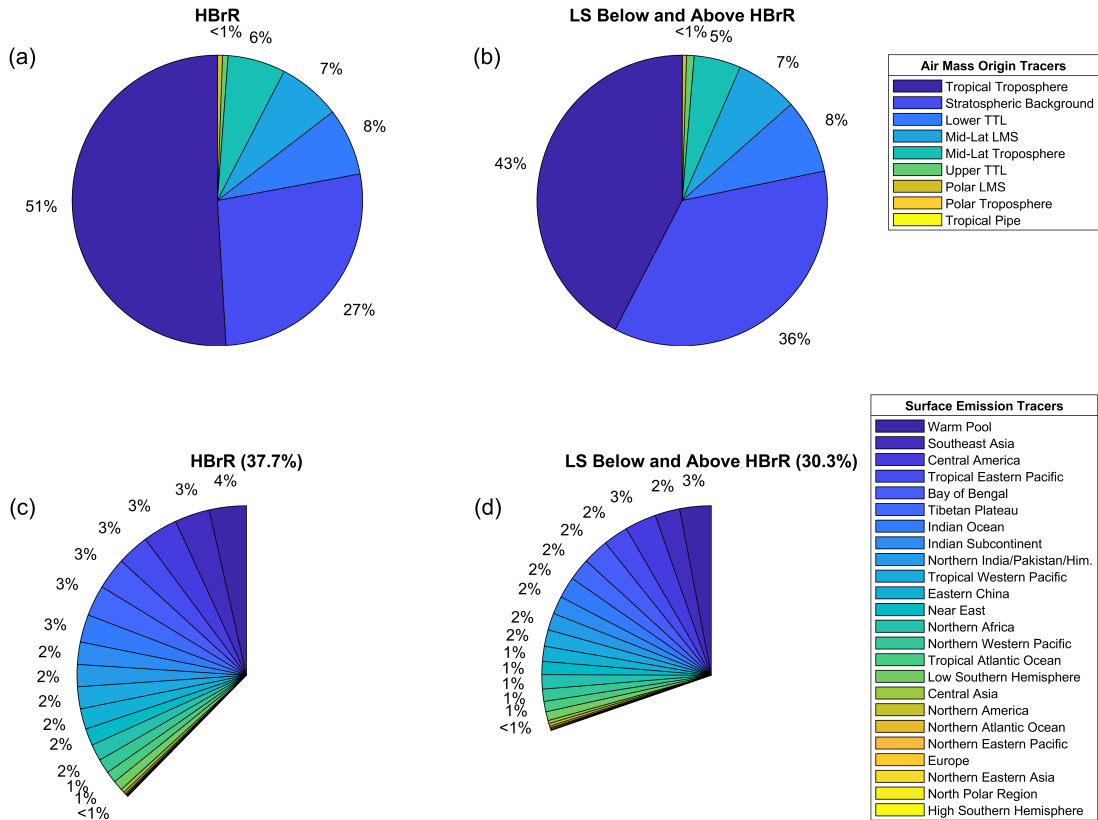


Figure 6.8: Relative contribution of the air mass origin (a–b) and surface emission (c–d) tracers during the WISE campaign obtained from CLaMS simulations. Contributions to the HBrR are shown in panels (a) and (c), while the contribution to the LS air below and above the HBrR are displayed in panels (b) and (d). Refer to Sect. 5.2 for the HBrR and LS below and above the HBrR definitions.

Over the five months of CLaMS simulation prior to the HALO measurements, the influx of tropospheric air to the HBrR is almost 10% more than the surrounding LS below and above the HBrR. In particular, this increase of tropical tropospheric air (+8.6%) and to a lesser degree extratropical tropospheric air (+1.2%) in the HBrR, results in additional transport of air masses from these source domains in the tropics (and extratropics) with elevated bromine compared to the surrounding LS (as shown in Fig. 6.6). Figure 6.6 illustrates the relative contributions of tropical  $\Theta_{\text{high}}/\text{PV}_{\text{low}}$  air vs the Ex–TP region transporting bromine to the LMS.

The elevated bromine observed in the tropical  $\Theta_{\text{high}}/\text{PV}_{\text{low}}$  region has fractions up to 92% (with a mean of  $84 \pm 2\%$ ) originating from the tropical troposphere (Fig. 6.7 (b)). As expected, air from the tropical troposphere is transported into the tropical  $\Theta_{\text{high}}/\text{PV}_{\text{low}}$  region during the last 5 months caused by the large scale circulation. Therefore, the elevated bromine measured in the tropical  $\Theta_{\text{high}}/\text{PV}_{\text{low}}$  air during WISE can be categorized as air masses largely originating in the tropical troposphere as defined by the CLaMS origin tracer.

Yan et al. (2019) also showed similar contributions of  $> 40\%$  of air from the tropical UT (i.e.,

$\sim 18\%$  from the 350–360 K layer and  $\sim 22\%$  of the air from the 370–380 K layer) is transported into the NH LS with only small air mass fractions continuing vertically into the tropical pipe. These findings are further in agreement with those of von Hobe et al. (2021).

Large bromine sources, particularly the VSLS, are from tropical marine regions mainly in coastal areas (refer to Sect. 2.3). Therefore, surface emission tracers (for details see Sect. 3.4.1) from CLaMS simulations are also used to infer the contribution of young air masses ( $< 5$  months) from different surface regions in the UTLS (refer to Fig. 3.7). The surface emission regions with the largest contributions to the HBrR during the WISE campaign flights are grouped into larger regions and shown in Fig. 6.9 (refer to Fig. C.2 for all 24 surface emission tracers individually). The sum of the surface emission tracers (i.e., air masses younger than  $\sim 5$  months) contributing to the HBrR account for 37.7% of the air. The LS region below and above the HBrR, both recently received less surface air with an average of 30.3%. The larger tropical tropospheric air contribution to the HBrR as compared to the LS air below and above the HBrR seen in the air mass origin tracers above, is largely from recent surface emissions rather than the free troposphere.

The CLaMS simulations show that surface emissions from the Asian monsoon region (AMR; consisting of NIN, IND, INO, TIB, ECH, and BoB refer to Fig. 3.7) and from its tropical adjacent region (TAR; consisting of Wpool, SEA, TWP, TEP, NAF and Neast) have the strongest contributions of the various surface emission tracers to the LMS in late boreal summer and early fall. Maximum contributions of the AMR and TAR surface emissions are delivered to equivalent latitudes between 25–45°N and from  $\Theta = 325\text{--}390$  K (displayed in Fig. 6.9 (a–b)). The individual surface emission tracers contributing to the HBrR and surrounding LS can be found in Fig. 6.8 (c–d), Fig. C.2, and Table 6.1. The AMR accounts for 14.8% of the air in the HBrR, while air originating from the TAR contributes a further 15.2%. Together the AMR and TAR make up 30.0% of the air reaching the HBrR, which is 79.8% of all surface air masses. The LS air masses below and above the HBrR (shown in Fig. 6.8 (d)) receive  $\sim 1/4$  less surface (younger) air overall compared to the HBrR mainly because the AMR and the TAR contribute less, i.e., by a 3.4% and 3.3% decrease, respectively.

This is in general agreement with results of CLaMS simulations using a previous version of surface emission tracers for 2012 and 2008 (Vogel et al., 2016, 2019). They found that the northern Ex–LS in boreal summer was flooded with young air masses from the region of the Asian monsoon and from the tropical Pacific. Their results showed that 44–48% of young subtropical boundary layer air reached 360 K and 35–41% reached 380 K in the NH LMS. Similarly, the Asian monsoon air masses impacting the LMS was observed by Müller et al. (2016). Furthermore, this feature is in general agreement with findings of Orbe et al. (2015), who showed that in boreal summer and fall  $\sim 20\text{--}30\%$  of the mid-litudinal LMS air at 100 mb originated from the Asian planetary boundary layer (slightly further north than defined here). The outflow of the AMR into the LMS (shown in Fig. 6.9 (a)) has also been recently shown in a study by von Hobe et al. (2021), i.e., the main outflow is below 370 K with weaker outflow up to 380 K. Levine et al. (2007) previously concluded that vertical transport from the tropical boundary layer into the TTL is strongest over the Indian Ocean, Indonesia and the western Pacific Ocean through convection. They further concluded that the main outflow ( $\sim 95\%$ ) of air from the TTL is transported below 380 K into the LMS while only  $\sim 5\%$  is transported further upwards into the stratospheric ‘overworld’.

Recent CLaMS simulations by Hauck et al. (2020) show that in the NH the air mass fraction contribution to the LMS through extratropical transport is largest in September–November compared to other seasons. In Fall, these air mass fractions reach above 75% directly above the tropopause in the mid- to high-latitudes with increasing tropical contributions towards higher

### CLaMS Surface Emission Tracers

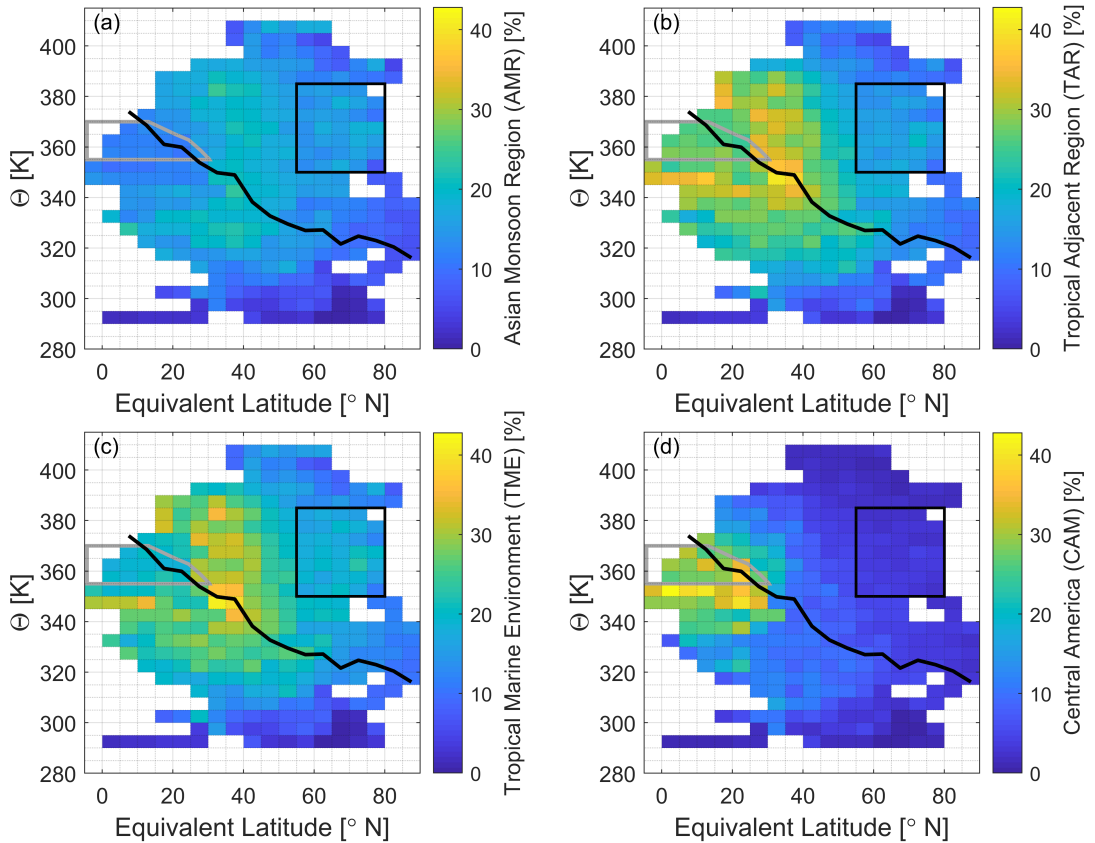


Figure 6.9: Relative contribution of surface emission tracers during the WISE campaign. The individual surface regions are displayed in Fig. 3.7. The Asian monsoon anticyclone region (AMR) consisting of NIN, IND, INO, TIB, ECH, and BoB (panel (a)), as well as its tropical adjacent region (TAR) consisting of Wpool, SEA, TWP, TEP, NAF, and Neast (panel (b)), contribute the largest fractions of surface air to the LMS HBrR (indicated by the black box). A subgroup of these regions, the tropical marine environment (TME consisting of SEA, Wpool, BoB, INO, TWP, and TEP) is particularly significant due to elevated emissions of brominated VSLs (panel (c)). The contribution from Central America (CAM) to the tropical UT/TTL is largely due to vertical transport of air by hurricanes Maria and Ophelia in fall 2017 (panel (d)). The gray outline marks the tropical  $\Theta_{\text{high}}/\text{PV}_{\text{low}}$  region and the black line is the average WMO tropopause. The HBrR and tropical  $\Theta_{\text{high}}/\text{PV}_{\text{low}}$  region are defined in Sect. 5.2.

potential temperatures. By 400 K, generally more than 50% of the air masses in the NH have a tropical origin with larger fractions towards the pole as the extratropical air entrained peaks at 50% around 50°N at 400 K (Hauck et al., 2020). Vogel et al. (2016) found that from July to October the contribution of younger air transported into the Ex-LS over northern Europe by quasi-horizontal transport travelling eastward along the subtropical jet, became increasingly stronger in the later months.

A subgroup of regions from the AMR and its TAR belonging to the tropical marine environment (TME; defined by SEA, Wpool, BoB, INO, TWP and TEP) in south eastern Asia alone contributes 17.7% to the HBrR, which is 47.0% of the air masses from the surface. The maximum TME air mass contribution is in the subtropics to mid-latitudes between 25–55°N from  $\Theta = 320\text{--}390$  K, but air masses with elevated TME contributions extend to the tropical UT/TTL and the HBrR (shown in Fig. 6.9 (c)). This suggests entrainment of TME air masses crossing the tropopause around 30°N with further transport to the tropical UT/TTL and LMS, in agreement with findings of Orbe et al. (2015). The surrounding LS air masses below and

Table 6.1: The air mass contributions of the CLaMS surface emission tracers (see Fig. 3.7) in the HBrR and the LS below and above the HBrR are listed (also shown in Fig. 6.8 (c–d), respectively). For the definitions of the HBrR in the LMS and the surrounding LS below and above the HBrR refer to Sect. 5.2.

<b>Emission Tracer (<math>\Omega_i</math>)</b>	<b>HBrR</b>	<b>LS Below &amp; Above</b>
Warm Pool (Wpool)	3.54 %	2.99 %
Southeast Asia (SEA)	3.34 %	2.37 %
Central America (CAM)	3.30 %	3.00 %
Tropical Eastern Pacific (TEP)	3.06 %	2.38 %
Bay of Bengal (BoB)	3.03 %	2.47 %
Tibetan Plateau (TIB)	2.95 %	2.11 %
Indian Ocean (INO)	2.63 %	2.03 %
Indian Subcontinent (IND)	2.14 %	1.71 %
Northern India/Pakistan/Him. (NIN)	2.11 %	1.62 %
Tropical Western Pacific (TWP)	2.10 %	1.57 %
Eastern China (ECH)	1.95 %	1.44 %
Near East (Neast)	1.61 %	1.25 %
Northern Africa (NAF)	1.59 %	1.37 %
Northern Western Pacific (NWP)	1.37 %	1.17 %
Tropical Atlantic Ocean (TAO)	1.10 %	0.99 %
Low Southern Hemisphere (LSH)	0.96 %	0.85 %
Central Asia (Casia)	0.37 %	0.29 %
Northern America (NAM)	0.20 %	0.25 %
Northern Atlantic Ocean (NAO)	0.11 %	0.16 %
Northern Eastern Pacific (NEP)	0.091 %	0.10 %
Europe (EUR)	0.068 %	0.10 %
Northern Eastern Asia (NEA)	0.046 %	0.051 %
North Polar Region (NPO)	0.0063 %	0.0092 %
High Southern Hemisphere (HSH)	0.0029 %	0.0022 %
<b>All Surface Regions (<math>\Omega = \sum_{i=1}^{n=24} \Omega_i</math>)</b>	<b>37.65 %</b>	<b>30.28 %</b>
<b>Asian Monsoon Region (AMR):</b> NIN+IND+INO+TIB+ECH+BoB	14.81 %	11.37 %
<b>Tropical Adjacent Region (TAR):</b> Wpool+SEA+TWP+TEP+NAF+Neast	15.23 %	11.93 %
<b>Tropical Marine Environment (TME):</b> SEA+Wpool+BoB+INO+TWP+TEP	17.69 %	13.81 %

above the HBrR receive 13.8% from the TME, i.e., a 3.9% decrease compared to the HBrR. The variations of the weighted average TME contribution per flight in the UTLS range from 17.3–30.1% at flight altitude with an average of  $21.5 \pm 3.5\%$  per flight (examples are shown in Figs. 5.2–5.3 (f) and Figs. 6.10–6.11 (b)).

The increased contribution of younger surface air to the HBrR compared to the surrounding air masses below and above, has a significant influence on the trace gas composition. In particular, considering the majority of the surface air masses are transported from regions with large biological activity and known bromine sources (Engel and Rigby et al. (2018)), i.e., the

tropical marine environment below the Asian monsoon anticyclone and its tropical adjacent regions. This highlights the influence of surface emissions from south eastern Asia on pollutants and in particular bromine in the northern LMS during boreal fall. Adcock et al. (2021) observed enhanced  $\text{CH}_3\text{Br}$  VMRs (up to 9 ppt) as well as  $\text{CH}_2\text{Br}_2$  and H-1211 VMRs (up to about 0.75 ppt and 3.5 ppt, respectively, which are comparable to Engel and Rigby et al. (2018)) at the tropopause in the Asian monsoon region in 2016/2017.

Using ERA-Interim reanalysis from the years 2007/2008, Vogel et al. (2019) showed that surface air masses can reach 360 K in a few days and reach 360–460 K within a few months in the tropics and subtropics due to the strong vertical spiral uplift associated with the Asian monsoon anticyclone including its tropical adjacent air masses. Using data from the ERA-Interim/ERA5 reanalysis, Bucci et al. (2020) showed that air from Nepal in July/August 2017 could rise through convection in the Asian monsoon anticyclone region with transport times up to the tropopause ( $> 17$  km) to be  $\sim 20$  days. Similarly, Ashfold et al. (2012) reported a transport time of less than 15 days of air masses from the West Pacific boundary layer ( $< 1$  km) up to the lower TTL ( $\sim 15$  km). The fast transport (on the order of days) from the Asian tropical planetary boundary layer to the TTL allows even the short-lived trace substances from the south east Asian region to reach the UTLS (Orbe et al., 2015).

The impact of maritime boundary sources to the chemical composition of the Asian monsoon anticyclone by convective uplift in tropical cyclones in the western Pacific is discussed by e.g., Vogel et al. (2014) and Li et al. (2017, 2021). A study by Liang et al. (2014) concludes that deep convection transports  $\sim 7.8$ – $8.4$  ppt brominated VSLs from the marine boundary layer of the tropical Indian Ocean, tropical western Pacific warm pool, and the Pacific coast of Mexico to the LMS. These brominated VSLs are half in the form of source gases and the other half consisting of product gases such as  $\text{BrO}$ , and only  $\sim 10\%$  is lost due to wet scavenging after transport to the tropopause. Hamer et al. (2020) similarly found that inside the convective system,  $\text{CHBr}_3$  (one of the VSLs) is the most efficient bromine gas to reach the UT as  $> 85\%$  of surface  $\text{CHBr}_3$  is transported to the tropical UT. In addition, they simulated the presence of 1 ppt of  $\text{Br}_y^{\text{inorg}}$  outside the convective system near Borneo, i.e., in the tropical adjacent regions, while inside the convection system  $\text{Br}_y^{\text{inorg}}$  ( $< 0.1$  ppt) is almost completely depleted due to washout. Therefore the solubility of the gases and local surrounding conditions may also impact the delivery to the TTL and finally the Ex-LS. This is partially when tropospheric  $\text{O}_3$  is low and prevents the soluble forms of bromine from reacting and converting to insoluble inorganic compounds.

### 6.3.2 Contributions to UTLS Bromine from Recent Tropical Cyclones

Interestingly, emissions from Central America (CAM) also contributed to elevated  $\text{Br}^{\text{tot}}$  in the tropical  $\Theta_{\text{high}}/\text{PV}_{\text{low}}$  air masses with maximum CAM air mass fractions around  $\Theta \sim 345$ – $370$  K during WISE (shown in Fig. 6.9 (d)). There are two flights with particularly large air mass fractions from CAM emissions observed during the campaign: RF08 and RF14 (discussed below) with flight segments in and around the tropical  $\Theta_{\text{high}}/\text{PV}_{\text{low}}$  region. During both flights, remnant air masses of two mesoscale convective systems from the Central American tropics were probed.

In reference for the following discussion, the average contribution of emissions from CAM in the UTLS (excluding RF08 and RF14) per flight is  $6.3\% \pm 4.6\%$  and ranging from 4.3–8.9%. Generally, the largest CAM emissions during the WISE campaign are seen in the tropical  $\Theta_{\text{high}}/\text{PV}_{\text{low}}$  air with a strong decrease in the LS. The average CAM emissions in the LS per flight is  $4.4\% \pm 2.5\%$  (ranging from 2.7–6.2%), with the exception of air masses during RF14 and RF15 (a third unique flight discussed below). Although larger CAM air mass fractions contribute to elevated bromine in the tropical  $\Theta_{\text{high}}/\text{PV}_{\text{low}}$  air, the HBrR only has 3.3% of the

air fraction from CAM similarly to the LMS which has mostly low CAM air mass contributions.

The first flight with long segments of large contributions of air masses from CAM was RF08 on Oct. 1, 2017 (Fig. 5.3 (f)). This flight, off the coast of Ireland over the Atlantic Ocean (up to 15.0°W), encountered the remnants of Hurricane Maria which had transitioned into an extratropical cyclone and later dissipated on Oct. 2, 2017 (Pasch et al., 2019). The average CAM surface air fraction along the flight track is  $18.0 \pm 13.0\%$  with the maximum contribution reaching 60.6% at 20:35 UTC at  $\Theta = 361$  K and  $\Delta\Theta = -11$  K (Fig. 5.3 (a) and (f)). However, sections with increased CAM air mass fractions only reached the UT while the two flight sections breaching into the LS have low CAM emissions. This low pressure system transported surface air with increased CAM air mass fractions (25–45%), CO, and N<sub>2</sub>O to the UT, bringing with it more brominated VSLs up to  $[\text{Br}^{\text{VSLs}}] = 5.8$  ppt at 17:29 UTC shown in Fig. 5.3 (g). This coincides with flight sections in the tropical  $\Theta_{\text{high}}/\text{PV}_{\text{low}}$  air, indicated by the light gray shaded sections. These flight segments in the tropical  $\Theta_{\text{high}}/\text{PV}_{\text{low}}$  air with large CAM air mass fractions additionally have  $\sim 20\%$  of the air mass fraction from the TME, resulting in the UT  $[\text{Br}^{\text{org}}] > 19.2$  ppt and  $[\text{Br}^{\text{tot}}] = 20.7\text{--}23.4$  ppt between 15:35–17:41 UTC. The combination of relatively large air mass fractions from CAM and TME in the tropical  $\Theta_{\text{high}}/\text{PV}_{\text{low}}$  air, results in some of the most-bromine-rich air observed during WISE. Even though the tropospheric portions of the flight had elevated CAM emissions, the LS sections only have an average CAM air mass fraction of  $3.1 \pm 1.7\%$  and low  $\text{Br}^{\text{tot}}$ . The LS  $\text{Br}^{\text{tot}}$  ranged from 17.1–18.9 ppt, which is below the LS average as indicated by the gray dotted line in Fig. 5.3 (g) between 13:14–15:07 UTC. Only a short flight segment reached the HBrR, which is indicated by the dark gray shading in Fig. 5.3 between 14:13–14:47 UTC, where the CAM air mass fraction is low ( $\sim 1\%$ ) while the TME air mass fraction is still  $\sim 11\%$ . Further insights of the flight segment between 18:40–20:00 UTC is analyzed in the study by Schäfler et al. (2021). They use H<sub>2</sub>O and O<sub>3</sub> lidar data as tropospheric and stratospheric tracers to discuss three mixing regimes near the tropopause fold indicating the presence of different air masses.

A second tropical cyclone encountered during WISE was Hurricane Ophelia. It made landfall over Ireland on Oct. 16, 2017 and dissipated over Norway on Oct. 18, 2017. It rapidly transported tropical air from Central America to Europe (Stewart, 2018). This is verified from data collected during RF14 on the Oct. 15, 2017 (Fig. 6.10, see also Fig. B.11 for other complementary data). A large influence of surface emission tracers from CAM is present with a flight average of  $23.3 \pm 11.8\%$  (shown in Fig. 6.10 (b)). The initial flight section between  $\sim 13:20\text{--}15:00$  UTC is just below  $\Theta = 355$  K with low equivalent latitudes (down to  $\sim 6^\circ\text{S}$ ), indicating these air masses were recently tropical air masses with large CAM air mass fractions. Unlike RF08, the transport of larger CAM air masses into the LMS is observed in this low pressure system. The average influence from CAM air masses in the LMS flight segments is  $20.8 \pm 5.4\%$ . These are the largest influxes of CAM emissions into the LMS detected during the WISE campaign.

Although RF14 does not have  $\text{Br}^{\text{org}}$  data available, the variability of air masses probed by the aircraft in the LMS is noticeable in  $\text{Br}_y^{\text{inorg}}$  mixing ratios. For example, between 16:04–16:58 UTC the aircraft flew in the LMS (up to  $\Delta\Theta = 16.7$  K) and relatively low  $[\text{Br}_y^{\text{inorg}}] = 2.2 \pm 0.4$  ppt was observed with high CAM emissions of  $22.3\% \pm 4.1\%$  and TME air fractions of  $30.4 \pm 2.5\%$ . Shortly after, between 17:04–17:46 UTC the aircraft cruised in the UT (around  $\Delta\Theta = -10.1 \pm 5.6$  K), where elevated  $\text{Br}_y^{\text{inorg}}$  was observed which reached up to 7.8 ppt. During this event low CO mixing ratios, low CAM emissions ( $6.2 \pm 2.0\%$ ), only slightly lower TME air mass fractions ( $24.2 \pm 3.6\%$ ) and large air mass lag-times (up to 1 yr old) were observed in the UT. This event characterizes an intrusion of stratospheric air into the UT with  $\text{Br}_y^{\text{inorg}} > 4$  ppt (indicated by the light blue shading).

A third flight, RF15 on Oct. 19, 2017 (Fig. 6.11, see also Fig. B.12 for other complementary

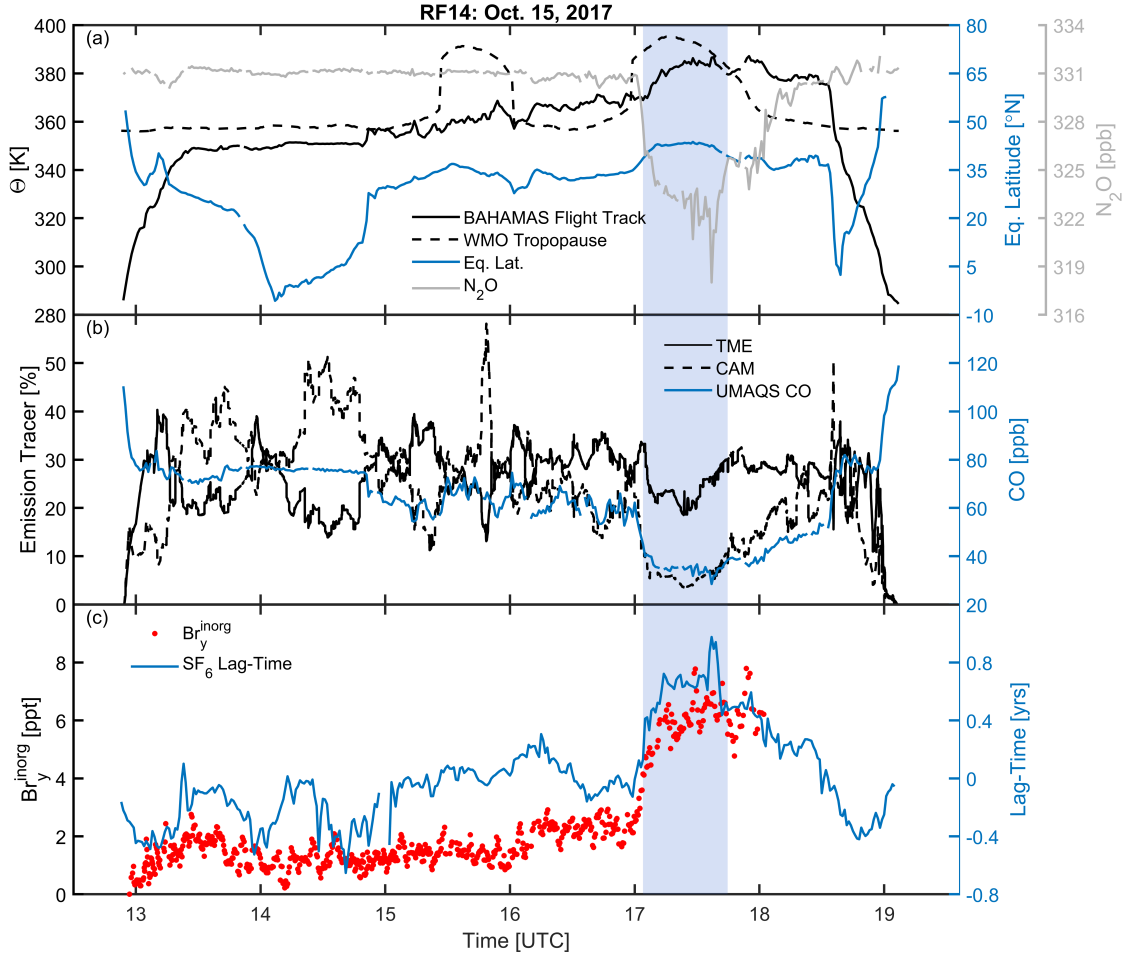


Figure 6.10: RF14 on Oct. 15, 2017 indicates recent air mass surface emissions from the tropical marine environment (TME) in south eastern Asia as well as elevated emissions from Central America (CAM) from a tropical cyclone. Panel (a) shows the potential temperature of the flight track and WMO tropopause (black solid and dashed lines, respectively; left axis) along with the equivalent latitude and  $\text{N}_2\text{O}$  VMR (blue and gray lines, respectively; right axis). Panel (b) shows the air mass fraction at flight altitude from the TME and CAM emission tracers (black solid and dashed lines, respectively; left axis), as well as the CO VMR (blue; right axis). Panel (c) shows the  $\text{Br}_y^{\text{inorg}}$  mixing ratio (red points; left axis) where available along with the air mass lag-time (blue line; right axis). The light blue shading indicates  $\text{Br}_y^{\text{inorg}} > 4$  ppt in the UT, i.e.,  $\Delta\Theta < 0$  K.

data), around Ireland and the UK likely still captured the former air masses from Hurricane Ophelia. The air of this flight is also characterized by a slightly elevated CAM influence in the LS mainly with an average surface emission of  $8.9 \pm 4.1\%$  at extratropical equivalent latitudes (Fig. 6.11 (b)). Only partial  $\text{Br}^{\text{org}}$  data is available including  $\text{CH}_3\text{Br}$  and the halons, both of which have slightly elevated VMRs in the LMS (Fig. 6.11 (c)).  $\text{CH}_3\text{Br}$  VMRs up to 7.8 ppt and the bromine mixing ratios from the halons up to 8.1 ppt are observed in the LMS ( $\Delta\Theta = 22$  K) with elevated CAM emissions around 14% (and TME air mass fractions  $\sim 27\%$ ). A similar event is again detected during the initial ascent between 09:25–09:38 UTC (light blue shading) after passing through a small stratospheric intrusion. Elevated  $\text{Br}_y^{\text{inorg}} > 4$  ppt and up to 9.2 ppt was observed in the UT around  $\Delta\Theta = -33.2 \pm 3.6$  K, while air mass fractions from CAM emissions were low ( $7.4 \pm 1.9\%$ ) and TME emissions were around  $25.0 \pm 1.8\%$ .

In summary, the synoptic-weather-system-related contributions from the CAM region evidently may directly impact observed UTLS bromine. The CLaMS simulations indicate the

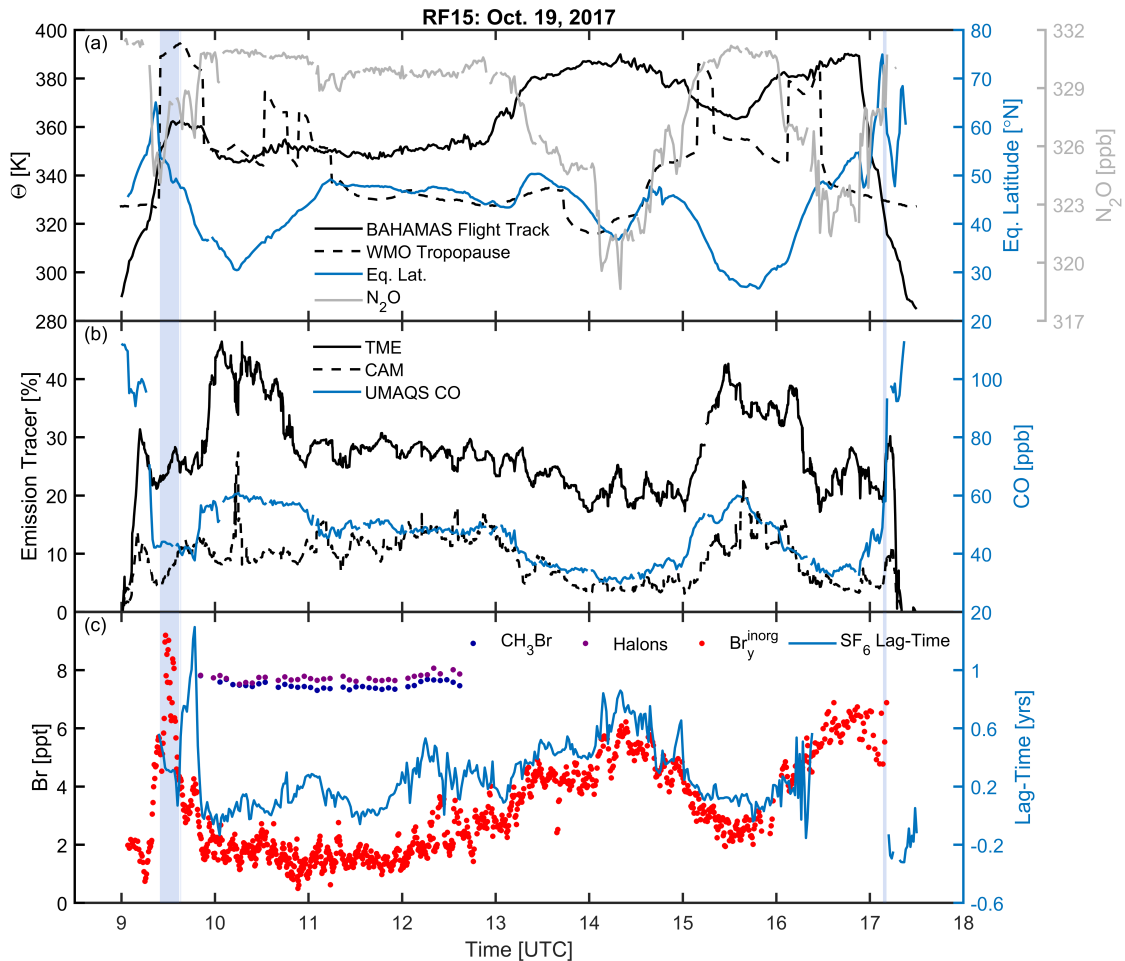


Figure 6.11: RF15 on Oct. 19, 2017 indicates recent air mass surface emissions from the tropical marine environment (TME) in south eastern Asia as well as elevated emissions from Central America (CAM) from remnants of a tropical cyclone. Panels (a–c) are given as in Fig. 6.10. Panel (c) additionally shows the individual bromine mixing ratios of CH<sub>3</sub>Br (dark blue points) and the halons (purple points) with limited availability.

variety of different air masses influencing the WISE campaign observations. Near to tropical tropopause, high CAM air mass fractions (through rapid vertical transport by hurricanes), as well as high TME air mass fractions (uplifted by local convection associated with the Asian summer monsoon) are observed. These large CAM and TME contributions result in significantly elevated  $Br^{tot}$  in the former tropical  $\Theta_{high}/PV_{low}$  air as seen during RF08. However, in the LMS there are lower air mass fractions from CAM but still relatively high TME contributions which also result in elevated  $Br^{tot}$ , i.e., the HBrR during eight flights. Additionally, the two events with higher  $Br_y^{inorg}$  observed in the UT (shaded light blue sections in Fig. 6.10–6.11), with comparatively lower CAM emissions and low CO and  $N_2O$  mixing ratios, are of particular interest. These events may indicate that air from the LMS intruded into the UT by recent STE events, which is discussed in a recent study by Kunkel et al. (2019).

## 6.4 Consequences for LMS Ozone

The isentropic transport of bromine-enriched air from the tropical UT/TTL into the LMS likely has a significant impact on ozone. In the HBrR, the average  $O_3$  measured is  $301 \pm 69$  ppb and ranging from 153–524 ppb (refer to Fig. 6.4 (e)). The LS below and above the HBrR has an

average of  $404 \pm 169$  ppb (range 73–791 ppb), largely due to the significant increase of  $O_3$  further into the ozone layer of the stratosphere that extends into the upper area of the HBrR. However, in the HBrR, lower  $O_3$  VMRs are measured with a slight increase again below the HBrR.

In order to investigate the influence of elevated bromine on the Ex–LS ozone, three simulations were conducted using the 3–D global TOMCAT model with 22 months integration time (refer to Sect. 3.4.2). The Base run was initialised with constant bromine VMRs (19.6 ppt from the Ex–TP region) along the entire tropopause. Run 1 and 2 each had elevated bromine boundary conditions in the tropical UT in addition to the Ex–TP boundary conditions from the Base run (refer to Table 3.3). The run 1 and 2 were initialised with additional  $[Br^{tot}]$  of 1.2 ppt and 2.1 ppt, respectively in the tropical UT. The Base run  $Br^{tot}$  as well as the relative changes of bromine in run 1 and 2 are displayed in Fig. 6.12. The increase in run 1 is mainly due to increased  $Br_y^{inorg}$ , while the increase of  $Br^{tot}$  in run 2 is largely due to additional  $Br^{VLSL}$ .

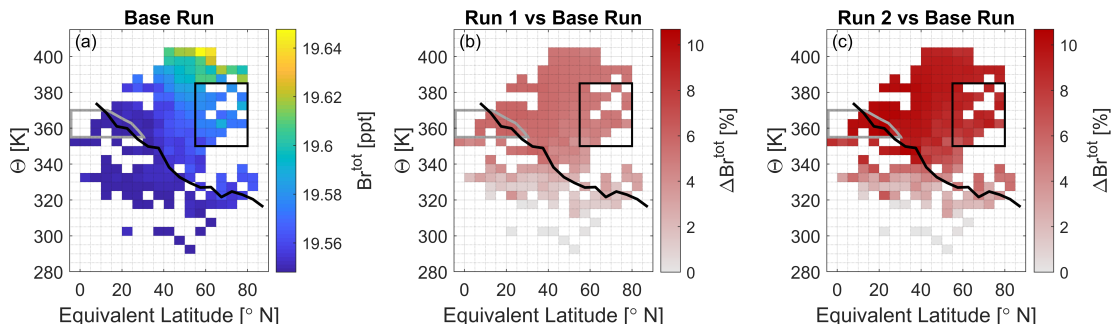


Figure 6.12: TOMCAT model results of  $Br^{tot}$  distributed in the UTLS during the WISE campaign period. Panel (a) displays the  $Br^{tot}$  VMR distribution from the Base run (refer to Table 3.3). Panel (b) shows the relative percentage change  $\Delta Br^{tot}$  between run 1 and the Base run. Panel (c) displays the relative  $\Delta Br^{tot}$  change between run 2 and the Base run. The black line is the campaign average WMO tropopause, the black box in the LMS is the HBrR and the gray outline marks the tropical  $\Theta_{high}/PV_{low}$  region (the latter two regions are defined in Sect. 5.2).

These increases of bromine in the tropical UT lead to additional destruction of ozone in the LMS. This can be used as a measure of the ozone sensitivity due to transport of bromine-enriched air from the tropical  $\Theta_{high}/PV_{low}$  region into the LS by the lower branch of the Brewer Dobson circulation. The TOMCAT  $O_3$  VMR distribution over the NH from the Base run is shown in Fig. 6.13 (a) ranging between  $\sim 30$ –840 ppb. TOMCAT  $O_3$  VMRs are comparable to the measured FAIRO  $O_3$  mixing ratios which range between  $\sim 30$ –760 ppb (Fig. 6.4 (e)). The maximum  $O_3$  simulated by TOMCAT in the Base run is larger than in situ measurements, in part due to the Base run excluding the elevated bromine that is observed.

The relative changes of TOMCAT simulated  $O_3$  between the Base run and either run 1 or 2 are displayed in Fig. 6.13 (b–c), respectively. The impact of increasing tropical UT bromine (run 1), leads to a  $5.0 \pm 0.4\%$  increase in  $Br^{tot}$  in the HBrR (refer to Fig. 6.12 (b)) as compared to the Base run which results in an  $O_3$  loss of  $-2.5 \pm 0.2\%$  (Fig. 6.13 (b)). Run 2 leads to an  $8.7 \pm 0.7\%$  increase in  $Br^{tot}$  in the HBrR (refer to Fig. 6.12 (c)) as compared to the Base run which results in an  $O_3$  loss of  $-2.8 \pm 0.2\%$  (refer to Fig. 6.13 (c)). In the HBrR, the change of absolute  $O_3$  mixing ratios is  $-6.6 \pm 1.1$  ppb (run 1) and  $-7.4 \pm 1.4$  ppb (run 2) (not shown). The decrease of ozone is not strictly linear with increasing  $Br^{tot}$ , partially due to the nature of the increased bromine ( $Br^{VLSL}$  vs  $Br_y^{inorg}$ ) differing between run 1 and 2, as well as other feedback loops such as via lower stratospheric  $HO_x$  species.

The average relative  $O_3$  loss throughout the whole LS is  $-2.6 \pm 0.6\%$  and  $-2.7 \pm 0.4\%$  for run 1 and 2, respectively. However, the largest relative  $O_3$  decreases are observed along the tropical tropopause where there is the largest bromine enhancement due to the initialisation.

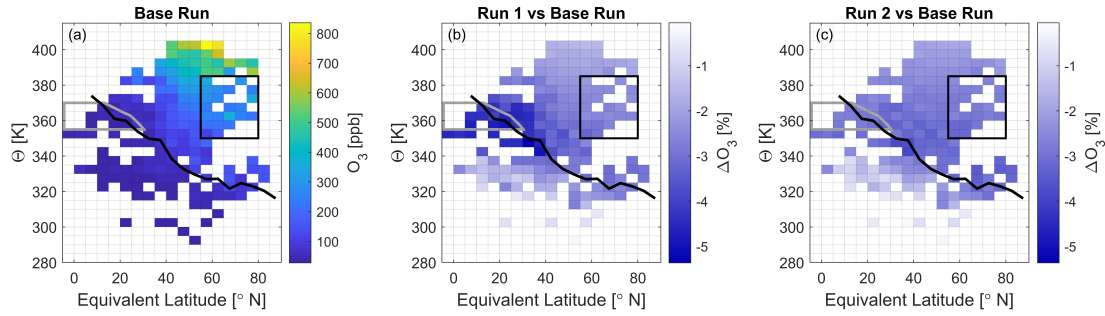


Figure 6.13: TOMCAT model results of  $O_3$  impacted by elevated  $Br^{tot}$  in the UTLS. Panel (a) displays the  $O_3$  VMR distribution from the Base run using constant  $Br^{tot}$  boundary conditions along the tropopause (refer to Table 3.3). Panel (b) shows the relative percentage change  $\Delta O_3$  between run 1 with elevated  $Br^{tot}$  in the tropical UT and the Base run. Panel (c) displays the relative change  $\Delta O_3$  between run 2 and the Base run. The black line is the campaign average WMO tropopause, the black box in the LMS is the HBrR and the gray outline marks the tropical  $\Theta_{high}/PV_{low}$  region.

Further significant decreases of  $O_3$  extend to the mid-latitudes along the tropopause. Run 1 has the strongest ozone decreases up to  $-5.4\%$  along the tropopause in the tropics up to  $40^\circ N$  equivalent latitude (in comparison to the Base Run). As the bromine increase in run 1 is mainly in the form of  $Br_y^{inorg}$ , this shows the efficiency and immediate destruction of ozone by  $Br_y^{inorg}$ . Run 2 has a maximum  $O_3$  decrease of  $-3.9\%$  however the strongest decreases are not near the tropical tropopause but rather along the mid-latitude tropopause. As the bromine increase of run 2 is largely in the form of  $Br^{VLSL}$ , ozone is not immediately destroyed because of the time delay for the conversion of  $Br^{org}$  to  $Br_y^{inorg}$ . Although the ozone destruction is not as strong near the source of increased bromine in run 2 compared to run 1, the ozone decrease extends further towards the pole just above the tropopause. This is reflected in the average  $O_3$  decrease along the entire tropopause. The relative ozone change along the tropopause up to  $\Delta\Theta < 20$  K results in  $-3.2 \pm 0.6\%$  and  $-3.0 \pm 0.4\%$  for run 1 and 2, respectively. These tropopause average changes are from available data between equivalent latitudes of  $22-88^\circ N$ , i.e., largely excluding the tropics.

A study by Hossaini et al. (2015) analysed the impact of increasing VLSL (bromine, chlorine and iodine) on  $O_3$  in the global LS. The model results showed LS  $O_3$  decreases of 4–12%, where the brominated VLSL account for  $\sim 85\%$  of the  $O_3$  destruction. In the TTL, the  $O_3$  impact just below 100 hPa was  $\sim -8\%$  with stronger decreases towards the tropopause and surface (Hossaini et al. (2015) supplement Fig. S1). While at 200 hPa at the North Pole the relative  $O_3$  change is  $\sim -5\%$ , also with stronger decreases at lower altitudes. These are comparable relative  $O_3$  percentage changes to this study when considering only the bromine VLSL impact as well as a significantly larger difference of the VLSL bromine loading (up to 8 ppt) in their model runs. If the transport of source gases injected into the stratosphere in the tropics increases as climate change progresses, the strongest decrease in  $O_3$  can be expected near the cold point tropopause in agreement with the simulations here (e.g., Hossaini et al. (2012a); Falk et al. (2017) and Ziska et al. (2017)).

## Chapter 7

# Summary and Outlook

In this dissertation various trace gases measured simultaneously from the HALO aircraft during the WISE campaign in the fall of 2017 in the northern hemisphere UTLS are investigated. These trace gases include  $\text{O}_3$ ,  $\text{NO}_2$ ,  $\text{BrO}$ ,  $\text{Br}^{\text{org}}$ ,  $\text{Br}_y^{\text{inorg}}$ , and  $\text{Br}^{\text{tot}}$ , as well as transport tracers ( $\text{CO}$  and  $\text{N}_2\text{O}$ ) and a tracer for the mean age of air ( $\text{SF}_6$ ). There were 15 flights, however only 11 with available  $\text{Br}^{\text{tot}}$  data. CLaMS simulations of  $\text{O}_3$ ,  $\text{NO}_2$ , and  $\text{BrO}$  mixing ratios are generally in good agreement with the measurements. The observations range from potential temperatures at the surface  $\sim 282$  K through the LS up to 410 K corresponding to  $\Delta\Theta = -50$  K to  $+88$  K relative to the WMO tropopause. The majority of the measurements were between 8.5–14.5 km altitude to focus on the LMS. The observations include air masses of the entire NH in equivalent latitudes (ranging from  $6^\circ\text{S}$ – $86^\circ\text{N}$ ) indicating geographical distributions as well as allowing for transport interpretation.

$\text{Br}^{\text{tot}}$  is assessed from simultaneous measurements of all relevant brominated source ( $\text{Br}^{\text{org}}$ ) and product (inferred  $\text{Br}_y^{\text{inorg}}$ ) gases. The  $\text{Br}^{\text{org}}$  source gases consist of  $\text{CH}_3\text{Br}$ , the four halons, and the five major brominated very short-lived substances measured with the novel in situ GhOST-MS system. The  $\text{Br}_y^{\text{inorg}}$  is inferred from remotely measured  $\text{BrO}$  with the mini-DOAS instrument scaled by the  $\text{BrO}/\text{Br}_y^{\text{inorg}}$  partitioning from CLaMS photochemical modelling. The resulting weighted average  $\text{Br}^{\text{tot}}$  in the LS is  $19.2 \pm 1.2$  ppt (the conservative uncertainty representing the  $1\sigma$  variability of the measurements). The average UTLS, i.e., including the tropospheric measurements,  $\text{Br}^{\text{tot}}$  is  $19.4 \pm 1.3$  ppt which includes larger  $\text{Br}^{\text{org}}$  measurements in the UT particularly in the tropics. The observations in this study largely agree with previous measurements of  $\text{Br}^{\text{tot}}$  in the UTLS (e.g., Engel and Rigby et al. (2018)), but the variability emphasizes some of the origins of  $\text{Br}^{\text{tot}}$  in the Ex-LS. Air mass lag-times inferred from  $\text{SF}_6$  measurements vary by over 3 years (from  $-1.1$  to  $2.6$  years) between the troposphere and LS.

Major insights into the causes of the  $\text{Br}^{\text{tot}}$  variability have been gained from studying the geographical distribution of the brominated gases as well as transport tracers as a function of equivalent latitude, both from observations (Fig. 6.4) and transport modelling (Figs. 6.7 and 6.9). The key findings of this investigation are summarized by the schematic in Fig. 6.6. Elevated  $\text{Br}^{\text{tot}}$  is observed in a persistent region extending into the LMS between potential temperatures  $\Theta = 350$ – $385$  K and equivalent latitudes  $55$ – $80^\circ\text{N}$  (see Sect. 5.2) of which a subsection,  $\text{HBrR}^*$ , has  $[\text{Br}^{\text{tot}}] = 20.9 \pm 0.8$  ppt. This bromine-rich air was predominantly isentropically transported from the tropical UT/TTL into the LMS.

The air mass origin tracers modelled by CLaMS agree with the observational data including the transport tracer distributions in the LMS. They indicate that the  $\text{HBrR}$  in the LMS has 51.2% of air originating from the tropical troposphere, and 6.4% from the mid-latitude troposphere which are mixed with 27.1% stratospheric background air. The remaining smaller contributions

are from other LS domains and  $< 1\%$  from the remaining tropospheric domains. In contrast, the LS air masses below and above the HBrR show a decreasing tropospheric (mainly tropical and less mid-litudinal) contribution and an approximately equivalent increasing stratospheric background contribution. This increase of approximately 10% young (tropical and extratropical) tropospheric air in the HBrR compared to the LS below and above it, is reflected in the bromine-rich air masses of the HBrR.

Additional CLaMS surface-emission simulations indicate that surface contributions account for 37.7% of the air masses within the HBrR of which the majority is from the Asian monsoon region (AMR) and its tropical adjacent region (TAR). Only a small fraction of air (3.3%) in the HBrR originates from Central America (CAM). The LS below and above the HBrR only receive 30.3% from surface regions, with most of the decreases observed in the AMR and its TAR contributions. This shows the efficiency of the vertical uplift in the AMR rapidly transporting surface air from the TAR and specifically the tropical marine environment (TME) in south eastern Asia into the tropical UT/TTL. The air masses are then transported further via the lower branch of the Brewer-Dobson circulation into the Ex-LS. This transport pathway in boreal late summer and fall has a direct impact on the trace gas composition and specifically of bromine in the NH LMS. Air masses from the coastal regions in south eastern Asia are injected into the LS around equivalent latitudes  $\sim 30^\circ\text{N}$  and transported to the tropical UT/TTL and the LMS by isentropic transport and are the main source of bromine-rich air masses in the HBrR.

Further, the data from WISE point to additional causes for varying bromine in the UT. Notably, air masses with high bromine mixing ratios were transported by two hurricanes from CAM into the tropical  $\Theta_{\text{high}}/\text{PV}_{\text{low}}$  region (defined in Sect. 5.2), of which the remnants were later observed to the west of the British Isles on Oct. 1, 2017 in RF08. These large CAM (and TME) contributions lead to the most bromine-rich air masses observed during WISE with  $[\text{Br}^{\text{tot}}] = 21.6 \pm 0.7$  ppt in the  $\Theta_{\text{high}}/\text{PV}_{\text{low}}$  region. Additionally, the WISE flights captured two STE events where stratospheric air of elevated  $\text{Br}_y^{\text{inorg}}$  was recently transported into the UT caused by breaking Rossby waves in the extratropics. Measurements and model results indicate multiple pathways for tropospheric air masses to reach the LMS, either by mid-litudinal STE in the extratropics or more often by isentropic transport from the tropical UT/TTL. The multiple pathways result in fluctuations of  $\text{Br}^{\text{tot}}$  in the NH LMS with a notable region of elevated bromine. This investigation complements previous studies emphasizing the importance of the transport of air masses via the lower branch of the Brewer Dobson circulation (e.g., Hoor et al. (2005); Levine et al. (2007); Bönisch et al. (2009); Vogel et al. (2016) and Hauck et al. (2020)).

The transport of younger bromine-rich (among other trace gases) tropospheric air masses into the LMS, directly impacts the LS  $\text{O}_3$ . In situ measurements indicate lower  $\text{O}_3$  VMRs coinciding within the HBrR in the LMS. The consequences of more  $\text{Br}^{\text{tot}}$  in the LS on  $\text{O}_3$  is further analysed with TOMCAT model simulations. An enhancement of  $\sim 1-2$  ppt  $\text{Br}^{\text{tot}}$  in the tropical UT and further in the LS through its isentropic transport, results in the LS  $\text{O}_3$  change of  $-2.6 \pm 0.7\%$  (average of two elevated bromine scenarios) conveying its sensitivity to bromine. However, the strongest  $\text{O}_3$  changes are observed within the 20 K layer directly above the tropopause resulting in  $-3.1 \pm 0.7\%$  of  $\text{O}_3$ .

Some limitations of this study due to the intrinsic characteristics or failure of the instruments are worth noting. These include restricting measurements to only daytime which eliminates some flight-time hours including several ascents and descents of the aircraft into Shannon airport (mini-DOAS instrument), failure to record  $\text{Br}^{\text{org}}$  data during four flights due to technical problems (GhOST instrument), and low signal-to-noise ratios for some of the brominated species due to their low mixing ratios. However, due to the large data set collected during this campaign, even with these limitations, the accumulation of data and the consistency of the results increases the

analysis confidence in this study. In particular, the  $1\sigma$  accuracy of the  $\text{Br}^{\text{tot}}$  data is a conservative uncertainty and the co-added error from the  $\text{Br}^{\text{org}}$  and  $\text{Br}_y^{\text{inorg}}$  measurements of the individual species should eventually be lower.

The continuous nature of these WISE flight measurements covering a large range of air mass lag-times even for individual flights, offers several advantages over previous mostly balloon and some aircraft related studies on  $\text{Br}^{\text{tot}}$ . This includes an improved space and time resolution as well as a higher precision and accuracy of inferred  $\text{Br}^{\text{tot}}$ . Another major advantage of the aircraft measurements is the ability to display a wide-spread behaviour of  $\text{Br}^{\text{org}}$ ,  $\text{Br}_y^{\text{inorg}}$ , and  $\text{Br}^{\text{tot}}$  in the investigated air masses. The multi-pathway transport of bromine (as well as of other gases) into the northern LMS via the major pathways may well be very specific for the region and season (mid-latitudes in boreal fall) investigated during the WISE campaign. However, it does suggest that bromine as well as other ozone-harming gases are not simply injected into the stratosphere from a single source region, but that a manifold of different pathways may act (e.g., Holton et al. (1995); Homeyer and Bowman (2013); Ploeger et al. (2015); Kunkel et al. (2019)).

In this respect, further probing the tropopause region and LS for  $\text{Br}^{\text{tot}}$  and other ozone depleting species is still required. Ultimately, the detected variability of  $\text{Br}^{\text{tot}}$  in the UTLS does not yield a sufficient understanding on  $\text{Br}^{\text{tot}}$  and its trend in the middle and upper stratosphere. Therefore further probing by ground- and balloon-based instrumentation, and satellites is required in the future.

There are recent HALO missions for which  $\text{Br}^{\text{tot}}$  can similarly be evaluated and analysed. Previous campaigns such as TACTS (2012) and POLSTRACC (2015–2016) similarly observed a wide range of NH air masses in the UTLS, for which bromine data should be available. The HALO SouthTRAC mission, which was the follow-on study of WISE, had deployments into the southern hemisphere in September and November 2019. The campaign was based in Rio Grande, Tierra del Fuego in southern Argentina with flights ranging from Oberpfaffenhofen, Germany to the Antarctica Peninsula. The instrument payload as well as the campaign goals were very similar to WISE and will allow for similar investigations as in this dissertation for the southern hemisphere.

Previous HALO campaigns in 2017–2019 with different objectives, dynamics, regions, and seasons than the WISE campaign may be limited to  $\text{BrO}$  and/or  $\text{Br}_y^{\text{inorg}}$  data depending on the campaign instrument payload. These campaigns consist of EMeRGe-EU (May–August 2017), EMeRGe-Asia (February–April 2018), CoMeT 1.0 (Carbon Dioxide and Methane Mission for HALO; May–June 2018), and CAFE-Africa (Chemistry of the Atmosphere Field Experiment in Africa; June–September 2018). All campaigns from 2017 onwards were campaigns I actively participated in.

In time, through the accumulation of additional bromine data across multiple campaigns (particularly TACTS (2012), POLSTRACC (2015–2016), WISE (2017), and SouthTRAC (2019)), one may be able to establish trends of  $\text{Br}^{\text{tot}}$  in the UTLS. This will improve the current understandings of the ozone behaviour in the LMS and the impacts potentially on climate change.

# Appendix A

## O<sub>3</sub> Fit Scenario Wavelength Comparisons for All WISE Flights

The O<sub>3</sub> fit window comparisons for 7 different wavelength ranges are compared using simulated and Kurucz reference SCDs for all flights during the WISE campaign. One example flight is described in the text (refer to Sect. 4.1.3) and shown in Fig. 4.11, while the remaining WISE flights can be found in the following figures (Figs. A.1–A.14). Generally the fit window labelled ‘O3.338.357\_Pukite’ (shown in red) has the best agreement between the Kurucz and simulated reference SCDs and agrees best with all other fit window SCD resulting from the simulated references.

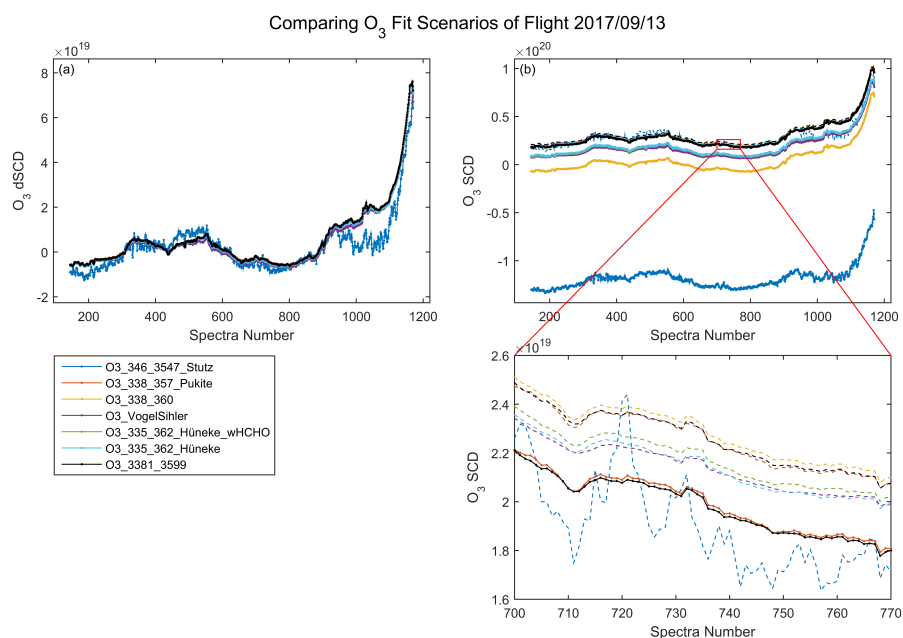


Figure A.1: WISE RF02 on Sept. 13, 2017. The panels are as given in Fig. 4.11 and details of the O<sub>3</sub> wavelength fit scenario windows are described in Table 4.3.

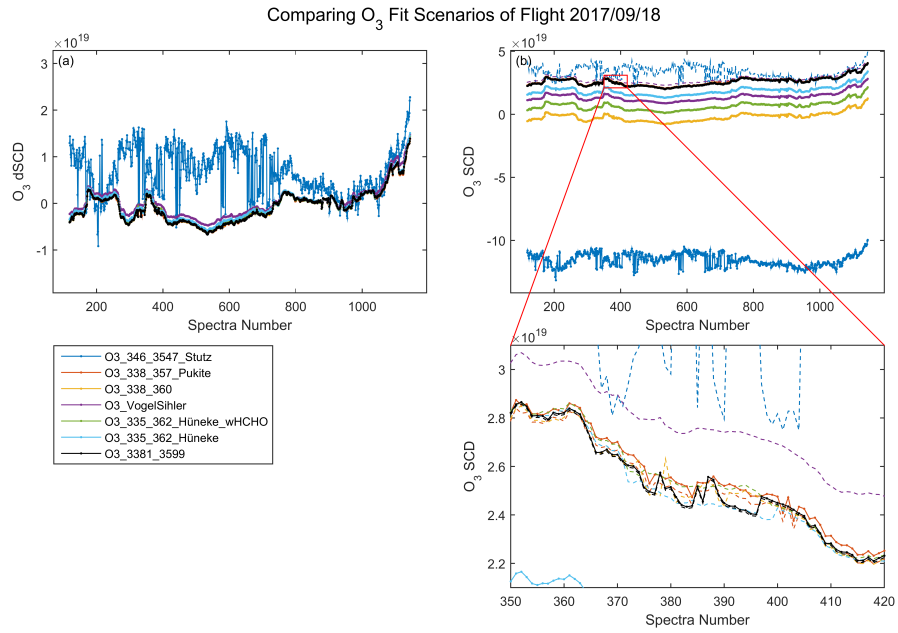


Figure A.2: WISE RF03 on Sept. 18, 2017. The panels are as given in Fig. 4.11 and details of the O<sub>3</sub> wavelength fit scenario windows are described in Table 4.3.

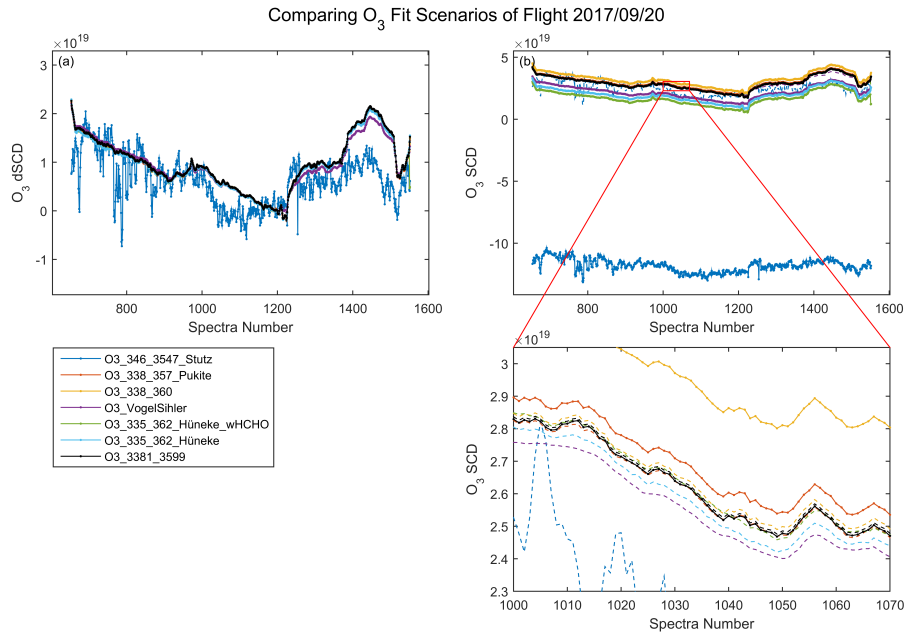


Figure A.3: WISE RF04 on Sept. 20, 2017. The panels are as given in Fig. 4.11 and details of the O<sub>3</sub> wavelength fit scenario windows are described in Table 4.3.

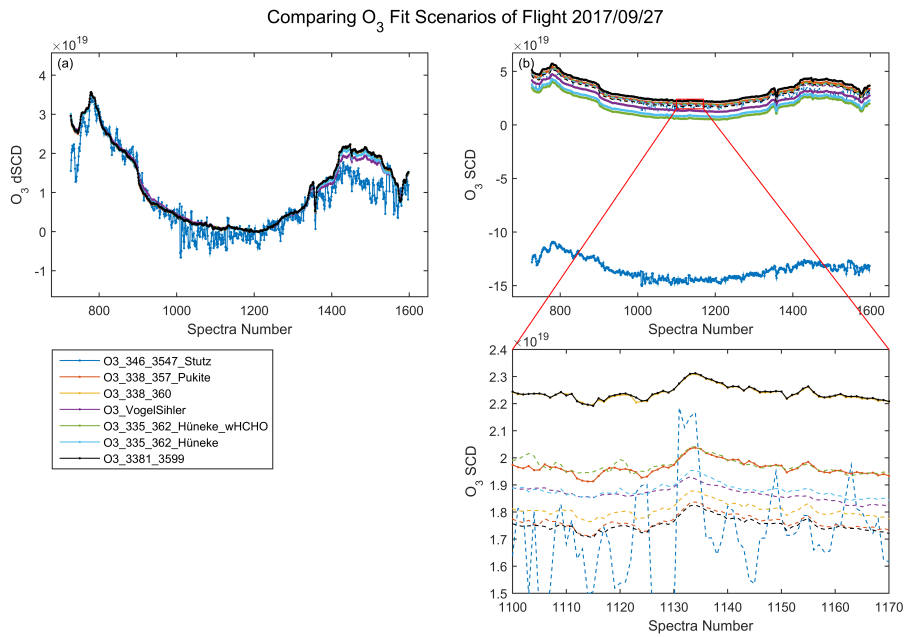


Figure A.4: WISE RF06 on Sept. 27, 2017. The panels are as given in Fig. 4.11 and details of the O<sub>3</sub> wavelength fit scenario windows are described in Table 4.3.

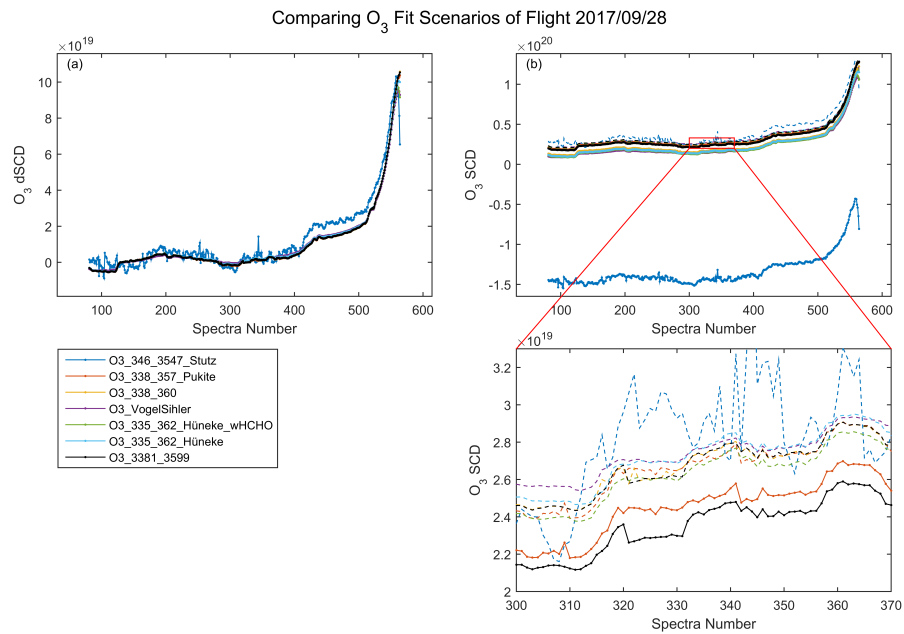


Figure A.5: WISE RF07 on Sept. 28, 2017. The panels are as given in Fig. 4.11 and details of the O<sub>3</sub> wavelength fit scenario windows are described in Table 4.3.

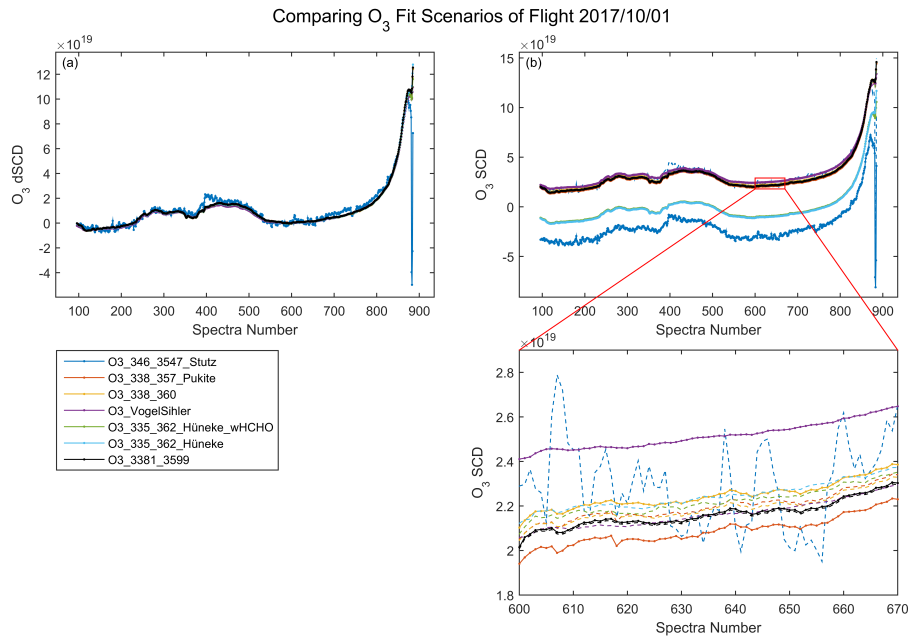


Figure A.6: WISE RF08 on Oct. 1, 2017. The panels are as given in Fig. 4.11 and details of the O<sub>3</sub> wavelength fit scenario windows are described in Table 4.3.

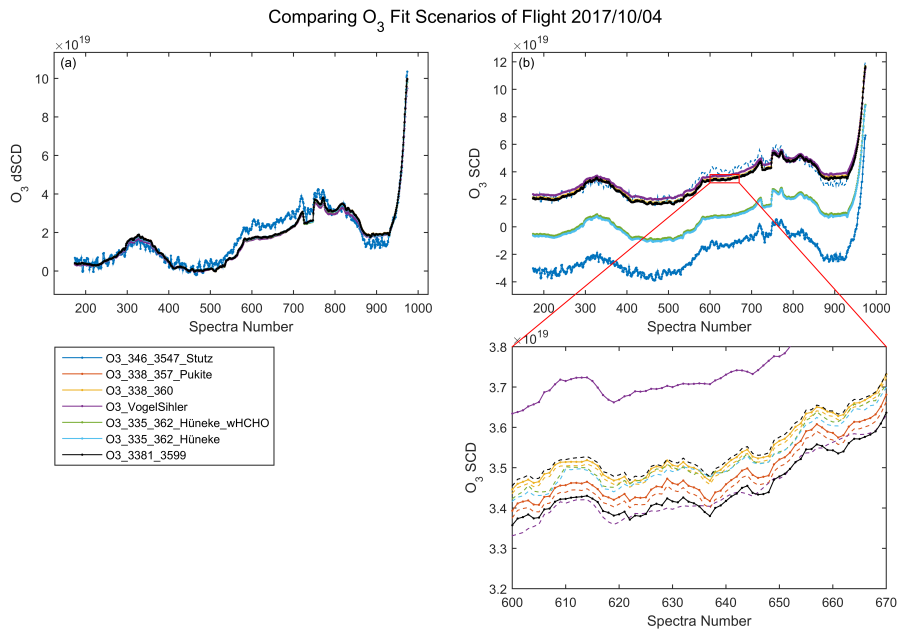


Figure A.7: WISE RF09 on Oct. 4, 2017. The panels are as given in Fig. 4.11 and details of the O<sub>3</sub> wavelength fit scenario windows are described in Table 4.3.

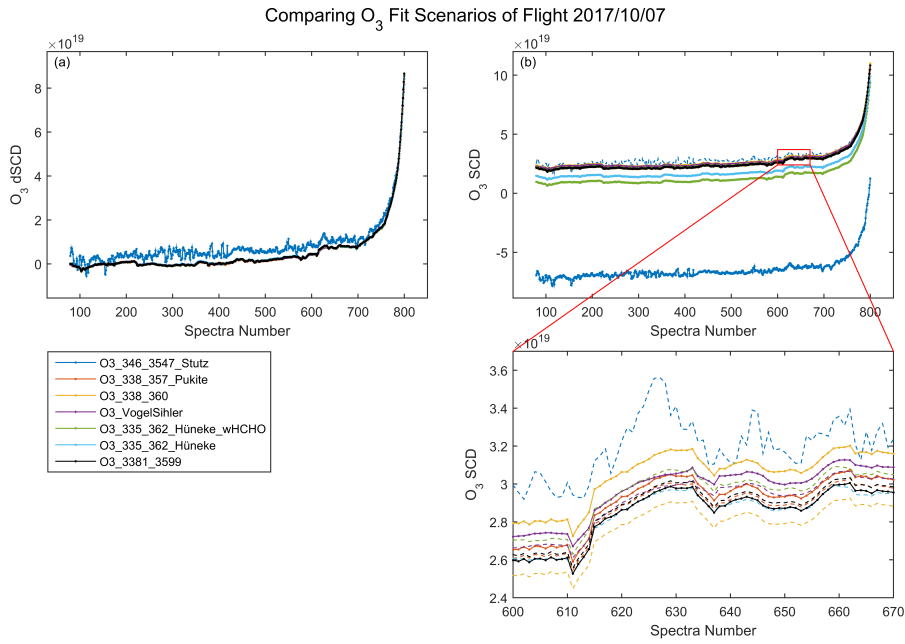


Figure A.8: WISE RF10 on Oct. 7, 2017. The panels are as given in Fig. 4.11 and details of the O<sub>3</sub> wavelength fit scenario windows are described in Table 4.3.

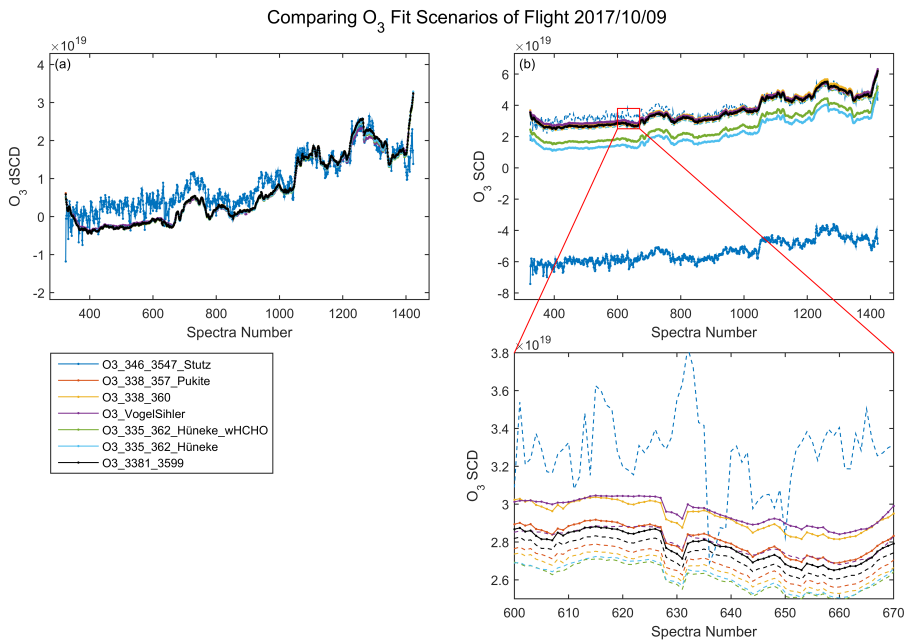


Figure A.9: WISE RF11 on Oct. 9, 2017. The panels are as given in Fig. 4.11 and details of the O<sub>3</sub> wavelength fit scenario windows are described in Table 4.3.

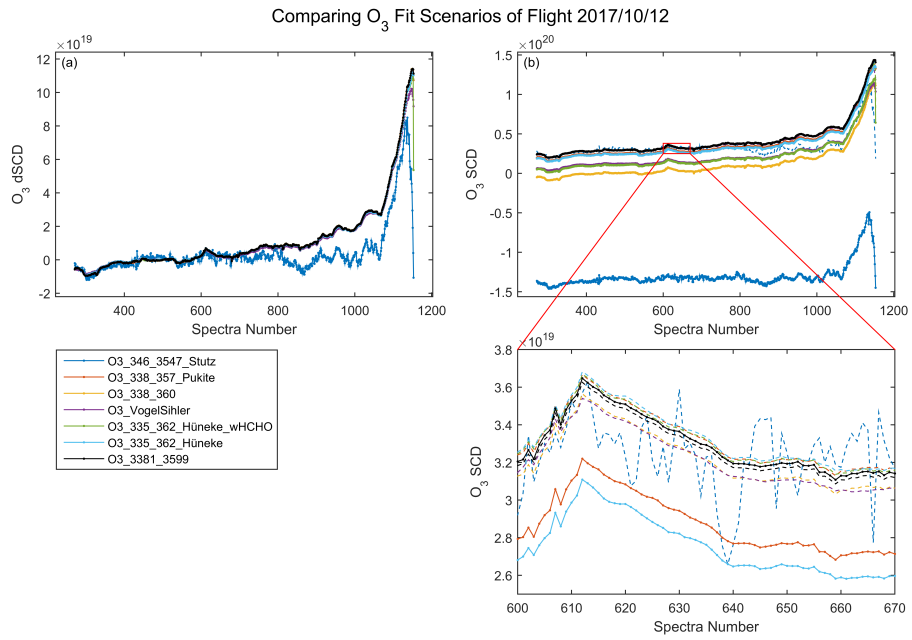


Figure A.10: WISE RF12 on Oct. 12, 2017. The panels are as given in Fig. 4.11 and details of the O<sub>3</sub> wavelength fit scenario windows are described in Table 4.3.

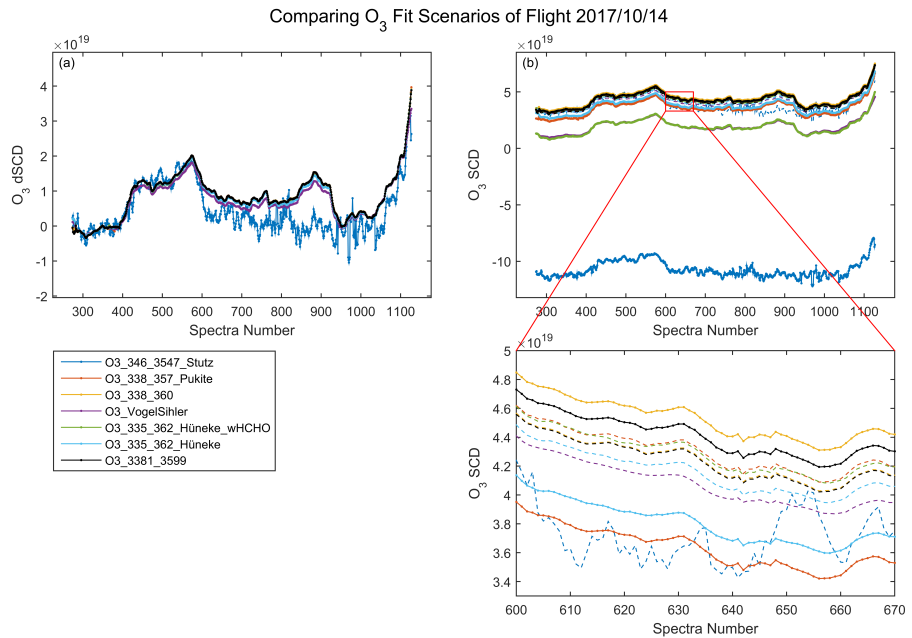


Figure A.11: WISE RF13 on Oct. 14, 2017. The panels are as given in Fig. 4.11 and details of the O<sub>3</sub> wavelength fit scenario windows are described in Table 4.3.

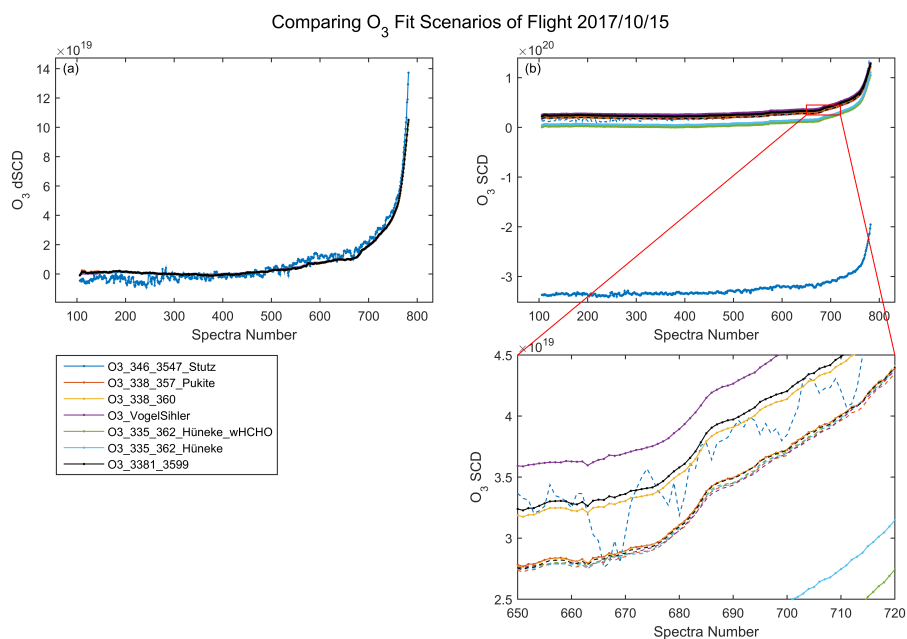


Figure A.12: WISE RF14 on Oct. 15, 2017. The panels are as given in Fig. 4.11 and details of the O<sub>3</sub> wavelength fit scenario windows are described in Table 4.3.

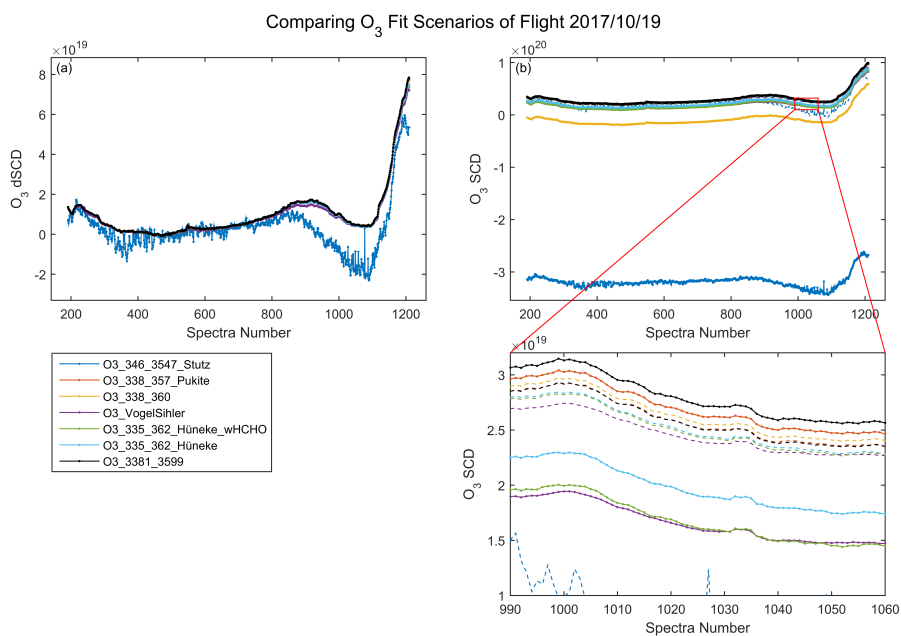


Figure A.13: WISE RF15 on Oct. 19, 2017. The panels are as given in Fig. 4.11 and details of the O<sub>3</sub> wavelength fit scenario windows are described in Table 4.3.

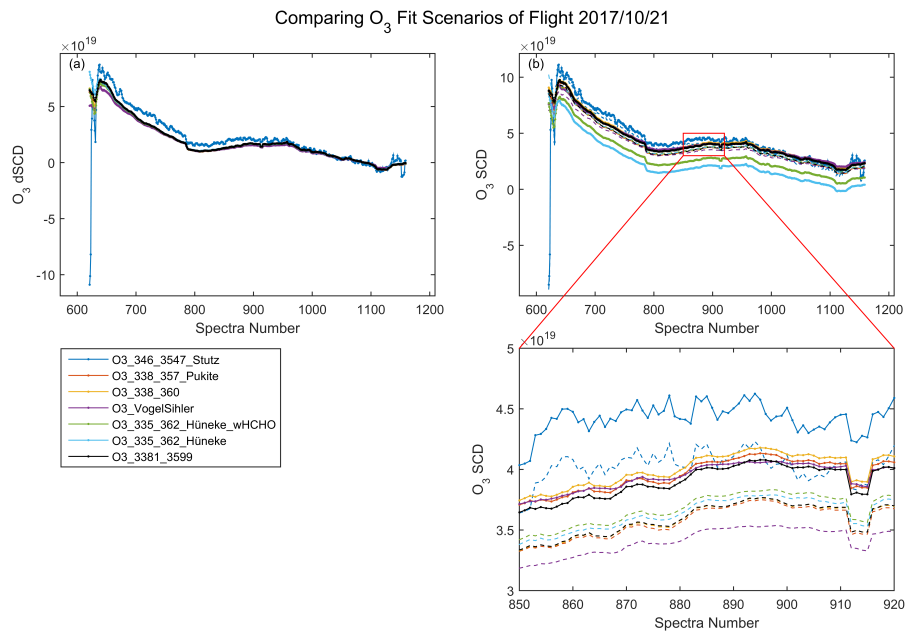


Figure A.14: WISE RF16 on Oct. 21, 2017. The panels are as given in Fig. A.13 and details of the O<sub>3</sub> wavelength fit scenario windows are described in Table 4.3.

## Appendix B

# Overview Results of Remaining WISE Flights

The overview results of two example flights (RF04 and RF08) have been described and discussed in the text above (refer to Sect. 5.3 and Figs. 5.2 and 5.3). The remaining 13 flights with flight tracks shown in Fig. 5.1 are shown below in Figs. B.1–B.13.

The flight tracks and tropopause (black solid and dashed lines, respectively) and equivalent latitude (blue line; right axis) are shown in panel (a) giving reference to the general location of the measurements. In panels (b–g) the various trace gases measured by the different instruments as well as vertically adjusted CLaMS curtains model results are displayed along each flight track for all available data. The panels are described as following: (b)  $\text{O}_3$  VMRs (FAIRO measurements—green solid line; CLaMS model—orange dashed line) as well as the CO VMR (UMAQS measurements—red line; right axis); (c)  $\text{NO}_2$  VMRs (mini-DOAS measurements—pink solid line; CLaMS model—orange dashed line); (d) BrO VMRs (mini-DOAS measurements—blue solid line; CLaMS model—orange dashed line); (e) CLaMS modelled  $\text{BrO}/\text{Br}_y^{\text{inorg}}$  (green dashed line) and  $\text{BrONO}_2/\text{Br}_y^{\text{inorg}}$  (brown dashed line) partitioning; (f) mean air mass lag-time inferred from  $\text{SF}_6$  GhOST measurements (black line) along with CLaMS TME and CAM emission tracers (orange solid and dashed lines respectively; right axis); (g)  $\text{Br}^{\text{org}}$  species ( $\text{CH}_3\text{Br}$ —dark blue points, plus the four halons—purple points, plus the five most relevant brominated VSLS—light blue points) to which the inferred  $\text{Br}_y^{\text{inorg}}$  (red points) is added for  $\text{Br}^{\text{tot}}$  results. The LS average is indicated by the gray dotted line in panel (g).

The light gray shading indicates flight sections within the tropical  $\Theta_{\text{high}}/\text{PV}_{\text{low}}$  region and the dark gray shading indicates flight sections in the HBrR. Refer to Sect. 5.2 for definitions of each of the regions, as well as Sect. 6.2 and onwards for discussions.

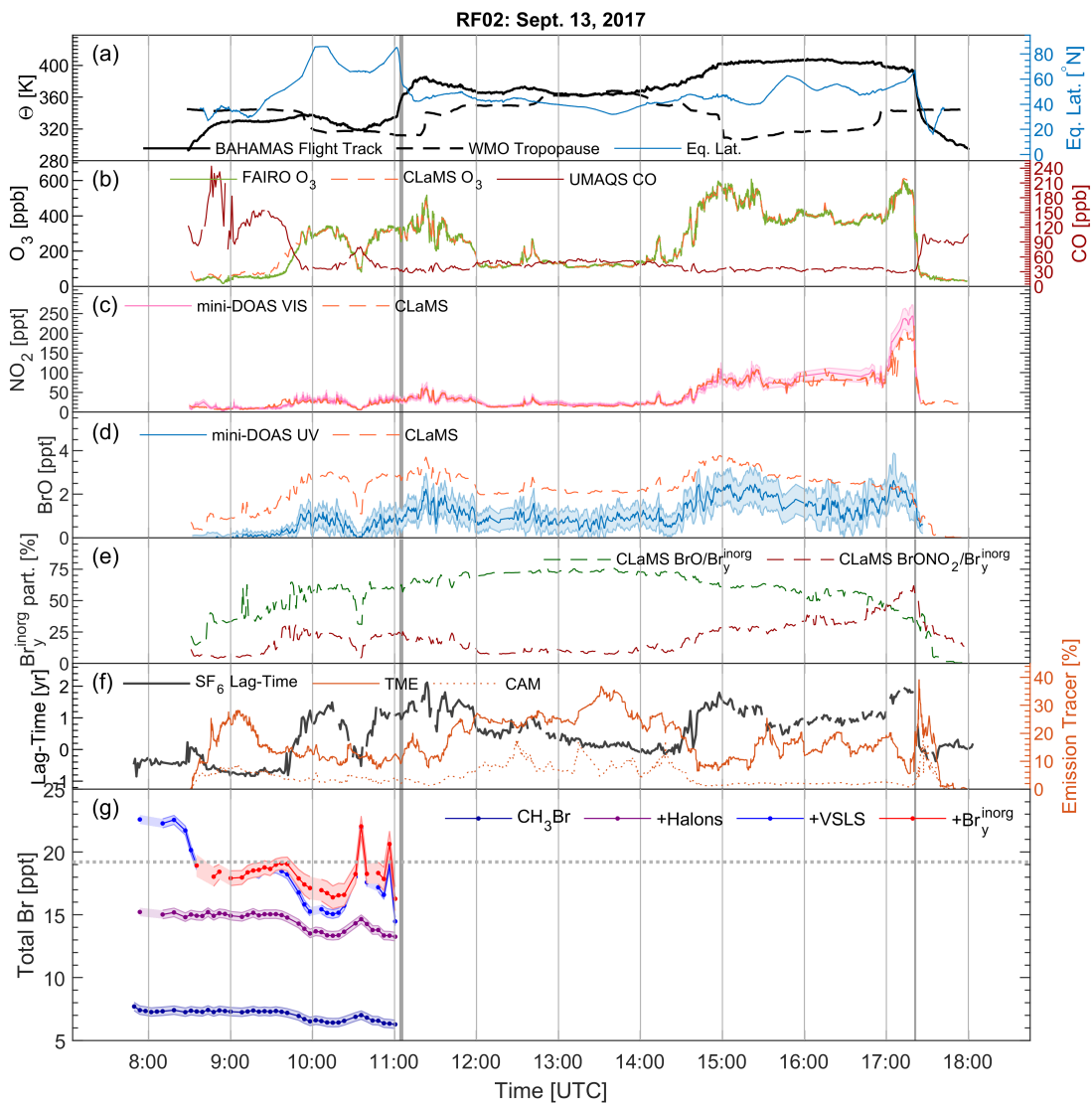


Figure B.1: Overview of WISE RF02 on Sept. 13, 2017. Panels (a–g) are as given in Sect. B.

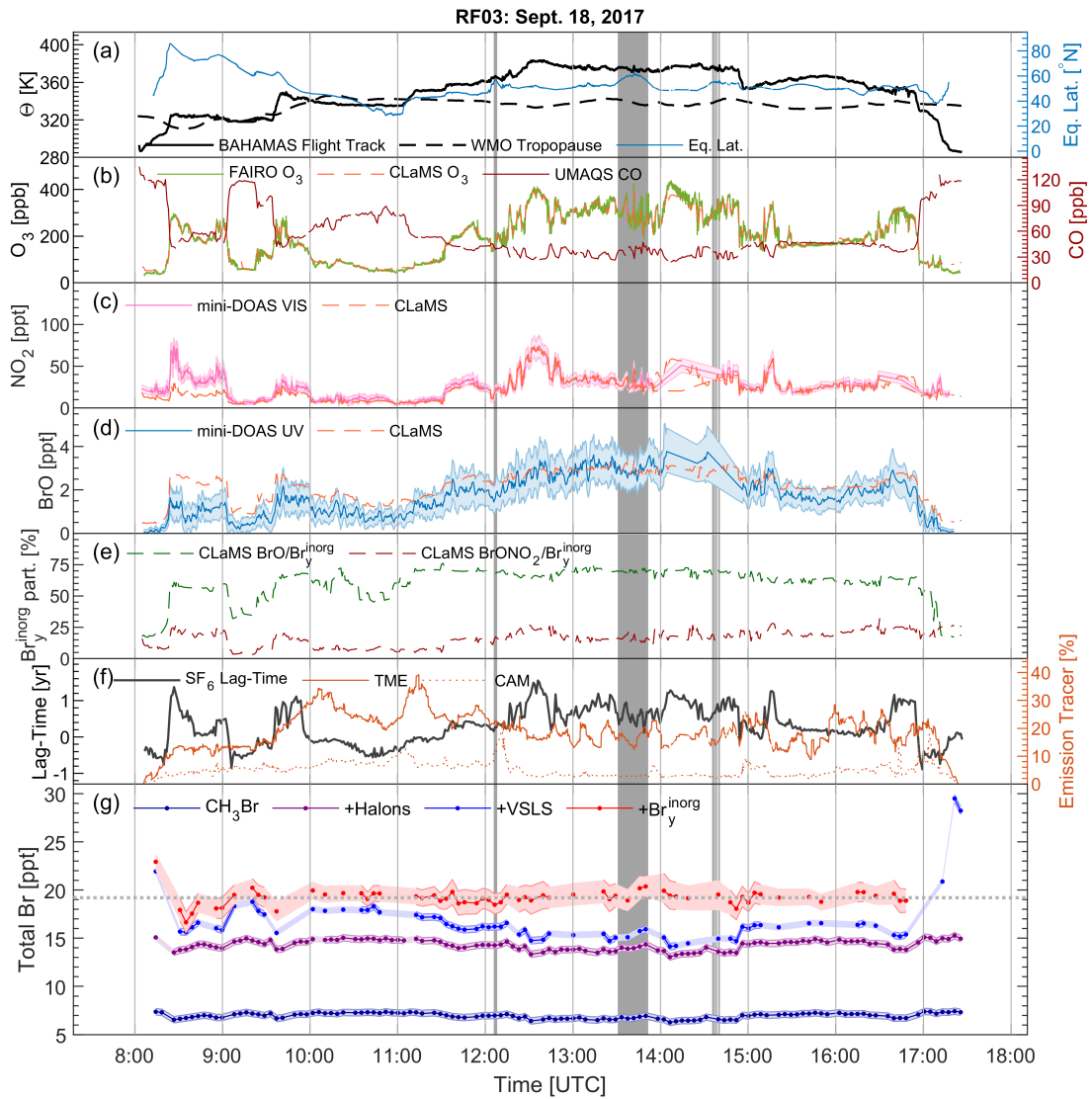


Figure B.2: Overview of WISE RF03 on Sept. 18, 2017. Panels (a–g) are as given in Sect. B.

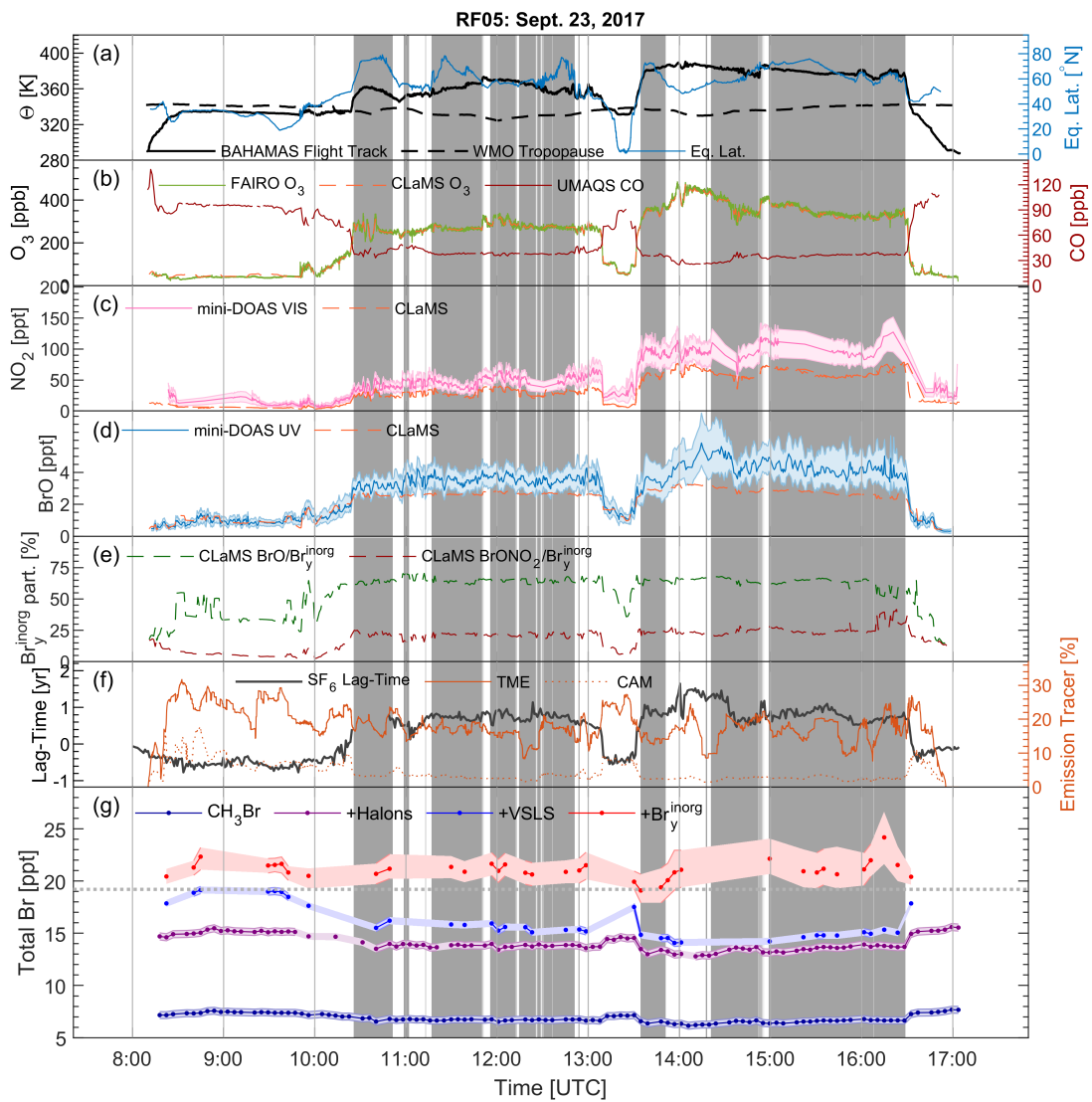


Figure B.3: Overview of WISE RF05 on Sept. 23, 2017. Panels (a–g) are as given in Sect. B.

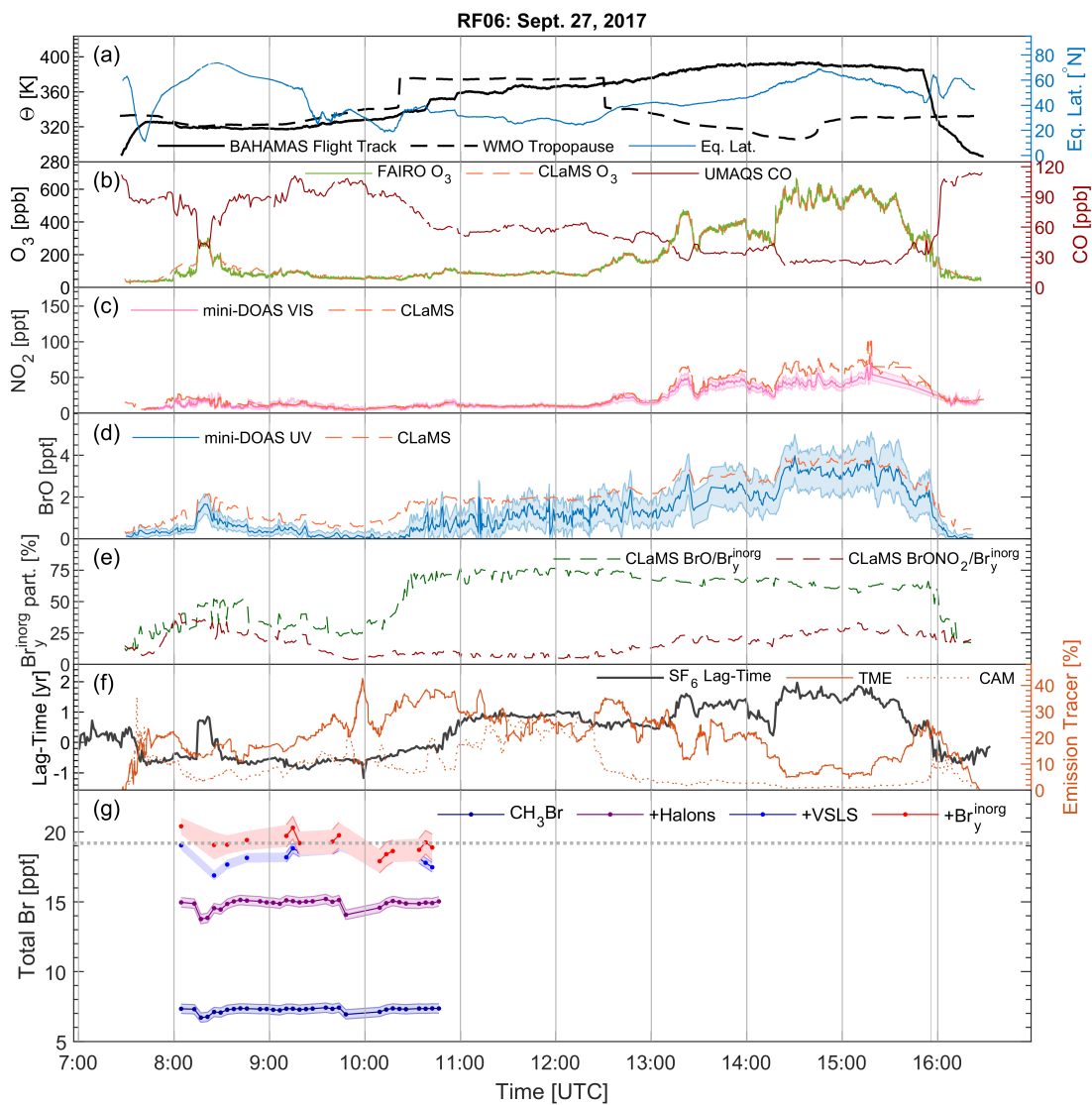


Figure B.4: Overview of WISE RF06 on Sept. 27, 2017. Panels (a–g) are as given in Sect. B.

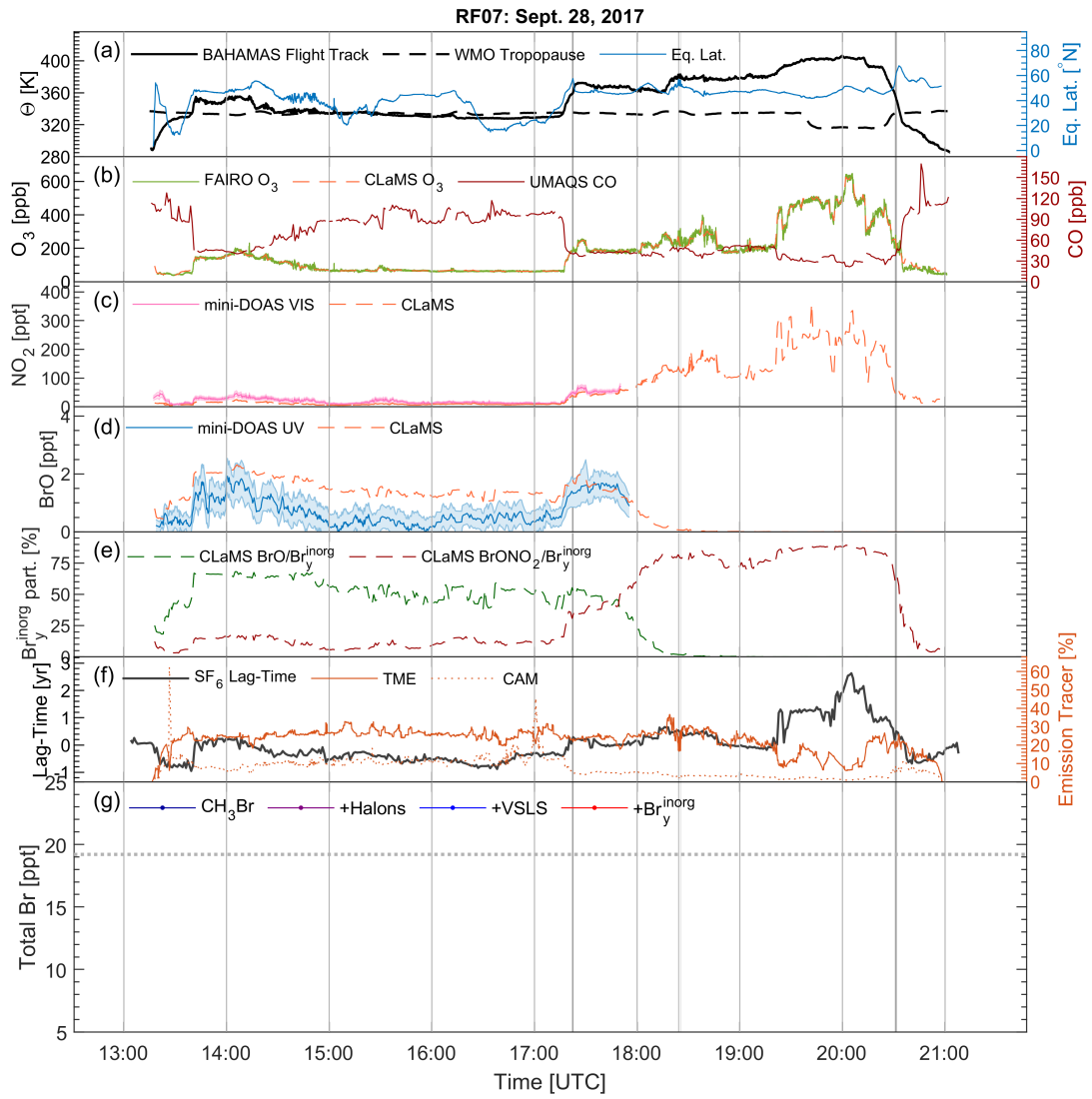


Figure B.5: Overview of WISE RF07 on Sept. 28, 2017. Panels (a–g) are as given in Sect. B.

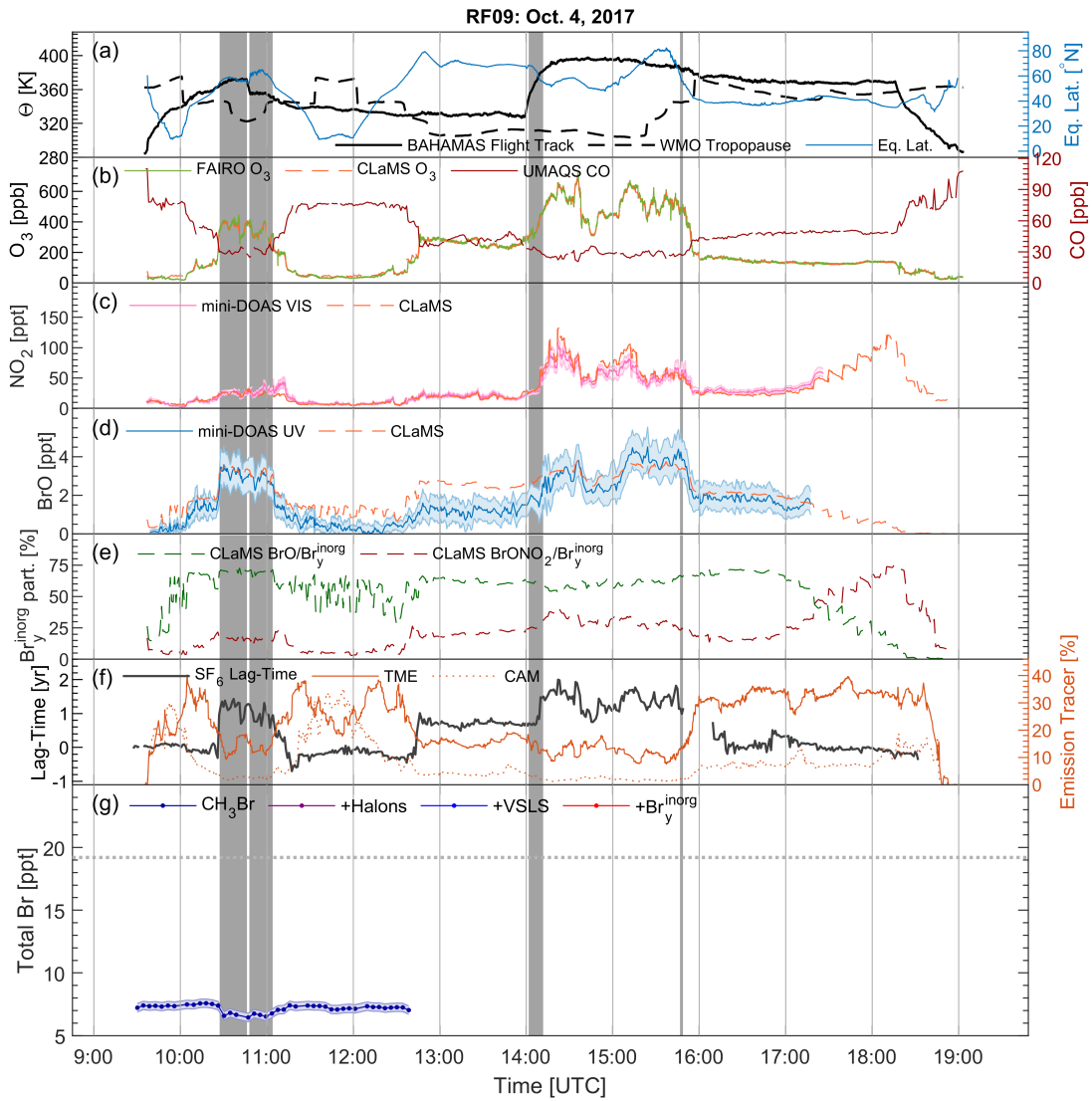


Figure B.6: Overview of WISE RF09 on Oct. 4, 2017. Panels (a–g) are as given in Sect. B.

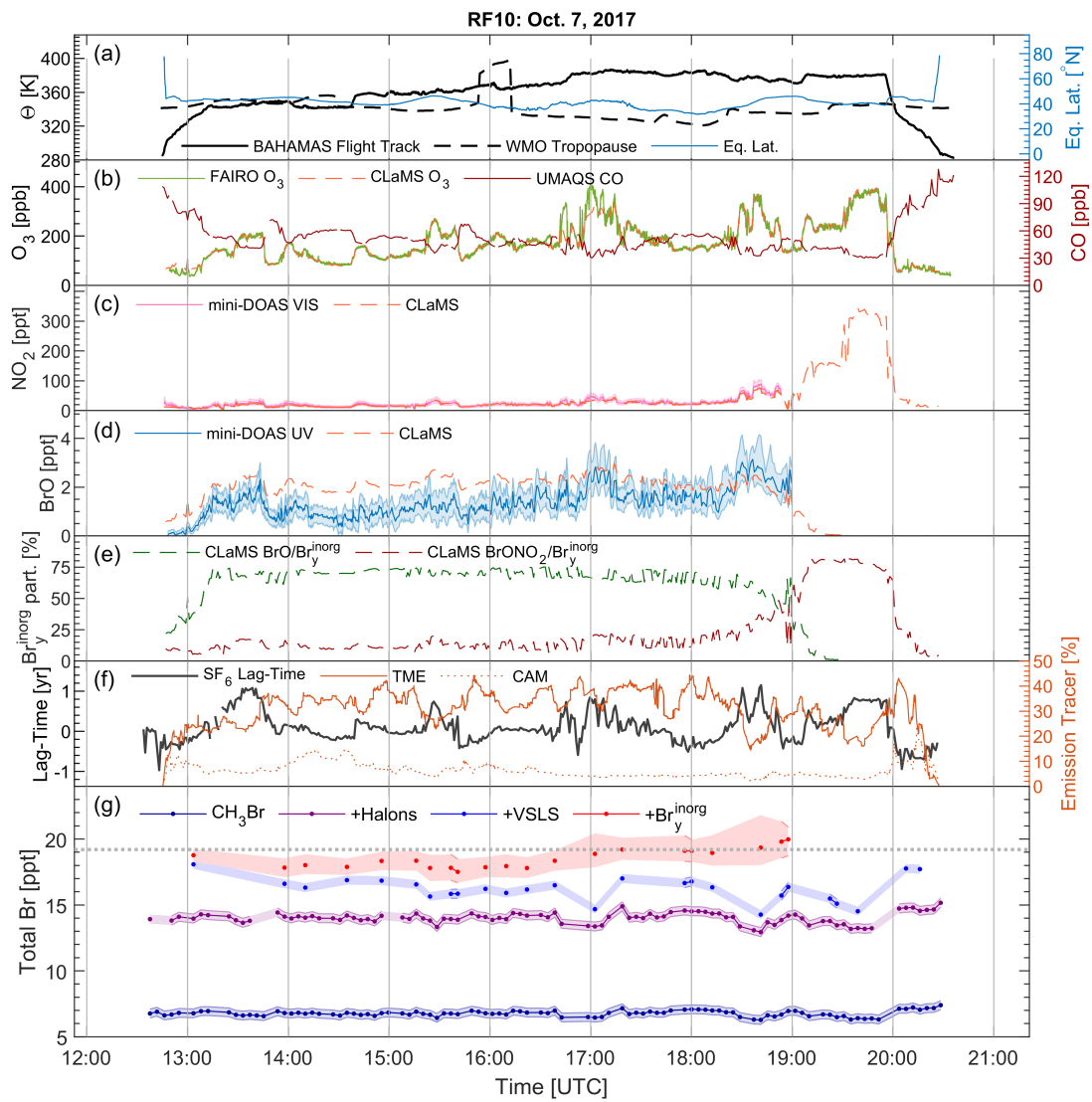


Figure B.7: Overview of WISE RF10 on Oct. 7, 2017. Panels (a–g) are as given in Sect. B.

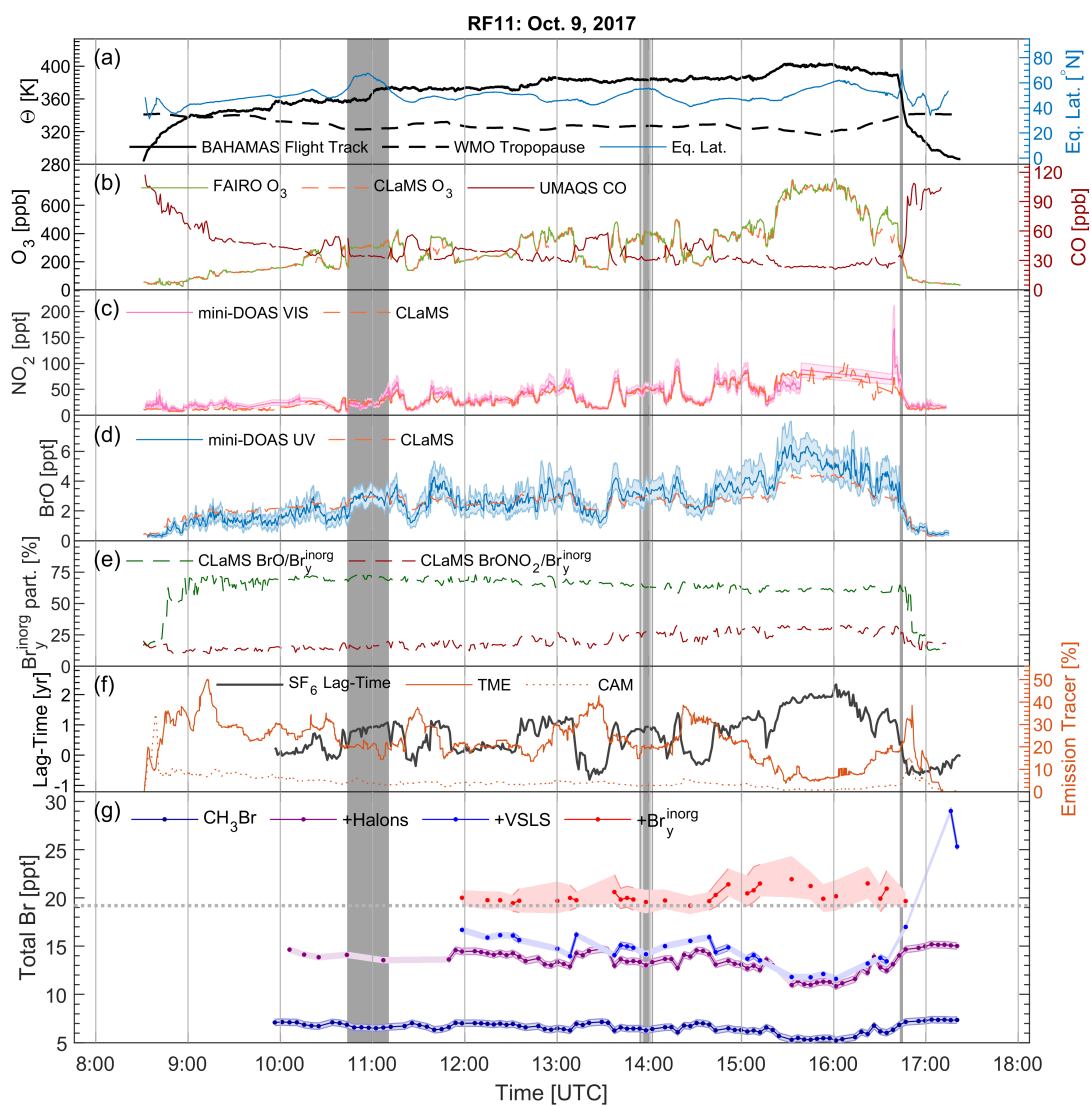


Figure B.8: Overview of WISE RF11 on Oct. 9, 2017. Panels (a–g) are as given in Sect. B.

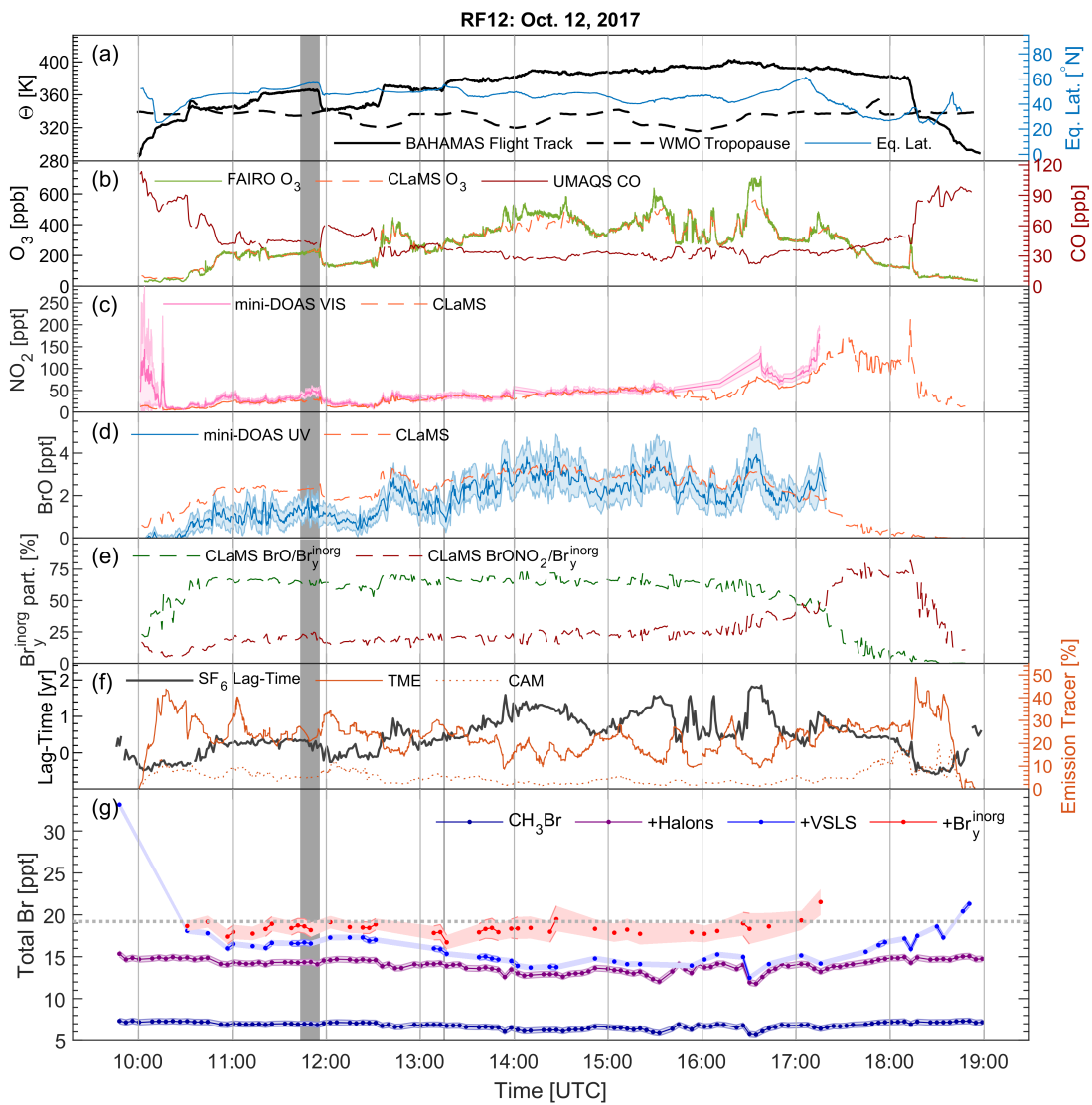


Figure B.9: Overview of WISE RF12 on Oct. 12, 2017. Panels (a–g) are as given in Sect. B.

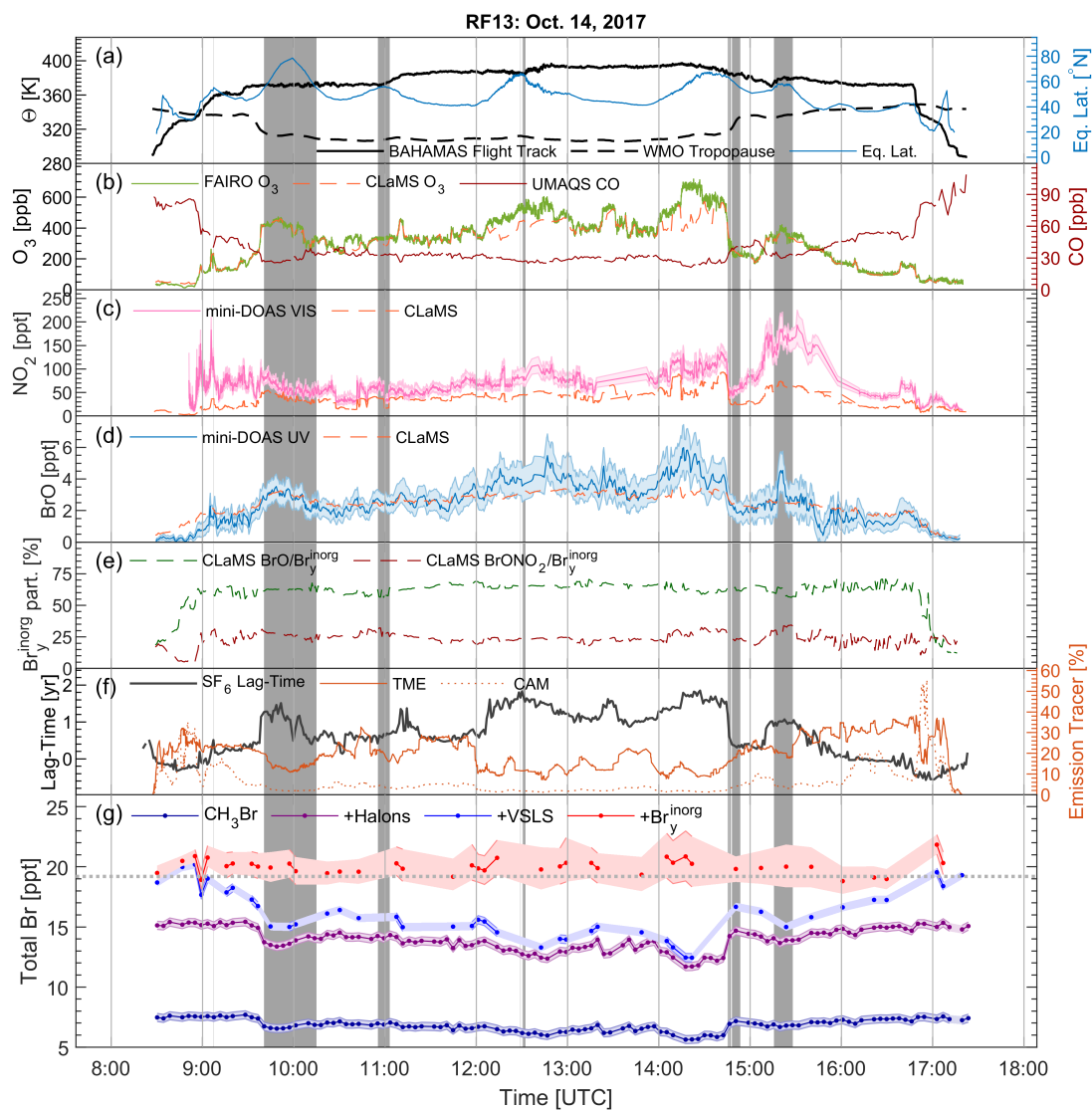


Figure B.10: Overview of WISE RF13 on Oct. 14, 2017. Panels (a–g) are as given in Sect. B.

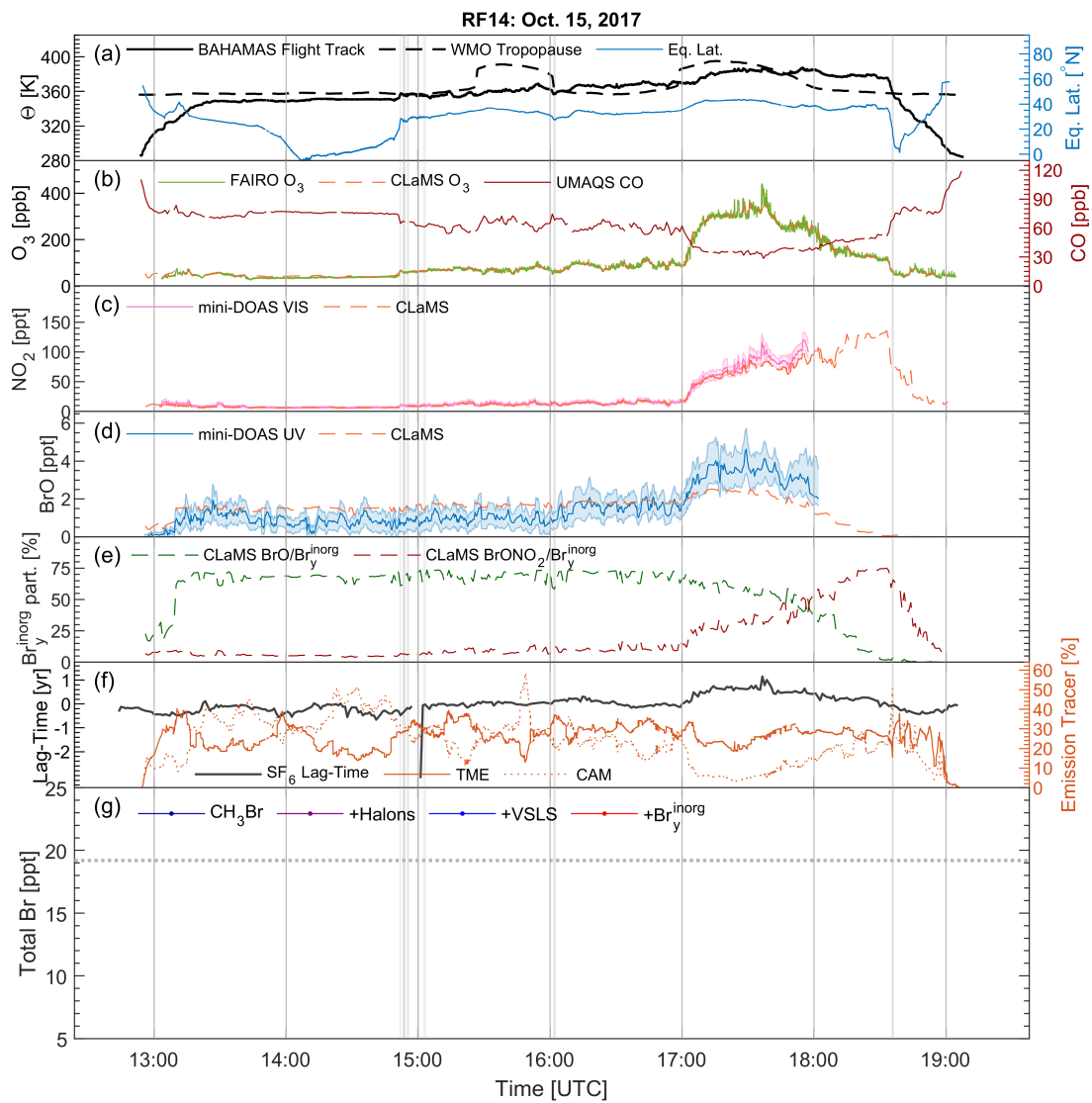


Figure B.11: Overview of WISE RF14 on Oct. 15, 2017. Panels (a–g) are as given in Sect. B.

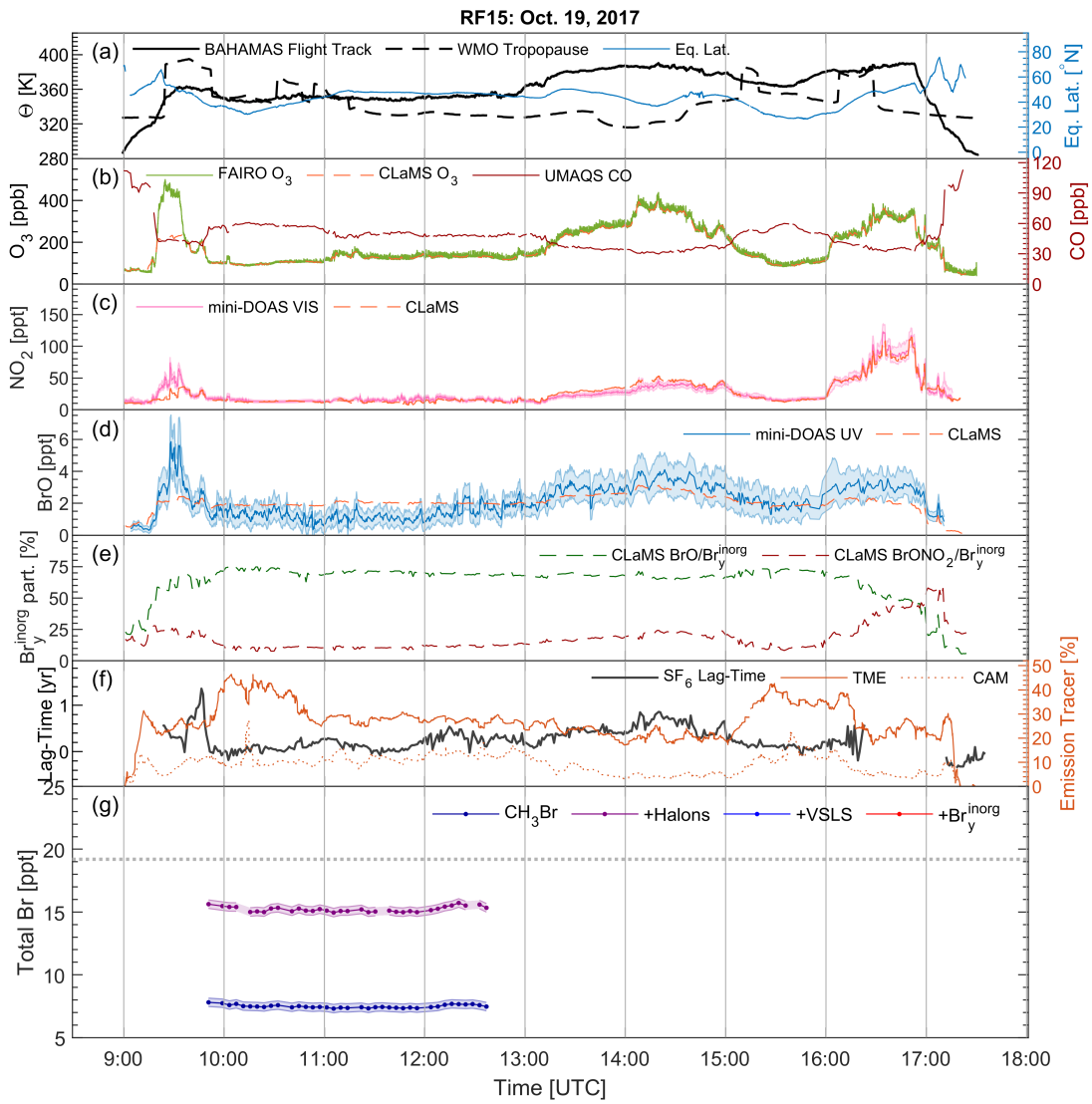


Figure B.12: Overview of WISE RF15 on Oct. 19, 2017. Panels (a–g) are as given in Sect. B.

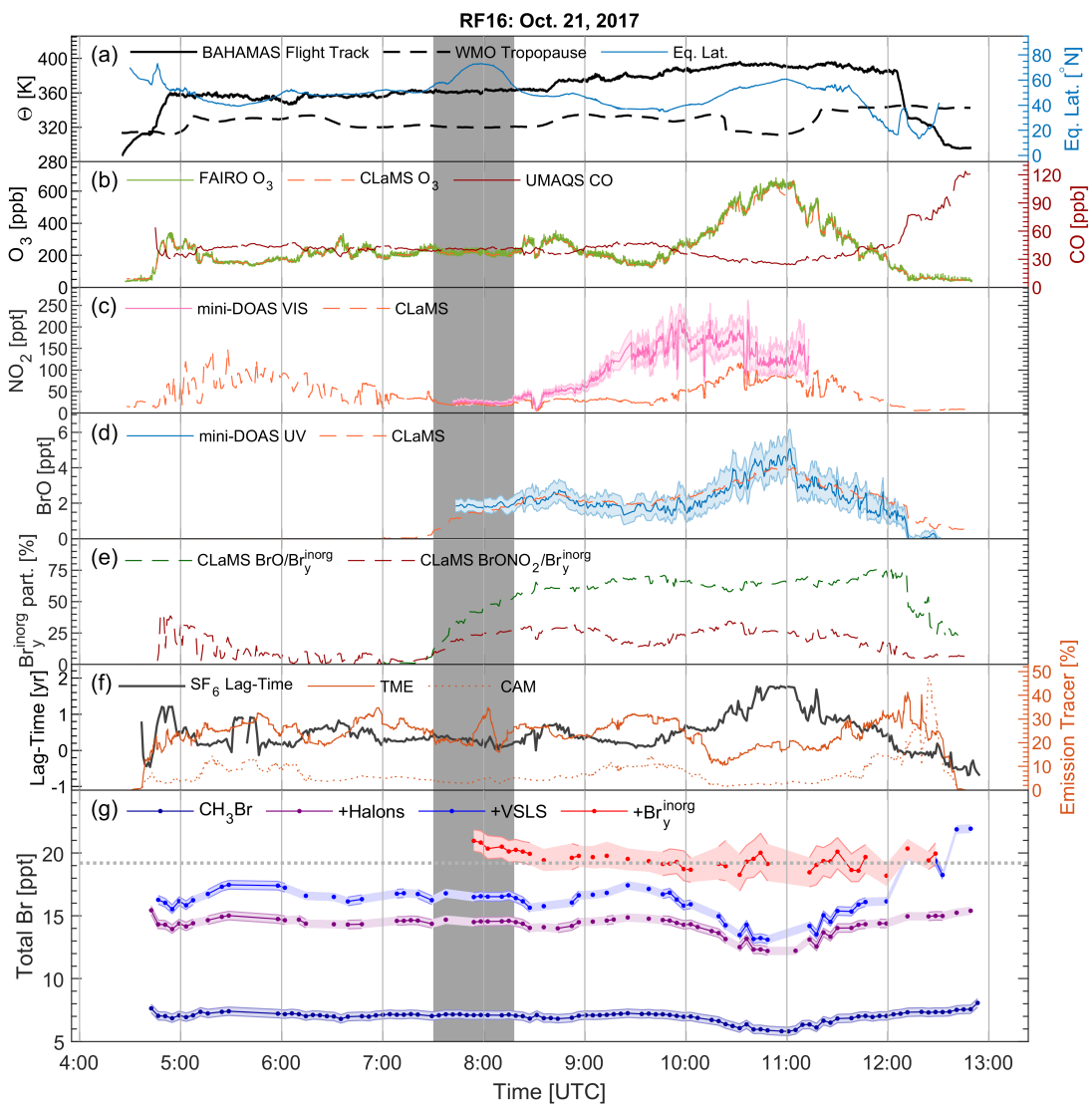


Figure B.13: Overview of WISE RF16 on Oct. 21, 2017. Panels (a–g) are as given in Sect. B.

# Appendix C

## All CLaMS Transport Tracers

The CLaMS transport tracers of all nine atmospheric air mass origin domains and 24 surface emission tracer regions are shown in Fig. C.1 and C.2, respectively.

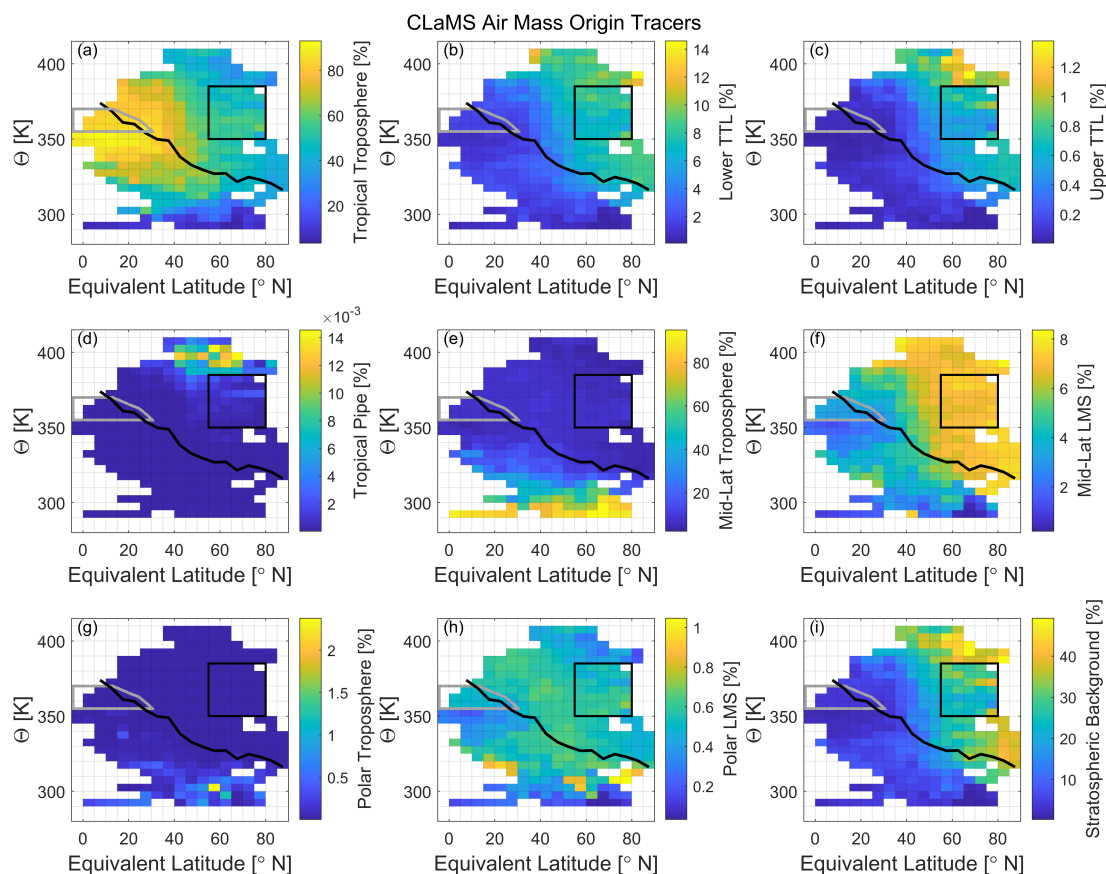


Figure C.1: Relative contribution of CLaMS air mass origin tracers during the WISE campaign. The nine different domains are as outlined in Fig. 3.6 and Table 3.2 (for more details refer to Vogel et al. (2011)). The black line is the average WMO tropopause, the black box indicates the HBrR, and the grey outline is the tropical  $\Theta_{\text{high}}/PV_{\text{low}}$  region (defined in Sect. 5.2).

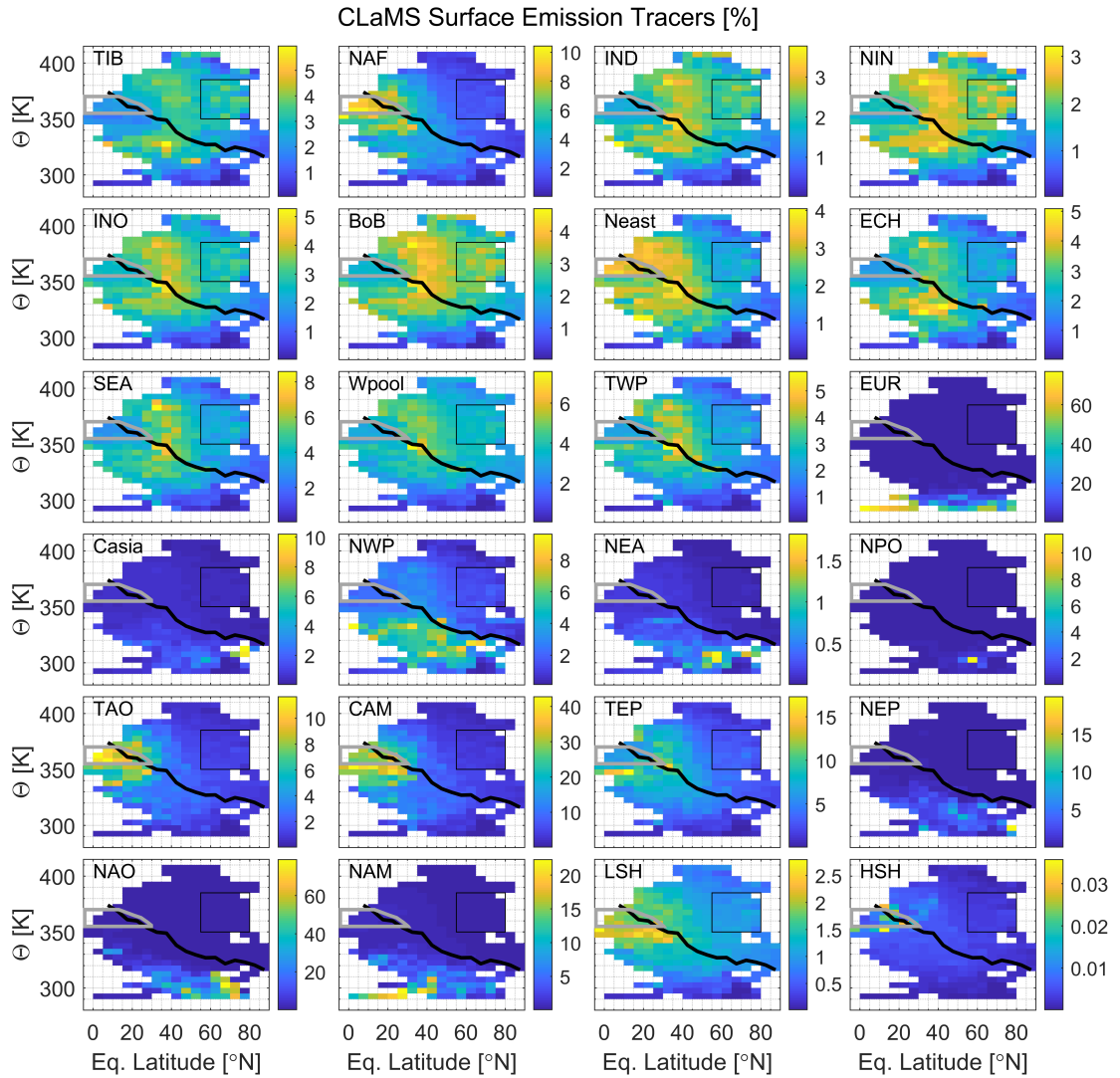


Figure C.2: Relative contribution of CLaMS surface emission tracers during the WISE campaign. The 24 different surface regions are displayed in Fig. 3.7. The black line is the average WMO tropopause, the black box indicates the HBrR, and the gray outline is the tropical  $\Theta_{\text{high}}/PV_{\text{low}}$  region (defined in Sect. 5.2).

# Publications by the Author

Within the framework of this dissertation the following article was submitted to a refereed journal:

**Rotermund, M. K.**, Bense, V., Chipperfield, M. P., Engel, A., Groß, J.-U., Hoor, P., Hüneke, T., Keber, T., Kluge, F., Schreiner, B., Schuck, T., Vogel, B., Zahn, A., and Pfeilsticker, K.: Organic and inorganic bromine measurements around the extratropical tropopause and lowermost stratosphere: Insights into the transport pathways and total bromine, *Atmos. Chem. Phys. Discuss.* [preprint], <https://doi.org/10.5194/acp-2021-202>, in review, 2021.

The following published article was referenced in this dissertation:

Kluge, F., Hüneke, T., Knecht, M., Lichtenstern, M., **Rotermund, M.**, Schlager, H., Schreiner, B., and Pfeilsticker, K.: Profiling of formaldehyde, glyoxal, methylglyoxal, and CO over the Amazon: normalized excess mixing ratios and related emission factors in biomass burning plumes, *Atmos. Chem. Phys.*, 20, 12363–12389, <https://doi.org/10.5194/acp-20-12363-2020>, 2020.

# Bibliography

- Adcock, K. E., Fraser, P. J., Hall, B. D., Langenfelds, R. L., Lee, G., Montzka, S. A., Oram, D. E., Röckmann, T., Stroh, F., Sturges, W. T., Vogel, B., and Laube, J. C.: Aircraft-Based Observations of Ozone-Depleting Substances in the Upper Troposphere and Lower Stratosphere in and Above the Asian Summer Monsoon, *J. Geophys. Res. Atmos.*, 126, e2020JD033137, <https://doi.org/10.1029/2020JD033137>, 2021.
- Aliwell, S., Van Roozendaal, M., Johnston, P., Richter, A., Wagner, T., Arlander, D., Burrows, J., Fish, D., Jones, R., Tørnkvist, K., et al.: Analysis for BrO in zenith-sky spectra: An intercomparison exercise for analysis improvement, *J. Geophys. Res. Atmos.*, 107, ACH-10, 2002.
- Aschmann, J. and Sinnhuber, B.-M.: Contribution of very short-lived substances to stratospheric bromine loading: uncertainties and constraints, *Atmos. Chem. Phys.*, 13, 1203–1219, <https://doi.org/10.5194/acp-13-1203-2013>, 2013.
- Aschmann, J., Sinnhuber, B.-M., Atlas, E. L., and Schauffler, S. M.: Modeling the transport of very short-lived substances into the tropical upper troposphere and lower stratosphere, *Atmos. Chem. Phys.*, 9, 9237–9247, <https://doi.org/10.5194/acp-9-9237-2009>, 2009.
- Aschmann, J., Sinnhuber, B.-M., Chipperfield, M. P., and Hossaini, R.: Impact of deep convection and dehydration on bromine loading in the upper troposphere and lower stratosphere, *Atmos. Chem. Phys.*, 11, 2671–2687, <https://doi.org/10.5194/acp-11-2671-2011>, 2011.
- Ashfold, M. J., Harris, N. R. P., Atlas, E. L., Manning, A. J., and Pyle, J. A.: Transport of short-lived species into the Tropical Tropopause Layer, *Atmos. Chem. Phys.*, 12, 6309–6322, <https://doi.org/10.5194/acp-12-6309-2012>, 2012.
- Badia, A., Reeves, C. E., Baker, A. R., Saiz-Lopez, A., Volkamer, R., Koenig, T. K., Apel, E. C., Hornbrook, R. S., Carpenter, L. J., Andrews, S. J., Sherwen, T., and von Glasow, R.: Importance of reactive halogens in the tropical marine atmosphere: a regional modelling study using WRF-Chem, *Atmos. Chem. Phys.*, 19, 3161–3189, <https://doi.org/10.5194/acp-19-3161-2019>, 2019.
- Ball, W. T., Alsing, J., Mortlock, D. J., Staehelin, J., Haigh, J. D., Peter, T., Tummon, F., Stübi, R., Stenke, A., Anderson, J., Bourassa, A., Davis, S. M., Degenstein, D., Frith, S., Froidevaux, L., Roth, C., Sofieva, V., Wang, R., Wild, J., Yu, P., Ziemke, J. R., and Rozanov, E. V.: Evidence for a continuous decline in lower stratospheric ozone offsetting ozone layer recovery, *Atmos. Chem. Phys.*, 18, 1379–1394, <https://doi.org/10.5194/acp-18-1379-2018>, 2018.
- Ball, W. T., Alsing, J., Staehelin, J., Davis, S. M., Froidevaux, L., and Peter, T.: Stratospheric ozone trends for 1985–2018: sensitivity to recent large variability, *Atmos. Chem. Phys.*, 19, 12731–12748, <https://doi.org/10.5194/acp-19-12731-2019>, 2019.
- Ball, W. T., Chiodo, G., Abalos, M., Alsing, J., and Stenke, A.: Inconsistencies between chemistry–climate models and observed lower stratospheric ozone trends since 1998, *Atmos. Chem. Phys.*, 20, 9737–9752, <https://doi.org/10.5194/acp-20-9737-2020>, 2020.
- Barrera, J. A., Fernandez, R. P., Iglesias-Suarez, F., Cuevas, C. A., Lamarque, J.-F., and Saiz-Lopez, A.: Seasonal impact of biogenic very short-lived bromocarbons on lowermost stratospheric ozone

- between 60° N and 60° S during the 21st century, *Atmos. Chem. Phys.*, 20, 8083–8102, <https://doi.org/10.5194/acp-20-8083-2020>, 2020.
- Bates, D. R. and Nicolet, M.: The photochemistry of atmospheric water vapor, *J. Geophys. Res.* (1896–1977), 55, 301–327, <https://doi.org/10.1029/JZ055i003p00301>, 1950.
- Bekki, S., Rap, A., Poulain, V., Dhomse, S., Marchand, M., Lefèvre, F., Forster, P. M., Szopa, S., and Chipperfield, M. P.: Climate impact of stratospheric ozone recovery, *Geophysical Research Letters*, 40, 2796–2800, 2013.
- Birner, T. and Bönisch, H.: Residual circulation trajectories and transit times into the extratropical lowermost stratosphere, *Atmos. Chem. Phys.*, 11, 817–827, <https://doi.org/10.5194/acp-11-817-2011>, 2011.
- Bobrowski, N., Hönninger, G., Galle, B., and Platt, U.: Detection of bromine monoxide in a volcanic plume, *Nature*, 423, 273–276, <https://doi.org/10.1038/nature01625>, 2003.
- Bogumil, K., Orphal, J., Homann, T., Voigt, S., Spietz, P., Fleischmann, O. C., Vogel, A., Hartmann, M., Kromminga, H., Bovensmann, H., Frerick, J., and Burrows, J. P.: Measurements of molecular absorption spectra with the SCIAMACHY pre-flight model: Instrument characterization and reference data for atmospheric remote sensing in the 230–2380 nm region, *J. Photochem. Photobiol. A.: Chem.*, 157, 167–184, [https://doi.org/10.1016/S1010-6030\(03\)00062-5](https://doi.org/10.1016/S1010-6030(03)00062-5), 2003.
- Bönisch, H., Engel, A., Curtius, J., Birner, T., and Hoor, P.: Quantifying transport into the lowermost stratosphere using simultaneous in-situ measurements of SF<sub>6</sub> and CO<sub>2</sub>, *Atmos. Chem. Phys.*, 9, 5905–5919, <https://doi.org/10.5194/acp-9-5905-2009>, 2009.
- Brasseur, G. and Solomon, S.: *Aeronomy of the Middle Atmosphere: Chemistry and Physics of the Stratosphere and Mesosphere* (3rd ed.), no. ISBN 978-90-277-2343-7 in 1383-8601, Springer: Dordrecht, The Netherlands, <https://doi.org/10.1007/978-94-009-4762-7>, 2005.
- Brinckmann, S., Engel, E., Bönisch, H., Quack, B., and E., A.: Short-lived brominated hydrocarbons – observations in the source regions and the tropical tropopause layer, *Atmos. Chem. Phys.*, 12, 1213–1228, <https://doi.org/10.5194/acp-12-1213-2012>, 2012.
- Bucci, S., Legras, B., Sellitto, P., D’Amato, F., Viciani, S., Montori, A., Chiarugi, A., Ravagnani, F., Ulanovsky, A., Cairo, F., and Stroh, F.: Deep-convective influence on the upper troposphere–lower stratosphere composition in the Asian monsoon anticyclone region: 2017 StratoClim campaign results, *Atmos. Chem. Phys.*, 20, 12 193–12 210, <https://doi.org/10.5194/acp-20-12193-2020>, 2020.
- Butchart, N. and Remsberg, E. E.: The Area of the Stratospheric Polar Vortex as a Diagnostic for Tracer Transport on an Isentropic Surface, *Journal of Atmospheric Sciences*, 43, 1319 – 1339, [https://doi.org/10.1175/1520-0469\(1986\)043<1319:TAOTSP>2.0.CO;2](https://doi.org/10.1175/1520-0469(1986)043<1319:TAOTSP>2.0.CO;2), 1986.
- Carpenter, L. J., Reimann, S., Burkholder, J. B., Clerbaux, C., Hall, B. D., Hossaini, R., Laube, J. C., and Yvon-Lewis, S. A.: Scientific assessment of ozone depletion: 2014, *Global Ozone Research and Monitoring Project–Report No. 55*, World Meteorological Organisation (WMO), Geneva, Switzerland, 10, 416, 2014.
- Chance, K. and Kurucz, R.: An improved high-resolution solar reference spectrum for earth’s atmosphere measurements in the ultraviolet, visible, and near infrared, *Journal of Quantitative Spectroscopy and Radiative Transfer*, 111, 1289 – 1295, <https://doi.org/10.1016/j.jqsrt.2010.01.036>, special Issue Dedicated to Laurence S. Rothman on the Occasion of his 70th Birthday., 2010.
- Chipperfield, M. P.: Multiannual simulations with a three-dimensional chemical transport model, *J. Geophys. Res. Atmos.*, 104, 1781–1805, <https://doi.org/10.1029/98JD02597>, 1999.
- Chipperfield, M. P.: New Version of the TOMCAT/SLIMCAT Off-Line Chemical Transport Model: Intercomparison of Stratospheric Tracer Experiments, *Q. J. R. Meteorolog. Soc.*, 132, 1179 – 1203, <https://doi.org/10.1256/qj.05.51>, 2006.

- Chipperfield, M. P., Dhomse, S., Hossaini, R., Feng, W., Santee, M. L., Weber, M., Burrows, J. P., Wild, J. D., Loyola, D., and Coldewey-Egbers, M.: On the Cause of Recent Variations in Lower Stratospheric Ozone, *Geophys. Res. Lett.*, 45, 5718–5726, <https://doi.org/10.1029/2018GL078071>, 2018.
- Chipperfield, M. P., Hossaini, R., Montzka, S. A., Reimann, S., Sherry, D., and Tegtmeier, S.: Renewed and emerging concerns over the production and emission of ozone-depleting substances, *Nat. Rev. Earth Environ.*, 1, 251–263, <https://doi.org/10.1038/s43017-020-0048-8>, 2020.
- Crutzen, P. J.: The influence of nitrogen oxides on the atmospheric ozone content, *Quarterly Journal of the Royal Meteorological Society*, 96, 320–325, <https://doi.org/10.1002/qj.49709640815>, 1970.
- Dee, D. P., Uppala, S. M., Simmons, A. J., Berrisford, P., Poli, P., Kobayashi, S., Andrae, U., Balmaseda, M. A., Balsamo, G., Bauer, P., Bechtold, P., Beljaars, A. C. M., van de Berg, L., Bidlot, J., Bormann, N., Delsol, C., Dragani, R., Fuentes, M., Geer, A. J., Haimberger, L., Healy, S. B., Hersbach, H., Hólm, E. V., Isaksen, I., Kallberg, P., Köhler, M., Matricardi, M., McNally, A. P., Monge-Sanz, B. M., Morcrette, J.-J., Park, B.-K., Peubey, C., de Rosnay, P., Tavolato, C., Thepaut, J.-N., and Vitart, F.: The ERA-Interim reanalysis: configuration and performance of the data assimilation system, *Quarterly Journal of the Royal Meteorological Society*, 137, 553–597, <https://doi.org/10.1002/qj.828>, 2011.
- Deutschmann, T., Beirle, S., Frieß, U., Grzegorski, M., Kern, C., Kritzen, L., Platt, U., Prados-Román, C., Puķīte, J., Wagner, T., et al.: The Monte Carlo atmospheric radiative transfer model McArtim: Introduction and validation of Jacobians and 3D features, *Journal of Quantitative Spectroscopy and Radiative Transfer*, 112, 1119–1137, 2011.
- Dhomse, S., Feng, W., Montzka, S., Hossaini, R., Keeble, J., Pyle, J., Daniel, J., and Chipperfield, M.: Delay in recovery of the Antarctic ozone hole from unexpected CFC-11 emissions, *Nature Commun.*, 10, <https://doi.org/10.1038/s41467-019-13717-x>, 2019.
- Dorf, M., Bösch, H., Butz, A., Camy-Peyret, C., Chipperfield, M. P., Engel, A., Goutail, F., Grunow, K., Hendrick, F., Hrechanyy, S., Naujokat, B., Pommereau, J.-P., Van Roozendaal, M., Sioris, C., Stroh, F., Weidner, F., and Pfeilsticker, K.: Balloon-borne stratospheric BrO measurements: comparison with Envisat/SCIAMACHY BrO limb profiles, *Atmos. Chem. Phys.*, 6, 2483–2501, <https://doi.org/10.5194/acp-6-2483-2006>, 2006a.
- Dorf, M., Butler, J., Butz, A., Camy-Peyret, C., Chipperfield, M., Kritzen, L., Montzka, S., Simmes, B., Weidner, F., and Pfeilsticker, K.: Long-term observations of stratospheric bromine reveal slow down in growth, *Geophysical research letters*, 33, 2006b.
- Dorf, M., Butz, A., Camy-Peyret, C., Chipperfield, M. P., Kritzen, L., and Pfeilsticker, K.: Bromine in the tropical troposphere and stratosphere as derived from balloon-borne BrO observations, *Atmos. Chem. Phys.*, 8, 7265–7271, <https://doi.org/10.5194/acp-8-7265-2008>, 2008.
- Engel, A., Rigby, M., (Lead Authors), Burkholder, J. B., Fernandex, R. P., Froidevaux, L., Hall, B. D., Hossaini, R., Saito, T., Vollmer, M. K., and Yao, B.: Update on Ozone-Depleting Substances (ODS) and Other Gases of Interest to the Montreal Protocol, Chapter 1 in *Scientific Assessment of Ozone Depletion: 2018*, Global Ozone Research and Monitoring Project—Report No. 58, World Meteorological Organization, Geneva, Switzerland, 2018.
- Fahey, D. and Hegglin, M.: Twenty Questions and Answers About the Ozone Layer: 2010 Update, *Scientific Assessment of Ozone Depletion: 2010*, World Meteorological Organisation (WMO), Geneva, Switzerland, p. 72pp., URL <https://csl.noaa.gov/assessments/ozone/2010/twentyquestions/>, [Reprinted from *Scientific Assessment of Ozone Depletion: 2010*, Global Ozone Research and Monitoring Project—Report No. 52, 516 pp., World Meteorological Organization, Geneva, Switzerland, 2011.], 2011.

- Falk, S., Sinnhuber, B.-M., Krzysztofiak, G., Jöckel, P., Graf, P., and Lennartz, S. T.: Brominated VLSL and their influence on ozone under a changing climate, *Atmos. Chem. Phys.*, 17, 11 313–11 329, <https://doi.org/10.5194/acp-17-11313-2017>, 2017.
- Farman, J., Gardiner, B., and Shanklin, J.: Large losses of total ozone in Antarctica reveal seasonal ClO<sub>x</sub>/NO<sub>x</sub> interaction, *Nature*, 315, 207–210, <https://doi.org/10.1038/315207a0>, 1985.
- Fernandez, R. P., Kinnison, D. E., Lamarque, J.-F., Tilmes, S., and Saiz-Lopez, A.: Impact of biogenic very short-lived bromine on the Antarctic ozone hole during the 21st century, *Atmospheric Chemistry and Physics*, 17, 1673–1688, <https://doi.org/10.5194/acp-17-1673-2017>, 2017.
- Fiehn, A., Quack, B., Marandino, C. A., and Krüger, K.: Transport Variability of Very Short Lived Substances From the West Indian Ocean to the Stratosphere, *J. Geophys. Res. Atmos.*, 123, 5720–5738, <https://doi.org/10.1029/2017JD027563>, 2018.
- Filus, M. T., Atlas, E. L., Navarro, M. A., Meneguz, E., Thomson, D., Ashfold, M. J., Carpenter, L. J., Andrews, S. J., and Harris, N. R. P.: Transport of short-lived halocarbons to the stratosphere over the Pacific Ocean, *Atmos. Chem. Phys.*, 20, 1163–1181, <https://doi.org/10.5194/acp-20-1163-2020>, 2020.
- Fix, A., Steinebach, F., Wirth, M., Schäfler, A., and Ehret, G.: Development and application of an airborne differential absorption lidar for the simultaneous measurement of ozone and water vapor profiles in the tropopause region, *Appl. Opt.*, 58, 5892–5900, <https://doi.org/10.1364/AO.58.005892>, 2019.
- Fleischmann, O. C., M., H., Burrows, J. P., and Orphal, J.: New ultraviolet absorption cross-sections of BrO at atmospheric temperatures measured by a time-windowing Fourier transform spectroscopy, *J. Photochem. Photobiol. A.: Chem.*, 168, 117–132, <https://doi.org/10.1016/j.jphotochem.2004.03.026>, 2004.
- Fueglistaler, S., Wernli, H., and Peter, T.: Tropical troposphere-to-stratosphere transport inferred from trajectory calculations, *J. Geophys. Res. Atmos.*, 109, <https://doi.org/10.1029/2003JD004069>, 2004.
- Fueglistaler, S., Dessler, A. E., Dunkerton, T. J., Folkins, I., Fu, Q., and Mote, P. W.: Tropical tropopause layer, *Rev. Geophys.*, 47, <https://doi.org/10.1029/2008RG000267>, 2009.
- Garny, H. and Randel, W. J.: Transport pathways from the Asian monsoon anticyclone to the stratosphere, *Atmos. Chem. Phys.*, 16, 2703–2718, <https://doi.org/10.5194/acp-16-2703-2016>, 2016.
- Gettelman, A., Hoor, P., Pan, L. L., Randel, W. J., Hegglin, M. I., and Birner, T.: The extratropical upper troposphere and lower stratosphere, *Rev. Geophys.*, 49, RG3003, <https://doi.org/10.1029/2011RG000355>, 2011.
- Grainger, J. and Ring, J.: Anomalous Fraunhofer Line Profiles, *Nature*, 193, 762, <https://doi.org/10.1038/193762a0>, 1962.
- Großmann, K.: Aircraft-borne DOAS limb observations of UV/visible absorbing trace gas species over Borneo: Implications for the photochemistry of iodine, volatile organic oxide degradation, and lightning-produced radicals, PhD thesis, Ruprecht-Karls-Universität Heidelberg, Heidelberg, Germany, URL <https://www.iup.uni-heidelberg.de/de/research/stratosphere/publications#theses>, 2014.
- Groß, J.-U., Engel, I., Borrmann, S., Frey, W., Günther, G., Hoyle, C. R., Kivi, R., Luo, B. P., Molleker, S., Peter, T., Pitts, M. C., Schlager, H., Stiller, G., Vömel, H., Walker, K. A., and Müller, R.: Nitric acid trihydrate nucleation and denitrification in the Arctic stratosphere, *Atmos. Chem. Phys.*, 14, 1055–1073, <https://doi.org/10.5194/acp-14-1055-2014>, 2014.

- Hamer, P. D., Marécal, V., Hossaini, R., Pirre, M., Krysztofiak, G., Ziska, F., Engel, A., Sala, S., Keber, T., Bönisch, H., Atlas, E., Krüger, K., Chipperfield, M., Catoire, V., Samah, A. A., Dorf, M., Siew Moi, P., Schlager, H., and Pfeilsticker, K.: Cloud-scale modelling of the impact of deep convection on the fate of oceanic bromoform in the troposphere: a case study over the west coast of Borneo, *Atmos. Chem. Phys. Discuss.*, 2020, 1–42, <https://doi.org/10.5194/acp-2020-655>, 2020.
- Harder, H., Camy-Peyret, C., Ferlemann, F., Fitzenberger, R., Hawat, T., Osterkamp, H., Schneider, M., Perner, D., Platt, U., Vradelis, P., et al.: Stratospheric BrO profiles measured at different latitudes and seasons: Atmospheric observations, *Geophysical research letters*, 25, 3843–3846, 1998.
- Harder, H., Bösch, H., Camy-Peyret, C., Chipperfield, M. P., Fitzenberger, R., Payan, S., Perner, D., Platt, U., Sinnhuber, B.-M., and Pfeilsticker, K.: Comparison of measured and modeled stratospheric BrO: Implications for the total amount of stratospheric bromine, *Geophys. Res. Lett.*, 27, 3695–3698, <https://doi.org/10.1029/1999GL011215>, 2000.
- Harris, N. R. P., Carpenter, L. J., Lee, J. D., Vaughan, G., Filus, M. T., Jones, R. L., OuYang, B., Pyle, J. A., Robinson, A. D., Andrews, S. J., Lewis, A. C., Minaeian, J., Vaughan, A., Dorsey, J. R., Gallagher, M. W., Le Breton, M., Newton, R., Percival, C. J., Ricketts, H. M. A., Bauguitte, S. J.-B., Nott, G. J., Wellpott, A., Ashfold, M. J., Flemming, J., Butler, R., Palmer, P. I., Kaye, P. H., Stopford, C., Chemel, C., Boesch, H., Humpage, N., Vick, A., MacKenzie, A. R., Hyde, R., Angelov, P., Meneguz, E., and Manning, A. J.: Coordinated Airborne Studies in the Tropics (CAST), *Bull. Am. Meteorol. Soc.*, 98, 145–162, <https://doi.org/10.1175/BAMS-D-14-00290.1>, 2017.
- Hauck, M., Bönisch, H., Hoor, P., Keber, T., Ploeger, F., Schuck, T. J., and Engel, A.: A convolution of observational and model data to estimate age of air spectra in the northern hemispheric lower stratosphere, *Atmos. Chem. Phys.*, 20, 8763–8785, <https://doi.org/10.5194/acp-20-8763-2020>, 2020.
- Hendrick, F., Van Roozendael, M., Chipperfield, M. P., Dorf, M., Goutail, F., Yang, X., Fayt, C., Hermans, C., Pfeilsticker, K., Pommereau, J.-P., Pyle, J. A., Theys, N., and De Mazière, M.: Retrieval of stratospheric and tropospheric BrO profiles and columns using ground-based zenith-sky DOAS observations at Harestua, 60°N, *Atmos. Chem. Phys.*, 7, 4869–4885, <https://doi.org/10.5194/acp-7-4869-2007>, 2007.
- Hendrick, F., Johnston, P. V., De Mazière, M., Fayt, C., Hermans, C., Kreher, K., Theys, N., Thomas, A., and Van Roozendael, M.: One-decade trend analysis of stratospheric BrO over Harestua (60°N) and Lauder (45°S) reveals a decline, *Geophys. Res. Lett.*, 35, <https://doi.org/10.1029/2008GL034154>, 114801, 2008.
- Hendrick, F., Rozanov, A., Johnston, P. V., Bovensmann, H., De Mazière, M., Fayt, C., Hermans, C., Kreher, K., Lotz, W., Sinnhuber, B.-M., Theys, N., Thomas, A., Burrows, J. P., and Van Roozendael, M.: Multi-year comparison of stratospheric BrO vertical profiles retrieved from SCIAMACHY limb and ground-based UV-visible measurements, *Atmos. Meas. Tech.*, 2, 273–285, <https://doi.org/10.5194/amt-2-273-2009>, 2009.
- Henriksen, T., Dahlback, A., Larsen, S. H., and Moan, J.: Ultraviolet-radiation and skin cancer. Effect of an ozone layer depletion, *Photochem. Photobiol.*, 51, 579–582, <https://doi.org/10.1111/j.1751-1097.1990.tb01968.x>, 1990.
- Hess, M., Koepke, P., and Schult, I.: Optical Properties of Aerosols and Clouds: The Software Package OPAC, *Bulletin of the American Meteorological Society*, 79, 831 – 844, [https://doi.org/10.1175/1520-0477\(1998\)079%3C0831:OPOAAC%3E2.0.CO;2](https://doi.org/10.1175/1520-0477(1998)079%3C0831:OPOAAC%3E2.0.CO;2), 1998.
- Holton, J. R., Haynes, P. H., McIntyre, M. E., Douglass, A. R., Rood, R. B., and Pfister, L.: Stratosphere-troposphere exchange, *Rev. Geophys.*, 33, 403–439, <https://doi.org/10.1029/95RG02097>, 1995.

- Homeyer, C. R. and Bowman, K. P.: Rossby Wave Breaking and Transport between the Tropics and Extratropics above the Subtropical Jet, *J. Atmos. Sci.*, 70, 607 – 626, <https://doi.org/10.1175/JAS-D-12-0198.1>, 2013.
- Hoor, P., Fischer, H., and Lelieveld, J.: Tropical and extratropical tropospheric air in the lowermost stratosphere over Europe: A CO-based budget, *Geophys. Res. Lett.*, 32, <https://doi.org/10.1029/2004gl022018>, 107802, 2005.
- Hossaini, R., Chipperfield, M. P., Dhomse, S., Ordóñez, C., Saiz-Lopez, A., Abraham, N. L., Archibald, A., Braesicke, P., Telford, P., Warwick, N., Yang, X., and Pyle, J.: Modelling future changes to the stratospheric source gas injection of biogenic bromocarbons, *Geophys. Res. Lett.*, 39, <https://doi.org/10.1029/2012GL053401>, 120813, 2012a.
- Hossaini, R., Chipperfield, M. P., Feng, W., Breider, T. J., Atlas, E., Montzka, S. A., Miller, B. R., Moore, F., and Elkins, J.: The contribution of natural and anthropogenic very short-lived species to stratospheric bromine, *Atmos. Chem. Phys.*, 12, 371–380, <https://doi.org/10.5194/acp-12-371-2012>, 2012b.
- Hossaini, R., Mantle, H., Chipperfield, M., Montzka, S., Hamer, P., Ziska, F., Quack, B., Krüger, K., Tegtmeier, S., Atlas, E., et al.: Evaluating global emission inventories of biogenic bromocarbons, *Atmos. Chem. Phys. Discuss.*, 13, 12 485–12 539, 2013.
- Hossaini, R., Chipperfield, M., Montzka, S., Rap, A., Dhomse, S., and Feng, W.: Efficiency of short-lived halogens at influencing climate through depletion of stratospheric ozone, *Nat. Geosci.*, 8, 186–190, <https://doi.org/10.1038/ngeo2363>, 2015.
- Hossaini, R., Patra, P. K., Leeson, A. A., Krysztofiak, G., Abraham, N. L., Andrews, S. J., Archibald, A. T., Aschmann, J., Atlas, E. L., Belikov, D. A., et al.: A multi-model intercomparison of halogenated very short-lived substances (TransCom-VSLS): linking oceanic emissions and tropospheric transport for a reconciled estimate of the stratospheric source gas injection of bromine, *Atmos. Chem. Phys.*, 16, 9163–9187, 2016.
- Hossaini, R., Chipperfield, M. P., Montzka, S. A., Leeson, A. A., Dhomse, S. S., and Pyle, J. A.: The increasing threat to stratospheric ozone from dichloromethane, *Nature Communications*, 8, 1–9, <https://doi.org/10.1038/ncomms15962>, 2017.
- Höpfner, M., Orphal, J., von Clarmann, T., Stiller, G., and Fischer, H.: Stratospheric BrONO<sub>2</sub> observed by MIPAS, *Atmos. Chem. Phys.*, 9, 1735–1746, <https://doi.org/10.5194/acp-9-1735-2009>, 2009.
- Hüneke, T.: The scaling method applied to HALO measurements: Inferring absolute trace gas concentrations from airborne limb spectroscopy under all sky conditions, PhD thesis, Ruprecht-Karls-Universität Heidelberg, Heidelberg, Germany, URL <https://www.iup.uni-heidelberg.de/de/research/stratosphere/publications#theses>, 2016.
- Hüneke, T., Aderhold, O.-A., Bounin, J., Dorf, M., Gentry, E., Grossmann, K., Groß, J.-U., Hoor, P., Jöckel, P., Kenntner, M., et al.: The novel halo mini-DOAS instrument: Inferring trace gas concentrations from air-borne UV/visible limb spectroscopy under all skies using the scaling method, *Atmos. Meas. Tech.*, pp. 4209–4234, 2017.
- Inai, Y., Fujita, R., Machida, T., Matsueda, H., Sawa, Y., Tsuboi, K., Katsumata, K., Morimoto, S., Aoki, S., and Nakazawa, T.: Seasonal characteristics of trace gas transport into the extratropical upper troposphere and lower stratosphere, *Atmos. Chem. Phys.*, 19, 7073–7103, <https://doi.org/10.5194/acp-19-7073-2019>, 2019.
- Irvine, W. M.: The formation of absorption bands and the distribution of photon optical paths in a scattering atmosphere, *Bull. Astron. Inst. Neth.*, 17, 266–279, 1964.

- Jensen, E.-J., Pfister, L., Jordan, D. E., Fahey, D. W., Newman, P. A., Thornberry, T., Rollins, A., Diskin, G., Bui, T. P., McGill, M., Hlavka, D., Lawson, R. P., Gao, R.-S., Pilewskie, P., Elkins, J., Hints, E., Moore, F., Mahoney, M. J., Atlas, E., Stutz, J., Pfeilsticker, K., Wofsy, S., Evan, S., and Rosenlof, K. H.: The NASA Airborne Tropical Tropopause EXperiment (ATTREX), SPARC newsletter, 41, 15 – 24, URL [http://issuu.com/sparc-climate/docs/41\\_sparcnewsletter\\_jul2013\\_web/24](http://issuu.com/sparc-climate/docs/41_sparcnewsletter_jul2013_web/24), 2013.
- Johnston, H.: Reduction of Stratospheric Ozone by Nitrogen Oxide Catalysts from Supersonic Transport Exhaust, *Science*, 173, 517–522, <https://doi.org/10.1126/science.173.3996.517>, 1971.
- Kaluza, T., Kunkel, D., and Hoor, P.: Composite analysis of the tropopause inversion layer in extratropical baroclinic waves, *Atmos. Chem. Phys.*, 19, 6621–6636, <https://doi.org/10.5194/acp-19-6621-2019>, 2019.
- Keber, T., Bönisch, H., Hartick, C., Hauck, M., Lefrancois, F., Obersteiner, F., Ringsdorf, A., Schohl, N., Schuck, T., Hossaini, R., Graf, P., Jöckel, P., and Engel, A.: Bromine from short-lived source gases in the extratropical northern hemispheric upper troposphere and lower stratosphere (UTLS), *Atmos. Chem. Phys.*, 20, 4105–4132, <https://doi.org/10.5194/acp-20-4105-2020>, 2020.
- Keller-Rudek, H., Moortgat, G. K., Sander, R., and Sörensen, R.: The MPI-Mainz UV/VIS Spectral Atlas of Gaseous Molecules of Atmospheric Interest, *Earth System Science Data*, 5, 365–373, <https://doi.org/10.5194/essd-5-365-2013>, 2013.
- Kluge, F.: Auswertung flugzeuggetragener DOAS Messungen von C<sub>2</sub>H<sub>2</sub>O<sub>2</sub>, CH<sub>2</sub>O, NO<sub>2</sub>, O<sub>3</sub> und O<sub>4</sub> über dem Amazonas-Regenwald während der ACRIDICON-CHUVA Messkampagne, Master thesis, Ruprecht-Karls-Universität Heidelberg, Heidelberg, Germany, 2018.
- Kluge, F., Hüneke, T., Knecht, M., Lichtenstern, M., Rotermund, M., Schlager, H., Schreiner, B., and Pfeilsticker, K.: Profiling of formaldehyde, glyoxal, methylglyoxal, and CO over the Amazon: normalized excess mixing ratios and related emission factors in biomass burning plumes, *Atmos. Chem. Phys.*, 20, 12363–12389, <https://doi.org/10.5194/acp-20-12363-2020>, 2020.
- Knapp, M.: Optische und Elektronische Charakterisierung des HALO mini-DOAS Instruments sowie eine Analyse der Unsicherheit in der Blickrichtung für die Skalierungsmethode, Bachelor thesis, Ruprecht-Karls-Universität Heidelberg, Heidelberg, Germany, 2016.
- Knecht, M.: Simulation of radiative field modification due to tropical clouds, Master’s thesis, University of Heidelberg, Heidelberg, Germany, URL [https://www.iup.uni-heidelberg.de/de/research/stratosphere/files/theses/masters/MA\\_thesis\\_Matthias\\_final.pdf](https://www.iup.uni-heidelberg.de/de/research/stratosphere/files/theses/masters/MA_thesis_Matthias_final.pdf), (last access: 29 January 2021), 2015.
- Ko, M. K. W., Newman, P. A., Reimann, S., and Strahan, E.: Lifetimes of Stratospheric Ozone-Depleting Substances, Their Replacements, and Related Species, SPARC Report, WCRP-15/2013, 1 – 255, URL <http://www.sparc-climate.org/publications/sparc-reports/>, 2013.
- Koenig, T. K., Volkamer, R., Baidar, S., Dix, B., Wang, S., Anderson, D. C., Salawitch, R. J., Wales, P. A., Cuevas, C. A., Fernandez, R. P., Saiz-Lopez, A., Evans, M. J., Sherwen, T., Jacob, D. J., Schmidt, J., Kinnison, D., Lamarque, J.-F., Apel, E. C., Bresch, J. C., Campos, T., Flocke, F. M., Hall, S. R., Honomichl, S. B., Hornbrook, R., Jensen, J. B., Lueb, R., Montzka, D. D., Pan, L. L., Reeves, J. M., Schauffler, S. M., Ullmann, K., Weinheimer, A. J., Atlas, E. L., Donets, V., Navarro, M. A., Riemer, D., Blake, N. J., Chen, D., Huey, L. G., Tanner, D. J., Hanisco, T. F., and Wolfe, G. M.: BrO and inferred Br<sub>y</sub> profiles over the western Pacific: relevance of inorganic bromine sources and a Br<sub>y</sub> minimum in the aged tropical tropopause layer, *Atmos. Chem. Phys.*, 17, 15245–15270, <https://doi.org/10.5194/acp-17-15245-2017>, 2017.
- Koenig, T. K., Baidar, S., Campuzano-Jost, P., Cuevas, C. A., Dix, B., Fernandez, R. P., Guo, H., Hall, S. R., Kinnison, D., Nault, B. A., Ullmann, K., Jimenez, J. L., Saiz-Lopez, A., and Volkamer,

- R.: Quantitative detection of iodine in the stratosphere, *Proceedings of the National Academy of Sciences*, 117, 1860–1866, <https://doi.org/10.1073/pnas.1916828117>, 2020.
- Konopka, P., Ploeger, F., Tao, M., Birner, T., and Riese, M.: Hemispheric asymmetries and seasonality of mean age of air in the lower stratosphere: Deep versus shallow branch of the Brewer-Dobson circulation, *J. Geophys. Res. Atmos.*, 120, 2053–2066, <https://doi.org/10.1002/2014JD022429>, 2015.
- Kovács, T., Feng, W., Totterdill, A., Plane, J. M. C., Dhomse, S., Gómez-Martín, J. C., Stiller, G. P., Haenel, F. J., Smith, C., Forster, P. M., García, R. R., Marsh, D. R., and Chipperfield, M. P.: Determination of the atmospheric lifetime and global warming potential of sulfur hexafluoride using a three-dimensional model, *Atmos. Chem. Phys.*, 17, 883–898, <https://doi.org/10.5194/acp-17-883-2017>, 2017.
- Kraus, S.: DOASIS: A Framework Design for DOAS, Informatik, Shaker Verlag, URL <http://www.shaker.eu/catalogue/Details.asp?ISBN=3-8322-5452-8>, 2006.
- Krautstrunk, M. and Giez, A.: The Transition From FALCON to HALO Era Airborne Atmospheric Research. In: Schumann U. (eds) *Atmospheric Physics. Research Topics in Aerospace.*, Springer-Verlag, Berlin, Heidelberg, URL [https://doi.org/10.1007/978-3-642-30183-4\\_37](https://doi.org/10.1007/978-3-642-30183-4_37), 2012.
- Kreycy, S., Camy-Peyret, C., Chipperfield, M., Dorf, M., Feng, W., Hossaini, R., Kritten, L., Werner, B., and Pfeilsticker, K.: Atmospheric test of the J (BrONO<sub>2</sub>)/kBrO+ NO<sub>2</sub> ratio: implications for total stratospheric Br<sub>y</sub> and bromine-mediated ozone loss, *Atmos. Chem. Phys.*, 13, 6263, 2013.
- Kunkel, D., Hoor, P., Kaluza, T., Ungermann, J., Kluschat, B., Giez, A., Lachnitt, H.-C., Kaufmann, M., and Riese, M.: Evidence of small-scale quasi-isentropic mixing in ridges of extratropical baroclinic waves, *Atmos. Chem. Phys.*, 19, 12607–12630, <https://doi.org/10.5194/acp-19-12607-2019>, 2019.
- Lampel, J., Pöhler, D., Tschritter, J., Frieß, U., and Platt, U.: On the relative absorption strengths of water vapour in the blue wavelength range, *Atmos. Meas. Tech.*, 8, 4329–4346, <https://doi.org/10.5194/amt-8-4329-2015>, 2015.
- Laube, J. C., Engel, A., Bönisch, H., Möbius, T., Worton, D. R., Sturges, W. T., Grunow, K., and Schmidt, U.: Contribution of very short-lived organic substances to stratospheric chlorine and bromine in the tropics – a case study, *Atmos. Chem. Phys.*, 8, 7325–7334, <https://doi.org/10.5194/acp-8-7325-2008>, 2008.
- Levenberg, K.: A method for the solution of certain non-linear problems in least squares, *Quarterly of Applied Mathematics*, 2, 164–168, URL <http://www.jstor.org/stable/43633451>, 1944.
- Levine, J. G., Braesicke, P., Harris, N. R. P., Savage, N. H., and Pyle, J. A.: Pathways and timescales for troposphere-to-stratosphere transport via the tropical tropopause layer and their relevance for very short lived substances, *J. Geophys. Res. Atmos.*, 112, <https://doi.org/10.1029/2005JD006940>, 2007.
- Li, D., Vogel, B., Bian, J., Müller, R., Pan, L. L., Günther, G., Bai, Z., Li, Q., Zhang, J., Fan, Q., and Vömel, H.: Impact of typhoons on the composition of the upper troposphere within the Asian summer monsoon anticyclone: the SWOP campaign in Lhasa 2013, *Atmos. Chem. Phys.*, 17, 4657–4672, <https://doi.org/10.5194/acp-17-4657-2017>, 2017.
- Li, D., Vogel, B., Müller, R., Bian, J., Günther, G., and Riese, M.: Tropical cyclones reduce ozone in the tropopause region over the western Pacific: An analysis of 18-year ozonesonde profiles, *Earth's Future*, 9, 2020EF001635, <https://doi.org/10.1029/2020EF001635>, 2021.
- Liang, Q., Stolarski, R. S., Kawa, S. R., Nielsen, J. E., Douglass, A. R., Rodriguez, J. M., Blake, D. R., Atlas, E. L., and Ott, L. E.: Finding the missing stratospheric Br<sub>y</sub>: a global modeling study of CHBr<sub>3</sub> and CH<sub>2</sub>Br<sub>2</sub>, *Atmos. Chem. Phys.*, 10, 2269–2286, <https://doi.org/10.5194/acp-10-2269-2010>, 2010.
- Liang, Q., Atlas, E., Blake, D., Dorf, M., Pfeilsticker, K., and Schauffler, S.: Convective transport of very short lived bromocarbons to the stratosphere, *Atmos. Chem. Phys.*, 14, 5781–5792, <https://doi.org/10.5194/acp-14-5781-2014>, 2014.

- Lörks, D.: Airborne spectroscopic measurements of BrO, OClO and NO<sub>2</sub> in the lowermost stratosphere during the Arctic winter 2015/2016: Implications for total bromine and the loss in ozone by the inter-halogen reaction BrO + ClO, Diploma thesis, Ruprecht-Karls-Universität Heidelberg, Heidelberg, Germany, URL <https://www.iup.uni-heidelberg.de/de/research/stratosphere/publications#theses>, 2019.
- Lucas, R. M., Yazar, S., Young, A. R., Norval, M., de Gruijl, F. R., Takizawa, Y., Rhodes, L. E., Sinclair, C. A., and Neale, R. E.: Human health in relation to exposure to solar ultraviolet radiation under changing stratospheric ozone and climate, *Photochem. Photobiol. Sci.*, 18, 641–680, <https://doi.org/10.1039/C8PP90060D>, 2019.
- Marquard, L. C., Wagner, T., and Platt, U.: Improved air mass factor concepts for scattered radiation differential optical absorption spectroscopy of atmospheric species, *J. Geophys. Res. Atmos.*, 105, 1315–1327, <https://doi.org/10.1029/1999JD900340>, 2000.
- Marquardt, D. W.: An Algorithm for Least-Squares Estimation of Nonlinear Parameters, *Journal of the Society for Industrial and Applied Mathematics*, 11, 431–441, URL <http://www.jstor.org/stable/2098941>, 1963.
- Martens, W. J. M., den Elzen, M. G. J., Slaper, H., Koken, P. J. M., and Willems, B. A. T.: The impact of ozone depletion on skin cancer incidence: An assessment of the Netherlands and Australia, *Environ. Model. Assess.*, 1, 229–240, <https://doi.org/10.1007/BF01872152>, 1996.
- Martin, J. E.: *Mid-Latitude Atmospheric Dynamics: A First Course*, ISBN 978-0-470-86464-7, John Wiley & Sons, Ltd, Chichester, England, 2006.
- McKenna, D. S., Groöß, J.-U., Günther, G., Konopka, P., Müller, R., Carver, G., and Sasano, Y.: A new Chemical Lagrangian Model of the Stratosphere (CLaMS) 2. Formulation of chemistry scheme and initialization, *J. Geophys. Res. Atmos.*, 107, ACH 4–1–ACH 4–14, <https://doi.org/10.1029/2000JD000113>, 2002a.
- McKenna, D. S., Konopka, P., Groöß, J.-U., Günther, G., Müller, R., Spang, R., Offermann, D., and Orsolini, Y.: A new Chemical Lagrangian Model of the Stratosphere (CLaMS) 1. Formulation of advection and mixing, *J. Geophys. Res. Atmos.*, 107, ACH 15–1–ACH 15–15, <https://doi.org/10.1029/2000JD000114>, 2002b.
- Mentges, J.: Light sources for calibration: Pen-Ray line sources for wavelength calibration, Quantum Design Europe GmbH, <https://qd-europe.com/de/en/product/light-sources-for-calibration/>, (accessed: 27.03.2021), 2021.
- Minikin, A., Beer, W., and Ziereis, H.: HALO: High Altitude and Long Range Research Aircraft, <http://www.halo.dlr.de>, (Last accessed: 07.07.2020), 2020.
- Müller, S., Hoor, P., Berkes, F., Bozem, H., Klingebiel, M., Reutter, P., Smit, H. G. J., Wendisch, M., Spichtinger, P., and Borrmann, S.: In situ detection of stratosphere-troposphere exchange of cirrus particles in the midlatitudes, *Geophysical Research Letters*, 42, 949–955, <https://doi.org/10.1002/2014GL062556>, 2015.
- Moan, J. and Dahlback, A.: The relationship between skin cancers, solar radiation and ozone depletion, *Br. J. Cancer*, 65, 916–921, <https://doi.org/10.1038/bjc.1992.192>, 1992.
- Moan, J., Grigalavicius, M., Baturaite, Z., Dahlback, A., and Juzeniene, A.: The relationship between UV exposure and incidence of skin cancer, *Photodermatology, Photoimmunology & Photomedicine*, 31, 26–35, <https://doi.org/10.1111/phpp.12139>, 2015.
- Molina, M. and Rowland, F.: Stratospheric sink for chlorofluoromethanes: chlorine atom-catalysed destruction of ozone, *Nature*, 249, 810–812, <https://doi.org/10.1038/249810a0>, 1974.

- Montzka, S. A., Butler, J. H., Hall, B. D., Mondeel, D. J., and Elkins, J. W.: A decline in tropospheric organic bromine, *Geophys. Res. Lett.*, 30, 1826–1829, <https://doi.org/10.1029/2003GL017745>, 2003.
- Müller, S., Hoor, P., Bozem, H., Gute, E., Vogel, B., Zahn, A., Bönisch, H., Keber, T., Krämer, M., Rolf, C., Riese, M., Schlager, H., and Engel, A.: Impact of the Asian monsoon on the extratropical lower stratosphere: trace gas observations during TACTS over Europe 2012, *Atmos. Chem. Phys.*, 16, 10573–10589, <https://doi.org/10.5194/acp-16-10573-2016>, 2016.
- NASA/LARC/SD/ASDC: SAGE III/ISS L1B Solar Event Transmission Data (HDF-EOS) V051, URL [https://doi.org/10.5067/ISS/SAGEIII/SOLAR\\_HDF4\\_L1B-V5.1](https://doi.org/10.5067/ISS/SAGEIII/SOLAR_HDF4_L1B-V5.1), 2017.
- Navarro, M. A., Atlas, E. L., Saiz-Lopez, A., Rodriguez-Lloveras, X., Kinnison, D. E., Lamarque, J.-F., Tilmes, S., Filus, M., Harris, N. R., Meneguz, E., et al.: Airborne measurements of organic bromine compounds in the Pacific tropical tropopause layer, *Proceedings of the National Academy of Sciences*, 112, 13789–13793, 2015.
- Novelli, P. C., Masarie, K. A., and Lang, P. M.: Distributions and recent changes of carbon monoxide in the lower troposphere, *J. Geophys. Res. Atmos.*, 103, 19015–19033, <https://doi.org/10.1029/98JD01366>, 1998.
- Obersteiner, F., Keber, T., Engel, A., Bönisch, H., and O’Doherty, S.: A versatile, refrigerant-and cryogen-free cryofocusing–thermodesorption unit for preconcentration of traces gases in air., *Atmos. Meas. Tech.*, 9, 2016.
- Orbe, C., Waugh, D. W., and Newman, P. A.: Air-mass origin in the tropical lower stratosphere: The influence of Asian boundary layer air, *Geophys. Res. Lett.*, 42, 4240–4248, <https://doi.org/10.1002/2015GL063937>, 2015GL063937, 2015.
- Ordóñez, C., Lamarque, J.-F., Tilmes, S., Kinnison, D. E., Atlas, E. L., Blake, D. R., Sousa Santos, G., Brasseur, G., and Saiz-Lopez, A.: Bromine and iodine chemistry in a global chemistry-climate model: description and evaluation of very short-lived oceanic sources, *Atmos. Chem. Phys.*, 12, 1423–1447, <https://doi.org/10.5194/acp-12-1423-2012>, 2012.
- Orkin, V. L., Khamaganov, V. G., Kozlov, S. N., and Kurylo, M. J.: Measurements of Rate Constants for the OH Reactions with Bromoform (CHBr<sub>3</sub>), CHBr<sub>2</sub>Cl, CHBrCl<sub>2</sub>, and Epichlorohydrin (C<sub>3</sub>H<sub>5</sub>ClO), *The Journal of Physical Chemistry A*, 117, 3809–3818, <https://doi.org/10.1021/jp3128753>, PMID: 23537427, 2013.
- Pan, L. L., Kunz, A., Homeyer, C. R., Munchak, L. A., Kinnison, D. E., and Tilmes, S.: Commentary on using equivalent latitude in the upper troposphere and lower stratosphere, *Atmos. Chem. Phys.*, 12, 9187–9199, <https://doi.org/10.5194/acp-12-9187-2012>, 2012.
- Pan, L. L., Honomichl, S. B., Kinnison, D. E., Abalos, M., Randel, W. J., Bergman, J. W., and Bian, J.: Transport of chemical tracers from the boundary layer to stratosphere associated with the dynamics of the Asian summer monsoon, *J. Geophys. Res. Atmos.*, 121, 14159–14174, <https://doi.org/10.1002/2016JD025616>, 2016.
- Pan, L. L., Atlas, E. L., Salawitch, R. J., Honomichl, S. B., Bresch, J. F., Randel, W. J., Apel, E. C., Hornbrook, R. S., Weinheimer, A. J., Anderson, D. C., Andrews, S. J., Baidar, S., Beaton, S. P., Campos, T. L., Carpenter, L. J., Chen, D., Dix, B., Donets, V., Hall, S. R., Hanisco, T. F., Homeyer, C. R., Huey, L. G., Jensen, J. B., Kaser, L., Kinnison, D. E., Koenig, T. K., Lamarque, J.-F., Liu, C., Luo, J., Luo, Z. J., Montzka, D. D., Nicely, J. M., Pierce, R. B., Riemer, D. D., Robinson, T., Romashkin, P., Saiz-Lopez, A., Schauffler, S., Shieh, O., Stell, M. H., Ullmann, K., Vaughan, G., Volkamer, R., and Wolfe, G.: The Convective Transport of Active Species in the Tropics (CONTRAST) Experiment, *Bull. Am. Meteorol. Soc.*, 98, 106–128, <https://doi.org/10.1175/BAMS-D-14-00272.1>, 2017.

- Pappalardo, G., Amodeo, A., Apituley, A., Comeron, A., Freudenthaler, V., Linné, H., Ansmann, A., Bösenberg, J., D'Amico, G., Mattis, I., Mona, L., Wandinger, U., Amiridis, V., Alados-Arboledas, L., Nicolae, D., and Wiegner, M.: EARLINET: towards an advanced sustainable European aerosol lidar network, *Atmos. Meas. Tech.*, 7, 2389–2409, <https://doi.org/10.5194/amt-7-2389-2014>, 2014.
- Parrella, J. P., Jacob, D. J., Liang, Q., Zhang, Y., Mickley, L. J., Miller, B., Evans, M. J., Yang, X., Pyle, J. A., Theys, N., and Van Roozendael, M.: Tropospheric bromine chemistry: implications for present and pre-industrial ozone and mercury, *Atmos. Chem. Phys.*, 12, 6723–6740, <https://doi.org/10.5194/acp-12-6723-2012>, 2012.
- Parrella, J. P., Chance, K., Salawitch, R. J., Canty, T., Dorf, M., and Pfeilsticker, K.: New retrieval of BrO from SCIAMACHY limb: an estimate of the stratospheric bromine loading during April 2008, *Atmos. Meas. Tech.*, 6, 2549–2561, <https://doi.org/10.5194/amt-6-2549-2013>, 2013.
- Pertain, P. T., Heidinger, A. K., and Stephens, G. L.: High spectral resolution atmospheric radiative transfer: Application of the equivalence theorem, *J. Geophys. Res. Atmos.*, 105, 2163–2177, <https://doi.org/10.1029/1999JD900328>, 2000.
- Pasch, R. J., Penny, A. B., and Berg, R.: National Hurricane Center Tropical Cyclone Report: Hurricane Maria (AL152017), Tech. rep., NOAA: National Hurricane Center, Miami, FL, USA, [https://www.nhc.noaa.gov/data/tcr/AL152017\\_Maria.pdf](https://www.nhc.noaa.gov/data/tcr/AL152017_Maria.pdf), 2019.
- Perliski, L. M. and Solomon, S.: On the evaluation of air mass factors for atmospheric near-ultraviolet and visible absorption spectroscopy, *J. Geophys. Res. Atmos.*, 98, 10 363–10 374, <https://doi.org/doi.org/10.1029/93JD00465>, 1993.
- Petty, G. W.: *A First Course In Atmospheric Radiation (Second Edition)*, ISBN 978-0-9729033-1-8, Sundog Publishing, Madison, Wisconsin, USA, 2006.
- Pfeilsticker, K., Sturges, W. T., Bösch, H., Camy-Peyret, C., Chipperfield, M. P., Engel, A., Fitzenberger, R., Müller, M., Payan, S., and Sinnhuber, B.-M.: Lower stratospheric organic and inorganic bromine budget for the Arctic winter 1998/99, *Geophys. Res. Lett.*, 27, 3305–3308, <https://doi.org/10.1029/2000GL011650>, 2000.
- Pielke, R. A.: *Layers of Earth's Atmosphere in Atmosphere: Gaseous Envelope*, Encyclopædia Britannica, Inc., URL <https://www.britannica.com/science/atmosphere/Troposphere#/media/1/41364/99826>, (accessed: 15.02.2021), 2021.
- Platt, U. and Stutz, J.: *Differential Optical Absorption Spectroscopy (DOAS), Principle and Applications*, ISBN 3-340-21193-4, Springer Verlag, Heidelberg, <https://doi.org/10.1007/978-3-540-75776-4>, 2008.
- Platt, U., Marquard, L., Wagner, T., and Perner, D.: Corrections for zenith scattered light DOAS, *Geophysical Research Letters*, 24, 1759–1762, <https://doi.org/10.1029/97GL01693>, 1997.
- Ploeger, F., Günther, G., Konopka, P., Fueglistaler, S., Müller, R., Hoppe, C., Kunz, A., Spang, R., Groß, J.-U., and Riese, M.: Horizontal water vapor transport in the lower stratosphere from subtropics to high latitudes during boreal summer, *J. Geophys. Res. Atmos.*, 118, 8111–8127, <https://doi.org/10.1002/jgrd.50636>, 2013.
- Ploeger, F., Abalos, M., Birner, T., Konopka, P., Legras, B., Müller, R., and Riese, M.: Quantifying the effects of mixing and residual circulation on trends of stratospheric mean age of air, *Geophysical Research Letters*, 42, 2047–2054, 2015.
- Pollack, J. B., Toon, O. B., and Wiedman, D.: Radiative properties of the background stratospheric aerosols and implications for perturbed conditions, *Geophysical Research Letters*, 8, 26–28, <https://doi.org/10.1029/GL008i001p00026>, 1981.

- Polvani, L. M., Previdi, M., England, M. R., Chiodo, G., and Smith, K. L.: Substantial twentieth-century Arctic warming caused by ozone-depleting substances, *Nat. Clim. Chang.*, 10, 130–133, <https://doi.org/10.1038/s41558-019-0677-4>, 2020.
- Pommrich, R., Müller, R., Grooß, J.-U., Konopka, P., Ploeger, F., Vogel, B., Tao, M., Hoppe, C. M., Günther, G., Spelten, N., Hoffmann, L., Pumphrey, H.-C., Viciani, S., D’Amato, F., Volk, C. M., Hoor, P., Schlager, H., and Riese, M.: Tropical troposphere to stratosphere transport of carbon monoxide and long-lived trace species in the Chemical Lagrangian Model of the Stratosphere (CLaMS), *Geoscientific Model Development*, 7, 2895–2916, <https://doi.org/10.5194/gmd-7-2895-2014>, 2014.
- Prinn, R. G., Weiss, R. F., Arduini, J., Arnold, T., DeWitt, H. L., Fraser, P. J., Ganesan, A. L., Gasore, J., Harth, C. M., Hermansen, O., Kim, J., Krummel, P. B., Li, S., Loh, Z. M., Lunder, C. R., Maione, M., Manning, A. J., Miller, B. R., Mitrevski, B., Mühle, J., O’Doherty, S., Park, S., Reimann, S., Rigby, M., Saito, T., Salameh, P. K., Schmidt, R., Simmonds, P. G., Steele, L. P., Vollmer, M. K., Wang, R. H., Yao, B., Yokouchi, Y., Young, D., and Zhou, L.: History of chemically and radiatively important atmospheric gases from the Advanced Global Atmospheric Gases Experiment (AGAGE), *Earth System Science Data*, 10, 985–1018, <https://doi.org/10.5194/essd-10-985-2018>, 2018.
- Puķite, J. and Wagner, T.: Quantification and parametrization of non-linearity effects by higher-order sensitivity terms in scattered light differential optical absorption spectroscopy., *Atmos. Meas. Tech.*, 9, 2016.
- Quack, B., Atlas, E., Petrick, G., Stroud, V., Schauffler, S., and Wallace, D.: Oceanic bromoform sources for the tropical atmosphere, *Geophys. Res. Lett.*, 31, <https://doi.org/10.1029/2004GL020597>, 2004.
- Ray, E. A., Moore, F. L., Elkins, J. W., Rosenlof, K. H., Laube, J. C., Röckmann, T., Marsh, D. R., and Andrews, A. E.: Quantification of the SF<sub>6</sub> lifetime based on mesospheric loss measured in the stratospheric polar vortex, *J. Geophys. Res. Atmos.*, 122, 4626–4638, <https://doi.org/10.1002/2016JD026198>, 2017.
- Riese, M., Ploeger, F., Rap, A., Vogel, B., Konopka, P., Dameris, M., and Forster, P.: Impact of uncertainties in atmospheric mixing on simulated UTLS composition and related radiative effects, *J. Geophys. Res. Atmos.*, 117, 2012.
- Riese, M., Kaufmann, M., and Hoor, P.: WISE 2017 (Wave-driven ISentropic Exchange), URL <https://www.wise2017.de>, (accessed: 07.07.2020), 2017.
- Rigby, M., Park, S., Saito, T., Western, L., Redington, A., Fang, X., Henne, S., Manning, A., Prinn, R., Dutton, G., et al.: Increase in CFC-11 emissions from eastern China based on atmospheric observations, *Nature*, 569, 546–550, 2019.
- Rolf, C., Vogel, B., Hoor, P., Afchine, A., Günther, G., Krämer, M., Müller, R., Müller, S., Spelten, N., and Riese, M.: Water vapor increase in the lower stratosphere of the Northern Hemisphere due to the Asian monsoon anticyclone observed during the TACTS/ESMVal campaigns, *Atmos. Chem. Phys.*, 18, 2973–2983, <https://doi.org/10.5194/acp-18-2973-2018>, 2018.
- Rothman, L. S., Gordon, I. E., Barbe, A., Benner, D. C., Bernath, P. F., Birk, M., Boudon, V., Brown, L. R., Campargue, A., Champion, J.-P., Chance, K., Coudert, L. H., Dana, V., Devi, V. M., Fally, S., Flaud, J.-M., Gamache, R. R., Goldman, A., Jacquemart, D., Kleiner, I., Lacombe, N., Lafferty, W. J., Mandin, J.-Y., Massie, S. T., Mikhailenko, S. N., Miller, C. E., Moazzen-Ahmadi, N., Naumenko, O. V., Nikitin, A. V., Orphal, J., Perevalov, V. I., Perrin, A., Predoi-Cross, A., Rinsland, C. P., Rotger, M., Šimečková, M., Smith, M. A. H., Sung, K., Tashkun, S. A., Tennyson, J., Toth, R. A., Vandaele, A. C., and Vander Auwera, J.: The HITRAN 2008 molecular spectroscopic database, *J. Quant. Spectrosc. Ra.*, 110, 533–572, <https://doi.org/10.1016/j.jqsrt.2009.02.013>, 2009.
- Rozanov, A., Kühn, S., Doicu, A., McLinden, C., Puķite, J., Bovensmann, H., Burrows, J. P., Deutschmann, T., Dorf, M., Goutail, F., Grunow, K., Hendrick, F., von Hobe, M., Hrechanyy, S., Lichtenberg, G., Pfeilsticker, K., Pommereau, J. P., Van Roozendaal, M., Stroh, F., and Wagner,

- T.: BrO vertical distributions from SCIAMACHY limb measurements: comparison of algorithms and retrieval results, *Atmos. Meas. Tech.*, 4, 1319–1359, <https://doi.org/10.5194/amt-4-1319-2011>, 2011.
- S. Chapman, F.: XXXV. On ozone and atomic oxygen in the upper atmosphere, *The London, Edinburgh, and Dublin Philosophical Magazine and Journal of Science*, 10, 369–383, <https://doi.org/10.1080/14786443009461588>, 1930.
- Sakazaki, T., Fujiwara, M., Mitsuda, C., Imai, K., Manago, N., Naito, Y., Nakamura, T., Akiyoshi, H., Kinnison, D., Sano, T., Suzuki, M., and Shiotani, M.: Diurnal ozone variations in the stratosphere revealed in observations from the Superconducting Submillimeter-Wave Limb-Emission Sounder (SMILES) on board the International Space Station (ISS), *J. Geophys. Res. Atmos.*, 118, 2991–3006, <https://doi.org/10.1002/jgrd.50220>, 2013.
- Sala, S., Bönisch, H., Keber, T., Oram, D., Mills, G., and Engel, A.: Deriving an atmospheric budget of total organic bromine using airborne in-situ measurements from the Western Pacific during SHIVA., *Atmospheric Chemistry & Physics*, 14, 2014.
- Salawitch, R. J., Weisenstein, D. K., Kovalenko, L. J., Sioris, C. E., Wennberg, P. O., Chance, K., Ko, M. K. W., and McLinden, C. A.: Sensitivity of ozone to bromine in the lower stratosphere, *Geophys. Res. Lett.*, 32, <https://doi.org/10.1029/2004GL021504>, 2005.
- Sander, S., Friedl, R., Abbat, J., Barker, J., Burkholder, J., Golden, D., Kolb, C., Kurylo, M., Moortgat, G., Wine, P., Huie, R., and Orkin, V.: Chemical kinetics and photochemical data for use in atmospheric studies: Evaluation Number 17, NASA Jet Propulsion Laboratory, 17, URL <http://jpldataeval.jpl.nasa.gov/pdf/JPL%2010-6%20Final%2015June2011.pdf>, 2011.
- Schäfler, A., Fix, A., and Wirth, M.: Mixing at the extratropical tropopause as characterized by collocated airborne H<sub>2</sub>O and O<sub>3</sub> lidar observations, *Atmos. Chem. and Phys.*, 21, 5217–5234, <https://doi.org/10.5194/acp-21-5217-2021>, 2021.
- Schanz, A., Hocke, K., and Kämpfer, N.: Daily ozone cycle in the stratosphere: global, regional and seasonal behaviour modelled with the Whole Atmosphere Community Climate Model, *Atmos. Chem. and Phys.*, 14, 7645–7663, <https://doi.org/10.5194/acp-14-7645-2014>, 2014.
- Schauffler, S., Atlas, E., Blake, D., Flocke, F., Lueb, R., Lee-Taylor, J., Stroud, V., and Travnicsek, W.: Distribution of brominated organic compounds in the upper troposphere and lower stratosphere, *J. Geophys. Res.*, 104, 21 513–21 535, <https://doi.org/10.1029/1999JD900197>, 1999.
- Schauffler, S. M., Heidt, L. E., Pollock, W. H., Gilpin, T. M., Vedder, J. F., Solomon, S., Lueb, R. A., and Atlas, E. L.: Measurements of halogenated organic compounds near the tropical tropopause, *Geophys. Res. Lett.*, 20, 2567–2570, <https://doi.org/10.1029/93GL02840>, 1993.
- Schauffler, S. M., Atlas, E. L., Flocke, F., Lueb, R. A., Stroud, V., and Travnicsek, W.: Measurement of bromine-containing organic compounds at the tropical tropopause, *Geophys. Res. Lett.*, 25, 317–320, <https://doi.org/10.1029/98GL00040>, 1998.
- Schmidt, J. A., Jacob, D., Horowitz, H. M., Hu, L., Sherwen, T., Evans, M. J., Liang, Q., Suleiman, R. M., Oram, D., Le Breton, M., et al.: Modeling the observed tropospheric BrO background: Importance of multiphase chemistry and implications for ozone, OH, and mercury, *J. Geophys. Res. Atmos.*, 121, 11–819, 2016.
- Schreiner, B.: Aircraft-borne measurements of nitrogen dioxide, formaldehyde, and nitrous acid in the lower and middle troposphere during the EMERGe-EU<sup>1</sup> campaign, Master thesis, Ruprecht-Karls-Universität Heidelberg, Heidelberg, Germany, 2018.
- Selkirk, H. B.: The tropopause cold trap in the Australian monsoon during STEP/AMEX 1987, *J. Geophys. Res. Atmos.*, 98, 8591–8610, <https://doi.org/10.1029/92JD02932>, 1993.

- Serdyuchenko, A., Gorshelev, V., Weber, M., Chehade, W., and Burrows, J. P.: High spectral resolution ozone absorption cross-sections - Part 2: Temperature dependence, *Atmos. Meas. Tech.*, 7, 625–636, <https://doi.org/10.5194/amt-7-625-2014>, 2014.
- Shepherd, T. G.: Issues in Stratosphere-troposphere Coupling, *Journal of the Meteorological Society of Japan. Ser. II*, 80, 769–792, <https://doi.org/10.2151/jmsj.80.769>, 2002.
- Sinnhuber, B.-M. and Folkins, I.: Estimating the contribution of bromoform to stratospheric bromine and its relation to dehydration in the tropical tropopause layer, *Atmos. Chem. Phys.*, 6, 4755–4761, <https://doi.org/10.5194/acp-6-4755-2006>, 2006.
- Sinnhuber, B.-M., Rozanov, A., Sheode, N., Afe, O. T., Richter, A., Sinnhuber, M., Wittrock, F., Burrows, J. P., Stiller, G. P., von Clarmann, T., and Linden, A.: Global observations of stratospheric bromine monoxide from SCIAMACHY, *Geophys. Res. Lett.*, 32, <https://doi.org/10.1029/2005GL023839>, 2005.
- Sinnhuber, B.-M., Sheode, N., Sinnhuber, M., Chipperfield, M. P., and Feng, W.: The contribution of anthropogenic bromine emissions to past stratospheric ozone trends: a modelling study, *Atmospheric Chemistry and Physics*, 9, 2863–2871, <https://doi.org/10.5194/acp-9-2863-2009>, 2009.
- Sioris, C. E., Kovalenko, L. J., McLinden, C. A., Salawitch, R. J., Van Roozendaal, M., Goutail, F., Dorf, M., Pfeilsticker, K., Chance, K., von Savigny, C., Liu, X., Kurosu, T. P., Pommereau, J.-P., Bösch, H., and Frerick, J.: Latitudinal and vertical distribution of bromine monoxide in the lower stratosphere from Scanning Imaging Absorption Spectrometer for Atmospheric Cartography limb scattering measurements, *J. Geophys. Res. Atmos.*, 111, <https://doi.org/10.1029/2005JD006479>, 2006.
- Slaper, H., Velder, G. J., Danie, J. S., Gruijl, F. R., and van der Leun, J. C.: Estimates of ozone depletion and skin cancer incidence to examine the Vienna Convention achievements, *Nature*, 384, 256–258, <https://doi.org/10.1038/384256a0>, 1996.
- Solomon, S., Garci, R. R., and Ravishankara, A. R.: On the role of iodine in ozone depletion, *J. Geophys. Res. Atmos.*, 99, 20 491–20 499, <https://doi.org/10.1029/94JD02028>, 1994.
- Stachnik, R. A., Millán, L., Jarnot, R., Monroe, R., McLinden, C., Kühn, S., Pukite, J., Shiotani, M., Suzuki, M., Kasai, Y., Goutail, F., Pommereau, J. P., Dorf, M., and Pfeilsticker, K.: Stratospheric BrO abundance measured by a balloon-borne submillimeterwave radiometer, *Atmos. Chem. Phys.*, 13, 3307–3319, <https://doi.org/10.5194/acp-13-3307-2013>, 2013.
- Stephens, G. L., Li, J., Wild, M., Clayson, C. A., Loeb, N., Kato, S., L’Ecuyer, T., Stackhouse Jr, P. W., Lebsock, M., and Andrews, T.: An update on Earth’s energy balance in light of the latest global observations, *Nature Geosci.*, 5, 691–696, <https://doi.org/10.1038/ngeo1580>, 2012.
- Stewart, S. R.: National Hurricane Center Tropical Cyclone Report: Hurricane Ophelia (AL172017), Tech. rep., NOAA: National Hurricane Center, Miami, FL, USA, [https://www.nhc.noaa.gov/data/tcr/AL172017\\_Ophelia.pdf](https://www.nhc.noaa.gov/data/tcr/AL172017_Ophelia.pdf), 2018.
- Stutz, J., Werner, B., Spolaor, M., Scalone, L., Festa, J., Tsai, C., Cheung, R., Colosimo, S. F., Tricoli, U., Raecke, R., et al.: A new Differential Optical Absorption Spectroscopy instrument to study atmospheric chemistry from a high-altitude unmanned aircraft, *Atmos. Meas. Tech.*, 10, 1017–1042, 2017.
- Thalman, R. and Volkamer, R.: Temperature dependent absorption cross-sections of O<sub>2</sub>-O<sub>2</sub> collision pairs between 340 and 630 nm and at atmospherically relevant pressure, *Phys. Chem. Chem. Phys.*, 15, 15 371–15 381, <https://doi.org/10.1039/C3CP50968K>, 2013.
- U.S. EPA: Updating the Atmospheric and Health Effects Framework Model: Stratospheric Ozone Protection and Human Health Benefits (EPA Publication Number

- 430R20005), Stratospheric Protection Division, Office of Air and Radiation, U.S. Environmental Protection Agency, URL <https://www.epa.gov/ozone-layer-protection/atmospheric-and-health-effects-framework-model-estimating-ultraviolet>, (accessed: 18.03.2021), 2020.
- Velders, G. J. M., Andersen, S. O., Daniel, J. S., Fahey, D. W., and McFarland, M.: The importance of the Montreal Protocol in protecting climate, *Proceedings of the National Academy of Sciences*, 104, 4814–4819, <https://doi.org/10.1073/pnas.0610328104>, 2007.
- Vogel, B., Pan, L. L., Konopka, P., Günther, G., Müller, R., Hall, W., Campos, T., Pollack, I., Weinheimer, A., Wei, J., Atlas, E. L., and Bowman, K. P.: Transport pathways and signatures of mixing in the extratropical tropopause region derived from Lagrangian model simulations, *J. Geophys. Res. Atmos.*, 116, <https://doi.org/10.1029/2010JD014876>, 2011.
- Vogel, B., Günther, G., Müller, R., Groß, J., Hoor, P., Krämer, M., Müller, S., Zahn, A., and Riese, M.: Fast transport from Southeast Asia boundary layer sources to northern Europe: rapid uplift in typhoons and eastward eddy shedding of the Asian monsoon anticyclone, *Atmos. Chem. Phys.*, 14, 12–745, 2014.
- Vogel, B., Günther, G., Müller, R., Groß, J.-U., and Riese, M.: Impact of different Asian source regions on the composition of the Asian monsoon anticyclone and of the extratropical lowermost stratosphere, *Atmos. Chem. Phys.*, 15, 13 699–13 716, <https://doi.org/10.5194/acp-15-13699-2015>, 2015.
- Vogel, B., Günther, G., Müller, R., Groß, J.-U., Afchine, A., Bozem, H., Hoor, P., Krämer, M., Müller, S., Riese, M., Rolf, C., Spelten, N., Stiller, G. P., Ungermann, J., and Zahn, A.: Long-range transport pathways of tropospheric source gases originating in Asia into the northern lower stratosphere during the Asian monsoon season 2012, *Atmos. Chem. Phys.*, 16, 15 301–15 325, <https://doi.org/10.5194/acp-16-15301-2016>, 2016.
- Vogel, B., Müller, R., Günther, G., Spang, R., Hanumanthu, S., Li, D., Riese, M., and Stiller, G. P.: Lagrangian simulations of the transport of young air masses to the top of the Asian monsoon anticyclone and into the tropical pipe, *Atmos. Chem. Phys.*, 19, 6007–6034, <https://doi.org/10.5194/acp-19-6007-2019>, 2019.
- Vollmer, M. K., Mühle, J., Trudinger, C. M., Rigby, M., Montzka, S. A., Harth, C. M., Miller, B. R., Henne, S., Krummel, P. B., Hall, B. D., Young, D., Kim, J., Arduini, J., Wenger, A., Yao, B., Reimann, S., O’Doherty, S., Maione, M., Etheridge, D. M., Li, S., Verdonik, D. P., Park, S., Dutton, G., Steele, L. P., Lunder, C. R., Rhee, T. S., Hermansen, O., Schmidbauer, N., Wang, R. H. J., Hill, M., Salameh, P. K., Langenfelds, R. L., Zhou, L., Blunier, T., Schwander, J., Elkins, J. W., Butler, J. H., Simmonds, P. G., Weiss, R. F., Prinn, R. G., and Fraser, P. J.: Atmospheric histories and global emissions of halons H-1211 (CBrClF<sub>2</sub>), H-1301 (CBrF<sub>3</sub>), and H-2402 (CBrF<sub>2</sub>CBrF<sub>2</sub>), *J. Geophys. Res. Atmos.*, <https://doi.org/10.1002/2015JD024488>, 2016.
- von Hobe, M., Ploeger, F., Konopka, P., Kloss, C., Ulanowski, A., Yushkov, V., Ravagnani, F., Volk, C. M., Pan, L. L., Honomichl, S. B., Tilmes, S., Kinnison, D. E., Garcia, R. R., and Wright, J. S.: Upward transport into and within the Asian monsoon anticyclone as inferred from StratoClim trace gas observations, *Atmos. Chem. Phys.*, 21, 1267–1285, <https://doi.org/10.5194/acp-21-1267-2021>, 2021.
- Vountas, M., Rozanov, V., and Burrows, J.: Ring effect: Impact of rotational Raman scattering on radiative transfer in Earth’s atmosphere, *Journal of Quantitative Spectroscopy and Radiative Transfer*, 60, 943–961, [https://doi.org/10.1016/S0022-4073\(97\)00186-6](https://doi.org/10.1016/S0022-4073(97)00186-6), 1998.
- Wagner, T., Chance, K., Frieß, U., Gil, M., Goutail, F., Hönninger, G., Johnston, P., Karlsen-Tørnkvist, K., Kostadinov, I., Leser, H., et al.: Correction of the Ring effect and I0-effect for DOAS observations of scattered sunlight, in: 1st DOAS Workshop, Heidelberg, Germany, pp. 13–14, 2001.

- Wagner, T., Burrows, J. P., Deutschmann, T., Dix, B., von Friedeburg, C., Frieß, U., Hendrick, F., Heue, K.-P., Irie, H., Iwabuchi, H., Kanaya, Y., Keller, J., McLinden, C. A., Oetjen, H., Palazzi, E., Petritoli, A., Platt, U., Postyljakov, O., Puķīte, J., Richter, A., van Roozendaal, M., Rozanov, A., Rozanov, V., Sinreich, R., Sanghavi, S., and Wittrock, F.: Comparison of box-air-mass-factors and radiances for Multiple-Axis Differential Optical Absorption Spectroscopy (MAX-DOAS) geometries calculated from different UV/visible radiative transfer models, *Atmos. Chem. Phys.*, 7, 1809–1833, <https://doi.org/10.5194/acp-7-1809-2007>, 2007.
- Wales, P. A., Salawitch, R. J., Nicely, J. M., Anderson, D. C., Canty, T. P., Baidar, S., Dix, B., Koenig, T. K., Volkamer, R., Chen, D., Huey, L. G., Tanner, D. J., Cuevas, C. A., Fernandez, R. P., Kinnison, D. E., Lamarque, J.-F., Saiz-Lopez, A., Atlas, E. L., Hall, S. R., Navarro, M. A., Pan, L. L., Schauffler, S. M., Stell, M., Tilmes, S., Ullmann, K., Weinheimer, A. J., Akiyoshi, H., Chipperfield, M. P., Deushi, M., Dhomse, S. S., Feng, W., Graf, P., Hossaini, R., Jöckel, P., Mancini, E., Michou, M., Morgenstern, O., Oman, L. D., Pitari, G., Plummer, D. A., Revell, L. E., Rozanov, E., Saint-Martin, D., Schofield, R., Stenke, A., Stone, K. A., Visionsi, D., Yamashita, Y., and Zeng, G.: Stratospheric Injection of Brominated Very Short-Lived Substances: Aircraft Observations in the Western Pacific and Representation in Global Models, *J. Geophys. Res. Atmos.*, 123, 5690–5719, <https://doi.org/10.1029/2017JD027978>, 2018.
- Wang, S., Schmidt, J. A., Baidar, S., Coburn, S., Dix, B., Koenig, T. K., Apel, E., Bowdalo, D., Campos, T. L., Eloranta, E., Evans, M. J., DiGangi, J. P., Zondlo, M. A., Gao, R.-S., Haggerty, J. A., Hall, S. R., Hornbrook, R. S., Jacob, D., Morley, B., Pierce, B., Reeves, M., Romashkin, P., ter Schure, A., and Volkamer, R.: Active and widespread halogen chemistry in the tropical and subtropical free troposphere, *Proc. Natl. Acad. Sci.*, 112, 9281–9286, <https://doi.org/10.1073/pnas.1505142112>, 2015.
- Wang, S., Kinnison, D., Montzka, S. A., Apel, E. C., Hornbrook, R. S., Hills, A. J., Blake, D. R., Barletta, B., Meinardi, S., Sweeney, C., Moore, F., Long, M., Saiz-Lopez, A., Fernandez, R. P., Tilmes, S., Emmons, L. K., and Lamarque, J.: Ocean Biogeochemistry Control on the Marine Emissions of Brominated Very Short-Lived Ozone-Depleting Substances: A Machine-Learning Approach, *J. Geophys. Res. Atmos.*, 124, 12 319–12 339, <https://doi.org/10.1029/2019JD031288>, 2019.
- Warwick, N. J., Pyle, J. A., Carver, G. D., Yang, X., Savage, N. H., O'Connor, F. M., and Cox, R. A.: Global modeling of biogenic bromocarbons, *J. Geophys. Res.*, 111, D24 305, <https://doi.org/10.1029/2006JD007264>, 2006.
- Wendisch, M. and Schwarz, A.: Atmospheric and Earth System Research with the High Altitude and Long Range Research Aircraft (HALO), <http://www.halo-spp.de/>, (Last accessed: 14.08.2020), 2020.
- Werner, B., Stutz, J., Spolaor, M., Scalone, L., Raecke, R., Festa, J., Colosimo, S. F., Cheung, R., Tsai, C., Hossaini, R., Chipperfield, M. P., Taverna, G. S., Feng, W., Elkins, J. W., Fahey, D. W., Gao, R.-S., Hints, E. J., Thornberry, T. D., Moore, F. L., Navarro, M. A., Atlas, E., Daube, B. C., Pittman, J., Wofsy, S., , and Pfeilsticker, K.: Probing the subtropical lowermost stratosphere and the tropical upper troposphere and tropopause layer for inorganic bromine, *Atmos. Chem. Phys.*, 17, 1161–1186, <https://doi.org/10.5194/acp-17-1161-2017>, 2017.
- Wetzel, G., Oelhaf, H., Höpfner, M., Friedl-Vallon, F., Ebersoldt, A., Gulde, T., Kazarski, S., Kirner, O., Kleinert, A., Maucher, G., Nordmeyer, H., Orphal, J., Ruhnke, R., and Sinnhuber, B.-M.: Diurnal variations of BrONO<sub>2</sub> observed by MIPAS-B at midlatitudes and in the Arctic, *Atmos. Chem. Phys.*, 17, 14 631–14 643, <https://doi.org/10.5194/acp-17-14631-2017>, 2017.
- Wetzel, G., Friedl-Vallon, F., Glatthor, N., Groß, J.-U., Gulde, T., Höpfner, M., Johansson, S., Khosrawi, F., Kirner, O., Kleinert, A., Kretschmer, E., Maucher, G., Nordmeyer, H., Oelhaf, H., Orphal, J., Piesch, C., Sinnhuber, B.-M., Ungermann, J., and Vogel, B.: Pollution trace gases C<sub>2</sub>H<sub>6</sub>, C<sub>2</sub>H<sub>2</sub>, HCOOH, and PAN in the North Atlantic UTLS: observations and simulations, *Atmos. Chem. Phys. Discuss.*, 2020, 1–39, <https://doi.org/10.5194/acp-2020-1215>, 2020.

- Wilmouth, D. M., Hanisco, T. F., Donahue, N. M., and Anderson, J. G.: Fourier transform ultraviolet spectroscopy of the  $A^2\Pi_{3/2} \leftarrow X^2\Pi_{3/2}$  transition of BrO, *The journal of physical chemistry a*, 103, 8935–8945, 1999.
- Wisher, A., Oram, D., Laube, J., Mills, G., Van Velthoven, P., Zahn, A., and Brenninkmeijer, C.: Very short-lived bromomethanes measured by the CARIBIC observatory over the North Atlantic, Africa and Southeast Asia during 2009–2013, *Atmos. Chem. Phys.*, 14, 3557–3570, 2014.
- WMO: Meteorology A Three-Dimensional Science: Second Session of the Commission for Aerology, World Meteorological Organisation (WMO), Geneva, Switzerland, VI, 137, 1957.
- WMO: Scientific assessment of ozone depletion: 2010, *Global Ozone Research and Monitoring Project No. 52*, World Meteorological Organisation (WMO), Geneva, Switzerland, 52, 516pp, 2011.
- WMO: Scientific assessment of ozone depletion: 2018, *Global Ozone Research and Monitoring Project No. 58*, World Meteorological Organisation (WMO), Geneva, Switzerland, 58, 588pp, 2018.
- Wofsy, S. C., McElroy, M. B., and Yung, Y. L.: The chemistry of atmospheric bromine, *Geophysical Research Letters*, 2, 215–218, <https://doi.org/10.1029/GL002i006p00215>, 1975.
- Yan, X., Konopka, P., Ploeger, F., Podglajen, A., Wright, J. S., Müller, R., and Riese, M.: The efficiency of transport into the stratosphere via the Asian and North American summer monsoon circulations, *Atmos. Chem. Phys.*, 19, 15 629–15 649, <https://doi.org/10.5194/acp-19-15629-2019>, 2019.
- Yang, X., Cox, R. A., Warwick, N. J., Pyle, J. A., Carver, G. D., O'Connor, F. M., and Savage, N. H.: Tropospheric bromine chemistry and its impacts on ozone: A model study, *J. Geophys. Res. Atmos.*, 110, <https://doi.org/10.1029/2005JD006244>, 2005.
- Yokouchi, Y., Hasebe, F., Fujiwara, M., Takashima, H., Shiotani, M., Nishi, N., Kanaya, Y., Hashimoto, S., Fraser, P., Toom-Sauntry, D., Mukai, H., and Nojiri, Y.: Correlations and emission ratios among bromoform, dibromochloromethane, and dibromomethane in the atmosphere, *J. Geophys. Res. Atmos.*, 110, <https://doi.org/10.1029/2005JD006303>, d23309, 2005.
- Zahn, A., Weppner, J., Widmann, H., Schlote-Holubek, K., Burger, B., Kühner, T., and Franke, H.: A fast and precise chemiluminescence ozone detector for eddy flux and airborne application, *Atmos. Meas. Tech.*, 5, 363–375, <https://doi.org/10.5194/amt-5-363-2012>, 2012.
- Ziska, F., Quack, B., Abrahamsson, K., Archer, S. D., Atlas, E., Bell, T., Butler, J. H., Carpenter, L. J., Jones, C. E., Harris, N. R. P., Hepach, H., Heumann, K. G., Hughes, C., Kuss, J., Krüger, K., Liss, P., Moore, R. M., Orlikowska, A., Raimund, S., Reeves, C. E., Reifenhäuser, W., Robinson, A. D., Schall, C., Tanhua, T., Tegtmeier, S., Turner, S., Wang, L., Wallace, D., Williams, J., Yamamoto, H., Yvon-Lewis, S., and Yokouchi, Y.: Global sea-to-air flux climatology for bromoform, dibromomethane and methyl iodide, *Atmos. Chem. Phys.*, 13, 8915–8934, <https://doi.org/10.5194/acp-13-8915-2013>, 2013.
- Ziska, F., Quack, B., Tegtmeier, S., Stemmler, I., and Krüger, K.: Future emissions of marine halogenated very-short lived substances under climate change, *J. Atmos. Chem.*, 74, 245– 260, <https://doi.org/10.1007/s10874-016-9355-3>, 2017.

# Acknowledgements

I would first and foremost like to thank my supervisor Prof. Dr. Klaus Pfeilsticker for his continuous support as well as the many research campaigns where he provided the opportunity to partake in. His guidance and discussions were always helpful and encouraging. Second, I would like to thank my fellow group members for their help in operating the mini-DOAS instrument and comradery during the many campaigns as well as analysis procedures and work at the IUP.

I would like to thank the Deutsches Zentrum für Luft- und Raumfahrt (DLR) for the support to get the mini-DOAS instrument certified and the DLR Flugexperimente Team at Oberpfaffenhofen, in particular, Frank Probst, Martina Hierle, Dr. Andreas Minikin, and Andrea Hausold, for the support given during the WISE mission. Special thanks also to the scientific coordinators of the WISE campaign, Prof. Dr. Peter Hoor (University Mainz) and Prof. Dr. Martin Riese (Forschungszentrum Jülich; FZJ).

I would further like to thank the following groups for providing the diverse data sets as well as feedback of the analysis covered in this dissertation. They include Prof. Dr. Andreas Engel, Timo Keber and Dr. Tanja Schuck from the Goethe University Frankfurt who provided the GhOST measurements; Dr. Andreas Zahn and his group from the Karlsruhe Institute of Technology (KIT) who provided FAIRO data; and Prof. Dr. Peter Hoor and Dr. Vera Bense from the Johannes Gutenberg University Mainz who provided the UMAQS data. Additionally, I would like to thank Dr. Jens-Uwe Groß and Dr. Bärbel Vogel from the FZJ who provided the CLaMS simulations; and Prof. Dr. Martyn Chipperfield from the University of Leeds who provided the TOMCAT model results. I would like to acknowledge the computing time for the CLaMS curtain simulations were granted on the supercomputer JURECA at Jülich Supercomputing Centre (JSC), and the TOMCAT/SLIMCAT simulations were performed on the Leeds ARC and national Archer HPC machines. The HALO aircraft, instrument measurements, and model simulations used in this dissertation were funded by a variety of projects by the German Research Foundation (Deutsche Forschungsgemeinschaft; DFG), German Federal Ministry of Education and Research (BMBF), and the NERC SISLAC project.

I acknowledge EARLINET for providing aerosol LIDAR profiles available at <https://data.earlinet.org/>. The research leading to these results has received funding from the European Union's Horizon 2020 research and innovation programme under grant agreement No 654109 and previously from the European Union Seventh Framework Programme (FP7/2007-2013) under grant agreement n° 262254. I also acknowledge the use of SAGE III - ISS aerosol data, which were obtained from the NASA Langley Research Center Atmospheric Science Data Center.

And lastly, I would like to thank my family and friends for their support and encouragement throughout my education and proof reading countless documents including this dissertation.